

# Atomic structure and electronic properties of self-assembled clusters on silicon surfaces

vorgelegt von  
Diplom-Physiker  
**Martin Franz**  
geb. in Karlsruhe

Von der Fakultät II – Mathematik und Naturwissenschaften  
der Technischen Universität Berlin  
zur Erlangung des akademischen Grades

Doktor der Naturwissenschaften  
– Dr. rer. nat. –  
genehmigte Dissertation

Promotionsausschuss:

Vorsitzender: Prof. Dr. rer. nat. Thomas Möller

Berichter: Prof. Dr. rer. nat. Mario Dähne

Berichter: Priv.-Doz. Dr. rer. nat. Philipp Ebert

Tag der wissenschaftlichen Aussprache: 08. Dezember 2015

Berlin 2015



---

# Abstract

In this thesis, the growth, the atomic structure as well as the electronic properties of self-assembled magic clusters and of thin rare earth silicide films on Si surfaces are investigated using scanning tunneling microscopy and spectroscopy. Self-assembled magic clusters on surfaces are promising structures to utilize the fascinating properties of clusters as zero-dimensional nanoobjects in future applications, e.g. in high density memory devices or in catalysis.

For Sb on the Si(111)7×7 surface, the growth of pure Si clusters as well as of so-called Sb ringlike clusters is observed. The latter are found to exhibit different stoichiometries within the same basic structure by replacing Si atoms by Sb atoms, influencing strongly their electronic properties.

The widely studied magic In and Ga clusters on Si(111) are used as a model system to study the detailed charge redistribution that takes place on the surface during the cluster formation as well as the effects of cluster accumulation on the electronic properties. In addition, the Si(557) surface, which is vicinal to Si(111), is used as a template to enable the growth of one-dimensional chains of magic clusters.

Nanostructures induced by the rare earth metals Tb and Dy on Si surfaces are the material system most comprehensively studied in this thesis.

For Dy and Tb on Si(111), the same two types of magic clusters are observed, which is related to the chemical similarity of the trivalent rare earth metals. These are the so-called off-center rare earth silicide cluster and the centered rare earth silicide clusters, for which the atomic structure could be identified and a semiconducting behavior is found by scanning tunneling spectroscopy. Moreover, the centered rare earth silicide clusters show a switching between two stable configurations.

On the Si(001)2×1 surface, a completely different growth behavior is observed. Here, also magic Dy silicide clusters form, but the clusters show a one-dimensional ordering and assemble into chains consisting of different numbers of magic clusters.

The thin film growth of Tb on Si(111) shows many similarities with the growth behavior observed for other trivalent rare earth metals in this parameter regime. For submonolayer Tb coverages, a  $2\sqrt{3}\times 2\sqrt{3}$  R30° superstructure, a 5×2 superstructure as well as nanorods showing either a 2×1 or a 4×1 superstructure on top are observed. For the 5×2 superstructure an existing structure model is refined and a detailed investigation is derived on how registry shifts lead to the different configurations of this structure. In the monolayer-to-multilayer regime, the growth of the TbSi<sub>2</sub> monolayer with 1×1 periodicity and of the Tb<sub>3</sub>Si<sub>5</sub> multilayer with  $\sqrt{3}\times\sqrt{3}$  R30° periodicity is found.



---

# Zusammenfassung

Diese Arbeit untersucht das Wachstum, die atomare Struktur sowie die elektronischen Eigenschaften von selbstorganisierten magischen Clustern und dünnen Seltenerdsilizidfilmen auf Si-Oberflächen mittels Rastertunnelmikroskopie und -spektroskopie. Selbstorganisierte magische Cluster auf Oberflächen sind vielversprechende Strukturen, um die faszinierenden Eigenschaften, die Cluster als nulldimensionale Nanoobjekte aufweisen, in zukünftigen Anwendungen z. B. in hochdichten Speichermedien oder in der Katalyse nutzbar zu machen.

Für Sb auf der Si(111)7×7-Oberfläche wird das Wachstum von reinen Si-Clustern als auch von sogenannten Sb-Ringcluster beobachtet. Letzere bilden eine gleiche atomare Grundstruktur mit unterschiedlichen Stöchiometrien, indem Si-Atome durch Sb-Atome ersetzt werden, was ihre elektronischen Eigenschaften stark beeinflusst.

Die bereits ausführlich erforschten magischen In- und Ga-Cluster auf Si(111) werden als Modellsystem verwendet um die genaue Ladungsumverteilung, die während der Clusterbildung stattfindet, sowie die Effekte, die Ansammlungen von Clustern auf die elektronischen Eigenschaften haben, zu studieren. Außerdem wird die Si(557)-Oberfläche – eine Vizinalfläche zu Si(111) – als strukturiertes Substrat verwendet, um das Wachstum eindimensionaler Ketten von magischen Clustern zu ermöglichen.

Nanostrukturen, die von Seltenen Erden auf Si-Oberflächen gebildet werden, bilden das am umfangreichsten untersuchte Materialsystem in dieser Arbeit.

Aufgrund der chemischen Ähnlichkeit der dreiwertigen Seltenen Erden bilden sich die gleichen zwei Clusterarten für Tb und Dy auf der Si(111)-Oberfläche. Dies sind die sogenannten kantenzentrierten und zentrierten Seltenerdsilizidcluster, für die jeweils die atomare Struktur identifiziert und ein halbleitendes Verhalten in Rastertunnelspektroskopie Messungen beobachtet wird. Darüberhinaus zeigen die zentrierten Seltenerdsilizidcluster ein Umschalten zwischen zwei stabilen Konfigurationen.

Auf der Si(001)2×1-Oberfläche wird ein komplett anderes Wachstumsverhalten beobachtet. Hier bilden sich ebenfalls magische Dy-Silizidcluster, allerdings ordnen sich diese eindimensional und bilden Ketten bestehend aus unterschiedlich vielen magischen Clustern.

Das Wachstum dünner Tb-Silizidfilme auf Si(111) zeigt viele Ähnlichkeiten mit dem Wachstumsverhalten anderer Seltener Erden in diesem Parameterbereich. Für Submonolagenbedeckungen werden eine  $2\sqrt{3}\times 2\sqrt{3}$  R30°-Überstruktur, eine 5×2-Überstruktur sowie Nanostäbchen, die entweder eine 2×1- oder eine 4×1-Überstruktur bilden, beobachtet. Für die 5×2-Überstruktur wird ein bestehendes Strukturmodell weiterentwickelt und im Detail untersucht, wie Positionsverschiebungen unterschiedliche Konfigurationen hervorrufen. Im Bedeckungsbereich von Monolagen bis Multilagen wird das Wachstum der TbSi<sub>2</sub>-Monolage mit 1×1-Periodizität sowie das Wachstum der Tb<sub>3</sub>Si<sub>5</sub>-Multilage mit  $\sqrt{3}\times\sqrt{3}$  R30°-Periodizität gefunden.



# Contents

<b>1</b>	<b>Introduction</b>	<b>11</b>
<b>I</b>	<b>Theoretical and experimental background</b>	<b>15</b>
<b>2</b>	<b>Scanning tunneling microscopy and spectroscopy</b>	<b>17</b>
2.1	The principle of scanning tunneling microscopy . . . . .	17
2.2	Theory of tunneling . . . . .	19
2.2.1	The Bardeen approach . . . . .	19
2.2.2	The Tersoff-Hamann approximation and beyond . . . . .	21
2.3	Tunneling spectroscopy . . . . .	21
2.3.1	Voltage dependent STM images . . . . .	21
2.3.2	Point spectroscopy . . . . .	22
<b>3</b>	<b>Material system</b>	<b>25</b>
3.1	Excursion: From gas phase clusters to clusters on surfaces . . . . .	25
3.1.1	Gas phase clusters . . . . .	25
3.1.2	Clusters on surfaces . . . . .	30
3.2	Silicon . . . . .	32
3.2.1	The Si(111) surface . . . . .	33
3.2.2	The Si(557) surface . . . . .	36
3.2.3	The Si(001) surface . . . . .	37
3.3	Epitaxial growth . . . . .	39
3.4	Thin film growth techniques . . . . .	40
3.5	Self-assembled magic clusters on surfaces . . . . .	41
3.5.1	Magic clusters on the Si(111)7×7 surface . . . . .	43
3.5.2	Magic clusters on the Si(001) surface . . . . .	48
3.6	Epitaxial rare earth silicide nanostructures on Si(111) . . . . .	49
3.6.1	Submonolayer rare earth coverages on Si(111) . . . . .	49
3.6.2	Two-dimensional rare earth silicides . . . . .	52
3.6.3	Three-dimensional rare earth silicides . . . . .	53

---

<b>4</b>	<b>Experimental setup</b>	<b>57</b>
4.1	The UHV system . . . . .	57
4.2	The scanning tunneling microscope . . . . .	59
4.3	Tip preparation . . . . .	61
4.4	Sample preparation . . . . .	61
4.4.1	Preparation of clean silicon surfaces . . . . .	61
4.4.2	Growth of self-assembled nanostructures on silicon surfaces . . . . .	63
<b>II</b>	<b>Results and discussion</b>	<b>65</b>
<b>5</b>	<b>Sb induced clusters on the Si(111) surface</b>	<b>67</b>
5.1	General growth behavior . . . . .	68
5.2	Double-row clusters . . . . .	72
5.3	Magic Sb ringlike clusters . . . . .	74
5.3.1	Atomic structure of Sb ringlike clusters . . . . .	77
5.3.2	Electronic properties of Sb ringlike clusters . . . . .	81
5.4	Conclusions . . . . .	85
<b>6</b>	<b>Magic In and Ga clusters</b>	<b>87</b>
6.1	Magic In clusters on the planar Si(111) surface . . . . .	87
6.1.1	General growth behavior . . . . .	87
6.1.2	Electronic properties . . . . .	89
6.2	Magic Ga clusters on the planar Si(111) surface . . . . .	95
6.3	Magic In clusters on the Si(557) surface . . . . .	97
6.3.1	The clean Si(557) surface . . . . .	98
6.3.2	Growth of magic In clusters on Si(557) . . . . .	100
6.4	Conclusions . . . . .	106
<b>7</b>	<b>Rare earth silicide clusters on Si(111)</b>	<b>109</b>
7.1	General growth behavior . . . . .	110
7.2	Off-center rare earth silicide clusters . . . . .	112
7.2.1	Atomic structure of off-center rare earth silicide clusters . . . . .	114
7.2.2	Electronic properties of off-center rare earth silicide clusters . . . . .	115
7.3	Centered rare earth silicide clusters . . . . .	117
7.3.1	Atomic structure of centered rare earth silicide clusters . . . . .	120
7.3.2	Bistable switching of centered rare earth silicide clusters . . . . .	122
7.3.3	Electronic properties of centered rare earth silicide clusters . . . . .	127
7.4	Conclusions . . . . .	130

---

<b>8 Dy silicide clusters on the Si(001)2×1 surface</b>	<b>131</b>
8.1 General growth behavior . . . . .	131
8.2 One-dimensional ordering of Dy induced magic clusters on Si(001) . . . . .	134
8.3 Voltage dependent appearance of Dy induced magic clusters on Si(001) . . . . .	136
8.4 Structural considerations . . . . .	138
8.5 Conclusions . . . . .	141
<b>9 Thin Tb silicide films on Si(111)</b>	<b>143</b>
9.1 General growth behavior . . . . .	143
9.2 The submonolayer Tb coverage regime . . . . .	147
9.2.1 The $2\sqrt{3}\times 2\sqrt{3}$ R30° superstructure . . . . .	147
9.2.2 The 5×2 superstructure . . . . .	151
9.2.3 The 2×1 and 4×1 nanorods . . . . .	157
9.3 The monolayer-to-multilayer regime . . . . .	160
9.3.1 The 1×1 superstructure . . . . .	161
9.3.2 The $\sqrt{3}\times\sqrt{3}$ superstructure . . . . .	165
9.4 Conclusions . . . . .	166
<b>10 Summary and outlook</b>	<b>167</b>
<b>Bibliography</b>	<b>171</b>
<b>List of abbreviations</b>	<b>191</b>
<b>List of publications</b>	<b>193</b>
<b>Instruction of students</b>	<b>195</b>
<b>Acknowledgments</b>	<b>197</b>



---

# Chapter 1

## Introduction

Why are self-assembled magic clusters on surfaces such an interesting research topic? Clusters in general are nanobjects with sizes in between atoms on the one side and bulk materials on the other side. Hence, they represent ideal model systems to study how fundamental physical properties emerge with increasing system size. The most intensively studied systems in cluster science are gas phase clusters in high vacuum. Here, magic clusters, i.e. clusters with an enhanced stability at a certain size or structure and thus forming preferentially, are observed for several materials [1–3]. In such small systems, quantum size effects play an important role and might be also employed in promising future applications. However, free clusters in vacuum are not suitable for an application. Therefore, the clusters need to be brought on a surface or implemented into a matrix material, what can be done using different approaches.

In one approach, mass selected clusters with a known size are produced in the gas phase and are then deposited on the surface. Nevertheless, the preparation of surfaces with an adequate coverage and without a destruction of the clusters during the landing process is rather challenging. In addition, an implementation into industrial production processes seems rather difficult. Here, a second approach, in which the clusters are prepared directly on the surface employing self-assembled growth, is advantageous. Especially the growth on Si, which is still the most widely used substrate material in the semiconductor industry [4], should allow an easy implementation into the existing fabrication processes.

A self-assembled growth of clusters showing magic numbers very similar to those found for the gas phase clusters could indeed be demonstrated by Lai and Wang in 1998 [5]. However, these clusters still show a size variation while the ability to grow large numbers of identical clusters would represent the ultimate perfection in nanofabrication. But even the fabrication of such monodispersed clusters is possible, when a structured surface is used as a template. Here, the Si(111)7×7 surface [6] was found to be an especially suitable template and the formation of monodispersed clusters was shown on this surface, first for the group-III elements Ga, In, and Al [7–10], but later also for a variety of other materials [11–16]. The clusters thereby form within the triangular half unit cells of the 7×7 reconstruction. Due to the periodicity of the substrate, this approach also enables the possibility to grow ordered two-dimensional arrays of clusters [7–10]. Although an even further confinement might be achieved by the preparation of

one-dimensional arrays of identical clusters, the research in this field is still in its infancy with only few works dealing with cluster chains [17–20].

Besides a fundamental interest in the properties of such zero-dimensional nanostructures, they might also be employed in applications as mentioned above. The small size and thus the extremely high densities that can be obtained make clusters on surfaces interesting for applications in catalysis [21–24] or for a further miniaturization of nanodevices such as high density memories [25–28]. Most of the studies published in this field so far concentrated on other surfaces, although first investigations for self-assembled clusters on the Si(111)7×7 surface found promising properties, showing e.g. an enhancement of methanol dissociation reactions for Al nanoclusters [24] or the growth of magnetic nanostructures of Co on top of Al nanoclusters [27, 28].

Recently, also a switching between two stable configurations was found for Pb-Si clusters on the Si(111)7×7 surface [29]. This shows that atomic scale switches, similar to those demonstrated before on the basis of other material systems [30–35], are also possible with clusters on Si(111)7×7. Such atomic scale switches are extremely interesting for an application as logic gates or memory devices. However, most of the systems only operate at cryogenic temperatures or are prepared by atomic manipulation using an STM [36], which is an extremely slow method. A similar switching behavior operating at room temperature found for clusters formed by self-assembly would tremendously raise the chance for an implementation into future nanoscale devices.

To investigate self-assembled magic clusters on surfaces, scanning tunneling microscopy [37] is the method of choice since a lot of information on the growth and the atomic structure can be obtained from the atomically resolved images this technique offers. On the other hand, in its spectroscopic mode, a scanning tunneling microscope also enables the possibility to investigate the local electronic structure of nanostructures with atomic precision.

In this work, the atomic and electronic properties of clusters formed from various materials (Sb, In, Ga, Dy, Tb, Si) on different Si surfaces [Si(111), Si(001), Si(557)] are investigated using scanning tunneling microscopy and spectroscopy. Regarding the rare earth metal Tb, thin films on the Si(111) surface are additionally investigated in order to understand the growth behavior in the cluster regime in more detail and because these films represent very interesting nanostructures themselves.

For other rare earth metals, which are chemically very similar, the possibility to grow a variety of different nanostructures depending on the preparation conditions was found. For submonolayer rare earth coverages, a  $2\sqrt{3}\times 2\sqrt{3}$  R30° superstructure, a  $5\times 2$  superstructure, and a  $2\times 1$  superstructure is observed, while for higher coverages two-dimensional and three-dimensional silicides form [38–55]. The two-dimensional monolayer silicides thereby exhibit extremely low Schottky barriers on *n*-type Si making them interesting for ohmic contacts [39, 50, 56, 57].

The present thesis is organized as follows. In the first part, the theoretical and experimental background regarding scanning tunneling microscopy and thin film growth techniques is presented. In addition, it contains an excursion about how the research on self-assembled

---

magic clusters can be associated with the field of cluster science in general. Furthermore, the state of the art regarding the used Si surfaces, self-assembled clusters on these surfaces as well as thin rare earth silicide films on Si(111) is pointed out. Afterwards, the experimental setup of the used scanning tunneling microscope as well as the sample preparation techniques are described.

The second part then covers the results for the different material systems and their discussion. In chapter 5, the results regarding the growth of Sb induced clusters on Si(111) as well as the atomic and electronic properties of magic ringlike clusters found in this material system are described. Chapter 6 then presents the results for magic In and Ga clusters on Si(111) and for magic In clusters on the Si(557) surface, which is vicinal to Si(111). Then, the chapters 7 to 9 cover investigations on rare earth silicide nanostructures on Si surfaces. Thereby, clusters formed after deposition of Tb and Dy on the Si(111)7×7 surface are described in chapter 7, Dy induced clusters on Si(001) in chapter 8, and the results on thin Tb silicide films in the submonolayer to multilayer coverage range in chapter 9. Finally, chapter 10 summarizes the results and gives an outlook.



## Part I

# Theoretical and experimental background



---

## Chapter 2

# Scanning tunneling microscopy and spectroscopy

In 1981, Gerd Binnig, Heinrich Rohrer, Christoph Gerber, and Edmund Weibel at the IBM research laboratory in Rüschlikon combined vacuum tunneling between a metallic tip and a sample surface with the ability of scanning the tip over the surface. This was the birth of the scanning tunneling microscope (STM), an instrument allowing to look at solid surfaces with atomic resolution in real space [37]. The direct imaging in real space is particularly important to investigate non-periodic structures on surfaces, such as defects or nanostructured samples for which area averaging methods like diffraction fail. However, the real breakthrough of the STM came in fall of 1982 with the first atomically resolved images of the Si(111)7×7 reconstruction [58], the surface which also represents the most commonly used substrate in the present thesis. Another powerful tool that an STM offers is scanning tunneling spectroscopy (STS) with its ability to obtain information on the local electronic structure of the surface. Already five years after their invention, G. Binnig and H. Rohrer were awarded the Nobel Prize in physics in 1986 [59]. Based on the STM, a variety of different scanning probe microscopes (SPM) were developed in the following decades, differing in the sample-probe interaction used to create the image. One example is the atomic force microscope (AFM) which uses attractive or repulsive forces between tip and sample and is therefore not limited to conductive samples like the STM. A method to expand the capability of STM to the investigation of buried structures is cross-sectional scanning tunneling microscopy (XSTM).

### 2.1 The principle of scanning tunneling microscopy

The basic operation principle of the STM shown in Fig. 2.1 is quite simple. A voltage  $V_T$  is applied between a sharp metallic tip, usually made from W or PtIr, and a metallic or semiconducting surface. If the tip is then brought into a distance  $s$  of about one nm above the surface, a tunneling current  $I_T$  can be measured. This current appears without a mechanical contact between tip and sample due to the quantum mechanical tunneling effect and is not explainable within classical physics. Since this current depends strongly on the tip-sample

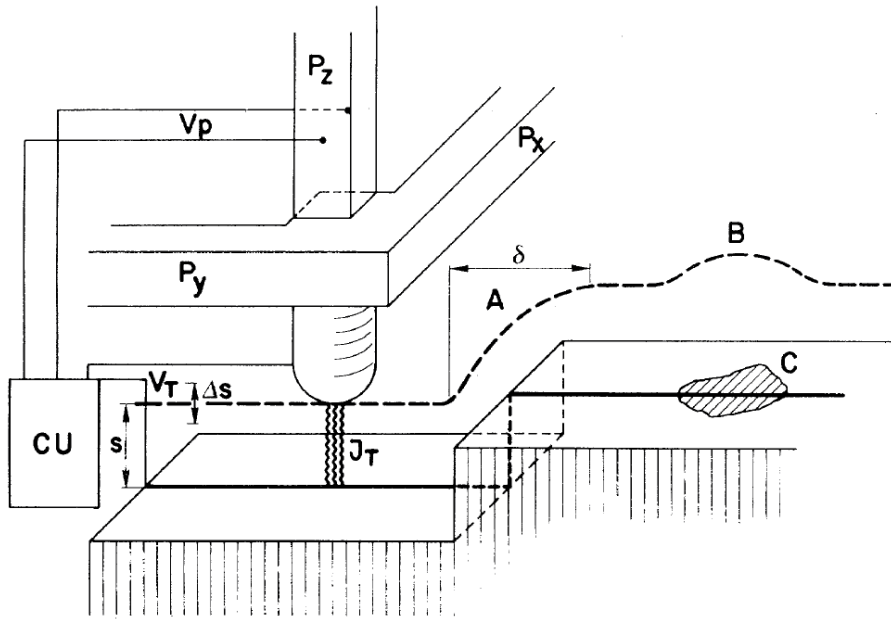


**Figure 2.1:** The principle of operation of the scanning tunneling microscope. A metallic tip is scanned over a surface using the piezoelectric elements  $P_x$ ,  $P_y$ , and  $P_z$ . A control unit (CU) applies a voltage  $V_T$  between tip and sample, measures the tunneling current  $I_T$ , and adjusts the tip height by applying an appropriate voltage  $V_p$  to the  $z$ -piezo to obtain a constant current image. The dashed line indicates the scan line including a surface step (A) and a chemical inhomogeneity (B). From [37].

separation, it can be used to image the surface. For this purpose the tip is scanned over the surface while the tunneling current is measured. The scanning is usually realized using piezo elements. In Fig. 2.1 a simple tripod consisting of three piezo rods  $P_x$ ,  $P_y$ , and  $P_z$  is used. Today, tube piezos are commonly used [60].

For obtaining STM images, two modes exist. In the constant current mode, which is the most widely used one, the tunneling current is kept constant by a feedback loop that adjusts the tip height. Here, the tip follows the topography of the surface as it is shown in Fig. 2.1 for a surface step at point A. The image is then generated from the voltage  $V_p$  that is applied to the  $P_z$  piezo element.

The other operation mode is the so called constant height mode where the tip is scanned over the surface at a constant height. Here, directly the tunneling current is used to construct the STM image.

Both modes have advantages and disadvantages, e.g. the constant height mode is much faster, since no feedback loop is used. Constant height images can be obtained even at video sampling rates allowing to study e.g. atomic diffusion or growth processes. On the other hand this mode cannot be used for rough surfaces since the tip could touch the surface. Thus, the constant current mode was used to acquire all STM images presented in the present thesis.

In Fig. 2.1 another contrast mechanism is denoted. At point C, a chemical inhomogeneity exists. The bump in the scan line at point B indicates that this can also induce a difference

in the tunneling probability. This is related to the fact that the tunneling current not only depends on the tip-sample separation as written above in a simplistic manner, but also on the local density of states (LDOS) as it will be demonstrated in the following section.

## 2.2 Theory of tunneling

The phenomenon, on which STM is based, is the tunneling of electrons through a vacuum barrier between the tip and the sample. As mentioned before, this effect cannot be described within classical physics, since the vacuum barrier is classically forbidden for the electrons. However, in quantum mechanics, the electron wavefunctions of the sample and the tip decay exponentially into the barrier. If there is an overlap of the wavefunctions, electrons can tunnel from the tip into the sample and vice versa. By additionally applying a voltage between tip and sample, a net tunneling current appears. A commonly used theoretical description of the tunneling process is the time-dependent perturbation approach developed by Bardeen [61]. The following sections present a sketch of the derivation of the tunneling current using the Bardeen perturbation approach as well as the Tersoff-Hamann approximation which relies on the Bardeen approach. Thereby, it basically follows the derivation presented in Ref. [62]. For a more detailed treatment, the reader is referred to various textbooks on the subject [62–65].

### 2.2.1 The Bardeen approach

Instead of solving the Schrödinger equation for the combined tip-sample system, the Bardeen approach first considers two separate subsystems for the tip and the sample. As the tip approaches the sample, the potential  $U$  in the barrier becomes different from the potentials of the free tip  $U_T$  and the free sample  $U_S$ . Thus, a perturbation of the sample potential occurs. The corresponding potential surfaces are shown in Fig. 2.2 (b) to (d). For conducting perturbation calculations, a separation surface is drawn between the tip and the sample as it is shown in Fig. 2.2 (a).

Starting at  $t < 0$ , with the potential of the tip being turned off, the Schrödinger equation provides

$$\left(-\frac{\hbar^2}{2m_e}\Delta + U_S\right)\Psi_\mu = E_\mu\Psi_\mu \quad (2.1)$$

and

$$\left(-\frac{\hbar^2}{2m_e}\Delta + U_T\right)\chi_\nu = E_\nu\chi_\nu \quad (2.2)$$

for the stationary states of the sample  $\Psi_\mu$  and the tip  $\chi_\nu$ .

At  $t = 0$ , the potential of the tip is turned on as a perturbation. The time-dependent Schrödinger equation for the combined system is then

$$i\hbar\frac{\partial\Psi}{\partial t} = \left(\frac{\hbar^2}{2m_e}\Delta + U_S + U_T\right)\Psi. \quad (2.3)$$

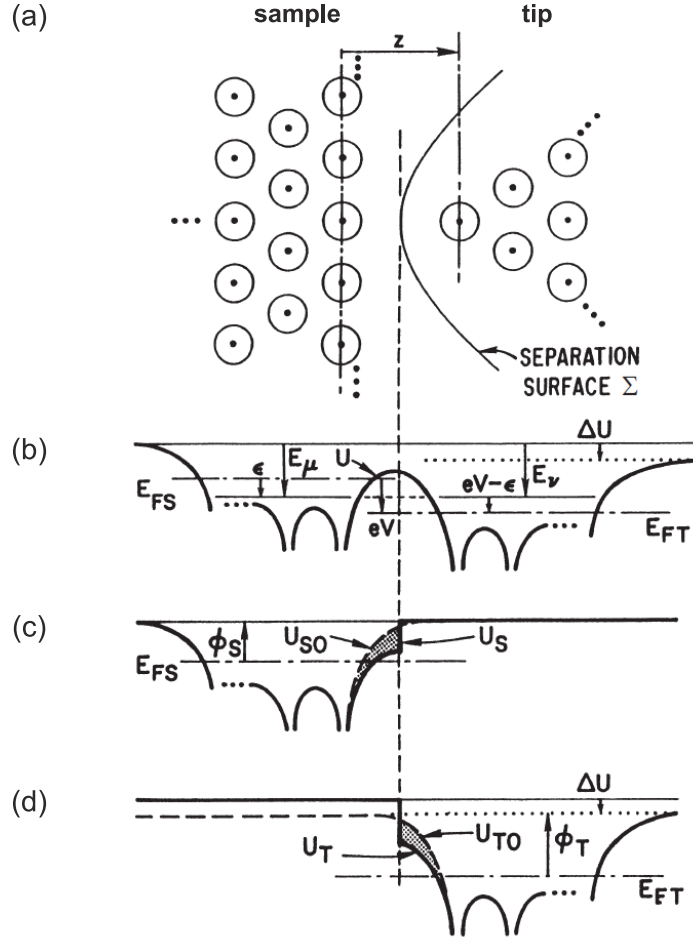


**Figure 2.2:** (a) The tip-sample situation used in the Bardeen perturbation approach. Between the two subsystems tip and sample a separation surface is drawn. (b) The potential surface of the combined system. (c,d) The potential surface of the sample subsystem (c) and of the tip subsystem (d). From [66].

Using a complete and orthogonal set of tip wavefunctions, the transition probability of an electron from  $\Psi_\mu$  to  $\chi_\nu$  in first-order perturbation theory is given by the Fermi golden rule:

$$w_{\mu\nu} = \frac{2\pi}{\hbar} |M_{\mu\nu}|^2 \delta(E_\nu - E_\mu). \quad (2.4)$$

The delta function indicates that only elastic tunneling is considered.  $M_{\mu\nu}$  is the tunneling matrix element

$$M_{\mu\nu} = -\frac{\hbar^2}{2m_e} \int_{\Sigma} (\chi_\nu^* \nabla \Psi_\mu - \Psi_\mu \nabla \chi_\nu^*) \cdot dS \quad (2.5)$$

which is defined as the surface integral over the separation surface between tip and sample and has the dimension of energy.

By integrating over all sample and tip states, the tunneling current for the applied voltage  $V$  is obtained. For simplification, the summation over discrete states is thereby replaced by the integration over the density of states (DOS)  $\rho(E)$ , thus the tunneling matrix element  $M$  does no more depend on the discrete states but only on the energy. Assuming additionally that the feature size in the energy spectrum is much larger than  $k_B T$ , the tunneling current simplifies

to

$$I = \frac{4\pi e}{\hbar} \int_0^{eV} \rho_T(E_F^T - eV + \epsilon) \rho_S(E_F^S + \epsilon) |M|^2 d\epsilon, \quad (2.6)$$

with  $\rho_T$  and  $\rho_S$  being the LDOS of tip and sample and  $E_F^T$  and  $E_F^S$  the Fermi energies of tip and sample, respectively.

### 2.2.2 The Tersoff-Hamann approximation and beyond

For real systems, the detailed electronic structure of the tip is usually not known. Hence, without making an assumption for the wavefunction, the calculation of the tunneling matrix element and the tunneling current according to the Bardeen approach is not possible. In the popular Tersoff-Hamann approximation [67, 68], the tip is modeled as a spherical potential well while the sample is treated exactly. Using this assumption, the tunneling matrix element simplifies to

$$M_{\mu\nu} = -\frac{2\pi C \hbar^2}{\kappa m_e} \Psi_\mu(\underline{R}), \quad (2.7)$$

with the decay constant  $\kappa$ , a constant  $C$ , and  $\underline{R}$  being the position of the topmost tip atom. Hence, the tunneling matrix element is proportional to the wavefunction of the sample at the position of the tip. Using Eq. 2.7 and further assuming a constant DOS for the tip, Eq. 2.6 becomes

$$I(\underline{R}, V) \propto \int_0^{eV} \rho_S(\underline{R}, E_F^S + \epsilon) d\epsilon, \quad (2.8)$$

where  $\rho_S(\underline{R}, E)$  is the LDOS of the sample at the position of the tip.

Although the Tersoff-Hamann approximation can explain the spatial resolution on larger superstructures on metals and semiconductors, it fails e.g. in explaining the large corrugation amplitudes experimentally observed on low Miller-index metal surfaces. Therefore other tip wavefunctions have to be taken into account, as it has been done by Chen in a generalization of the Tersoff-Hamann theory for general wavefunctions [69]. A detailed description of this approach can again be found in Ref. [62].

## 2.3 Tunneling spectroscopy

The dependency of the tunneling current on the LDOS of the analyzed sample surface extends the capabilities of an STM from acquiring atomically resolved images to the possibility of obtaining information on the local electronic structure of the surface.

### 2.3.1 Voltage dependent STM images

The simplest way to obtain information on the electronic structure is the recording of constant current images with different applied tunneling voltages. Since only the states between the Fermi levels of tip and sample contribute to the tunneling current (cf. Eq. 2.6) it is in principle possible to selectively image different electronic states. Fig. 2.3 shows simplified one-dimensional energy diagrams for a system consisting of a metallic tip with a constant DOS and a metallic surface exhibiting a distribution of surface states. Without applying a voltage

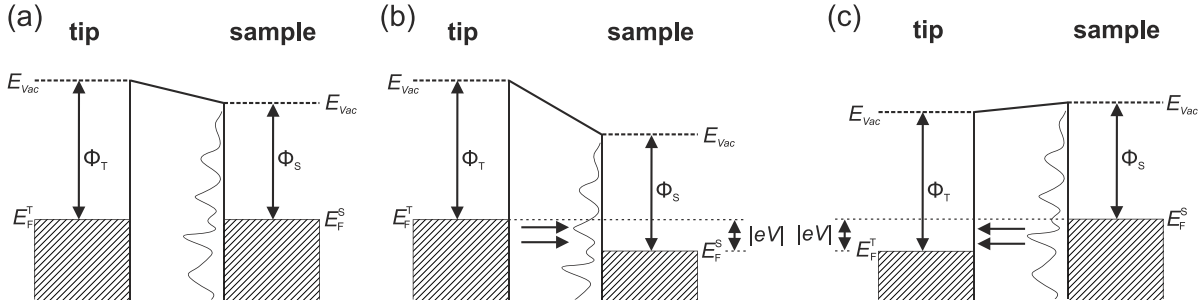


**Figure 2.3:** Schematic energy level diagrams for a one-dimensional tip-sample system separated by a small vacuum gap. (a) Without an applied tunneling voltage  $V_T$ , the Fermi levels of tip  $E_F^T$  and sample  $E_F^S$  are equal in thermodynamic equilibrium. They are separated from the vacuum level  $E_{vac}$  by the work functions of the tip and the sample  $\Phi_T$  and  $\Phi_S$ , respectively. When applying a positive voltage with respect to the sample (b), electrons can tunnel from the tip into the sample, while for a negative tunneling voltage (c), the electrons tunnel from the sample into the tip. Adapted from [70].

[Fig. 2.3 (a)], the Fermi levels of tip  $E_F^T$  and sample  $E_F^S$  are equal. In contrast, when a tunneling voltage  $V_T$  is applied to the sample, the Fermi levels are shifted. For a positive tunneling voltage as shown in Fig. 2.3 (b), the Fermi level of the tip is shifted upwards by the amount  $|eV_T|$  with respect to  $E_F^S$ . This situation results in a net tunneling current from filled tip states into empty sample states (empty states image). In contrast, when applying a negative tunneling voltage, a filled states image is obtained.

This effect often provides also a chemical sensitivity: Between atoms of different elements or in different bonding configurations, often a charge transfer occurs, e.g. due to different electronegativities. This can result in a filling of the states located at one type of atom and a depletion of electrons at the atoms of the other type, thus offering the possibility to selectively image the respective atoms by changing the polarity of the tunneling voltage.

Voltage dependent STM images can either be recorded successively or by scanning every line several times with a different voltage. The latter method provides superimposable images at different voltages, while the first method has the disadvantage, that thermal drift or creep of the scan piezos can cause difficulties regarding the direct comparison of the images.

Voltage dependent STM images can provide a quick and laterally resolved overview if the appearance of the images changes for different tunneling voltages, particularly for different polarities. However, constant current images always show a mixture between geometric and electronic features that are not easily distinguishable from each other. In particular, always all states between the Fermi level and the applied tunneling voltage contribute to the image. Hence, it is not possible with this method to image selected electronic states. Therefore, other spectroscopic techniques are needed.

### 2.3.2 Point spectroscopy

A method to directly investigate the electronic structure at a specific point of interest is taking local  $I-V$  spectra at a fixed tip-sample separation. Therefore, the tip is moved to the desired position, the feedback loop is turned off, and the voltage is scanned while the tunneling current

is measured. This procedure is usually repeated several times at each point for averaging. Since the feedback is turned off, the current is allowed to become extremely small or even zero without crashing into the sample, making it possible e.g. to estimate the local band gap of a semiconducting sample.

Often easier to interpret is the differential conductivity given by the first derivative of the tunneling current  $dI/dV$ . It is obtained from Eq. 2.8 to

$$\frac{dI}{dV} \propto \rho_S(\underline{R}, E_F^S + eV). \quad (2.9)$$

Thus, the differential conductivity is directly proportional to the LDOS of the sample at the position of the tip and at the energy  $E_F + eV$ . Such  $dI/dV$ - $V$  spectra can be either obtained by numerical differentiation or directly measured simultaneously with the  $I$ - $V$  curve by applying a small modulation on the voltage and using a lock-in amplifier.

However, the measured  $dI/dV$  signal usually becomes too small for small tunneling voltages. As found theoretically by Lang [71] and experimentally by Stroscio *et al.* [72], the term  $(dI/dV)/(I/V)$  shows a better agreement with the LDOS of the surface [65, 71–74]. In addition, this dimensionless quantity is relatively independent of the tip-sample separation, thus the separation can also be varied during the measurement in the so-called variable gap mode to improve the signal quality [65, 75, 76]. For samples that exhibit a band gap, the singularity at  $I = 0$  is eliminated by applying the approach introduced by Prietsch *et al.* [77]. Thereby,  $(I/V)$  is replaced by  $\sqrt{(I/V)^2 + c^2}$ , with  $c$  being a small constant just above the noise level.



---

## Chapter 3

# Material system

### 3.1 Excursion: From gas phase clusters to clusters on surfaces

Clusters are small particles in the size range between single atoms or molecules on the one side and bulk matter on the other side. Their small size leads to new physical and chemical properties. Since these properties vary with the cluster size, it is possible to adjust them systematically, for example to create novel materials or to study the transition from single atoms or molecules to solid materials [3, 78–81].

Thereby, clusters can be classified – a bit arbitrarily – into three groups: small, medium and large clusters. The properties of small clusters vary strongly with their size. Here, one atom more or less already influences their properties. The properties of medium sized clusters still vary smoothly with their size, while for large clusters the properties approach those of the corresponding bulk material. For small and medium sized clusters, a large fraction of the atoms are at the cluster surface, making such clusters very interesting for an application as catalysts.

Since a boom in cluster science started in the 1980's the most intensively studied objects were free clusters in high vacuum. Here, the interaction between the clusters and the environment is negligible, making them an ideal model system to study the properties of such quantum systems [3, 78–81]. However, to build cluster based devices or to make them accessible to other experimental techniques, the clusters have to be brought onto a substrate. This can be realized either by a deposition of gas phase clusters on a surface (cf. section 3.1.2) or by directly fabricating clusters on surfaces (cf. section 3.5).

#### 3.1.1 Gas phase clusters

Free clusters can be produced in different types of cluster sources. Most sources are based on the same basic principle: The material for the cluster fabrication is already present or has to be brought into the gas phase. This gas is then cooled down leading to the condensation of clusters.

The oldest and simplest source is the gas aggregation source, where a metal or another solid material is evaporated into a (streaming) rare gas. The atoms are cooled down by collisions

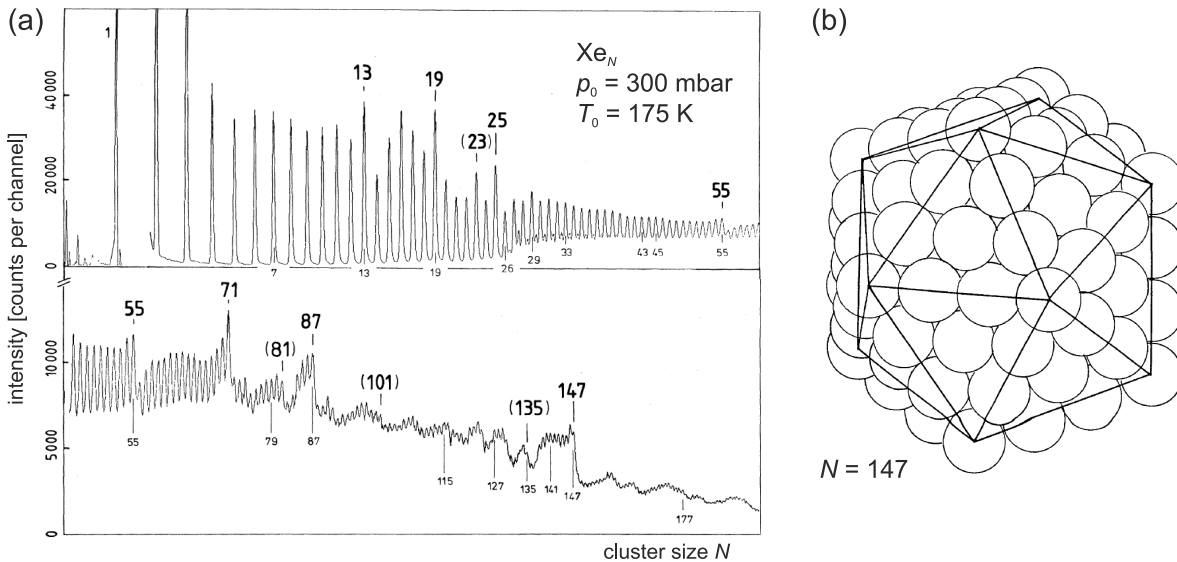


**Figure 3.1:** (a) Mass spectra of Xe clusters showing an enhanced intensity for certain cluster sizes. These so called magic numbers could be associated with closed geometric shells. From [1]. The magic sizes of 13, 55, 147 correspond to closed icosahedral geometries, as shown in (b) for the 147 atom cluster. From [85].

with the rare gas atoms. When their energy gets lower than the binding energy of a dimer, dimers form from three-body collisions. These dimers then act as nuclei for the condensation of larger clusters. In nature, cloud or fog formation follows the same principle [3, 23, 78, 79, 82–84].

Other common sources are supersonic jets, where a gas of atoms under high pressure is expanded through a small nozzle into vacuum. This adiabatic expansion leads to a dramatic cooling of the atoms and the formation of clusters. Laser vaporization sources, ion and magnetron sputtering sources, or arc discharge sources are also used to produce clusters [3, 23, 78, 79, 82–84].

All sources produce cluster beams with a more or less broad distribution of cluster sizes. In order to investigate properties as a function of the cluster size, a mass filter has to be implemented into the experimental setup adjacent to the source. The most common mass filters are quadrupoles and time-of-flight mass spectrometers. Both techniques require charged clusters, so if the cluster source does not already produce charged clusters, they need to be ionized by a laser or electron beam prior to mass selection [3, 23, 80, 83, 84]. Afterwards, experiments at one selected cluster size are possible.

But even the mass spectra often contain interesting information as they may contain a lot of structure. In the following, examples that were historically relevant in cluster physics are briefly described.

In Fig. 3.1 (a), a mass spectrum of Xe clusters obtained by Echt *et al.* [1] is shown. For several cluster sizes, the spectrum shows an enhanced intensity. These so called magic numbers correspond to particularly stable clusters. For the rare gas clusters, the magic numbers could be assigned to the geometric structure [1, 86–89]. The atoms in the clusters are van der Waals bonded, resulting in a tendency to form closed packed structures. For small clusters this is the Mackay icosahedron shown in Fig. 3.1 (b) for the case of three closed shells [85]. For

an icosahedral structure, shell closure is obtained for  $N = 13, 55, 147, 309, 561$  etc. atoms. These numbers are nicely reproduced in the mass spectrum. The other magic numbers in the spectrum (e.g. 19 or 25) could be associated with extensions of icosahedral structures, where additional atomic layers form caps on the facets.

For icosahedra, the number of nearest neighbor bonds is higher than for a section of the face centered cubic (fcc) crystal lattice with the same number of atoms. However, with the pentagonal symmetry they show, it is not possible to build up a bulk crystal. Thus, for larger clusters, the non-uniform interatomic distances lead to mechanical stress and a transition to the fcc lattice [3, 78, 90–94].

Besides the rare gases, magic numbers due to closed atomic shells are also observed for other clusters. For Ca and Mg clusters again an icosahedral structure is observed [90]. In contrast, alkali halide, Al and In clusters form – already for small sizes – structures with a local geometry very similar to the crystal lattice. Alkali halide clusters form ion cuboids [90, 95, 96] while In and Al clusters form octahedra [90].

But not only geometric reasons can lead to magic numbers. In Fig. 3.2 (a), a mass spectrum of Na clusters taken by Knight *et al.* [2] is shown. Here, the pronounced peaks for the atomic numbers  $N = 8, 20, 40,$  and  $58$  are associated with closed electronic shells [2, 84, 97–106]. For alkali metals, the bulk electronic structure is well described by the nearly free-electron model. Similarly, Knight *et al.* [2] found that the electronic structure of the clusters is in good agreement with the one of a spherical potential well. Using the jellium model, where the ionic core is replaced by a uniform positive background charge, Ekardt [99] obtained the potential shown in Fig. 3.2 (b) for a  $\text{Na}_{20}$  cluster. In the figure, the occupation of the states with the valence electrons is shown. The stability of the  $\text{Na}_{20}$  cluster arises from the fact, that for the 20<sup>th</sup> electron, the  $2s$  orbital gets completely filled. For open shells, the Jahn-Teller effect leads to a distortion [107]. Therefore an ellipsoid-shell-model was introduced to reveal the fine structure in the mass spectrum [103–106]. Similar to Na clusters [2, 100–102], magic numbers due to electronic shell closings are observed for other alkali metals [98, 108, 109] and noble metals [110, 111].

Another fascinating cluster came into the focus of science when Kroto *et al.* [112] studied mass spectra of carbon clusters produced by laser vaporization of graphite. They found a large peak at  $N = 60$  that became completely dominant after tuning the experimental conditions. This was the discovery of the so called fullerenes (named after the architect Richard Buckminster Fuller), a whole family of large carbon molecules. Like graphite or graphene, a single sheet of graphite [113], they are composed of  $sp^2$  hybridized carbon. But, to avoid dangling bonds at the borders of a small graphite sheet, 12 pentagons are incorporated into the hexagonal lattice to induce a bending and allow the formation of hollow cages. The most famous fullerene  $\text{C}_{60}$  consists of 12 pentagons and 20 hexagons having the structure of a truncated icosahedron [112, 114, 115].

These results show that a lot of information is already present in mass spectra of clusters. Nevertheless, for further investigation other spectroscopic techniques such as optical or infrared spectroscopy, photoelectron spectroscopy (PES) or Raman spectroscopy need to be applied.

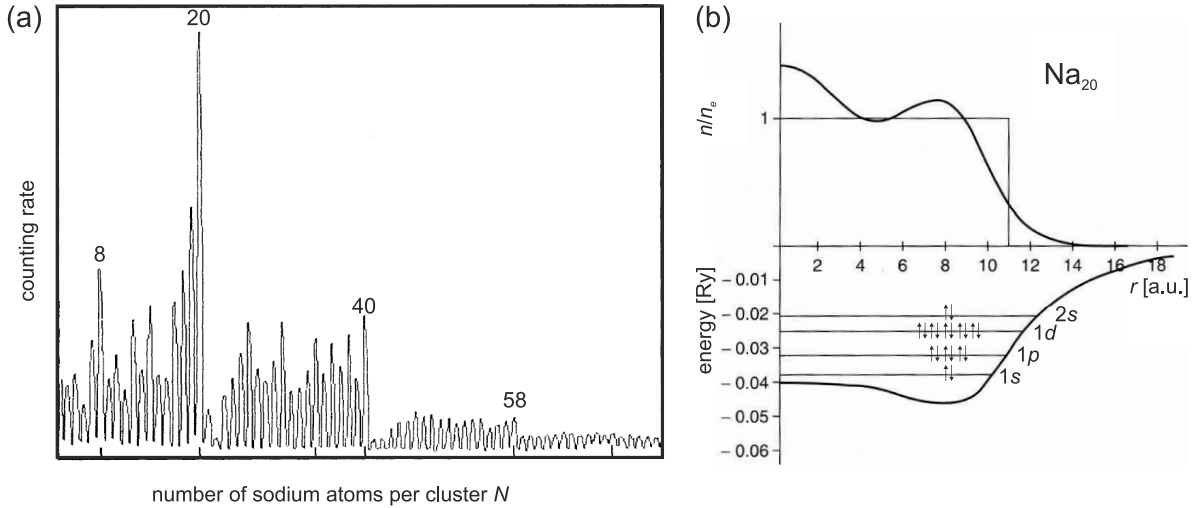


**Figure 3.2:** (a) Mass spectrum of Na clusters. From [2]. (b) Self-consistent charge density and effective potential derived from the spherical jellium model for a  $\text{Na}_{20}$  cluster. The energy level structure and the occupation with valence electrons is indicated. From [99].

It was already mentioned that clusters are intermediate objects between atoms and bulk crystals. As the transition in the geometric structure was studied using mass spectrometry, one is also able to analyze the transition from the discrete electronic states of atoms to the electron bands present in solids using PES. A scheme of this evolution of the electron bands is shown in Fig. 3.3 (a). With increasing cluster size the energy levels become gradually broader until they finally form the quasi continuous bands of a solid [78,116]. Due to the extremely low density of states, small clusters of elements that are metals as solids can show a band gap or better a gap between the HOMO (highest occupied molecular orbital) and the LUMO (lowest unoccupied molecular orbital). For example, the  $\text{Ag}_8$  cluster shows a HOMO-LUMO gap of 1.3 eV, which is decreasing with increasing cluster size until a metallic behavior is observed [116].

An experimental observation of this band-gap closure is presented in Fig. 3.3 (b) on the basis of PES data of selected  $\text{Hg}_N^-$  clusters [117]. The small peak in the spectra arises from the additional electron that occupies the otherwise empty  $6p$  band, while the broad onset at higher binding energies corresponds to the fully occupied  $6s$  band. With increasing cluster size the small peak moves towards higher binding energies, meaning that the band gap shrinks. From extrapolation, the authors expect the full closure of the band gap at a size of  $N = 400 \pm 30$ .

But not only the cluster size influences the properties fundamentally. So far, only elemental clusters, meaning clusters consisting of one atomic species were mentioned. Doping clusters with atoms of another species can also influence their properties drastically. Here, only transition metal doped Si clusters are picked as an example due to the similarity of the materials with the ones used in this thesis.

In contrast to carbon clusters, pure Si clusters form more compact structures [118–120] [see Fig. 3.4 (a,b,c)]. This behavior results from the different hybridization which is  $sp^3$  for Si, but can be either  $sp^2$  (like in graphite, graphene or fullerenes) or  $sp^3$  (diamond) for carbon. For  $sp^3$  hybridized Si, a fullerene-like structure would result in a high number of unsaturated dangling

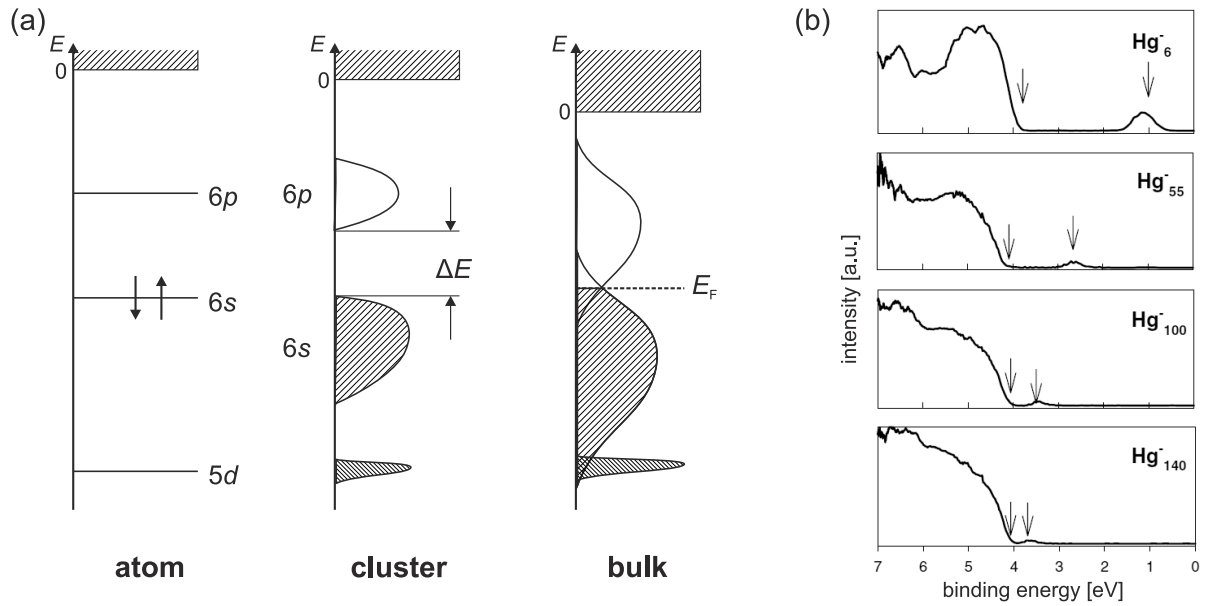


**Figure 3.3:** (a) Schematic energy diagrams showing the energy levels of a single Hg atom, a small Hg cluster with a band gap of  $\Delta E$  and Hg bulk material. Adapted from [78]. (b) Photoelectron spectra of selected  $\text{Hg}_N^-$  clusters recorded with a photon energy of  $h\nu = 7.9$  eV showing the closure of the energy gap. The small peak at lower binding energies (indicated by the right arrows) is assigned to the additional electron occupying the 6p band, the onset at higher binding energies (left arrows) to the occupied 6s band. From [117].

bonds and is therefore unfavored. However, adding suitable impurity atoms that saturate these dangling bonds can change the geometry of the Si clusters completely.

Many experimental and theoretical studies were performed on transition metal [120–137] and lanthanide metal [137–139] doped Si clusters ( $\text{MSi}_N$ ) consisting of  $N$  Si atoms and one transition metal (e.g. Sc, Ti, V, Cr) or lanthanide metal atom (e.g. Tb, Lu, Ho, Eu). Fig. 3.4 (d,e,f) shows calculated geometries for  $\text{VSi}_6^+$  to  $\text{VSi}_{16}^+$  clusters. In comparison to Fig. 3.4 (a,b,c), a change in the geometry is observed. For small clusters the Si cage is too small to incorporate the transition metal atom resulting in so called exohedral clusters with the metal atom attached at the surface of the cluster. When the clusters become large enough, the transition metal atom is incorporated into a cage of Si atoms (endohedral clusters). The cluster size  $N$ , where this transition from exohedral to endohedral clusters occurs, depends on the dopant atom. For the transition metals Mn, Cr, V, Ti, and Sc,  $10 < N < 17$  was found [131, 132, 136].

Especially symmetric structures are found for the endohedral clusters  $\text{ScSi}_{16}^-$ ,  $\text{TiSi}_{16}$ , and  $\text{VSi}_{16}^+$  [123, 125–127, 129, 130] that form closed Frank-Kaspar-polyhedra [140]. Besides the geometric shell closure, these clusters also show an electronic shell closure, although this is not necessarily a criterion for the stability of a cage geometry [127, 134]. The electronic shell closure can be understood within the jellium model [128–130] described above for alkali metal clusters. It is assumed that three valence electrons from each Si atom are used to form the bonds of the cage. The remaining valence electrons from the Si atoms together with the valence electrons of the transition metal are then treated as a free-electron gas [129]. Regarding the example of the  $\text{TiSi}_{16}$  cluster, 16 electrons come from the Si cage and four from the Ti

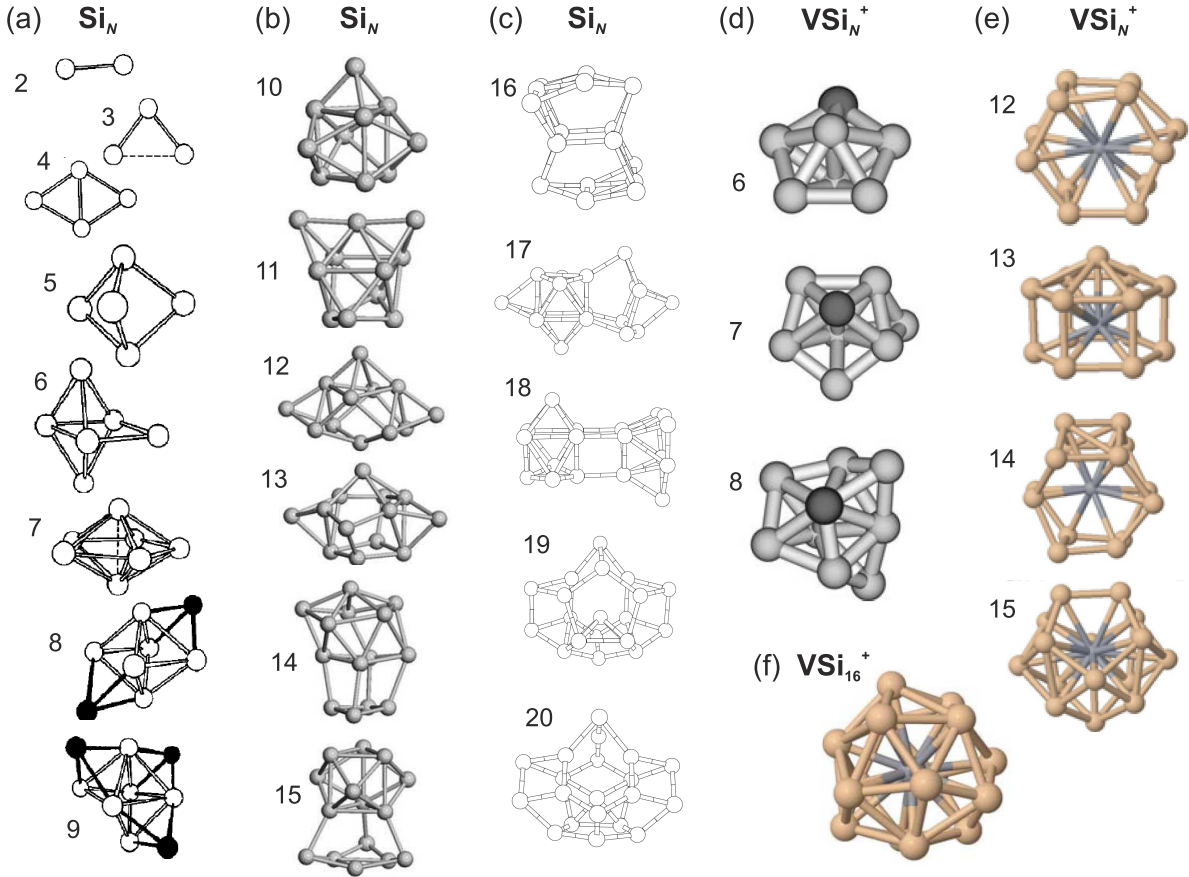


**Figure 3.4:** Calculated structures for (a-c) pure  $\text{Si}_N$  clusters and (d-f)  $\text{VSi}_N^+$  clusters. For small cluster sizes (d) exohedral  $\text{VSi}_N^+$  clusters form, while for  $N > 11$ , the metal atom is incorporated into a Si cage (e). The  $\text{VSi}_{16}^+$  cluster forms a highly symmetric Frank-Kasper polyhedron (f). From: (a) [118], (b) [120], (c) [119] (d) [133], (e) [126], and (f) [127].

atom. For the resulting 20 electrons a shell closure ( $1s^21p^61d^{10}2s^2$ ) is achieved within the potential derived from the jellium model, very similar as discussed above for the  $\text{Na}_{20}$  cluster (cf. Fig. 3.2). The high stability of these magic clusters is also reflected in the large HOMO-LUMO gaps around 2 eV that were found theoretically [129, 130] and experimentally [125, 135, 136].

This section can only give a brief and by far not complete overview on the studies done with gas phase clusters. For a deeper insight into this fascinating field, the reader is referred to a number of books and review articles dealing with gas phase clusters in general [3, 78–81, 141–143], or with atomic shells [90] and electronic shells [84, 103, 144] in detail.

### 3.1.2 Clusters on surfaces

Free clusters represent an ideal model system for the investigation of the fascinating properties that such nanosystems show. Nevertheless, for an application in devices or catalysis the clusters have to be implemented into a matrix or brought on a surface. One approach is to produce clusters in the gas phase and deposit these clusters on a substrate [23, 82, 83, 145, 146].

This method has several advantages, for instance the possibility to study the same clusters in the gas phase and deposited on a substrate, or the ability to prepare films consisting of only

one cluster size. But the method is also experimentally very challenging. The mass selected cluster beams have to be very intense to obtain a density of clusters on the surface large enough to employ the typical surface science techniques such as PES or STM. Moreover, to ensure a clean surface an ultra-high vacuum (UHV) environment is necessary.

Depending on various parameters, e.g. the kinetic energy of the clusters, the chosen cluster-substrate combination, the substrate temperature, or the cluster size, different cluster-surface interactions can occur.

In principle, a kinetic energy that stays well below the binding energy between the atoms of the cluster will not lead to a fragmentation of the clusters upon deposition. This case is often referred to as soft landing. Here, the composition of the cluster is usually unaffected, while often a change in the cluster shape occurs. Using STM soft landing has been verified e.g. for Si clusters on a Ag(111) surface [147]. In addition, it has been demonstrated that soft landing can be achieved using a rare gas buffer layer [148].

On weakly interacting surfaces or at elevated temperatures, however, a diffusion of the clusters on the surface may lead to coalescence or agglomeration into larger particles [82, 149, 150].

Obviously, to study the properties of clusters on surfaces, soft-landed clusters are best suited. Many studies dealt with the catalytic properties of supported clusters [23, 151]. For example, Au nanoparticles on metal oxides show a remarkable catalytic activity, although Au as a bulk material is inert [21, 152, 153]. Studies on size selected small Au clusters that were soft-landed on a MgO surface demonstrated the capability of Au<sub>8</sub> clusters to oxidize CO into CO<sub>2</sub> even at 140 K [22, 154].

Another interesting topic is the electronic structure of deposited clusters. Will the clusters keep their electronic level structure and how does the surface influence the electronic properties? The ideal method to deal with such problems is scanning tunneling spectroscopy. Tunneling spectra taken on small Pt clusters on highly oriented pyrolytic graphite show discrete peaks that may be related to the electronic level structure [145, 155].

An alternative route towards cluster related devices is the formation of clusters directly on the surface via self-organized growth. This approach, which is used in the present thesis, has several advantages, for example the growth of such clusters could easily be implemented into the current fabrication of semiconductor devices. On the other hand, in comparison to the deposition of size selected clusters, it is more challenging to obtain a narrow size distribution of the grown clusters or even monodispersed clusters. Nevertheless, this has been achieved using a template approach which is described in section 3.5 in detail.

However, since the clusters investigated in this work as well as most self-assembled magic clusters studied by other groups were grown on Si surfaces, Si as well as its relevant surfaces will be introduced at first in the following section.

## 3.2 Silicon

The application of Si or Si containing compounds for different purposes has a long lasting tradition. After O, Si is with 25.7% of the earth's crust weight the second most abundant element making it easily available [156]. Since sand and clay contain Si compounds, important materials like brick, concrete, and glass are already some sort of "silicon technology". Si is also added to steel to influence its properties. But, particularly from a solid state physicists point of view, most importantly, it is the most widely used material in the information technology [4].

As a crystal, Si forms the diamond structure with a lattice constant of  $a_0 = 0.543$  nm [157] as shown in Fig. 3.5 (a). This structure can be seen as an fcc lattice with an atomic basis consisting of two atoms at  $(0, 0, 0)$  and  $\frac{a_0}{4}(1, 1, 1)$ . The tetrahedral configuration of the atoms with four nearest neighbors provides an optimum overlap of the  $sp^3$ -type covalent bonds. Thereby, the bonds with a length of  $b = a_0 \frac{\sqrt{3}}{4} = 0.235$  nm run along  $\langle 111 \rangle$  crystallographic directions.

Crystalline Si is an elemental semiconductor with a band gap of 1.12 eV at room temperature [157]. In Fig. 3.5 (b) the band structure of the bulk Si crystal is shown. The valence and conduction bands are formed by the bonding and antibonding configurations of the  $3s3p^3$  hybrids, respectively. The band gap is indirect, limiting the use of Si in light emitting devices. For doping, group-III elements (mainly B) are used as acceptors and group-V elements (mainly P) as donors [4].

The primary surface orientations of the Si crystal are (001), (111), (110), and (113). In this thesis, the growth of clusters and thin films on the Si(111) surface, the Si(557) surface that is vicinal to Si(111), and on the Si(001) surface is studied. Hence, these surfaces are described in more detail in the following sections, and Table 3.1 summarizes some structural parameters of the Si(111) and the Si(001) surface.

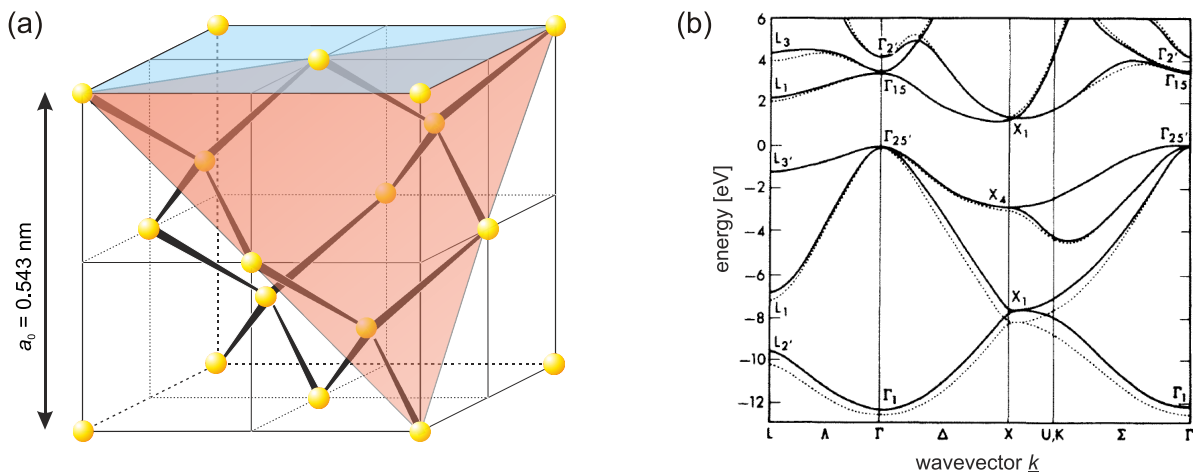


**Figure 3.5:** (a) The diamond lattice in which Si crystallizes. A (111) plane is indicated in red, an (001) plane in blue. Adapted from [158]. (b) Calculated electronic band structure of crystalline Si. It is characterized by an indirect band gap between the valence band and the conduction band. From [159].

surface orientation	surface lattice constant	density of atoms ( $\text{cm}^{-2}$ )	single layer step height
Si(111)	$a_0/\sqrt{2} = 0.384 \text{ nm}$	$7.83 \cdot 10^{14}$	$a_0/\sqrt{3} = 0.314 \text{ nm}$
Si(001)	$a_0/\sqrt{2} = 0.384 \text{ nm}$	$6.78 \cdot 10^{14}$	$a_0/4 = 0.136 \text{ nm}$

**Table 3.1:** Some structural parameters of the Si(111) and the Si(001) surface.

### 3.2.1 The Si(111) surface

With only one dangling bond per atom of the unreconstructed surface, the Si(111) surface [red plane in Fig. 3.5 (a)] has the lowest dangling bond density among all stable Si surfaces. Thus, it is the preferential cleavage plane of the Si crystal. Nevertheless, the bulk terminated Si(111) surface, as it is shown in Fig. 3.6 (a), is energetically unfavorable resulting in the formation of a  $2 \times 1$  reconstruction directly after cleaving the crystal along the (111) plane. Surface reconstructions are typical for semiconductor surfaces where a significant directional bonding is present. Thereby, the atoms of the surface layers rearrange in order to lower the energy of the surface, e.g. by reducing the density of dangling bonds [160–162]. In this thesis, the Wood notation [163] is used to denote the resulting superstructures.

The structure model for the Si(111) $2 \times 1$  reconstruction shown in Fig. 3.6 (b) was first proposed by Pandey [164]. For its formation, the bonds between the first and the second surface layer rearrange, resulting in the formation of chains. Due to the chain formation, the distance between the dangling bonds is reduced and a  $\pi$ -bonding occurs. This leads to the opening of a band gap between the occupied  $\pi$  and the unoccupied  $\pi^*$  states [72, 165].

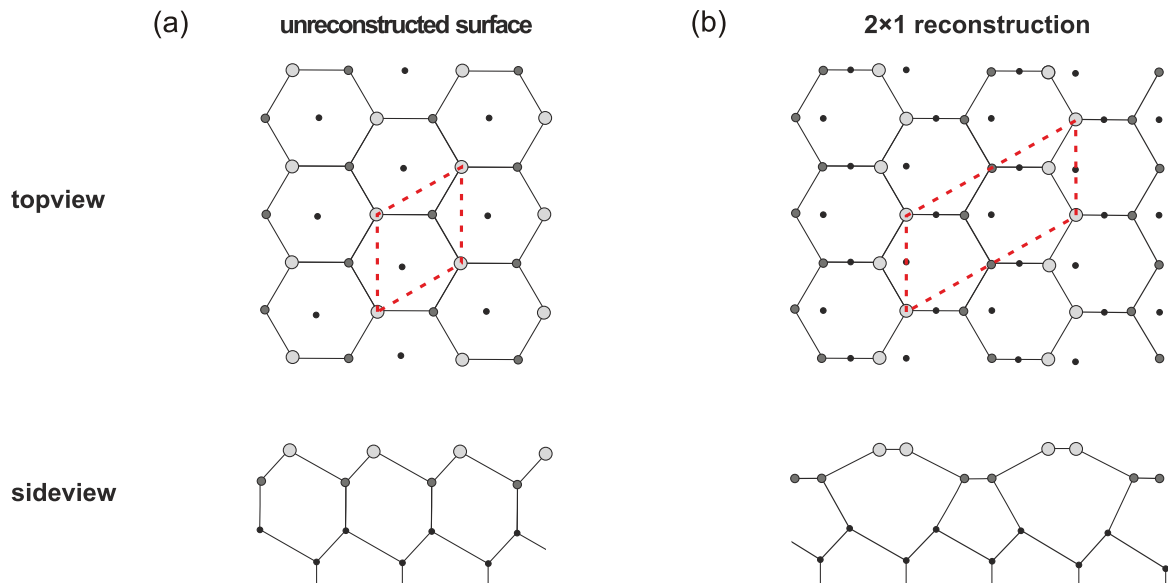


**Figure 3.6:** The Si(111) surface: (a) The unreconstructed surface. The dashed red diamond indicates the  $1 \times 1$  unit cell. (b) The Si(111) $2 \times 1$  reconstruction with the unit cell marked by the dashed red line.

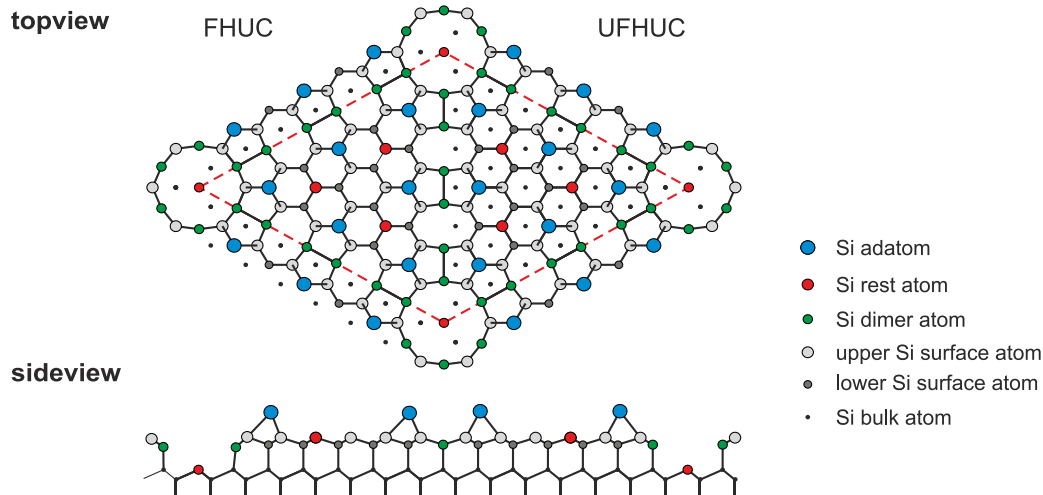


**Figure 3.7:** The DAS model of the Si(111)7×7 surface. The unit cell is indicated by the dashed red line, the faulted half unit cell and the unfaulted half unit cell are marked by FHUC and UFHUC, respectively. Adapted from [6].

An additional energy gain is obtained by a tilting of the chains [not shown in Fig. 3.6 (b)]. Only the incorporation of this tilting leads to an agreement of experimental [72,165–171] and theoretical [172–176] studies of the Si(111)2×1 surface.

However, the 2×1 reconstruction is not the lowest energy structure. This is the Si(111)7×7 reconstruction, into which the 2×1 reconstruction irreversibly converts upon annealing the surface. After the first low energy electron diffraction (LEED) observation in 1959 [177], it took 26 years to solve the structure of this reconstruction. It was in 1985, two years after the first atomically resolved STM images of the 7×7 were reported [58], when Takayanagi *et al.* [6,178] proposed their dimer-atom-stacking fault (DAS) model (Fig. 3.7). Nevertheless, the structural elements of this model were already proposed earlier, e.g. the concept of adatoms each reducing the number of dangling bonds by two was proposed by Harrison [179]. Also the formation of dimers and corner holes at the boundaries between the faulted and unfaulted halves of the unit cell was predicted, before Takayanagi *et al.* analyzed transmission electron diffraction patterns and correctly combined the structural elements as follows [180,181]:

The corners of the rhombic unit cell are formed by depressions, the so called corner holes. The 7×7 unit cell itself consists of two nonequivalent triangular half unit cells (HUCs) separated from each other by a row of three dimers. The dimer row leads to a shift of half a surface lattice constant and induces a stacking fault with respect to the bulk Si crystal in every second half unit cell. Additionally twelve adatoms and six rest atoms are found on the unit cell. The formation of this structure drastically reduces the number of unsaturated dangling bonds from 49 for the case of a bulk terminated 7×7 cell to 19. This renders the 7×7 reconstruction the most stable Si(111) structure, although its formation requires a transport of Si atoms from steps, since a 7×7 unit cell contains more atoms than are present on the unreconstructed surface [182–184]. Besides the 7×7, other similar DAS reconstructions such as the 3×3, 5×5, or 9×9 exist, but they

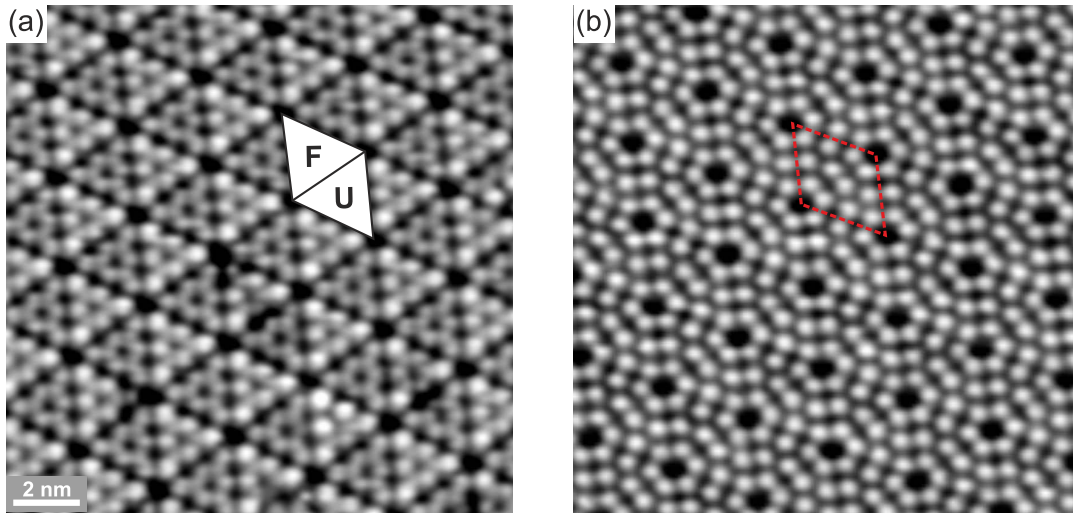


**Figure 3.8:** (a) Filled states STM image (sample voltage  $V_S = -1.5$  V; tunneling current  $I_T = 100$  pA) and (b) empty states STM image ( $V_S = +1.5$  V;  $I_T = 100$  pA) of the Si(111) $7\times 7$  surface. A unit cell is exemplarily marked in both images. In (a), the faulted half unit cell (marked with F) appears slightly brighter than the unfaulted half unit cell (marked with U).

occur only under special experimental conditions, e.g. when not sufficient atoms are present to form the  $7\times 7$  reconstruction or in the case of limited surface areas [185,186].

In Fig. 3.8, filled and empty states STM images of the Si(111) $7\times 7$  surface are shown. In both images, the corner holes appear as dark depressions in the corners of the unit cell, and the twelve adatoms per unit cell are clearly resolved and appear as bright protrusions. Additionally, in the filled states image [Fig. 3.8 (a)] the difference between the two half unit cells can be seen. Here, the faulted half unit cell (FHUC) appears slightly brighter than the unfaulted half unit cell (UFHUC). The main reason for the different appearance is electronic contrast [182], although the adatoms of the UFHUC were also found to be positioned slightly higher [192,193].

The electronic properties of the Si(111) $7\times 7$  surface were studied experimentally by angle resolved photoemission spectroscopy (ARPES) and inverse photoemission spectroscopy [187–189,194,195], by STS [190,191,196,197] as well as theoretically [184,198,199]. The experimental results are summarized in Fig. 3.9. By photoemission, three occupied bands ( $S_1$  to  $S_3$ ) and one unoccupied band ( $U_1$ ) of surface states were found [see Fig. 3.9 (a)]. The ability of the STS technique to obtain locally resolved information on the electronic structure of the surface enables the assignment of these bands. From atomically resolved tunneling spectra [Fig. 3.9 (b)] and STS images [Fig. 3.9 (c)] [190,191,196], the band  $S_1$  and  $U_1$  could be assigned to the occupied and unoccupied adatom states. The band  $S_1$  extends to above the Fermi level, thus rendering the surface metallic. The remaining two bands  $S_2$  and  $S_3$  correspond to the states from the six rest atoms and to backbonds of the adatoms, respectively. These assignments are confirmed by theoretical calculations [184,198,199].

At a temperature of about 850 °C a reversible transition from  $7\times 7$  to a disordered surface takes place [200–202]. In the LEED pattern, the  $7\times 7$  spots disappear and a “ $1\times 1$ ” reconstruction is observed.

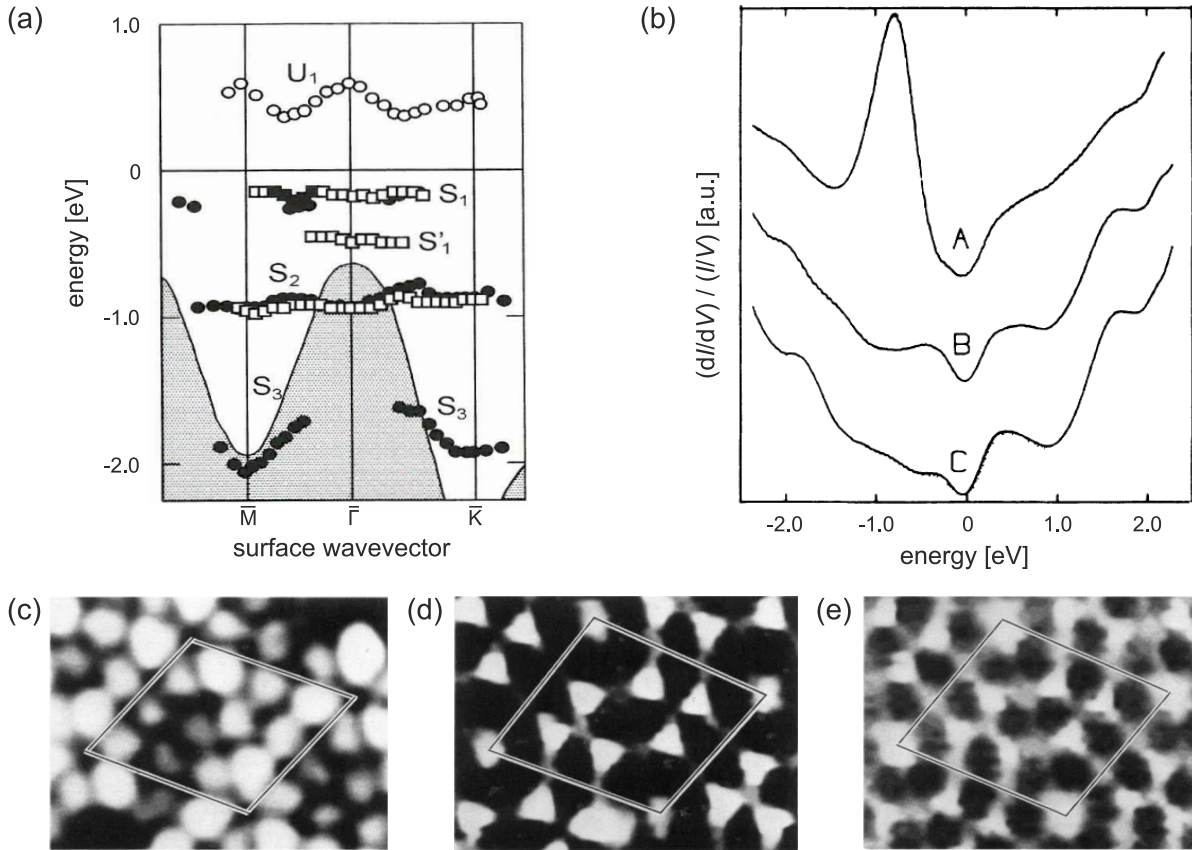


**Figure 3.9:** Electronic properties of the Si(111) $7\times 7$  surface. (a) Dispersion of the surface states. The occupied states were measured using photoemission spectroscopy by Mårtensson *et al.* [187] and Uhrberg *et al.* [188], the unoccupied states using inverse photoemission spectroscopy by Nicholls and Reihl [189]. From [162]. (b) Atomically resolved tunneling spectra taken on rest atoms (A), corner adatoms (B), and center adatoms (C). From [190]. (c-e) STS images of the occupied surface states showing the adatom state at  $-0.35$  V (c), the rest atom state at  $-0.8$  V (d), and the backbond state at  $-1.7$  V. From [191].

### 3.2.2 The Si(557) surface

The Si(557) surface is a vicinal Si(111) surface with a miscut angle of  $9.45^\circ$  towards the  $[\bar{1}\bar{1}2]$  direction. It was found that it reconstructs into an atomically perfect grating structure consisting of alternating Si(111) terraces and triple steps [203]. An overview STM image of a well prepared Si(557) surface showing the high accuracy of the step structure is displayed in Fig. 3.10 (a). Although it has been studied quite intensively [203–209], the detailed atomic structure of the surface, especially that of the triple step is still a subject of discussion. While Kirakosian *et al.* proposed a (112)-orientation of the steps [203], later a (113)-orientation [204] and a combination of a double and a single step [205] were proposed.

In most studies, no atomically resolved images could be obtained on the triple step or they were influenced by tip artifacts [206, 207]. Hence, the most convincing among the proposed structure models is the one developed by Teys *et al.* [205] based on atomically resolved STM images of the triple step [see Fig. 3.10 (b)] in combination with spot-profile analysis LEED (SPA-LEED) data. In this model, which is shown in Fig. 3.10 (c), the (111) terrace has a width of one  $7\times 7$  unit cell plus two atomic rows that form an additional row of adatoms (R)

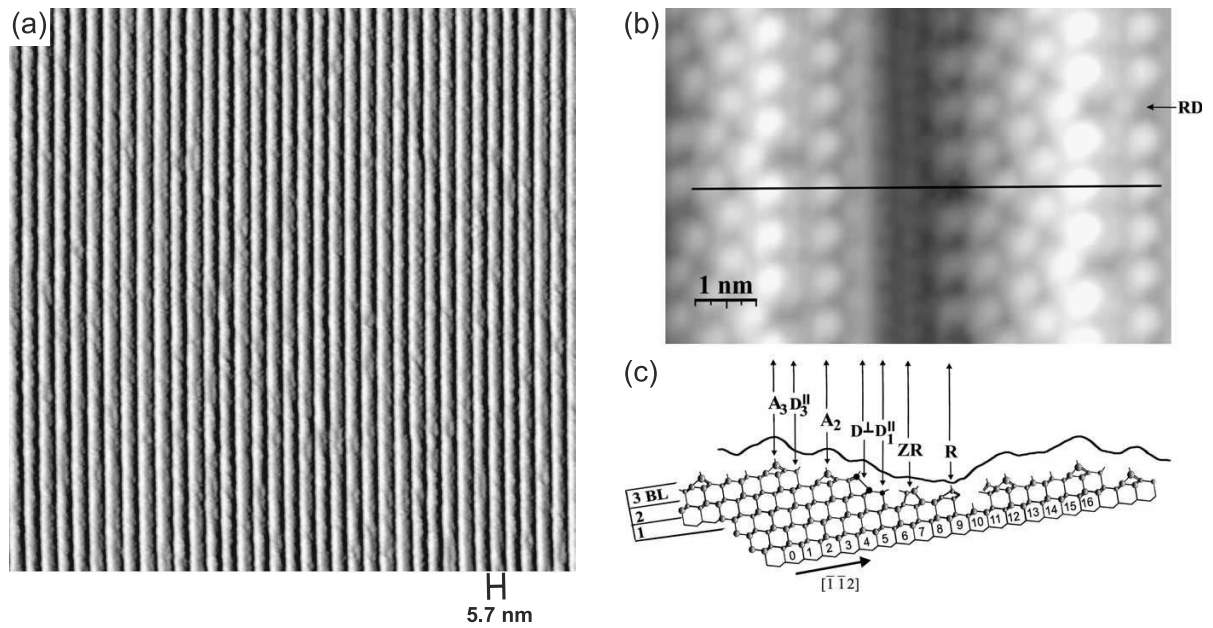


**Figure 3.10:** (a) Overview STM image of the Si(557) surface. From [203]. (b) Atomically resolved STM image of the triple step. From [205]. (c) Height profile along the black line in (b) together with the proposed structure model. From [205].

at the bottom of the step. The triple step itself is formed by a combination of a double step and a single step with another row of adatoms ( $A_2$ ) on the intermediate terrace. The overall width of this reconstruction amounts to 16 atomic rows, hence the actual surface orientation is not (557), but (7 7 10), a finding that differs from Ref. [203], but is supported by SPA-LEED measurements. Nevertheless, in the following, the surface is referred to as Si(557) since the wafers used within this work are nominally Si(557) oriented.

In addition, it was found that, depending on the detailed preparation conditions or by using slightly misaligned Si(557) wafers, a variety of step arrays with different periodicities can be obtained [208, 209].

### 3.2.3 The Si(001) surface

Cutting the diamond lattice along (001), as it is indicated by the blue plane in Fig. 3.5, results in the formation of two dangling bonds per surface atom [see Fig. 3.11 (a)]. To reduce this high number of dangling bonds and thus the total energy, neighboring pairs of atoms form dimers [Fig. 3.11 (b,c)], lowering the total energy by about 2 eV per dimer. This results in the formation of a  $2 \times 1$  reconstruction which was first observed by Schlier and Farnsworth in 1959 [177] using LEED. Since the orientation of the dangling bonds switches by  $90^\circ$  from one (001) plane to the next, two orthogonally oriented  $2 \times 1$  domains form on neighboring terraces separated by single layer steps. The orientation of the dimer rows then alternates from parallel to perpendicular with respect to the step edges resulting in different types of step edges called  $S_a$  and  $S_b$  steps, respectively [210].

For a symmetric dimer geometry as shown in Fig. 3.11 (b) both dimer atoms are equivalent, what would lead to partly filled dangling bonds. To further minimize the total energy, the

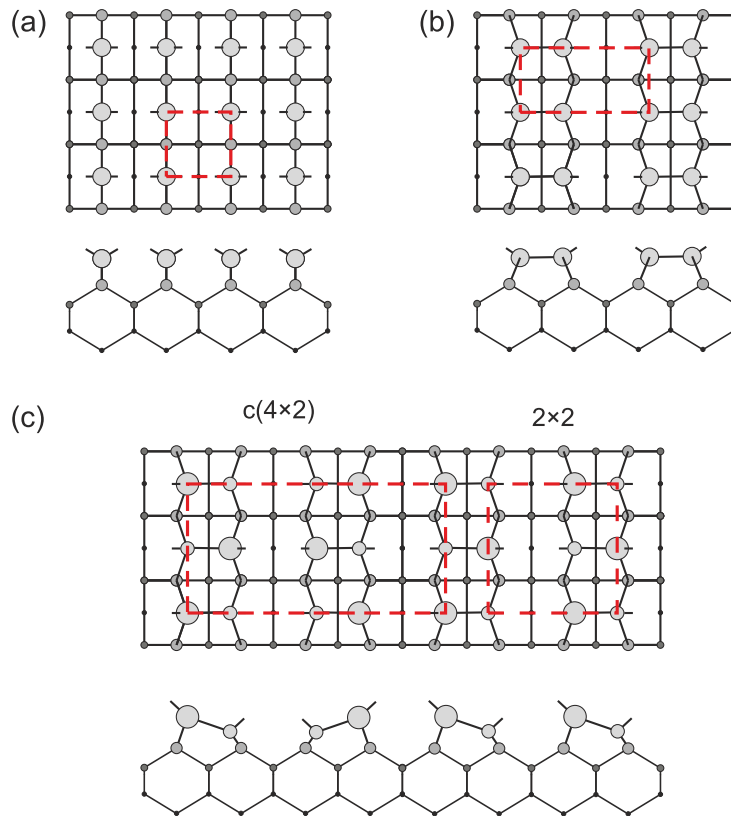


**Figure 3.11:** The Si(001) surface. (a) The unreconstructed surface: Every surface atom exhibits two dangling bonds, resulting in a total number of two dangling bonds per  $1 \times 1$  unit cell. (b) Symmetric dimers: Dimer formation lowers the dangling bond density by a factor of two and results in a  $2 \times 1$  reconstruction. (c) Tilted dimers: Incorporation of a slight tilting of the dimers results in further energy minimization. The tilt direction alternates along the dimer rows. Depending on the alignment of neighboring rows, either a  $c(4 \times 2)$  or a  $2 \times 2$  reconstruction forms. The corresponding unit cells are indicated by dashed red lines.

dimers undergo a Jahn-Teller distortion and a slight tilting of the dimers of about  $18^\circ$  is induced lowering the symmetry. The resulting structure is shown in Fig. 3.11 (c). As a consequence of the rearrangement, the dangling bonds of the upper dimer atom become fully occupied, while the dangling bonds located at the lower dimer atoms become empty, resulting in a semiconducting behavior of the Si(001) $2 \times 1$  surface. The asymmetric dimer model results in an energy gain of approximately 0.1 eV per dimer [211] and is well established both experimentally [212–216] and theoretically [211, 217–220].

However, in STM images taken at room temperature like those shown in Fig. 3.12 most of the dimers appear symmetric. Tilted dimers are only observed in filled states STM images near step edges or other defects [see Fig. 3.12] [221, 222]. Molecular dynamics calculations showed that the tilted dimers are flipping with a rate of about 5 THz. Since an STM measurement is much too slow to resolve this process, only an averaged image where the dimers appear symmetric is obtained [211, 224]. In the STM images shown in Fig. 3.12, the dimer rows are clearly resolved. Within the rows, a dimer appears as an elongated protrusion in the filled states image, while in the empty states image two small round protrusions appear. Thereby,

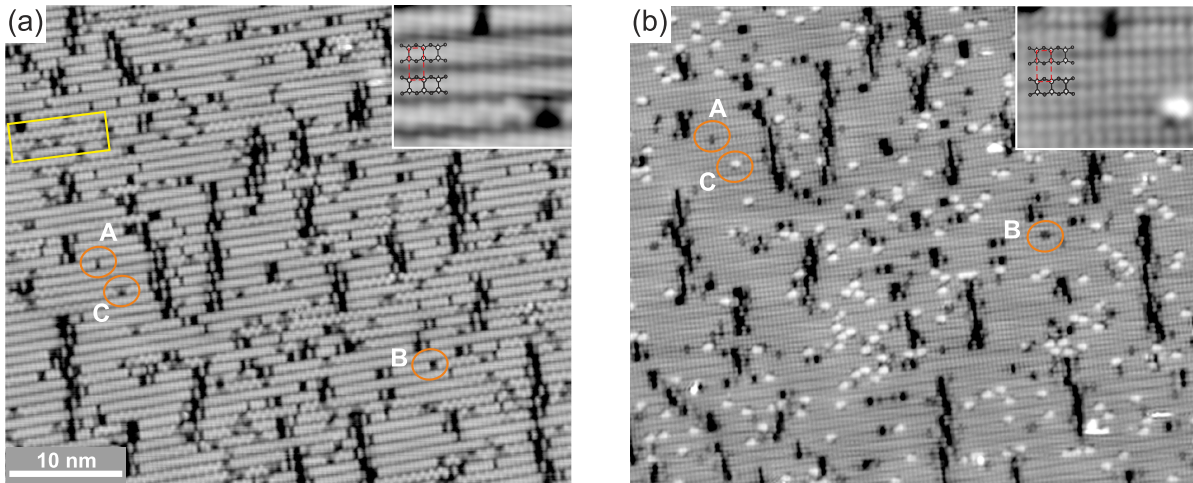


**Figure 3.12:** (a) Filled states STM image ( $V_S = -1.5$  V;  $I_T = 100$  pA) and (b) empty states STM image ( $V_S = +1.5$  V;  $I_T = 100$  pA) of the Si(001) surface. The different types of defects are marked with A, B, and C according to Hamers and Köhler [223]. In (a), the yellow box marks an area where a  $c(4 \times 2)$  arrangement of buckled dimers is observed. The insets show enlarged views of the same  $4 \times 3$  nm<sup>2</sup> large area with the structure model being overlaid on the STM images.

the elongated protrusion leading to the bright contrast in the filled states shows the actual location of the dimer rows, while in the empty states image the shorter distance between the small round protrusions is found at the positions of the trenches between the dimer rows resulting in an inverted contrast with respect to the filled states STM images (cf. insets in Fig. 3.12) [225, 226].

When performing an STM experiment at a temperature of 120 K, the flipping of the dimers is frozen and tilted dimers are observed more frequently [227]. Here, an interaction between neighboring dimers results in an alternating buckling within one row and a  $2 \times 2$  or a  $c(4 \times 2)$  periodicity depending on the registry between adjacent rows as shown in Fig. 3.11 (c).

Due the presence of defects on the surface shown in Fig. 3.12, the  $c(4 \times 2)$  reconstruction is observed locally in the area indicated by a yellow rectangle in (a). The major structural defects on this surface are missing dimer defects. According to Hamers and Köhler [223], the typical types of defects can be classified into three types, namely type A (single dimer vacancy), type B (double dimer vacancy), and type C. In Fig. 3.12 (a,b), locations where such defects occur are exemplarily indicated by orange ovals. The ordering of the missing-dimer defects into rows that is observed on the surface might be caused by a small Ni contamination that occurred during sample preparation [228–230].

### 3.3 Epitaxial growth

Epitaxial growth is the growth of a crystalline film on a crystalline substrate. Thereby, the word epitaxy is composed of the Greek words  $\acute{\epsilon}\pi\iota$  meaning “on” and  $\tau\acute{\alpha}\xi\varsigma$  meaning “arrangement”. Depending on the film and substrate material, epitaxy is divided into homoepitaxy, when substrate and film are of the same material, and heteroepitaxy, when the film material is

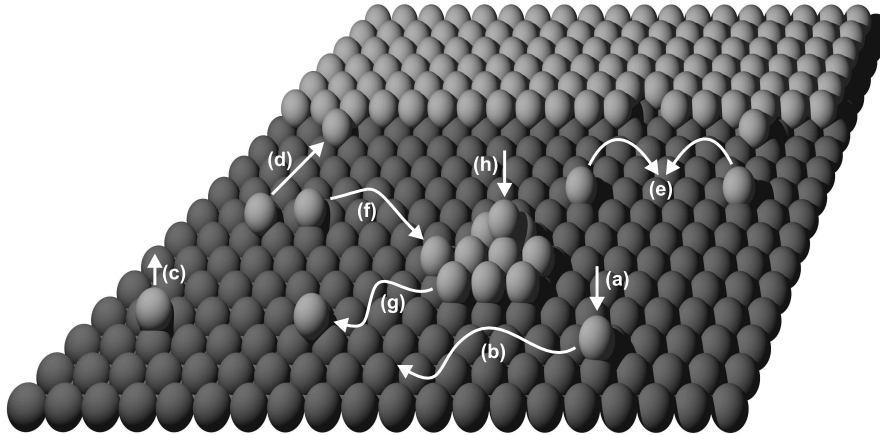


**Figure 3.13:** Illustration of the fundamental processes that occur during epitaxial growth. (a) deposition of atoms on the surface; (b) diffusion of adatoms on the surface; (c) desorption from the surface; (d) attachment of adatoms at steps; (e) nucleation of islands; (f) attachment of adatoms at islands; (g) detachment of atoms from islands; (h) deposition of atoms on top of an island. Adapted from [232].

different from the substrate material. In both cases, the phenomenon of epitaxial growth is based on a few fundamental processes, of which some are shown in Fig. 3.13. After being deposited on a surface [Fig. 3.13 (a)], adatoms may diffuse on the surface [Fig. 3.13 (b)], when their energy is higher than the activation energy for diffusion, or they might desorb from the surface again [Fig. 3.13 (c)]. When diffusion takes place, the adatoms may encounter either a step where they are attached [Fig. 3.13 (d)] or another adatom and form nuclei for two-dimensional islands [Fig. 3.13 (e)]. Such islands can grow through attachment of further adatoms [Fig. 3.13 (f)] or shrink through detachment of atoms [Fig. 3.13 (g)]. The small island nuclei are metastable as they may decay back into individual adatoms. However, when the size of an island has overcome a critical size, the probability of growth becomes larger than the decay probability and the island becomes stable. Another process that might occur is the deposition of atoms on an island [Fig. 3.13 (h)]. A quantitative description of the processes is possible using rate equations [231–234].

Since the growth often takes place at conditions far from equilibrium, kinetic limitations can play a role. If either the step density or the mobility of the adatoms on the surface is very low, the growth at preexisting steps can be neglected. The growth then occurs via island nucleation. If on the other hand, the mobility of the adatoms is high enough to reach a step, step-flow growth will take place [232, 233].

### 3.4 Thin film growth techniques

The atoms that form the epitaxial layers may be provided by different ways, defining the respective growth technique. The most widely used techniques are molecular beam epitaxy (MBE) and metalorganic vapor phase epitaxy (MOVPE), where the atoms to be deposited are

present as a vapor or bonded in molecules in the gas phase. Nevertheless, the atoms may also be present in the liquid phase (liquid phase epitaxy – LPE) or as an amorphous solid (solid phase epitaxy – SPE). In this work, reactive deposition epitaxy (RDE) and SPE as two specific modifications of MBE are used to grow different types of nanostructures.

MBE is conceptually very simple. The film material is usually present as a solid and is evaporated by a Knudsen cell to form an atomic or a molecular beam. This molecular beam hits the surface of the substrate, which is usually kept at an elevated temperature to ensure epitaxial growth. Thereby, the substrate temperature has to be high enough to enable diffusion of the atoms or molecules on the surface, and, on the other hand, it should be low enough to avoid desorption or diffusion-induced intermixing between the epitaxial layers. The comparatively low growth rates (typically below one monolayer per second) usually lead to very smooth surfaces of the grown films. In addition, the sources may be switched on and off via mechanical shutters very fast. Thus, the composition or doping of the layers can be changed with atomic accuracy. The whole MBE process takes place in an UHV environment allowing in-situ growth monitoring e.g. by reflection high energy electron diffraction (RHEED) or reflectance anisotropy spectroscopy.

A special regime of MBE growth is SPE. Here, the material is first deposited on the substrate at room temperature or even below. This results in the formation of an amorphous film that is crystallized after deposition by postgrowth annealing. During crystallization, the crystalline-amorphous interface moves from the substrate to the outer surface. In RDE, which is the second method employed in the present thesis, the substrate is heated during deposition.

### 3.5 Self-assembled magic clusters on surfaces

The direct growth of magic clusters on surfaces is a rather novel field of research. The first speculations on the existence of surface magic clusters (SMCs) in the Pt/Pt(111) system were published in 1992 [235]. However, a later STM investigation could not confirm this assumption [236]. The first observation of clusters on surfaces exhibiting sizes with an enhanced stability similar to the magic gas phase clusters (cf. section 3.1.1) was then reported in 1998 by Lai and Wang [5]. In a two step process, they deposited Ga on the Si(111) surface leading to the formation of several types of triangular Ga SMCs on a  $\sqrt{3}\times\sqrt{3}$  Ga/Si(111) surface [see Fig. 3.14 (a)] [5, 237]. By analyzing the cluster sizes, they found four prominent peaks corresponding to triangles with  $n = 2, 3, 4,$  and  $5$  atoms on their edges, as shown in Fig. 3.14 (b). With about 50%, the  $n = 4$  cluster is the most abundant cluster type. This demonstrates the particular stability of this cluster which was also proved by theoretical calculations [240, 241], and can be understood by counting the number of dangling bonds that remain at Si atoms in the surrounding area of the clusters due to missing Ga  $\sqrt{3}\times\sqrt{3}$  atoms. The environment of the  $n = 4$  cluster has a minimum absolute number of dangling bonds, thus representing some sort of “closed shell” structure [238].

Another example of two-dimensional islands with magic sizes, discovered at the same time as the Ga induced SMC, is shown in Fig. 3.14 (c). It was found that the size distribution

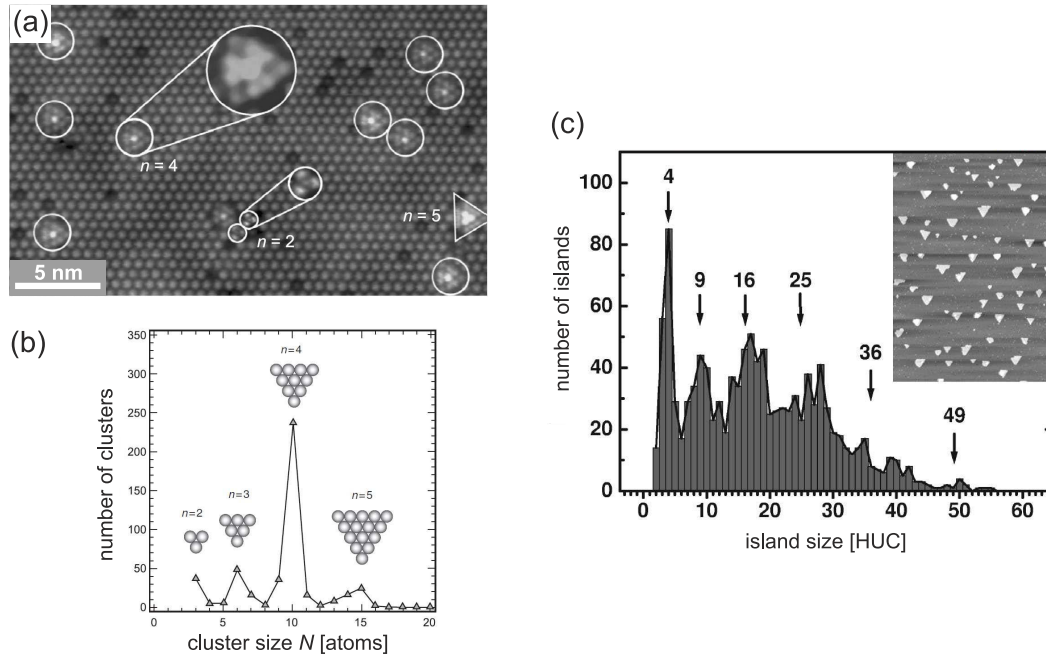


**Figure 3.14:** Examples of magic clusters on surfaces. (a) Empty states STM image of Ga induced SMCs on the  $\sqrt{3} \times \sqrt{3}$  Ga/Si(111) surface.  $n = 2$  and  $n = 4$  clusters are marked by small and large circles, one  $n = 5$  cluster by the triangle. The insets show magnified views of the  $n = 2$  and  $n = 4$  clusters. Here,  $n$  denotes the length of the edges. From [238]. (b) Histogram of the size distribution of the Ga induced SMC. From [5]. (c) Magic sizes of  $7 \times 7$  islands on the Si(111) $7 \times 7$  surface observed during Si(111) homoepitaxy. In the histogram, several peaks corresponding to magic islands are present. The inset shows an STM image of the Si(111) surface covered with the triangular islands. From [239].

of islands forming during Si(111) homoepitaxy exhibits several peaks corresponding to magic sizes [239]. The driving force behind this effect is the  $7 \times 7$  reconstruction with its two different half unit cells (cf. section 3.2.1). The higher cost of energy for lifting the reconstruction in the faulted half unit cell leads to a nucleation barrier for the further growth and in this way to the formation of triangular magic islands.

These two examples demonstrate that clusters with magic sizes due to a geometric shell closure very similar to the gas phase clusters described in section 3.1.1 may also be found on surfaces. For Ag clusters grown on Pb islands on Si(111) even a transition from electronic shell closure to a geometric one was observed [242].

Nevertheless, the mentioned clusters still show some size variation. The next level of precision in creating tailor-made nanostructures would be the ability to control the growth in such a way that only identical clusters of the same size and atomic structure form on the surface. The first such monodispersed clusters observed were magic Si clusters that form on the Si(111) $7 \times 7$  surface [243]. These clusters are smaller than the magic Si islands shown in Fig. 3.14 (c) and form predominantly in single half unit cells of the  $7 \times 7$  reconstruction.

Such a formation of clusters at conditions, where the surface reconstruction remains at least partly intact, was found to be a well suited method to grow monodispersed magic clusters. Particularly the Si(111) $7 \times 7$  surface was found to be an excellent template for the growth of

clusters of various materials. Since this approach was also employed in this thesis, the state of the art in research on magic clusters on the Si(111)7×7 surface is summarized in the following section. Previous results on self-assembled clusters on the Si(001) surface which is the second surface used within this thesis are then summarized in section 3.5.2

It should be mentioned that the so-called ring clusters that some silicide forming materials (Co [244–248], Ni [246, 249–252], Fe [246, 253], Pd [246], Pt [246], and Ir [246]) induce on Si(111) were discovered even earlier than the Ga induced clusters mentioned above. These clusters form after high temperature deposition of the metal on the Si(111) surface. Thereby, the 7×7 reconstruction is destroyed and for most of the metals two different types of clusters form: the so-called  $\sqrt{7}$  ring clusters and  $\sqrt{19}$  ring clusters. Both types form preferentially at step edges, domain boundaries, or other defect sites. At higher coverages, these clusters arrange into a  $\sqrt{7}\times\sqrt{7}$  R19.1° and a  $\sqrt{19}\times\sqrt{19}$  R19.1° lattice, respectively. This nucleation behavior thus represents rather the initial growth of a usual surface reconstruction than surface magic clusters which would grow randomly distributed on the surface.

### 3.5.1 Magic clusters on the Si(111)7×7 surface

The fundamental mechanisms in the adsorption and diffusion of additional atoms on the Si(111)7×7 surface that result in the above mentioned template effect have been studied in a number of theoretical works [254–259]. It was found that the additional atoms find so-called “basins of attraction” located around the rest atoms of the 7×7 reconstruction where they get trapped. Within each basin, they can diffuse very fast, while diffusion from one basin to another or across the border of the half unit cell is less probable due to large energy barriers [254, 255]. Furthermore it was found that an attractive interaction between adsorbates in neighboring half unit cells promotes the cluster formation [257–259].

Beyond the growth of monodispersed clusters, the template approach paves the way towards the ultimate level of precision. Due to the conservation of the periodicity, the use of a reconstructed surface as a template offers the possibility to produce two-dimensional arrays of identical clusters. The most perfectly ordered and most extensively studied arrays are those of the group-III metals Ga, Al, and In on the Si(111)7×7 surface that are described in detail further below. However, the ability to grow ordered arrays of clusters was also demonstrated for other materials, e.g. Na [11], Tl [260–262], Ge [263, 264], Sn [265], Pb [12], Mn [266–268], and Cu [269].

Additionally, for many systems the growth of magic clusters within 7×7 HUCs is observed, but without being able to produce ordered arrays. Besides the aforementioned magic Si clusters [243, 270–272], this was demonstrated for a number of other systems including Fe [14], Co [13, 273], Ag [274, 275], Au [15], Zn [16], and K [276, 277]. Exemplarily, the Co and Fe induced silicide clusters are described in detail later, due to their similarity with the rare earth silicide clusters investigated in this thesis.

A special behavior is found for magic clusters of the alkali metals [11, 276–278] where two phases are observed upon cluster formation. At coverages below a critical value of  $\sim 0.08 \text{ ML}^1$  a two-dimensional adatom gas is formed. Here, the alkali atoms, while being strongly bound to the surface, are highly mobile and diffuse within the “basins of attraction” mentioned above. Then, at coverages exceeding the critical value, the formation of magic clusters sets in.

Beyond the two-dimensional ordered lattices of clusters, a few studies targeting a one-dimensional ordering were also conducted. Here two approaches were successful. In the first approach, regularly stepped surfaces were used to grow one-dimensional chains of Si and Ge clusters at step edges [18–20]. The second approach employed domain boundaries of the  $5 \times 5$  Ge/Si(111) surface to obtain a one-dimensional ordering of magic In and Ga clusters [17].

### Magic clusters of group-III metals

Deposition of the group-III metals Ga, In, and Al at appropriate growth conditions results in the formation of clusters with very similar properties. In all cases, centered triangular  $M_6\text{Si}_3$  clusters ( $M = \text{Ga, In, Al}$ ) form within the  $7 \times 7$  HUCs [7–10, 24, 238, 279–292]. The Ga clusters were discovered first in 2001 by Lai and Wang [7]. In 2002, Jia *et al.* [8] and Kotlyar *et al.* [9] independently found the formation of the magic Al clusters, and Li *et al.* [10] that of the magic In clusters. The In and Al clusters were already observed in earlier works studying the initial growth at low metal coverages and low growth temperatures [281, 282] but not described as magic clusters.

An atomic structure model of the clusters is shown in Fig. 3.15 (a). For their formation, no Si diffusion from other HUCs is needed since the clusters incorporate the former Si center adatoms that were already present in the corresponding HUC. For the trivalent group-III metals, such an arrangement results in a reduction of the number of dangling bonds in the HUC from nine to three, disregarding the dangling bonds at the rest atoms inside the corner holes. Only the dangling bonds located at the corner adatoms remain, giving an explanation for the extraordinary stability of these clusters.

Many structural details can directly be derived from atomically resolved STM images as shown in Fig. 3.15 (b) and (c). Due to a charge transfer from the group-III metals to the Si atoms, the empty states are mainly located at the group-III atoms and six bright protrusions appear at their locations in the empty states image [Fig. 3.15 (b)]. In contrast, in the filled states image the three cluster Si atoms are imaged resulting in an appearance as a smaller triangle. A further strong contrast is observed at the remaining corner Si adatoms of the HUC. Supported by structure determination conducted by first principles calculations [8, 10, 279, 280, 283, 286], LEED [283], and RHEED [287], this structure model is well established.

For Ga, a clustering within the  $7 \times 7$  half unit cells is already observed for deposition at room temperature. However, the resulting clusters have an irregular shape and size. For preparing identical magic clusters, the surface needs to be heated to an appropriate temperature during

---

<sup>1</sup>One monolayer (ML) is thereby defined as one adsorbate atom per  $1 \times 1$  unit cell of the unreconstructed surface.

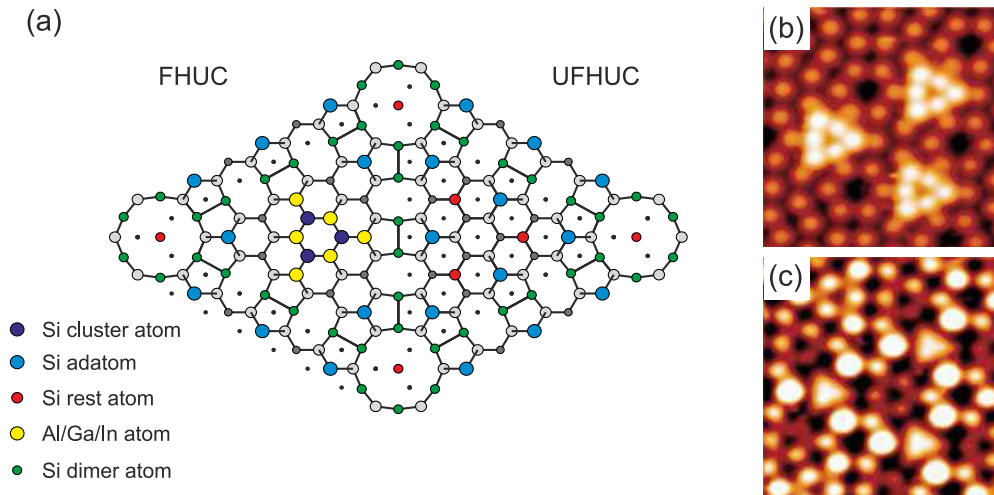


**Figure 3.15:** (a) Atomic structure of the magic group-III metal clusters on the Si(111) $7\times 7$  surface. The clusters consist of six metal and three Si atoms forming a triangle centered within the  $7\times 7$  half unit cell. Adapted from [7]. (b) Empty states STM image ( $V_S = +1.0$  V) and (c) filled states STM image ( $V_S = -1.5$  V) of the magic In clusters. From [293].

growth. For Ga, the reported temperatures are between 250 °C and 400 °C [7, 238, 283, 287], for In between 100 °C and 200 °C [10, 238, 279], and for Al between 250 °C and 550 °C [8, 9, 24, 238, 279, 280, 290]. Then, the In clusters are stable up to temperatures of about 200 °C to 300 °C [10, 279, 294], the Ga clusters up to about 400 °C to 450 °C [7, 284], and the Al clusters up to about 500 °C to 550 °C [279, 280, 288].

The maximum coverage is obtained, when every  $7\times 7$  HUC is covered with one magic cluster. This corresponds to twelve metal atoms per unit cell, being equivalent to 0.24 ML. For this coverage, a perfectly ordered two-dimensional lattice of clusters is formed, as shown in Fig. 3.16 (a) for magic Al clusters.

At lower coverages, a preferential growth of the clusters on the FHUC of the  $7\times 7$  reconstruction can be observed [7, 10, 279, 290]. Among the group-III metal clusters, the magic In clusters

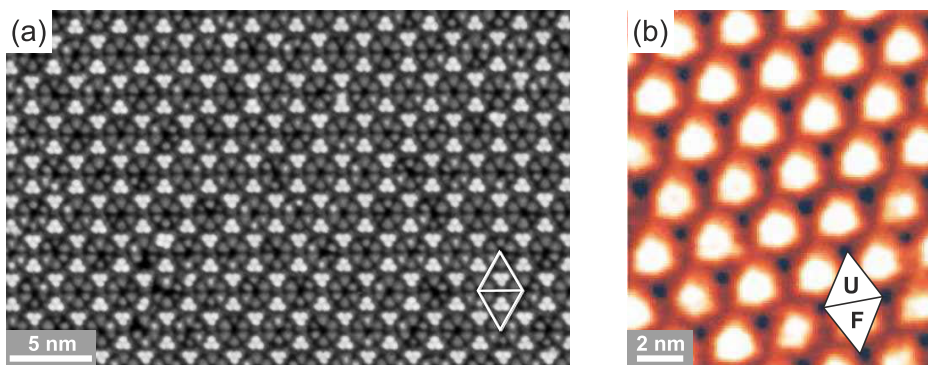


**Figure 3.16:** Perfectly ordered arrays of magic clusters on the Si(111) $7\times 7$  surface. (a) Al cluster array at 0.24 ML coverage, where every  $7\times 7$  HUC is covered with an identical magic cluster. From [238]. (b) In cluster array at 0.12 ML coverage, with only the FHUCs being covered with magic clusters. From [10].

show the highest preference for covering exclusively the FHUC, which is preserved until almost all FHUCs are occupied. Hence, the In clusters allow the preparation of a second type of two-dimensional lattice where only all FHUCs are covered [see Fig 3.16 (b)]. Such a preferential occupation of the FHUC, however, is found for most magic cluster systems on Si(111)7×7.

Besides the growth and the atomic structure, the electronic properties of group-III metal clusters on Si(111)7×7 were also studied using STS [10, 292, 293, 295], PES [296], and density functional theory (DFT) [286, 295]. It was found that, in contrast to the Si(111)7×7 surface being metallic due to the presence of surface states in the band gap (cf. section 3.2.1), the clusters are semiconducting with an energy gap opening around the Fermi level. In Fig. 3.17, atomically resolved STS data of the magic In clusters are shown. The tunneling spectra taken on the cluster clearly show local energy gaps around 0.9 eV, which vary slightly from site to site, while the spectra taken on adatoms of the uncovered 7×7 HUC show a metallic behavior. The value obtained for the energy gap is also consistent with PES results from the same group [296]. In the literature on self-assembled magic clusters on surfaces, such energy gaps are mostly denoted as band gaps, although HOMO-LUMO gaps would be the more correct denotation, since a band structure has not developed yet for these small clusters. For uniformity reasons, the local energy gaps of the clusters are also referred to as band gaps in the present thesis.

In contrast to In, Ga, and Al, the group-III element Tl shows a different growth behavior. For room temperature deposition, clusters with irregular sizes grow almost exclusively on the FHUCs, while for higher growth temperatures the simultaneous growth of different cluster types is observed [260–262].

### Magic Co and Fe silicide clusters

In contrast to the aforementioned group-III metals, the 3d ferromagnetic metals Fe and Co are highly reactive and form silicides. Nevertheless, it was demonstrated that the deposition of small amounts of these metals at temperatures between 130 °C and 170 °C for Fe [14] and between 210 °C and 250 °C for Co [13, 273] leads to the formation of magic clusters. The

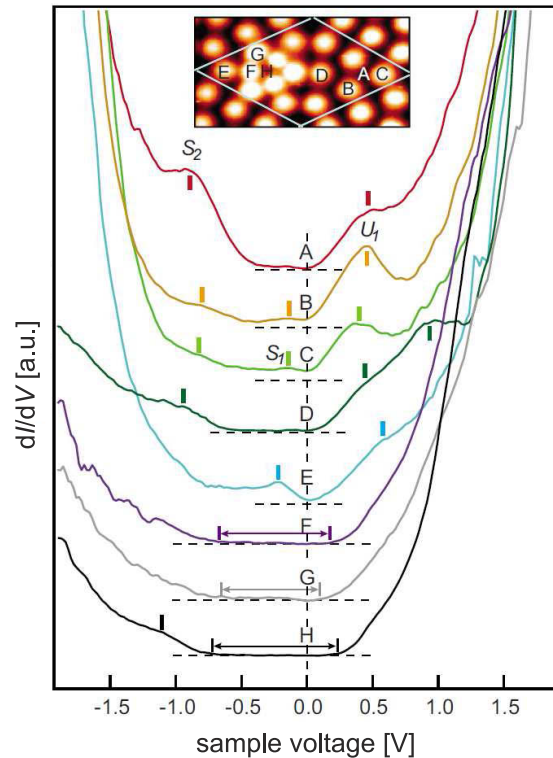


**Figure 3.17:** Site-resolved scanning tunneling spectroscopy on a magic In cluster on the Si(111)7×7 surface. A–H represent  $dI/dV$ – $V$  spectra taken at positions indicated in the inset. The spectra taken on the magic cluster show an energy gap with values of 0.9 eV (F), 0.8 eV (G), and 1.0 eV (H). From [293].

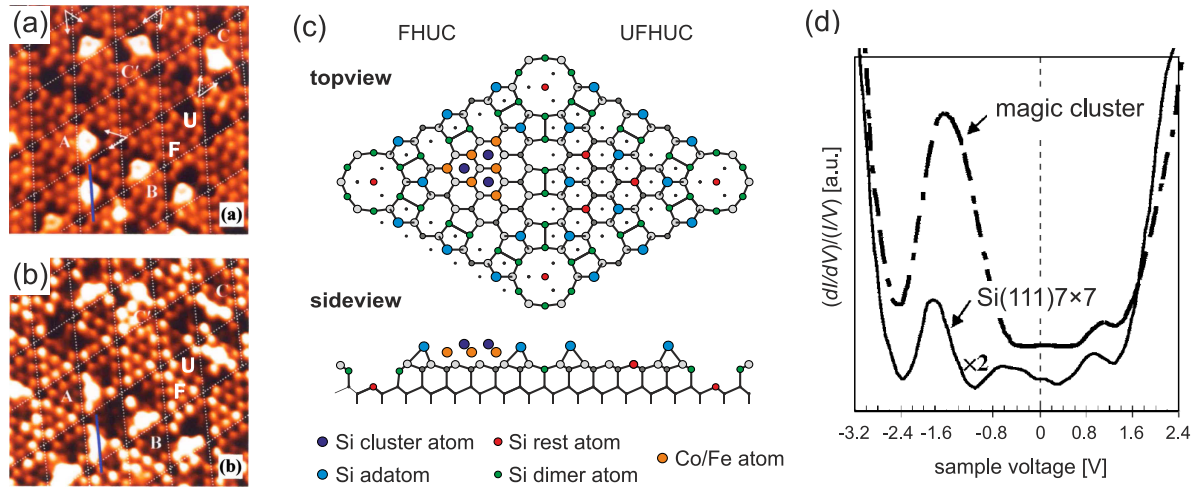


**Figure 3.18:** Properties of the magic Co and Fe silicide clusters on Si(111)7 $\times$ 7. (a) Empty states STM image ( $V_S = +1.8$  V) and (b) filled states STM image ( $V_S = -1.8$  V) of the same area showing magic Co clusters formed after depositing 0.06 ML Co at 230 °C. The faulted and unfaulted HUCs are marked by F and U, respectively. From [13]. (c) Atomic structure model of the magic Co and Fe clusters in topview and sideview. Adapted from [13]. (d) Averaged  $(dI/dV)/(I/V)-V$  spectra of the magic Co clusters and of the uncovered Si(111)7 $\times$ 7 surface. The spectra taken on the clusters clearly show a band gap of about 0.8 eV. From [273].

clusters are randomly distributed over the surface and occupy mainly the FHUCs of the 7 $\times$ 7 reconstruction. In Fig. 3.18 (a) to (c), empty and filled states STM images as well as the atomic structure model of the Fe and Co magic clusters are shown.

The clusters are not located centered within the 7 $\times$ 7 HUCs, but off-center near the center of an edge. Each cluster consists of six metal atoms and three Si atoms forming a triangle [see Fig. 3.18 (c)]. Similar to the group-III metal clusters, the three center Si adatoms are incorporated into the cluster, while the corner Si adatoms are unaffected by the cluster formation. Hence, again no Si diffusion from other HUCs is needed to form the clusters. In the final configuration of the clusters, the Si atoms are located slightly above the Co atoms, emphasizing the silicide character of the clusters.

In addition, also STS measurements were conducted on the magic Co clusters [273]. The obtained averaged  $(dI/dV)/(I/V)-V$  spectra are shown in Fig. 3.18 (d). In comparison to the spectra taken on the uncovered Si(111)7 $\times$ 7 which are clearly metallic, the Co magic clusters exhibit semiconducting properties with a band gap of  $\sim 0.8$  eV.

It has to be noticed that the authors of the cited studies were not able to produce ordered cluster arrays. The maximum cluster coverage is reached at about 0.1 ML Fe, where only  $\sim 30\%$  of the HUCs are occupied with magic clusters. At this coverage, the adsorption sites on the other HUCs are covered with other cluster types or defects, preventing a further growth of magic clusters [14].

### 3.5.2 Magic clusters on the Si(001) surface

Compared to the Si(111) surface, clusters on the Si(001) surface have been studied much less intensively. This might be related to the  $2\times 1$  surface reconstruction, for which a template effect as for the  $7\times 7$  reconstruction is not expected. To the best of my knowledge, only magic clusters of the group-III metals In [238, 297–308] and Al [238, 307, 309–312] were studied on Si(001) up to now. In both cases, deposition of a few percents of a monolayer at  $\sim 500$  °C results in the formation of magic clusters with an identical structure that are distributed randomly across the surface [see Fig. 3.19].

The structure model, which is shown in Fig. 3.19 (b), was first proposed by Bunk *et al.* [305] and is supported by experimental [305, 306] and theoretical studies [310, 311, 313, 314]. The stable pyramid-like cluster consists of six metal atoms and seven Si atoms and occupies a  $4\times 3$  area of the surface.

When increasing the metal coverage, the cluster density increases, but the spatial distribution of the clusters on the surface is still random. This behavior distinguishes the magic clusters from other metal-induced surface reconstructions that would preferentially nucleate at step edges or other defect sites and, even at very low coverages, form domains consisting of several unit cells.

The saturation coverage is obtained at  $\sim 0.5$  ML. At this coverage, the clusters are closely packed and form a two-dimensional lattice. Here, In and Al behave differently. For In, a well ordered  $4\times 3$  lattice as shown in Fig. 3.20 (a) is formed by just stringing together the SMC described by the model mentioned above.

In the case of Al, besides the cluster formation, also a substitutional incorporation of Al atoms into the top Si(001) layer takes place. These two competing processes result in a poorer ordering. Nevertheless, also for Al ordered domains of SMC are found, but they show a  $4\times 5$  periodicity instead of a  $4\times 3$  one [see Fig. 3.20 (b)]. This is explained by an alternating arrangement of the regular  $4\times 3$  clusters and reduced  $4\times 2$  clusters as shown in Fig. 3.20 (c) [307, 312].

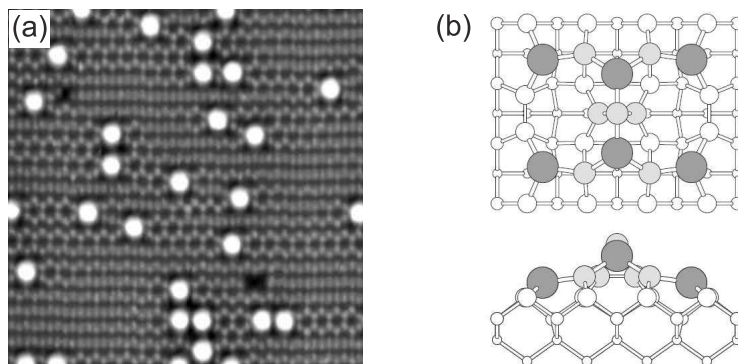


**Figure 3.19:** Magic group-III metal clusters on Si(001). (a) Filled states ( $50\times 50$  nm<sup>2</sup>,  $V_S = -1.8$  V) STM image of In magic clusters formed upon deposition of 0.15 ML of In at 500 °C. From [307]. (b) Atomic structure model of the group-III metal SMC in topview and sideview, as proposed by Bunk *et al.* [305]. White and light gray balls indicate Si atoms, dark gray balls group-III metal atoms. From [238].

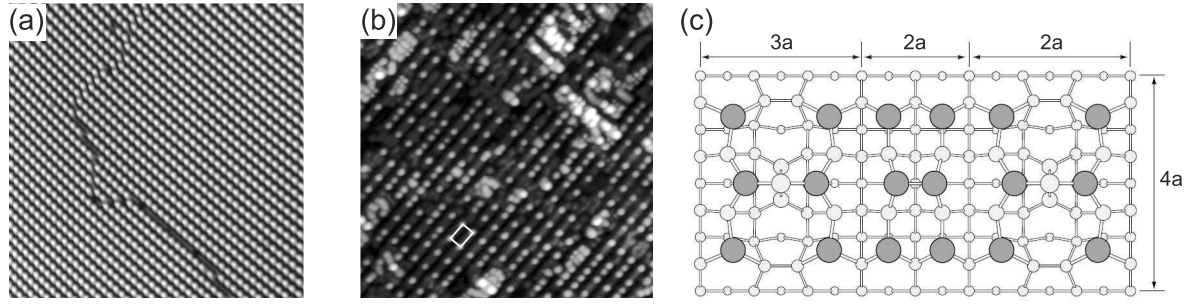


**Figure 3.20:** Two-dimensional lattices of magic group-III metal clusters on Si(001). (a) Filled states STM image ( $50 \times 50 \text{ nm}^2$ ,  $V_S = -1.8 \text{ V}$ ) of the  $4 \times 3$  In magic cluster lattice on Si(001). (b) Filled states STM image ( $50 \times 50 \text{ nm}^2$ ,  $V_S = -2.1 \text{ V}$ ) of the  $4 \times 5$  Al magic cluster lattice on Si(001). Both images taken from [307]. (c) Atomic structure of the  $5 \times 4$  lattice, consisting of  $4 \times 3$  clusters described by the model of Bunk *et al.* [305] and  $4 \times 2$  clusters. From [307].

Further In deposition on the preexisting  $4 \times 3$  superlattice leads to a modification of up to 40% of the clusters [298, 301, 302, 308]. Here,  $\text{Si}_6\text{In}_8$  clusters form by incorporation of an additional In atom [302]. While the  $\text{Si}_6\text{In}_7$  clusters were found to be semiconducting, the electronic properties of the “doped”  $\text{Si}_6\text{In}_8$  clusters are not yet finally clarified, since STS found a metallic behavior [301], in contrast to a nonmetallic nature observed using ARPES [308].

## 3.6 Epitaxial rare earth silicide nanostructures on Si(111)

Besides magic clusters on Si surfaces, an essential part of the present thesis covers the self-assembled growth of rare earth silicide nanostructures on the Si(111) surface, hence the state of the art in research on these structures is summarized here.

Depending on the preparation conditions, a variety of interesting structures was found to appear upon deposition of trivalent rare earth metals on the Si(111) surface. At submonolayer coverages, various superstructures that are described in detail in the following section form. At a coverage of about one monolayer, a two-dimensional metallic  $\text{RESi}_2$  layer (RE represents a rare earth metal) forms (section 3.6.2), while at higher coverages the hexagonal bulk silicide exhibiting a defected  $\text{AlB}_2$  type structure forms (section 3.6.3). For thin rare earth silicide films, extraordinarily low Schottky barriers were found on *n*-type Si(111), making them very interesting for an application as ohmic contacts [39, 50, 57].

### 3.6.1 Submonolayer rare earth coverages on Si(111)

The deposition of submonolayer amounts of a trivalent rare earth metal combined with annealing leads to the formation of various submonolayer phases. In Fig. 3.21, overview STM images of the Si(111) surface covered with different rare earth metals are shown. Two phases, namely a  $2\sqrt{3} \times 2\sqrt{3} \text{ R}30^\circ$  and a  $5 \times 2$  superstructure were found to form for all three shown rare earth metals, while a  $2 \times 1$  superstructure was only observed for Er and Dy.

A  $2\sqrt{3} \times 2\sqrt{3} \text{ R}30^\circ$  superstructure is observed for Dy [46, 316, 317], Er [42, 45, 315], and Ho [47]. High resolution STM images of the Dy induced  $2\sqrt{3} \times 2\sqrt{3} \text{ R}30^\circ$  are shown in Fig. 3.22 (a)

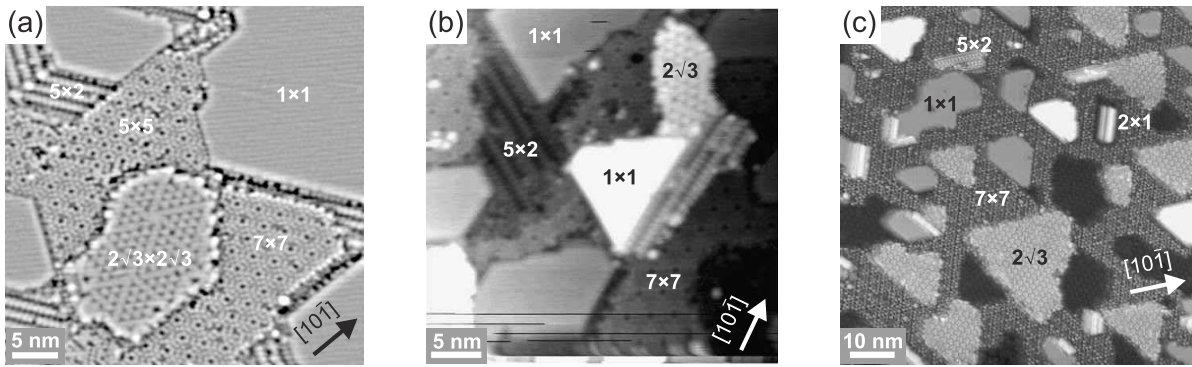


**Figure 3.21:** Rare earth submonolayer structures on Si(111). STM overview images of (a) 0.6 ML Dy on Si(111) (from [46]), (b) 0.4 ML Ho on Si(111) (from [47]), and (c) 0.4 ML Er on Si(111) (from [315]). Areas with clean Si(111)  $7\times 7$  and  $5\times 5$  as well as the rare earth induced  $2\sqrt{3}\times 2\sqrt{3}$   $R30^\circ$ ,  $5\times 2$ , and  $2\times 1$  superstructures are indicated in the images.

and (b). The superstructure forms as domains that are separated by domain boundaries forming a triangular network. In empty states STM images [Fig. 3.22 (a)], the structure appears as rings formed by six protrusions. In contrast, in filled states STM images three bright features form “windmill-like” structures [42, 46]. Since the rare earth atoms are predominantly imaged in the empty states images due to their lower electronegativity as compared to Si [156, 318], the six protrusions could be assigned to rare earth atoms forming hexagons that are adsorbed

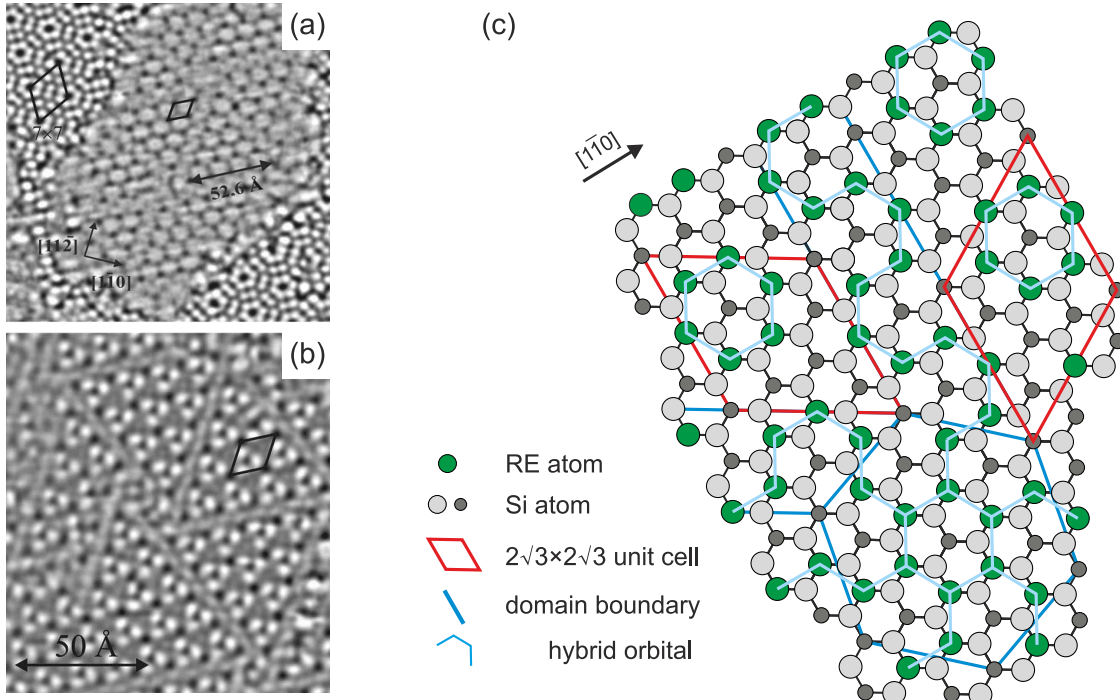


**Figure 3.22:** The rare earth induced  $2\sqrt{3}\times 2\sqrt{3}$   $R30^\circ$  superstructure on the Si(111) surface. (a) Empty states STM image ( $V_S = +0.6$  V) and (b) filled states STM image ( $V_S = -1.4$  V). From [46]. A  $2\sqrt{3}\times 2\sqrt{3}$   $R30^\circ$  unit cell is exemplarily indicated in both STM images, in (a) a  $7\times 7$  unit cell is additionally indicated. (c) Atomic structure model of the  $2\sqrt{3}\times 2\sqrt{3}$   $R30^\circ$  structure including the dislocation network. Adapted from [46].

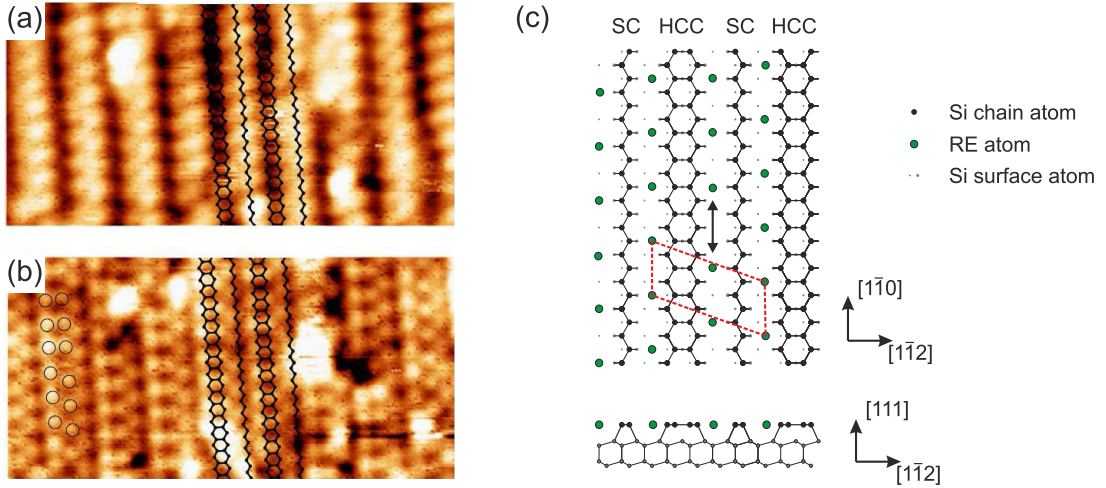


**Figure 3.23:** The rare earth induced  $5 \times 2$  reconstruction on the Si(111) surface. (a) Empty states STM image ( $19 \times 9 \text{ nm}^2$ ,  $V_S = +1.9 \text{ V}$ ,  $I_T = 180 \text{ pA}$ ) and (b) filled states STM image ( $19 \times 9 \text{ nm}^2$ ,  $V_S = -1.9 \text{ V}$ ,  $I_T = 180 \text{ pA}$ ). From [43]. (c) Atomic structure model proposed for the Gd induced  $5 \times 2$  superstructure in topview and sideview. Adapted from [43]. The structure consists of alternating Seiwatz chains (SC) and honeycomb chains (HCC) made of Si atoms and of atomic rows of rare earth atoms with a  $\times 2$  periodicity in between. In (b), the open circles denote the two different configurations resulting from a registry shift of the adsorbates as it is indicated by the arrows in (c).

on the unreconstructed Si(111) surface. The resulting structure model for the  $2\sqrt{3} \times 2\sqrt{3}$   $R30^\circ$  including the dislocation network is shown in Fig. 3.22 (c).

The second structure that appears in all three images shown in Fig. 3.21 is a chain like  $5 \times 2$  reconstruction. It forms in three domains with chains along  $\langle 1\bar{1}0 \rangle$  directions. Besides Dy [46], Er [45, 315], and Ho [47], this superstructure is also observed for Gd [43, 44, 319], where also the stabilization of single domains using a vicinal surface was demonstrated [44].

Similar to the  $2\sqrt{3} \times 2\sqrt{3}$   $R30^\circ$  superstructure, the appearance of the  $5 \times 2$  reconstruction in STM images shows a strong bias dependence [see Fig. 3.23 (a) and (b)]. A structure model, which was proposed by Battaglia *et al.* [43, 319], is shown in Fig. 3.23 (c). Herein, the  $5 \times 2$  reconstruction is formed by alternating Seiwatz chains [320] and honeycomb chains both consisting exclusively of Si atoms. The rare earth atoms are proposed to form chains with a  $\times 2$  periodicity, which are located in the channels between the Si chains.

Also based on simulated STM images, Battaglia *et al.* were able to identify the dark rows in the empty states STM images [see Fig. 3.23 (a)] as the Si honeycomb chains, while the adsorbate channels with the Seiwatz chain in between appear bright. In the filled states image [see Fig. 3.23 (b)] the structure appears as three rows. Two of them are assigned to the honeycomb chains, the one which appears to lie slightly lower to the Seiwatz chain. A shift within the adsorbate channel by one lattice constant along the chain direction leads to a change in the registry of the rare earth atoms with respect to the honeycomb chain. This is indicated by the arrows in Fig. 3.23 (c) and the open circles in (b). Thus, it was concluded that the  $5 \times 2$  reconstruction exists in two configurations. In the upper part, the rare earth metal atoms form

two parallel chains, while in the lower part a zigzag arrangement is found. In this work, a more detailed structural analysis is performed, refining this structure model (see section 9.2.2).

In the overview STM image shown in Fig. 3.21 (c), also rod shaped islands with a  $2 \times 1$  surface reconstruction appear. This phase is found for Er [42, 45, 315] and Dy [321] on Si(111). In addition, nanowires forming  $2 \times 1$  and  $4 \times 1$  superstructures are observed for Gd on vicinal Si(111) substrates [44, 322]. Regarding Er, the structure of the  $2 \times 1$  islands is assumed to correspond to an  $\text{ErSi}_{1.7}$  bilayer with a  $2 \times 1$  arrangement of the Si vacancies instead of the  $\sqrt{3} \times \sqrt{3}$   $R30^\circ$  arrangement usually found for the bulk silicide (cf. section 3.6.3) [45].

### 3.6.2 Two-dimensional rare earth silicides

As mentioned earlier, a two-dimensional  $\text{RESi}_2$  with  $1 \times 1$  periodicity forms on the Si(111) surface for rare earth coverages around 1 ML [48, 323–328]. However, smaller islands of this monolayer structure, characterized by straight edges along the  $\langle 1\bar{1}0 \rangle$  directions, are already found at lower coverages starting at around 0.5 ML (cf. Fig. 3.21). Its atomic structure is characterized by a hexagonal layer of rare earth atoms located underneath a buckled Si layer [see Fig. 3.24 (a) and (b)]. This Si top layer is similar to the unreconstructed Si(111) surface, but rotated by  $180^\circ$  [48, 326]. In Fig. 3.24 (b) and (c), atomically resolved STM images of the  $1 \times 1$  reconstruction are shown [46]. At both polarities, the buckled Si atoms of the surface layer are imaged.

Besides the atomic structure, also the electronic properties of two-dimensional rare earth silicides were investigated experimentally and theoretically [47, 317, 324, 325, 327, 328]. Figure 3.25 shows experimental results for the band dispersion of  $\text{ErSi}_2$  and  $\text{DySi}_2$  obtained using

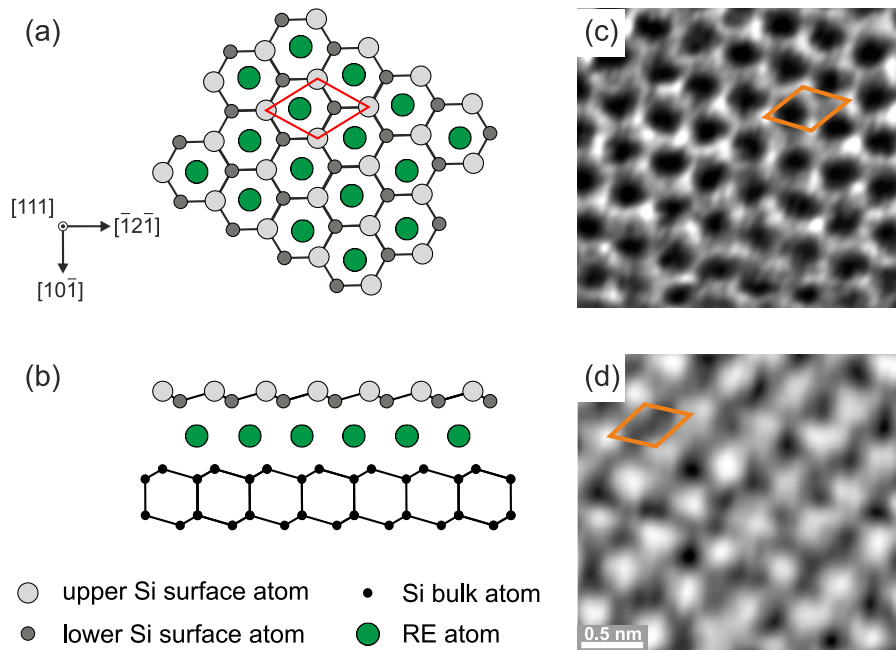


**Figure 3.24:** (a,b) Atomic structure model of the  $\text{RESi}_2$  monolayer in (a) topview and (b) sideview. Adapted from [48]. (c) Empty states STM image ( $V_S = +0.3$  V,  $I_T = 7$  nA) and (d) filled states STM image ( $V_S = -0.3$  V,  $I_T = 3$  nA). From [46].

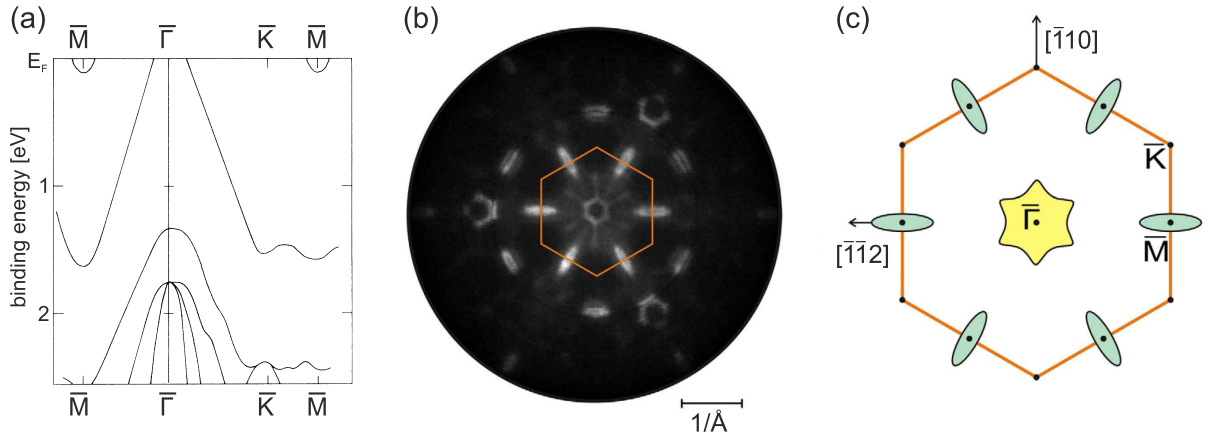


**Figure 3.25:** (a) Experimental band dispersion of  $\text{ErSi}_2$  along  $\bar{\Gamma}$ - $\bar{M}$ . From [329]. (b) Energy surface of the two-dimensional  $\text{DySi}_2$  monolayer on  $\text{Si}(111)$  at a binding energy of 0.04 eV. From [328]. (c) Scheme of the Fermi surface of  $\text{DySi}_2$ . The  $1 \times 1$  surface Brillouin zone is indicated by the orange line, electron and hole pockets in green and yellow, respectively. From [328].

ARPES. The band structure is characterized by different two-dimensional bands. In the shown energy range, two bands are found at the  $\bar{M}$  point. One shows a minimum at around 0.1 eV binding energy and crosses the Fermi level close to the  $\bar{M}$  point. This band forms the elliptical electron pockets found in the Fermi surface in (b) and (c). The second band has a minimum at around 1.65 eV, strongly disperses upwards when moving towards  $\bar{\Gamma}$ - $\bar{M}$ , and finally crosses the Fermi level near the  $\bar{\Gamma}$  point. This band is responsible for the hole pocket in the center of the Brillouin zone [cf. Fig. 3.25 (b) and (c)].

### 3.6.3 Three-dimensional rare earth silicides

At multilayer rare earth coverages, epitaxial  $\text{RE}_3\text{Si}_5$  layers of defected  $\text{AlB}_2$  type form [40, 46, 49, 51, 52, 55, 317, 323, 328–333]. The corresponding atomic structure model is shown in Fig. 3.26. As the two-dimensional silicide described in the previous section, the three-dimensional bulk silicide consists of a buckled Si surface layer with a planar hexagonal layer of rare earth metal atoms underneath. However, regarding the bulk layers, the structure changes. Here, planar Si layers alternate with planar rare earth metal layers. To avoid strain in these planar Si bulk layers, an ordered array of Si vacancies with a  $\sqrt{3} \times \sqrt{3}$  R30° periodicity is formed [51, 52, 329, 330].

Due to their identical surface termination,  $\text{RE}_3\text{Si}_5$  islands appear very similar to  $\text{RESi}_2$  islands in STM. An overview STM image of a sample with a Dy coverage of 2 ML is shown in Fig. 3.27. In the image,  $\text{DySi}_2$  and  $\text{Dy}_3\text{Si}_5$  both appear as flat terraces.

However, it is possible to distinguish between the two structures by examining the terrace edges. As mentioned before, the  $\text{RESi}_2$  monolayer exhibits straight edges along  $\langle 1\bar{1}0 \rangle$ . This behavior originates from a lower dangling bond density of the buckled Si top layer along these edges. For the bulk layers, the difference in the dangling bond density vanishes due to the

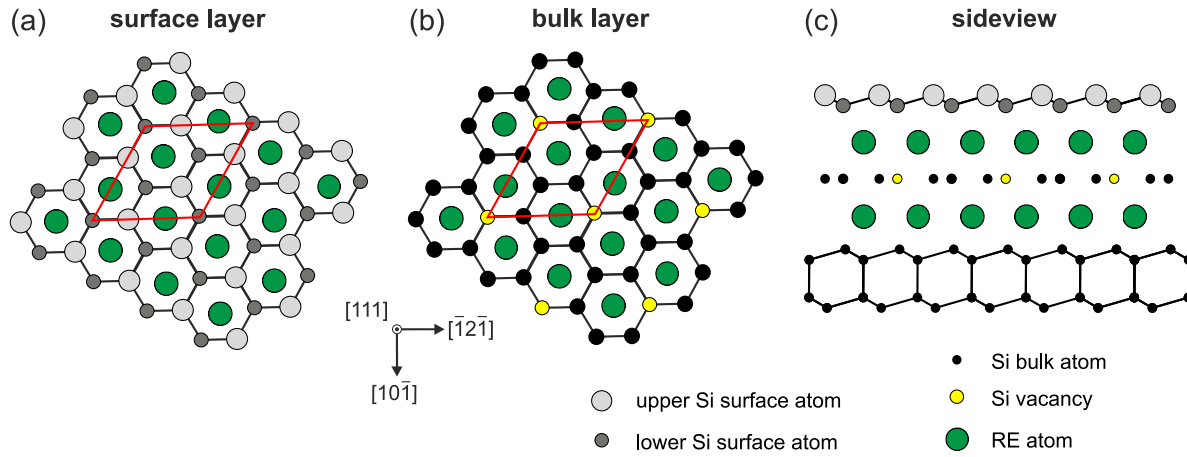


**Figure 3.26:** The atomic structure of the  $\sqrt{3}\times\sqrt{3}$   $R30^\circ$  reconstructed rare earth bulk silicide forming on the Si(111) surface. (a) Topview of the surface forming a buckled Si layer without vacancies. (b) Topview of the bulk layers with Si vacancies. (c) Sideview of the structure. Adapted from [330].

presence of the vacancies. Hence, with increasing layer thickness, the terrace edges become rounder as observed in Fig. 3.27 (a) [46, 334].

In atomically resolved STM images such as Fig. 3.27 (b), the  $\sqrt{3}\times\sqrt{3}$   $R30^\circ$  periodicity becomes visible. Depending on the registry of the vacancies with respect to the buckled Si top layer, two different types of images are obtained. In the STM image in Fig. 3.27 (b), a triangular grouping of bright protrusions appears. A similar appearance was also found by Martin-Gago *et al.* for  $\text{Er}_3\text{Si}_5$  [331] and is explained by a structural model with the vacancies being located underneath the lower Si atoms of the buckled surface layer as it is also shown in Fig. 3.26 (c).

However, other studies found a hexagonal arrangement of the protrusions with every third spot appearing darker [49, 51]. To explain such an appearance, the vacancy has to be located underneath an upper Si atom. In 2006, Rogero *et al.* [332] showed for  $\text{Y}_3\text{Si}_5$  that both types of atomically resolved images can be obtained on the same sample. Hence, both types of

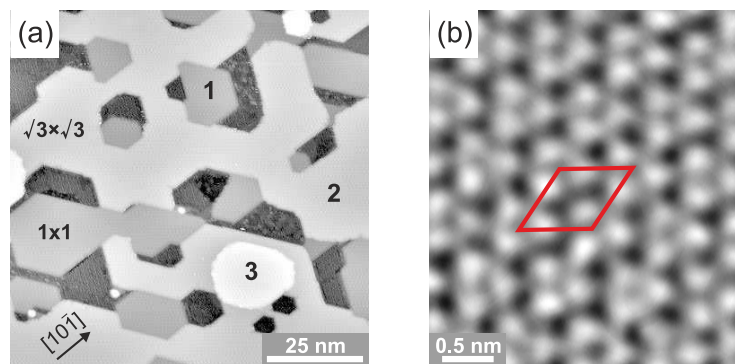


**Figure 3.27:** (a) Overview STM image of a Si(111) sample with a Dy coverage of 2 ML and subsequent annealing at 500 °C. In the image, the different phases as well as the thickness in monolayers are indicated. (b) Atomically resolved filled states STM image ( $V_S = -0.05$  V,  $I_T = 1$  nA). Both images taken from [46].

registries can form simultaneously although theoretical calculations show that the structure with the vacancies underneath the lower Si atoms is slightly preferred [332].



## Chapter 4

# Experimental setup

All experiments presented in this work were performed in an existing versatile UHV system, designed mainly for the growth and the investigation of nanostructures on Si surfaces. This UHV system, which mainly consists of two chambers, one used for the sample preparation, the second one housing a homebuilt STM, is described in section 4.1. Furthermore, the need of UHV is demonstrated and the techniques used to obtain such vacuum conditions are presented. In section 4.2, the setup of the STM is described in detail. Moreover, descriptions of the tip and the sample preparation processes are presented in sections 4.3 and 4.4, respectively.

### 4.1 The UHV system

For the preparation and investigation of clean surfaces, excellent vacuum conditions are essential. This is illustrated by the following estimation. The pressure  $p$  is determined by the number of particles with the mass  $m$  and the average velocity  $\langle v \rangle$  that hit a surface [160]:

$$p = 2m\langle v \rangle R, \quad (4.1)$$

with  $R$  being the impinging rate per surface area. The average thermal velocity is given by

$$m\langle v^2 \rangle / 2 = 3k_B T / 2. \quad (4.2)$$

Here,  $k_B$  is the Boltzmann constant and  $T$  the temperature. Thus, Eq. 4.1 can be written as

$$p = 2R\sqrt{3mk_B T}. \quad (4.3)$$

As an example, the pressure at which one monolayer gas atoms or molecules impinges on a Si(111) surface within one second is estimated in the following. As mentioned earlier, one monolayer (ML) is defined as one adsorbate atom per substrate atom. Thus, the impinging rate  $R$  has to be  $7.83 \cdot 10^{14} \text{cm}^{-2} \text{s}^{-1}$  (cf. Table 3.1). Assuming a temperature of 300 K and an atomic weight of 28 ( $\text{N}_2$ ) results in a pressure of about  $4 \cdot 10^{-6}$  mbar. Although the sticking coefficient of the impinging particles also plays a role, this nicely illustrates that even at high vacuum conditions, freshly prepared surfaces are contaminated again within seconds. Thus, to conduct STM experiments with a typical duration of several hours, pressures lower than  $10^{-9}$  mbar (UHV) are necessary.

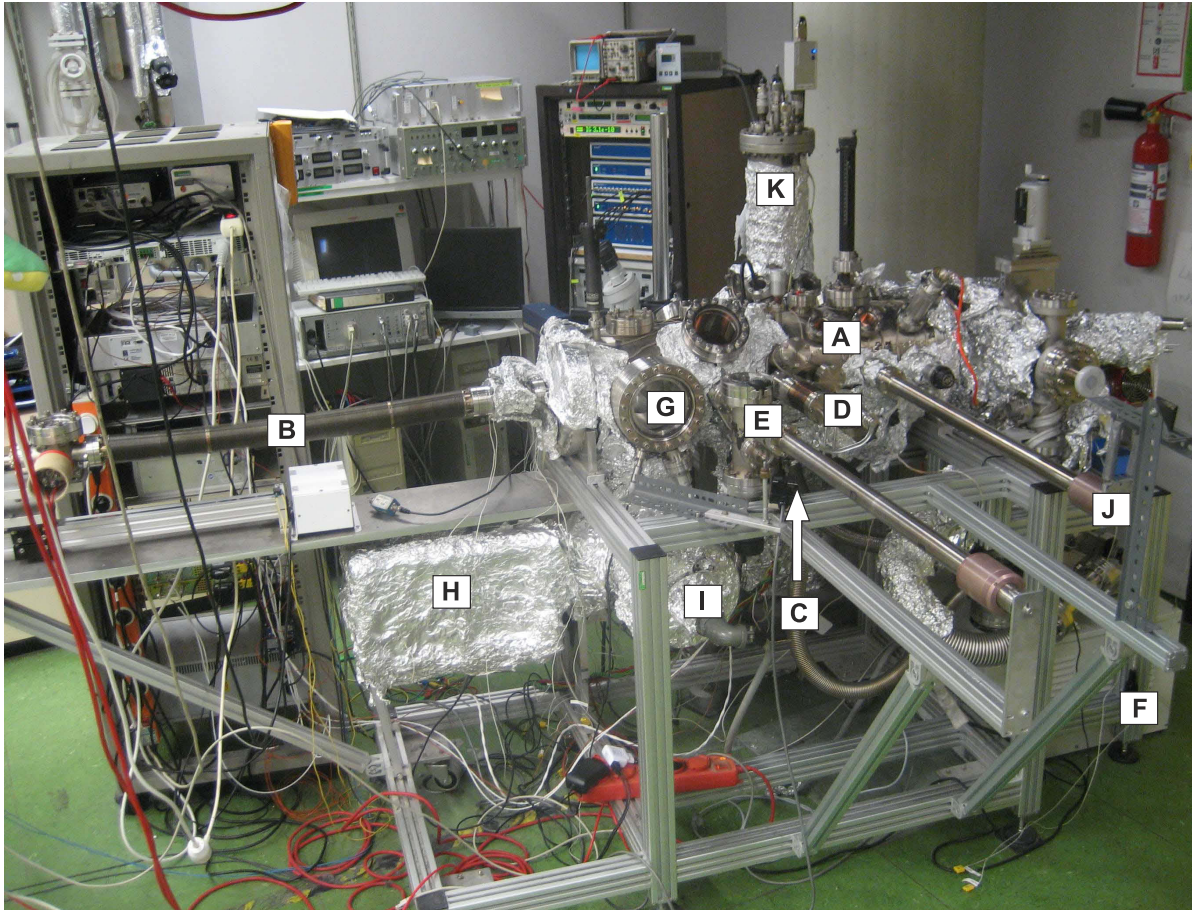


**Figure 4.1:** Photograph of the experimental UHV chamber setup used in this thesis.

To obtain such vacuum conditions, different vacuum pumps are used. In the chamber system used in this work, diaphragm, turbomolecular, titanium sublimation, and ion getter pumps are installed. Thereby, one ion getter pump and one titanium sublimation pump in each chamber are used during continuous operation, while a pumping station containing a turbomolecular pump and a diaphragm pump as backing pump are only used for initial pumping after venting a chamber as well as during bake-out, in order to avoid vibrations that might influence the STM measurements. Such a bake-out process, in which the whole chamber system is heated to 120 °C for at least 24 h, is necessary when a chamber has been vented, in order to remove water molecules adsorbed on the chamber walls. Otherwise, the typical base pressures of  $5 \cdot 10^{-11}$  mbar in the STM chamber and  $3 \cdot 10^{-10}$  mbar in the preparation chamber would not be achieved within an appropriate period of time. To measure these pressures, Bayard-Alpert hot-cathode ionization gauges are employed.

A photograph of the UHV chamber system is shown in Fig. 4.1. The large, horizontally mounted UHV chamber (A) represents the preparation chamber. It includes a manipulator (B) with sample heating facilities, various evaporators (C), and a quartz-crystal microbalance (D) to calibrate the deposition rates. A more detailed description of these parts of the system is found in section 4.4.

Up to five samples can be stored within this chamber in the so-called sample garage. In addition, a load-lock chamber (E) pumped by the turbomolecular pump (F) allows to introduce new tips or samples without breaking the vacuum. Additionally a combined LEED and Auger electron spectroscopy system (G) is installed in the preparation chamber. The ion getter pump of the preparation chamber is marked with H, while I indicates a cooling trap equipped with a titanium sublimation pump.

Using the magnetically coupled transfer rod marked with J, the sample can be transferred into the STM chamber (K) through a valve separating the two chambers to preserve the excellent vacuum conditions in the STM chamber during sample preparation and transferring. Besides the STM, which is described in the following section, this STM chamber contains a tip storage and heating facility and a wobble stick to manipulate and mount the STM tips.

## 4.2 The scanning tunneling microscope

The setup of the homebuilt STM used in this work is shown in Fig. 4.2. In (a), the actual STM unit is found in the lower part. It is shown in more detail in Fig. 4.2 (b). The sample stage with a mounted sample is located on the right, while on the left the inertial walker unit for the coarse positioning and the scanning of the tip is found. A detailed drawing of this walker unit is shown in (c). It is mounted on top of three stacks of crossed shear piezos with stainless steel

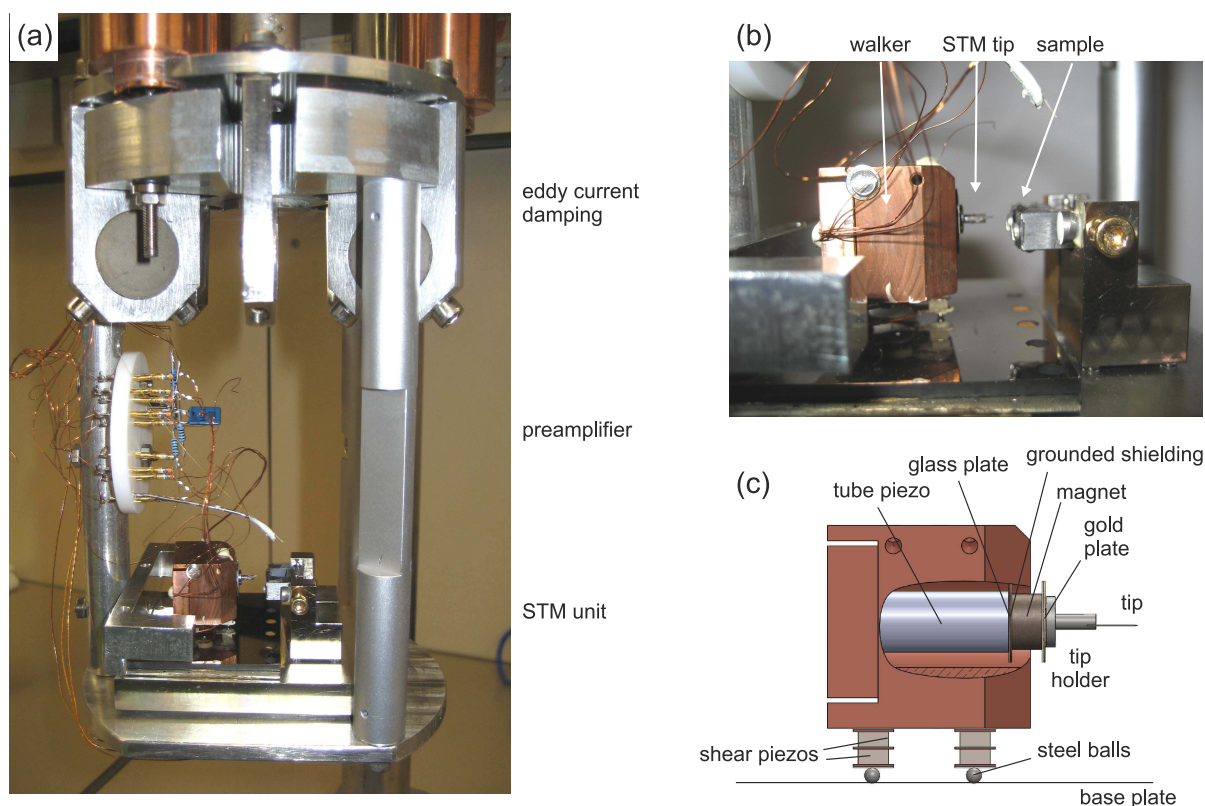


**Figure 4.2:** The setup of the used tunneling microscope. (a) Overview photograph of the STM system. (b) Detailed view of the scan head with the walker, the STM tip, and the sample stage. (c) Schematic drawing of the walker. In this sectional view, the scanner is visible.

balls underneath. Applying a sawtooth voltage to either the upper or the lower shear piezos allows moving the walker on the polished stainless steel base plate perpendicular or parallel to the sample surface, respectively. In contrast, when the voltage is only applied to two piezos, the walker rotates.

For the scanning of the tip, a piezo tube with its outer electrode being divided into four sectors is employed. This tube scanner is installed inside the walker unit, as shown in Fig. 4.2 (c). Applying a voltage between the inner and the outer electrodes leads to a motion in  $z$ -direction, while a bending of the tube and thus a tip motion in  $x$ - or  $y$ -direction is achieved by applying a voltage between two opposite electrodes. At the front end of the scanner tube a magnet is attached. This magnet holds the tip holder manufactured from magnetizable steel. The tunneling current is measured at the gold plate underneath the tip and is amplified by the in-vacuum preamplifier above the STM unit [see Fig 4.2 (a)].

To decouple the system from environmental vibrations, the whole scan head is vibration isolated using a spring suspension. Additionally, an eddy current damping system is implemented.

For data acquisition and control, two different systems were used. For the first measurements, a set of homebuilt electronics was used to control the STM and to supply the high voltages used for the scanner and the walker. For processing the data, a computer running a software originally written by M. Dähne was used. Within this work, this homebuilt control system has been replaced by a commercial scanning probe control system (Nanonis SPM controller by Specs Zurich GmbH).

However, the basic measurement procedure is similar for both systems. First, the tip has to be brought into a distance where a tunneling current is detected when a voltage is applied to the sample. This approach is done in two steps. First, the tip is positioned manually using the walker. The distance between tip and sample surface is thereby controlled with an optical microscope through a viewport of the UHV chamber. Through the microscope, also the mirror image of the tip is visible on the sample surface. When the tip and its image nearly touch each other, an automated approach mechanism is started as the second step. Here, the feedback loop is switched on and the scanner moves the tip towards the sample. If no tunneling current is measured, the tip is retracted and a walker step follows. To prevent a crash, the steps of the walker need to be smaller than the maximum scan range of the tube piezo in  $z$ -direction ( $\sim 1 \mu\text{m}$ ). This process is repeated until the tunneling contact is established. Then STM or STS measurements can be performed using the different software interfaces.

All STM images presented in this work were acquired using the constant current mode. For data analysis, the WSXM software [335] was used. To investigate the local electronic properties, STS was employed in this work. Here, point spectra with the feedback loop turned off were measured at locations of interest. In most cases,  $dI/dV$ - $V$  spectra were measured simultaneously using a software lock-in amplifier implemented in the Nanonis package. For the lock-in measurements, the tunneling voltage is modulated with a typical frequency of 1 kHz and a typical amplitude of 50 mV.

## 4.3 Tip preparation

A sharp and stable STM tip is a crucial part in an STM experiment to obtain a high resolution and to minimize tip changes or tip artifacts that often affect the quality of STM images. In this work, mainly electrochemically etched tungsten tips were used [336–338]. In addition, commercially available PtIr tips (Agilent Technologies) were tested. However, an advantage of these tips could not be observed. Thus, tungsten tips which can be produced in the laboratory by electrochemical etching in sodium hydroxide solution are preferred.

For this purpose, a tungsten wire with a diameter of 0.25 mm is at first annealed under nitrogen flow for improving the material quality. For etching, a commercial setup (W-Tek Tip Etching Tool by Omicron NanoTechnology GmbH) is used. Here, a piece of the tungsten wire is immersed into a glass beaker filled with 10% NaOH solution. Then, a voltage of 5 V is applied between the tungsten wire and a ringlike stainless steel cathode surrounding the wire. In the initiated etching process, a soluble tungsten oxide ( $\text{WO}_4^{2-}$ ) forms at the anode. Due to a shielding by sinking  $\text{WO}_4^{2-}$  ions, the dissolution of the tungsten wire is fastest close to the NaOH surface leading to a thinning of the wire until it finally breaks off. Since in this setup the upper part is used as a tip, it is important that the etching process is stopped immediately after the break off by the control electronics. Otherwise, the tip would get blunt again [336].

The quality of the resulting tips is then checked using an optical microscope, and suitable tips are cleaned in ethanol and deionized water before they are attached to a tip holder by spot-welding. Finally, the tips are transferred into the UHV system via the load-lock using tip shuttles each carrying up to three tips. Inside the STM chamber, the surface oxide is removed from the tips by electron bombardment.

## 4.4 Sample preparation

As mentioned before, excellent vacuum conditions are one major requirement to maintain a clean surface during an STM measurement. However, this implies that a clean sample surface is present. In this section, the different steps of the sample preparation from preparing a clean Si surface to the self-assembled growth of nanostructures are described.

### 4.4.1 Preparation of clean silicon surfaces

In the present work, Si surfaces with different orientations serve as substrates for the growth of self-assembled nanostructures. In Table 4.1, the properties of the used Si wafers are summarized.

In a first step, samples with dimensions of about  $10 \times 5 \text{ mm}^2$  are cut from Si wafers with the desired surface orientation. For this purpose, a scratch is applied using a diamond scribe followed by breaking the wafer along this scratch. Before being mounted to the sample holder, the samples are rinsed alternately with ethanol and deionized water for several times.

The used sample holder is shown in Fig. 4.3. The assembly consists of two parts manufactured from Mo which are electrically isolated from each other allowing direct current heating

orientation	manufacturer	doping	resistivity ( $\Omega\text{cm}$ )
Si(111)	MaTeck GmbH	<i>n</i> -type (P)	5
Si(111)	MaTeck GmbH	<i>n</i> -type (P)	0.3
Si(111)	MaTeck GmbH	<i>n</i> <sup>+</sup> -type (P)	0.0045-0.006
Si(557)	CrysTec GmbH	<i>p</i> -type (B)	1-20
Si(001)	MaTeck GmbH	<i>n</i> -type (P)	2

**Table 4.1:** Overview on the Si wafers used in this work.

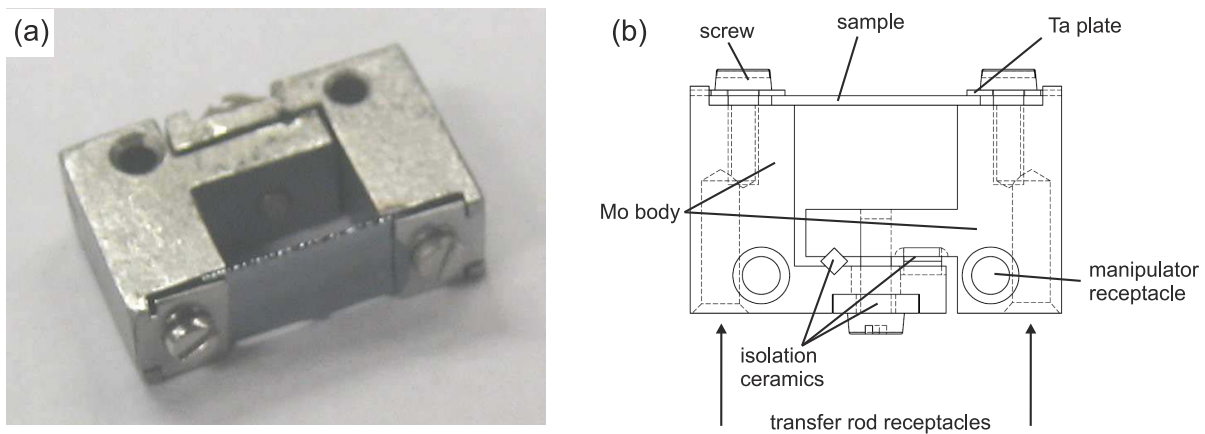


**Figure 4.3:** The sample holder used in this work. (a) Photograph of the sample holder with a Si sample installed. (b) Schematic drawing of the sample holder.

of the sample. The electrical isolation is achieved using pieces made of Shapal-M Soft™, a machinable ceramic consisting of aluminum nitride. It is compatible with the high temperatures used during the preparation process, offers a good thermal conductivity and the coefficient of thermal expansion fits very well to that of Mo. The sample itself is mounted under two plates made of Ta, which are fixed by screws. On the one hand, Ta and Mo are the materials of choice because of their compatibility with high temperatures. On the other hand stainless steel parts should be avoided in the proximity of the Si sample, since they might lead to a contamination with Ni which is a frequent problem. The completed assembly is then transferred into the UHV-system using the load-lock.

Inside the preparation chamber, clean Si surfaces are prepared by heating the samples. Therefore, the sample holder is placed on the manipulator, which allows heating by passing a direct current through the sample. Within this work, an analogous cleaning procedure is used for all surface orientations. In a first step after inserting the sample into the UHV, it is outgassed at 600 °C to 800 °C for several hours. Afterwards, the surface oxide is removed by the so-called flashing procedure. Here, starting from a base temperature of around 800 °C, the sample is repeatedly heated to higher temperatures up to 1200 °C for 10 s. When the rise in the chamber pressure during such a flashing cycle is negligible, the oxide is assumed

to be removed and the sample is cooled down slowly ( $\sim 1$  K/s) from at least  $830$  °C to room temperature to obtain a defect-free surface reconstruction.

The sample temperature is measured by an optical pyrometer with an accuracy of  $\pm 20$  °C and a measuring range from  $300$  °C to  $1400$  °C. However, for some preparations growth temperatures lower than  $300$  °C are used. In these cases, temperature-current calibration curves are measured and extrapolated towards lower temperatures. Therefore, highly  $n$ -doped wafers are used since they show a nearly linear dependence between temperature and current in the crucial temperature regime. However, for the available highly doped wafers, the accuracy of the alignment of the (111) plane is not as good as for the planar Si(111) wafers and a large number of steps is present. Thus, a pick-a-back construction consisting of two samples, with a standard  $n$ -type wafer mounted on top of a highly doped wafer that is used for the heating, is employed. Highly  $p$ -doped wafers are avoided, since B that is mostly used as the dopant leads to a modification of the surface [339–341].

In a first experiment, the surface quality is checked using STM for every new sample. This step is essential to make sure that the surface is clean and no contamination is present, since especially at the investigation of clusters, even small amounts of contaminants on the surfaces might appear very similar to the subjects of investigation.

#### 4.4.2 Growth of self-assembled nanostructures on silicon surfaces

In this work, the self-assembled growth of various nanostructures on Si surfaces was investigated. The basic preparation process of each of these nanostructures is as follows: The material of choice is deposited on a freshly prepared clean Si substrate using an evaporator. In a preceding experiment, the evaporation rate of the evaporator is determined using a quartz-crystal microbalance. Then, the desired coverage is deposited on the sample by opening a shutter in front of the evaporator for a certain time. To enable the self-assembled growth, the sample is heated. This heating is either done during the deposition in reactive deposition epitaxy (RDE) or afterwards in solid phase epitaxy (SPE).

In this work, In, Ga, Si, Sb, Dy, and Tb are used as adsorbates. For their evaporation, different types of evaporators are used. For Sb, Dy, and Tb, homebuilt electron beam evaporators with slightly modified designs are used. A scheme of an electron beam evaporator similar to those used for Dy and Tb is shown in Fig. 4.4 (a). The material to be evaporated is placed inside a W crucible surrounded by a filament. In this evaporator type, the crucible is heated by electrons that are released from the filament through thermionic emission and accelerated towards the crucible by a high voltage between  $350$  V and  $500$  V. In the Sb evaporator, a Ta cone is used instead of a W crucible.

In contrast, for In, Ga, and Si, effusion cells, in which the crucible is directly heated by thermal contact to a filament, are employed. For In, a homebuilt effusion cell with a boron-nitride crucible is used, while for Ga and Si, commercial effusion cells are employed. These commercial cells are equipped with water cooling, and thermocouples are installed underneath the crucibles allowing a precise adjustment of the cell temperature. For Ga, a dual filament

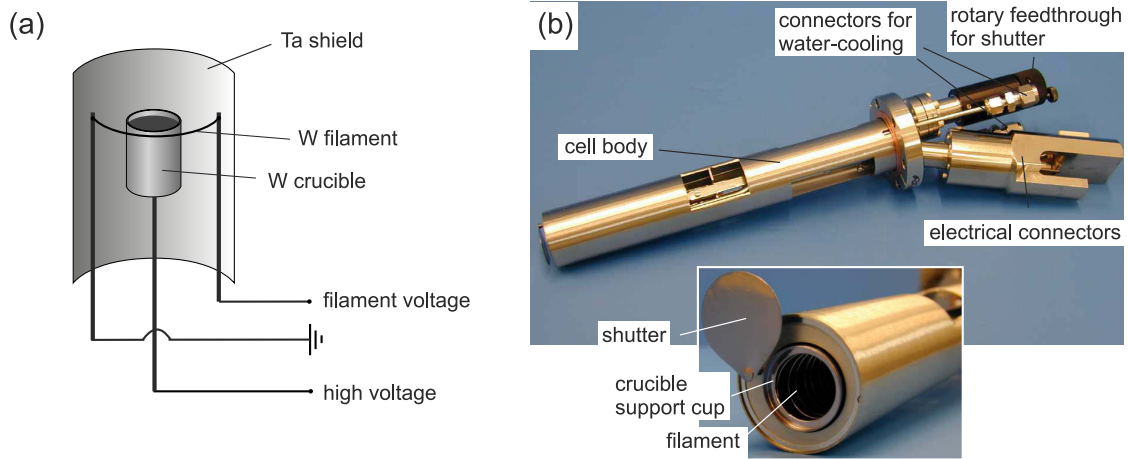


**Figure 4.4:** Examples of evaporators used within this work. (a) Homebuilt electron beam evaporator as used for evaporating Dy and Tb. Adapted from [342]. (b) Commercial high temperature effusion cell as used for Si evaporation. From [343].

effusion cell (DCA Instruments Oy) with a boron nitride crucible is used, while for Si a high temperature effusion cell (DCA Instruments Oy) with a Ta crucible is employed.

The high thermal radiation caused by the effusion cells does not allow to use the quartz-crystal microbalance to determine the evaporation rate. Here, the evaporation rate was calibrated by growing well-known structures and evaluating their relative surface coverage. Therefore, Si(111) homoepitaxy was employed for Si, while for Ga and In, directly the number of magic clusters on Si(111)7×7, each containing six metal atoms (cf. section 3.5.1), was determined.

## Part II

# Results and discussion



---

## Chapter 5

# Sb induced clusters on the Si(111) surface

The deposition of Sb on Si can strongly influence its properties. As a group-V element, Sb represents a donor when being incorporated into a Si crystal and is in fact frequently used for *n*-type doping in Si-MBE [344–348]. In addition, it acts as a surfactant, e.g. enabling a two-dimensional growth of Ge layers on Si instead of the otherwise forming three-dimensional islands [349–354]. Hence, it strongly influences both the electronic properties of Si and the growth behavior, making Sb induced clusters on Si surfaces very interesting objects to investigate.

However, to the best of my knowledge, clusters of group-V elements on the Si(111)7×7 surface were not investigated in detail up to now. This is in strong contrast to the other common dopant system in Si, the group-III metals, for which numerous studies on magic clusters on Si surfaces exist (see section 3.5).

Although Sb induced clusters were not in the focus up to now, the growth of Sb on the Si(111) surface has been intensively studied. Thereby, a variety of different surface phases was observed [355–364]. In addition, a formation of cluster-like structures was found for room temperature deposition [365] as well as for Sb deposition on a Si(111) surface partly covered with a  $\sqrt{3}\times\sqrt{3}$ -Ga superstructure [366]. However, in these studies the clusters were not the main topic and no magic clusters were observed. This might be related to the rather high growth temperatures used in the majority of these works. To take advantage of the template effect, moderate growth temperatures are required in order to maintain the basic structure of the Si(111)7×7 substrate.

Thus, in this work, the growth behavior, the atomic structure, and the electronic properties of Sb induced clusters on the Si(111)7×7 surface are studied using STM and STS. Therefore, lower growth temperatures and Sb coverages as compared to most existing studies were employed.

## 5.1 General growth behavior

To investigate the growth behavior of Sb induced clusters on the Si(111) $7\times 7$  surface, the growth parameters were varied in a wide range. Therefore, Sb coverages between 0.04 ML and 0.47 ML, growth temperatures between 200 °C and 550 °C, and deposition rates ranging from 0.03 ML/min to 0.32 ML/min were employed. In addition, two different growth techniques to enable the self-assembled growth of clusters were employed. As mentioned earlier, Sb is deposited directly on the sample held at growth temperature in RDE, while in SPE the deposition takes place at room temperature, followed by an annealing of the sample. Using RDE, a much more homogenous growth is obtained, thus this method was primarily used. Regarding the deposition rate, no fundamental influence on the cluster growth is observed within the studied range. Hence, the remaining two growth parameters are the Sb coverage and the growth temperature.

In Fig. 5.1 (a) to (c), overview filled states STM images for three different sets of growth parameters are shown. In all images, the  $7\times 7$  periodicity of the substrate is maintained and the dominating structures on the surface are small clusters forming within single  $7\times 7$  HUCs. Besides clusters, sometimes also islands extending over several HUCs are found, as indicated in (a) and (c).

However, when comparing the STM images in more detail, a fundamentally different cluster growth is observed. It is found, that almost all forming clusters can be assigned to three cluster types. These are so-called double-row clusters, ringlike clusters, and different types of bright clusters. In the image shown in (a), mainly double-row clusters form. A detailed filled states STM image of the double-row clusters is shown in (d). These clusters appear as two rows formed from two or three protrusions, being aligned parallel to an edge of the  $7\times 7$  HUC. Sometimes the rows appear slightly bent.

In contrast, an almost exclusive formation of ringlike clusters is observed in (b). These ringlike clusters appear as bright features located near the center of an edge of the  $7\times 7$  HUC, as can be seen in the filled states STM image shown in (e).

The third main class of clusters are the so called bright clusters, of which a large number is found in (c), and which are shown in more detail in (f). Here, different types of bright clusters are found. This behavior with three different types of clusters is representative for the whole investigated parameter range.

As already evident from the STM images shown in (a) to (c), there are distinct regimes of growth parameters, for which a preferential growth of one of the three cluster types is found. By analyzing the cluster types forming for the different sample preparations investigated in this work, a rough phase diagram for the corresponding parameter range could be obtained as shown in Fig. 5.1 (g). The three differently colored and numbered regimes correspond to parameter regimes where double-row clusters (I), ringlike clusters (II), and bright clusters (III) are found. However, as indicated in (g), the regimes are not clearly distinguishable from each other, but show overlaps, as can be seen e.g. in (c), where a formation of both bright clusters

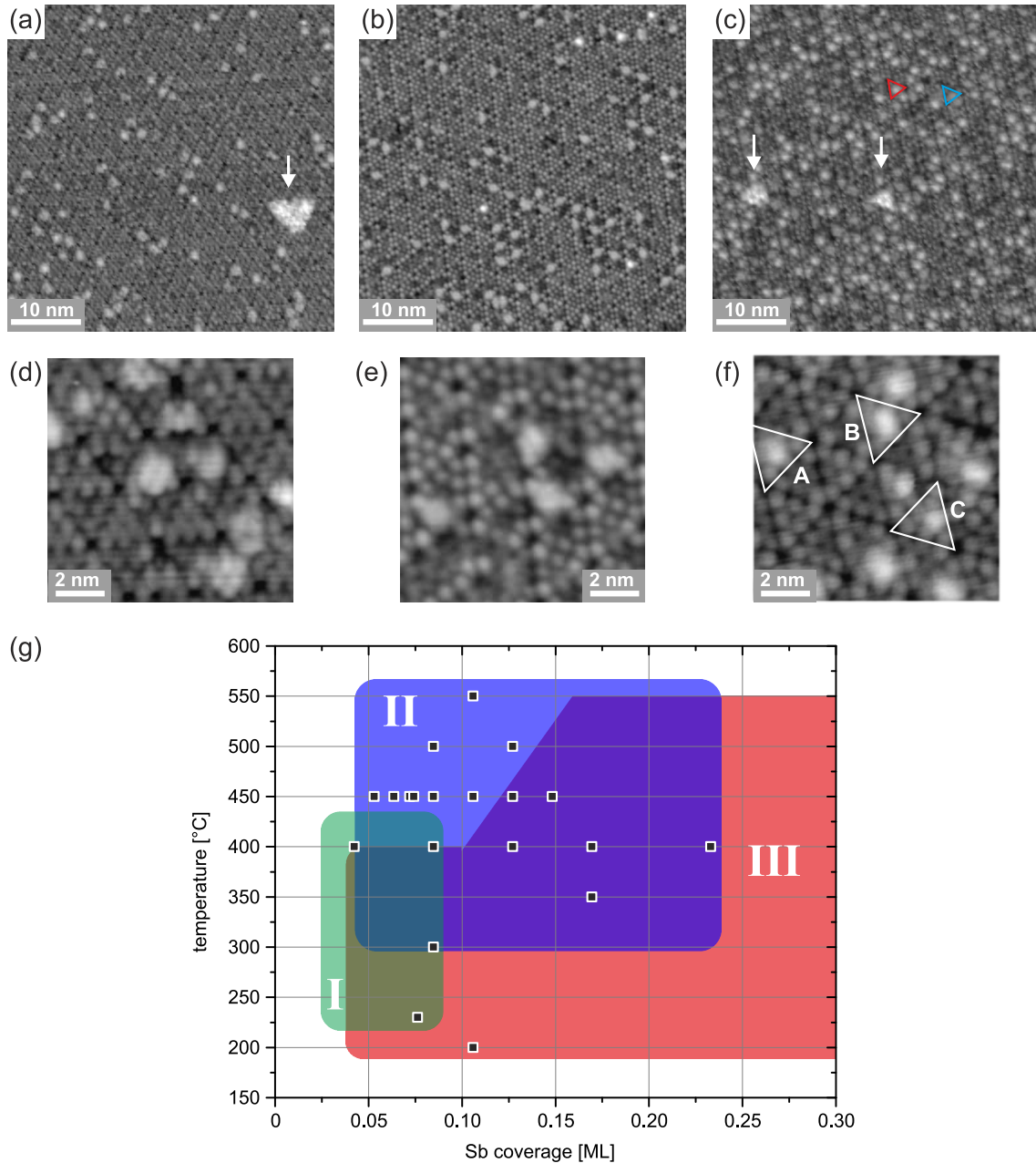


**Figure 5.1:** (a-c) Representative overview STM images for the three growth regimes of Sb induced clusters on the Si(111) surface. (a) Regime I with mainly double-row clusters forming (0.04 ML Sb deposited at 400 °C;  $V_S = -1.5$  V;  $I_T = 500$  pA). (b) Regime II with an almost exclusive formation of ringlike clusters (0.07 ML Sb deposited at 450 °C;  $V_S = -2.0$  V;  $I_T = 200$  pA). (c) Regime III with a large number of bright clusters (exemplarily indicated by a red triangle) forming besides ringlike clusters (exemplarily indicated by a blue triangle) (0.17 ML Sb deposited at 400 °C;  $V_S = -2.0$  V;  $I_T = 500$  pA). The white arrows mark islands extending over several HUCs. (d-f) Detailed filled states STM images of (d) double-row clusters ( $V_S = -1.25$  V;  $I_T = 500$  pA), (e) ringlike clusters ( $V_S = -2.0$  V;  $I_T = 200$  pA), and (f) bright clusters ( $V_S = -1.5$  V;  $I_T = 200$  pA). In (f) bright clusters appearing differently are marked. (g) Sketch of the Sb/Si(111) phase diagram for the range, in which a growth of Sb induced clusters was found. The green, blue, and red areas marked by the numbers I, II, and III indicate the growth regimes, in which double-row, ringlike, and bright clusters grow, respectively. The points indicate sample preparations that were investigated within this work.

and ringlike clusters is found on the same sample, as exemplarily indicated by the red and blue triangles marking a bright and a ringlike cluster, respectively.

The double-row clusters are the first clusters forming at low Sb coverages and low growth temperatures. A detailed analysis of these clusters is conducted in section 5.2.

In regime II, which is drawn in blue in Fig. 5.1 (g), ringlike clusters are found. For these clusters, an extremely homogenous growth is observed with an almost exclusive formation of ringlike clusters for Sb coverages between 0.05 ML and 0.12 ML and growth temperatures between 450 °C and 550 °C. The ideal growth temperature was found to be 450 °C, where high coverages of ringlike Sb clusters could be obtained. At higher growth temperatures, the number of ringlike clusters decreases. This might be related to the larger diffusion length of the Sb atoms on the surface at higher temperatures, allowing a diffusion to step edges and the formation of other Sb induced structures. Also a desorption of Sb might already take place in this temperature regime, although in literature, a sticking coefficient of almost unity was reported for Sb on the Si(111) surface for temperatures below 600 °C [344, 347].

Regime III, in which the bright clusters are found, extends over a large range of growth parameters. Bright clusters are found for low coverages and low growth temperatures just as for high coverages and high growth temperatures. Always, not only one particular type of bright clusters is observed, but differently appearing ones. This is exemplarily indicated in Fig. 5.1 (f). Here, some clusters as the one marked A appear larger and are often found to exhibit a centered triangular appearance within the HUC. Besides these clusters, also smaller ones, appearing either as an elongated feature (B), or as a single protrusion (C) are found. It is known that Sb evaporates not in form of single atoms, but as  $\text{Sb}_4$  molecules [346, 367]. The observed bright clusters might then be assigned to  $\text{Sb}_4$  molecules that did not completely dissociate into single atoms and are thus not available for the formation of other cluster types such as the ringlike clusters. In this model, the different types of bright clusters may then be Sb tetramers, trimers, dimers, and monomers that do not have to be chemisorbed on the surface. The cluster marked A might correspond either to an Sb tetramer or a trimer, B with its elongated appearance to an Sb dimer, and C to an Sb monomer. The formation of the bright clusters at low growth temperatures supports this model, since these temperatures might be too low for a complete dissociation of  $\text{Sb}_4$ . The additional observation at high coverages and high growth temperatures is not that obvious at first sight. For the higher coverages investigated, always also a high number of ringlike clusters is present on the surface [cf. Fig. 5.1 (c)]. Maybe, adsorption sites for a physisorption of Sb atoms are already too rare on the surface, hindering a complete dissociation of  $\text{Sb}_4$ . However, to verify these assumptions, further investigations and a comparison with theoretical calculations are needed.

Besides the growth of the different cluster types, also the uncovered areas with the  $7\times 7$  reconstruction undergo changes in all samples investigated within this work. This is shown exemplarily for one preparation in Fig. 5.2. In the filled states STM image shown in (a), many adatoms of the  $7\times 7$  reconstruction appear brighter, while in the empty states STM image of the same area shown in (b), the same adatoms appear lower as compared to the surrounding  $7\times 7$  surface. These differently appearing adatoms are assigned to Sb atoms that

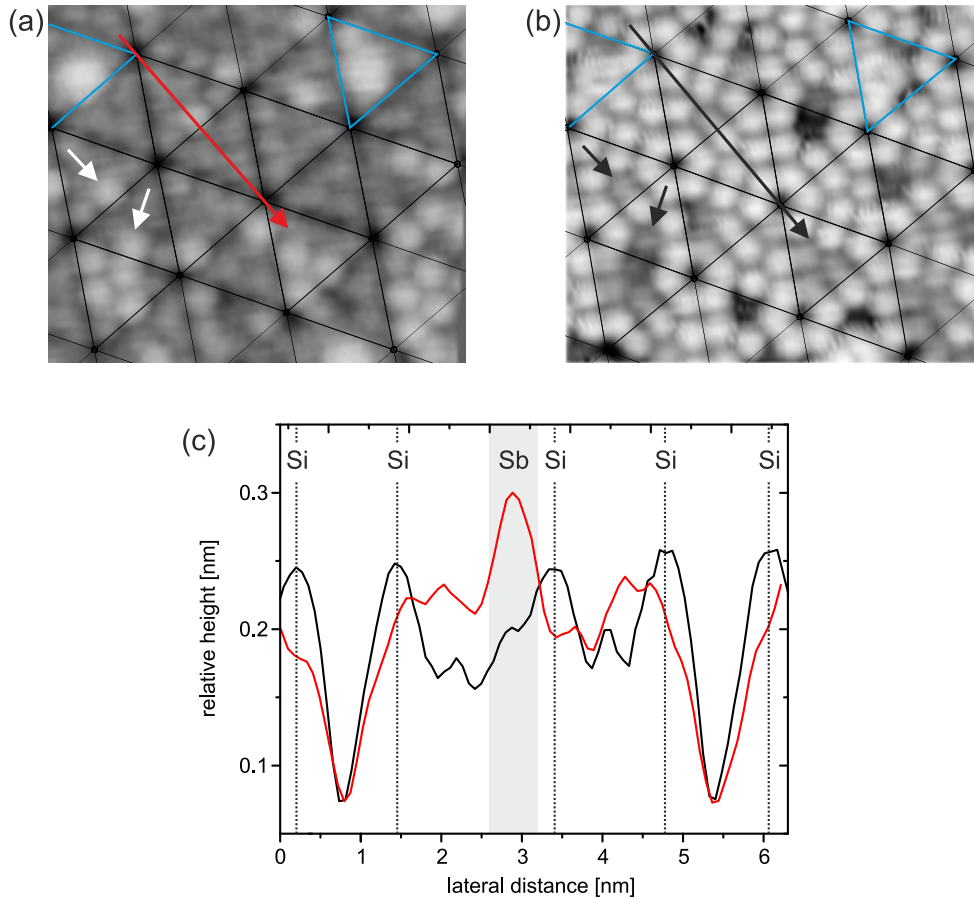


**Figure 5.2:** (a) Filled states ( $V_S = -2.0$  V;  $I_T = 500$  pA) and (b) empty states STM images ( $V_S = +2.0$  V;  $I_T = 500$  pA) of the same area of a sample with an Sb coverage of 0.08 ML deposited at 500 °C. Besides two ringlike clusters marked in blue, Sb atoms that substituted adatoms of the Si(111) $7\times 7$  reconstruction are found as exemplarily marked by the small white and black arrows. (c) Height profiles taken along the red and black arrows in (a) and (b), respectively. The dotted lines marked with Si indicate unchanged Si adatoms, while the gray area marked by Sb indicates the position, where an Sb atom substituted a Si adatom of the  $7\times 7$  reconstruction.

substituted Si adatoms of the Si(111) $7\times 7$  surface. Such adatom substitutions were already observed earlier with a similar appearance and explained by completely filled dangling bonds at the Sb adatoms [358]. When Sb atoms with their five valence electrons bind to three Si atoms, the two remaining electrons entirely fill the remaining dangling bond. In contrast, for Si, the dangling bonds are only partially filled. Thus, in empty states STM images, the Si adatoms appear higher than Sb atoms, while for the filled states the Sb adatoms are imaged with a higher appearance. The observed effect is thus mostly electronic, although the larger covalent radius of Sb as compared to Si [368] might enhance the contrast at least in the filled states images. As derived from the height profiles shown in (c), the Sb adatoms appear about 0.06 nm higher than the Si adatoms in the filled states image and about 0.05 nm lower than the Si adatoms in the empty states image, which corresponds nicely with the values measured in Ref. [358].

Adatom substitutions were found in the complete investigated growth parameter range. For higher Sb coverages the  $7\times 7$  surface is intensively disturbed by the adatom substitution as well as the cluster formation. At a rather high coverage of 0.47 ML, still many bright clusters form but also many islands exceeding over several HUCs appear, which may already represent precursors of the Sb induced reconstructions forming at higher Sb coverages and growth temperatures [355–364].

In the following sections, the results on the double-row clusters and the ringlike clusters are discussed in more detail.

## 5.2 Double-row clusters

As already mentioned, double-row clusters are observed for the lowest used Sb coverages between 0.04 ML and 0.08 ML and temperatures between 230 °C and 400 °C. Figure 5.3 shows again STM images of the sample already shown in Fig. 5.1 (a) and (d). For this preparation, the highest number of double-row clusters was found. In detailed filled states STM images such as Figs. 5.1 (d) and 5.3 (b), they appear as two rows formed by five to six bright protrusions. The rows are thereby aligned parallel to an edge of the  $7\times 7$  HUC. However, in clusters with one row consisting of two protrusions, the row consisting of three protrusions can appear slightly bent. In addition, in such clusters the protrusion in the middle of a triple row can appear brighter than the two outer ones, as indicated by the arrow in Fig. 5.3 (b). Unfortunately, it was not achieved to obtain filled and empty states STM images at the same location of the surface due to large thermal drift present during the measurements. Hence, it is not possible to make a direct assignment between double-row clusters with one explicit appearance. However, due to the predominant formation of double-row clusters at the present preparation conditions, structures with a similar frequency of occurrence in the empty states may also be assigned to double-row clusters. Figure 5.3 (c) shows detailed empty states images of clusters assigned to double-row clusters. In contrast to the filled states images, the clusters here appear mainly as one row formed by two spots.

In the following, the composition of the double-row clusters is discussed. At the preparation conditions with a predominant formation of double-row clusters, a large number of adatom substitutions is found on the surface besides the clusters. By analyzing the number of adatom substitutions for the preparation shown in Fig. 5.3, it is found that about 85% of the Sb atoms deposited on the surface substituted Si adatoms of the  $7\times 7$  reconstruction. Thus, only 15% of the deposited Sb is available for the cluster formation. The relatively large density of clusters found on the surface can thus only be explained by a very low average Sb content of the clusters. In addition, the Si atoms which are released by the adatom substitution may also participate in the cluster formation. Thus, it may be concluded that also the formation of pure Si clusters might be possible at these preparation conditions.

Indeed, clusters appearing very similar to the double-row clusters are known from Si(111) homoepitaxy [369–372]. In fact, the situation that is found here is very similar to Si(111) homoepitaxy, since mostly Si atoms released from the adatom substitutions are present on

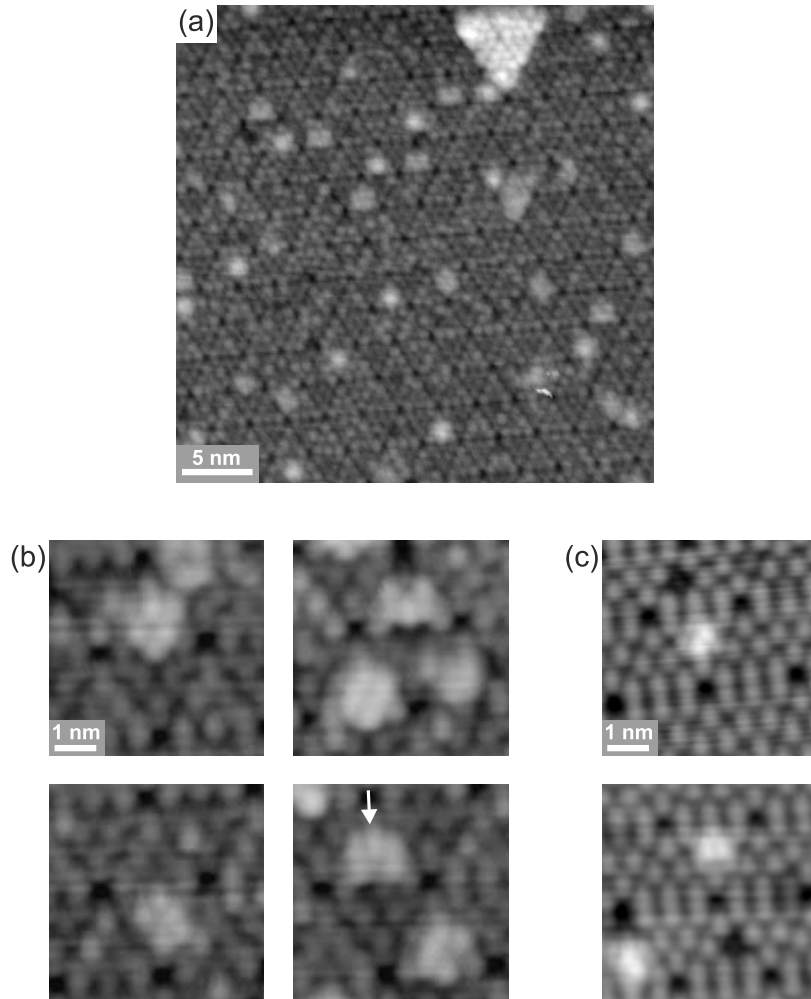


**Figure 5.3:** (a) Filled states overview STM image ( $V_S = -2.5$  V;  $I_T = 100$  pA) of a Si(111) sample with an Sb coverage of 0.04 ML deposited at 400 °C. (b) Detailed filled states STM images of Sb induced double-row clusters ( $V_S = -1.3$  V;  $I_T = 500$  pA). (c) Corresponding detailed empty states STM images ( $V_S = +1.3$  V;  $I_T = 500$  pA).

the surface, and the Sb atoms are predominantly bound in the adatom substitutions. These Si atoms then may diffuse on the surface and behave similar to Si atoms deposited in a homoepitaxy experiment. Indeed, triangular islands with the  $7 \times 7$  reconstruction and a height corresponding to a single Si(111) step are found on the surface [see Figs. 5.1 (a) and 5.3 (a)], in good agreement with those found in Si(111) homoepitaxy [239, 373, 374]. Hence, it may be assumed that the double-row clusters forming at low Sb coverages and growth temperatures, similar to those used in the mentioned Si(111) homoepitaxy studies, are pure Si clusters that form with the Si atoms released from the large number of adatom substitutions, which is observed at these preparation conditions.

To further prove this assumption, Si homoepitaxy experiments were also performed within this work for comparison. Figure 5.4 shows STM results for a Si(111) sample with a Si coverage of 0.2 ML deposited at 350 °C. In the overview image shown in (a), the typical formation of triangular Si(111) islands is observed. As already mentioned in section 3.5, such triangular islands form in a kinetically limited growth process due to a larger cost of energy for lifting

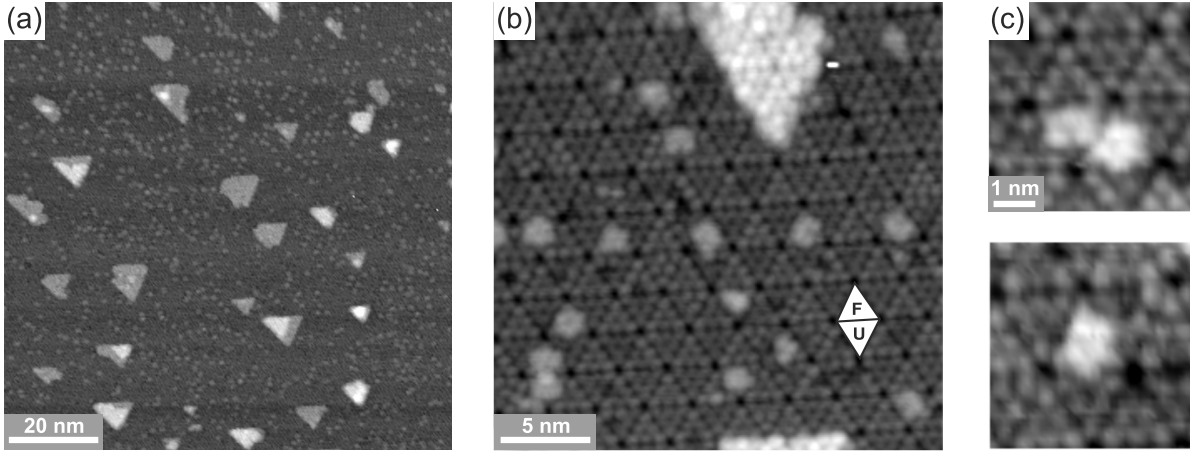


**Figure 5.4:** (a) Overview filled states STM image ( $V_S = -2.5$  V;  $I_T = 100$  pA) of a sample with a coverage of 0.2 ML Si deposited at 350 °C. (b) More detailed filled states STM image ( $V_S = -2.0$  V;  $I_T = 100$  pA) showing the forming double-row clusters besides an Si(111) island with  $7 \times 7$  reconstruction. (c) Detailed filled states STM images of double-row clusters forming during Si homoepitaxy ( $V_S = -2.0$  V;  $I_T = 200$  pA).

the reconstruction of the FHUC as compared to the UFHUC [239, 373, 374]. This results also in the high preference for one specific orientation of the triangles with UFHUCs forming the vertices of the triangles as can be seen from Fig. 5.4 (b).

However, besides these islands also clusters forming within single  $7 \times 7$  HUCs are found on the surface. When comparing more detailed filled states STM images of these clusters [Fig. 5.4 (b) and (c)] with filled states STM images of the Sb induced double-row clusters [Fig. 5.3 (a) and (b)], an identical appearance as two rows formed by five to six protrusions is found. In addition, the empty states images of the Sb induced double-row clusters shown in Fig. 5.3 (c) are in nice agreement with those of Si clusters in homoepitaxy published in Ref. [369]. Thus it is concluded that the double-row clusters observed in this work are indeed the same pure Si clusters that are observed in Si homoepitaxy and which are assumed to be precursors for the formation of the two-dimensional Si(111) islands [369–372].

The exclusive formation of double-row clusters at extremely low Sb coverages and low growth temperatures may be explained as follows: At higher Sb coverages, more Sb atoms are present on the surface and the formation of Sb-Si binary clusters becomes more probable hindering the formation of pure Si clusters. At higher growth temperatures, the diffusion length of the Si atoms increases and with this also the growth rate of the two-dimensional islands. Hence, at the higher temperatures most of the Si atoms form islands or are able to diffuse to a step edge resulting in step-flow growth. The observation of saw-tooth like Si(111) step edges at higher growth temperatures additionally supports this view.

### 5.3 Magic Sb ringlike clusters

As can be seen already from a comparison of the overview STM images shown in Fig. 5.1 (a) to (c), the ringlike clusters show the most homogeneous growth of the different Sb induced cluster

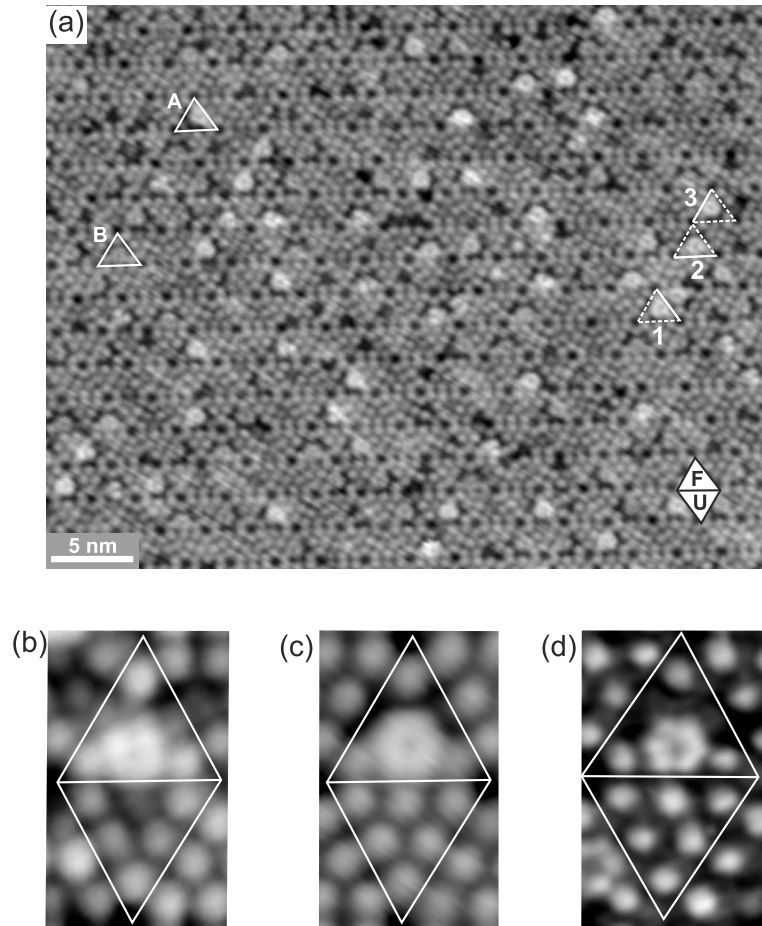


**Figure 5.5:** (a) Overview empty states STM image ( $V_S = +1.3$  V;  $I_T = 100$  pA) of a sample with a coverage of 0.11 ML Sb deposited at 450 °C. (b) Detailed filled states STM image ( $V_S = -1.0$  V;  $I_T = 100$  pA) and (c,d) detailed empty states images of ringlike clusters obtained with (c)  $V_S = +1.5$  V;  $I_T = 500$  pA, and (d)  $V_S = +1.5$  V;  $I_T = 1$  nA. In (a), a  $7 \times 7$  unit cell showing the orientation of the FHUC (F) and the UFHUC (U) is indicated. In addition, A and B exemplarily mark clusters with high and low apparent heights, respectively. The HUCs marked with 1, 2, and 3 represent clusters showing the three possible equivalent orientations within the HUC. Thereby, the respective edge, near which the clusters appear, is indicated by the solid line of the triangle.

types that are found in the investigated parameter range. At growth temperatures between 450 °C and 550 °C, an almost exclusive formation of ringlike clusters is observed. Only at higher coverages, more and more bright clusters form, hindering up to now the preparation of complete two-dimensional arrays of ringlike clusters. However, at the ideal growth temperature of 450 °C, densities of ringlike clusters up to  $8 \cdot 10^{12}$  cm $^{-2}$  could be obtained as shown in Fig. 5.5 (a). Here, a ringlike cluster is found in about every second  $7 \times 7$  unit cell.

In contrast to the filled states images shown in Fig. 5.1 (b) and (e), where the clusters appear rather structureless as an oval protrusion located near an edge of the  $7 \times 7$  HUC, the clusters clearly show a ringlike appearance in empty states images such as Fig. 5.5 (a). For a more detailed discussion, high resolution STM images of single ringlike clusters are shown in Fig. 5.5 (b) to (d). With highest resolution, a ringlike appearance is also observed in filled states images such as (b), although mostly an appearance like the one in Fig. 5.1 (b) and (e)

is observed. In empty states images, a ringlike appearance as in (c) is routinely observed. When highest resolution is achieved, the clusters here appear as hexagons formed by six spots as visible in (d). However, for both polarities of the tunneling voltage, the ringlike clusters appear near the center of an edge of the  $7\times 7$  HUCs, with the corner adatoms of the  $7\times 7$  reconstruction appearing unaffected by the cluster formation. In contrast, the former Si center adatoms of the  $7\times 7$  reconstruction are no longer observed in HUCs with ringlike clusters. Due to the location of the observed features for the ringlike clusters near an edge of the HUCs, three equivalent orientations of the clusters within the HUC are possible which are exemplarily marked with 1, 2, and 3 in Fig. 5.5 (a). The solid line of the triangle marking the corresponding HUC thereby indicates the edge, near which the cluster is observed.

In Fig. 5.5 (a), also another feature of the ringlike clusters is found. When comparing different ringlike clusters, they show an identical appearance as a ring forming near the center of an edge of a  $7\times 7$  HUC, but different clusters are characterized by different apparent heights with respect to the surrounding surface. This is indicated in Fig. 5.5 (a) by A and B and shown in more detail in Fig. 5.6. Due to this appearance with different heights, the cluster density in Fig. 5.5 (a) is easily underestimated at first sight. When comparing again Fig. 5.5 (a) with Fig. 5.1 (b), it is evident that the height variation is predominantly observed in empty states images. In Fig. 5.6 (b), height profiles for four clusters appearing with different heights taken along the arrows indicated in (a) are shown. While the clusters marked in green and black appear higher than the surrounding  $7\times 7$  surface, the clusters marked in blue and red appear lower. Altogether, height differences of up to 0.13 nm between the highest appearing clusters and the lowest appearing clusters are observed.

This height variation may either be caused by structural differences between the clusters or by a different environment of the clusters like other clusters, adatom substitutions, steps, or other defects forming in their proximity. However, when analyzing the heights of various

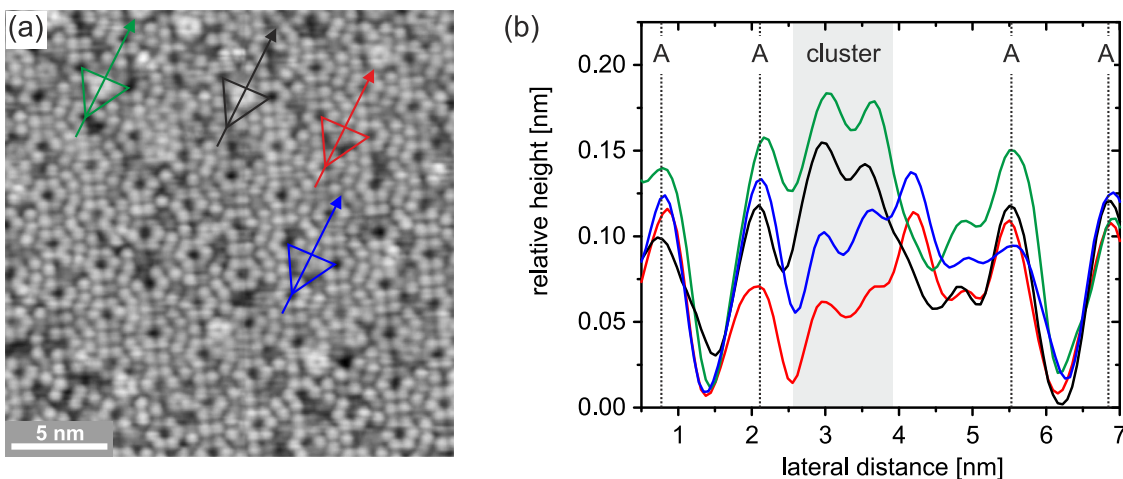


**Figure 5.6:** (a) Empty states STM image ( $V_S = +1.0$  V;  $I_T = 200$  pA) of a sample with a coverage of 0.11 ML Sb deposited at 450 °C. (b) Height profiles along the arrows indicated in (a). The gray box indicates the area, where ringlike clusters formed, the dotted lines marked with A indicate the positions of  $7\times 7$  adatoms.

clusters, no dependence on one of the mentioned structures in the close environment could be found. Thus, structural differences between the clusters have to be responsible for the observed height variations. A further discussion on its origins is conducted in the following section.

Additionally, the ringlike clusters show a strong preference for occupying the FHUCs of the  $7\times 7$  reconstruction, as can be seen from the overview image in Fig. 5.5 (a), where the orientation of the HUCs is indicated. By counting the clusters in several STM images for the preparations with the ideal growth temperature of  $450\text{ }^\circ\text{C}$ , it is found that as much as 97% of all ringlike clusters formed in the FHUC. Knowing the growth temperature and the relative population of the different half unit cells, it is possible to estimate the difference in the formation energies for a cluster in the unfaulted half unit cell and in the faulted half unit cell by employing the Boltzmann distribution:

$$n_U/n_F = \exp(-\Delta E/k_B T). \quad (5.1)$$

Here,  $n_F$  and  $n_U$  are the numbers of clusters occupying the FHUC and UFHUC, respectively,  $T$  is the substrate temperature during growth, and  $k_B$  the Boltzmann constant. Using the above mentioned values, an energy difference of  $\Delta E = (0.22 \pm 0.01)$  eV is obtained. This energy difference is, to the best of my knowledge, the highest value found for a cluster system on Si(111) $7\times 7$  so far. However, the centered Tb silicide clusters, which were also observed in this work for the first time, exhibit a similar energy difference, as described in detail in chapter 7. For other systems, much lower energy differences are found, e.g. 0.08 eV to 0.1 eV for magic In clusters [10, 279] and 0.09 eV for Co clusters [13].

### 5.3.1 Atomic structure of Sb ringlike clusters

To identify the atomic structure of the ringlike Sb clusters, first the average Sb content of the clusters is estimated. This is done based on the measurement shown in Fig. 5.5 (a), where 95% of all clusters are ringlike clusters and about every second  $7\times 7$  unit cell is occupied. Taking into account the adatom substitutions, an Sb content of the ringlike clusters of about six Sb atoms per cluster is derived. Doing the same estimation for the other measurements at the ideal growth temperature of  $450\text{ }^\circ\text{C}$ , similar values between five and seven Sb atoms are derived. Thus, the Sb content of the ringlike clusters is estimated to be about six Sb atoms.

However, besides assuming a reasonable Sb content, a structure model has also to be able to explain the further experimental observations:

1. The appearance of the ringlike clusters in filled and empty states STM images, including the location, where the clusters are observed, the unchanged Si corner adatoms as well as the missing Si center adatoms.
2. The observed variations in the apparent heights of different clusters.

In addition, the number of unfavorable dangling bonds should be minimized and the bonding geometries should correspond to typical bond lengths and bond angles.

In literature, several other systems of clusters on the Si(111) surface with clusters forming off-center within single  $7\times 7$  HUCs are known. These are first the so-called ring clusters forming from the transition metals Co [244–246, 248], Ni [246, 249–252], Fe [246, 253], Pd [246], Pt [246], and Ir [246] at high temperatures which were already mentioned in section 3.5. Although their appearance might be similar to the Sb ringlike clusters observed here, their growth behavior is substantially different. The transition metal ringclusters form at much higher temperatures and thereby destroy the underlying  $7\times 7$  reconstruction. They represent the initial states of either a  $\sqrt{7}\times\sqrt{7}$  R19.1° superstructure or a  $\sqrt{19}\times\sqrt{19}$  R19.1° superstructure with a preferential nucleation at defects and step edges rather than a growth of clusters within single  $7\times 7$  unit cells. In addition, their metal content of one and three atoms is not consistent with the estimated Sb content of the ringlike Sb clusters.

Other off-center clusters are found for Co [13, 273], Fe [14], and Mn [268]. These clusters form at lower temperatures between 80 °C and 230 °C. Especially the Co and Fe induced magic clusters show a similar ringlike appearance as the Sb ringlike clusters, also with missing Si center adatoms and the Si corner adatoms appearing unchanged. However, although a clear ringlike appearance is found in empty states images, STM images with the clusters appearing to be formed by six protrusions have not been published yet. In the proposed structure model, these clusters are built from six metal atoms and three Si atoms forming a triangle located near an edge of the HUC. Hence, also the metal content is in good agreement with the Sb content estimated for the Sb ringlike clusters. Nevertheless, the triangular structure cannot explain the highest resolution empty states STM images obtained in this work with the ringlike Sb clusters appearing as six protrusions. This is especially obvious from the simulated STM images published in Refs. [13, 14], in which the Co and Fe induced clusters clearly show a triangular appearance. Hence, also this structure model has to be excluded.

A third system showing similarities to the Sb ringlike clusters observed in this work are the magic Si clusters forming after annealing a Si(111) $7\times 7$  sample to about 500 °C and subsequent quenching to room temperature [243, 270–272] (cf. section 3.5). The STM images published for these clusters show a very good agreement with those obtained for the Sb ringlike clusters within this work with a rather structureless appearance in filled states images and an appearance as a ring formed by six protrusions in the empty states. However, no height variation is observed for the magic Si clusters and the Si content is estimated to be between nine and 15 atoms, being much higher than the Sb content of the ringlike clusters. In addition, no satisfying structure model was proposed yet. The only publication addressing the atomic structure of these clusters is Ref. [272] where the best agreement between simulated and experimental STM images is observed for a cluster consisting of eight Si atoms. However, in the calculated structure, the Si center adatoms are unchanged, what is clearly visible in the simulated STM images.

Thus, none of the structure models published up to now for clusters appearing off-center within single Si(111) $7\times 7$  HUCs is suitable to explain the present observations for the Sb ringlike clusters, and a new structure model needs to be developed.

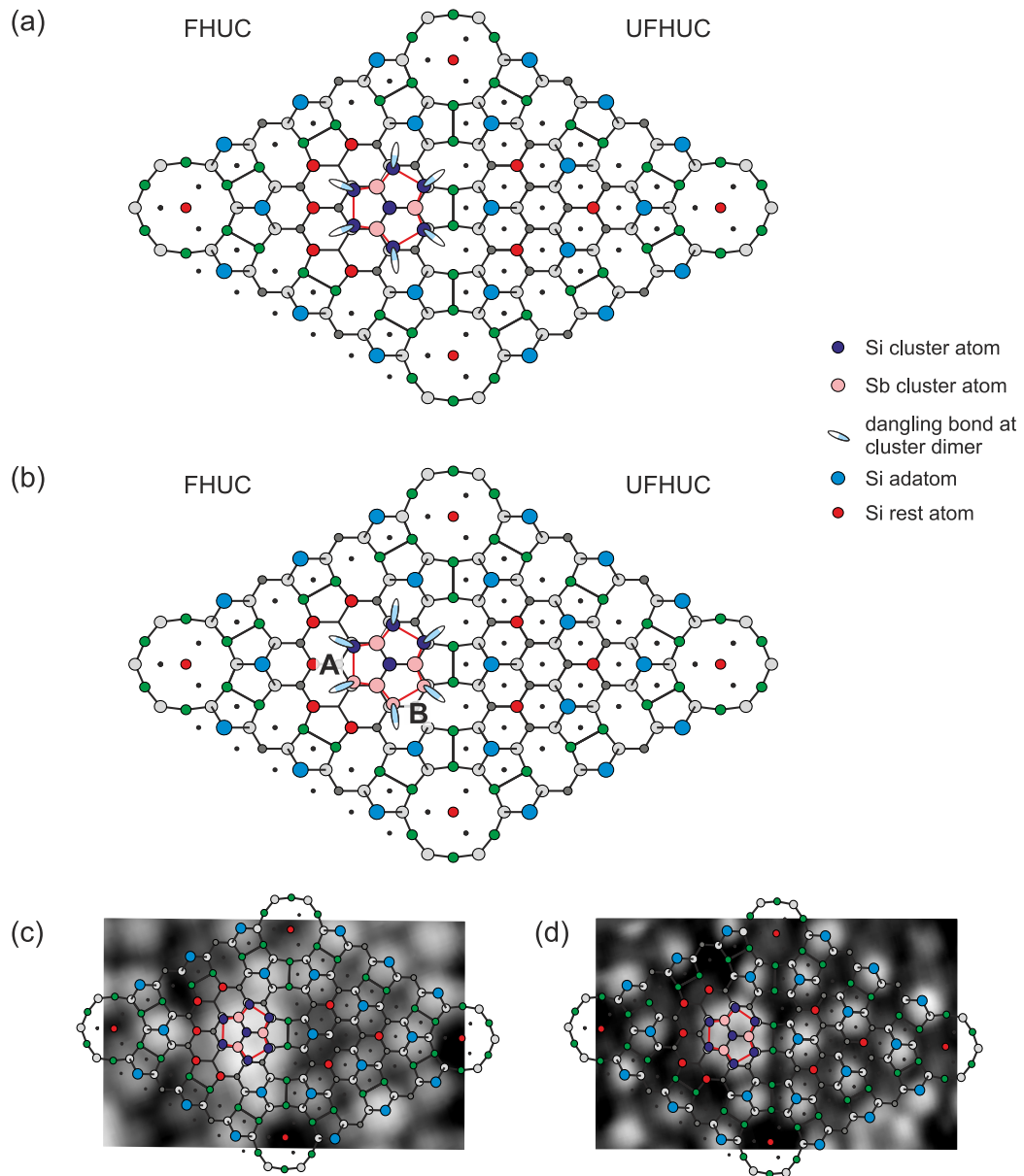


**Figure 5.7:** (a) Fundamental structure model for the ringlike Sb clusters. (b) Structure model with substitution of some Si cluster atoms by Sb atoms. In the dimer marked with A, one Si atom is replaced resulting in a mixed dimer, while at B, both Si dimer atoms are replaced. For both models, the filling of the dangling bonds at the cluster dimers is schematically indicated. (c,d) Atomic structure model shown in (a) overlaid on the (c) filled states and (d) empty states STM images, which have already been shown in Fig. 5.5 (b) and (d), respectively.

Therefore, several different structure models were considered for the Sb ringlike clusters, resulting in the one shown in Fig. 5.7 which is able to explain all the experimental observations. The basic structure is shown in (a). The cluster forms at an edge of an FHUC of the Si(111)7×7 reconstruction with the Si corner adatoms being unchanged and the Si center adatoms being removed. The cluster center is placed above a Si rest atom at the position, where the depression leading to the ringlike appearance is observed in the empty states STM images. It is formed by a Si atom bonding to three Sb atoms in an  $sp^3$ -like configuration. The three Sb atoms are

then surrounded by three dimers, in the basic model consisting of Si atoms corresponding to a  $\text{Sb}_3\text{Si}_7$  stoichiometry.

This structure can nicely explain the observed contrast in the STM images. As it is indicated schematically, the dangling bonds at the dimers are only partly filled, while the four atoms in the center all have fully saturated dangling bonds. The appearance in the empty states STM images as a ring composed of six bright spots can thus nicely be explained with the high tunneling probability found at the positions of the dangling bonds at the dimer atoms. The fully saturated dangling bonds in the cluster center may, on the other hand, explain the depression leading to the ringlike appearance. The partly filled dangling bonds at the dimer atoms should also be imaged in filled states images. However, the high density of filled states in the cluster center here may lead to the structureless appearance which is usually observed. The ringlike appearance that is sometimes also observed in filled states images such as the one shown in Fig. 5.5 (b) might be explained with the relatively low absolute value of the applied tunneling voltage of  $-1$  V. From the clean  $\text{Si}(111)7\times 7$  surface it is known that in filled states STM images acquired at low absolute tunneling voltage, mainly the dangling bonds at the adatoms are imaged since the other filled states are located lower in energy (see section 3.2.1) [196]. This might also be the case here, leading to the observation of mainly the dangling bonds at the dimer atoms and thus a ringlike appearance.

The nice agreement between the structure model and the filled and empty states STM images is demonstrated in Fig. 5.7 (c) and (d), where the structure model is overlaid on the STM images.

However, the structure model presented in Fig. 5.7 (a) is not yet able to explain the height variations observed for the Sb ringlike clusters. In addition, the Sb content of three Sb atoms is much lower than the one estimated from the experiments. Both difficulties are addressed now. It has been found already for the  $7\times 7$  reconstruction that Sb atoms easily substitute Si adatoms, an effect that was even found to lead to the formation of pure Si clusters, namely the double-row clusters. Hence, it may be assumed that Sb atoms also substitute Si dimer atoms in the ringlike clusters. This is schematically shown in Fig. 5.7 (b) for the dimers marked with A and B, where one dimer atom or both dimer atoms are substituted by Sb atoms, respectively. However, no formation of mixed dimers was found after the deposition of Sb on the  $\text{Si}(001)$  surface [375] where the dimer rows of the  $\text{Si}(001)2\times 1$  surface represent a similar local structure as it is found in the ringlike clusters, hence this configuration might be less probable.

Since Sb, as a group-V element has one valence electron more as compared to Si, the dangling bonds of substituted dimer atoms become completely filled. This results in a higher average filling of the six dangling bonds at the cluster dimers. It may now be assumed that a charge transfer between the six dangling bonds appears as it is also observed on the bare  $7\times 7$  surface, where it results in a complete saturation of the dangling bonds at the rest atoms and a fractional filling of the adatom dangling bonds [183, 190, 376]. Such a charge transfer may easily occur in the case of almost metallic structures, as is assumed here for the ringlike clusters and as it will be shown further below on the basis of STS measurements. Hence, the filling of dangling bonds at the dimer atoms increases with increasing Sb content of the clusters leading

to less empty states and thus a lower appearance in empty states STM images. The proposed structure model is in this way able to explain nicely the similar fundamental appearance of different ringlike clusters with only their apparent heights varying from cluster to cluster since the basic structure is identical, but the stoichiometry of the clusters changes. Within this model, Sb contents between three Sb atoms for the basic model as shown in Fig. 5.7 (a) and nine Sb atoms when all dimer atoms are Sb atoms are in principle possible, being in nice agreement with the average Sb content of six estimated from the experimental data.

However, many unsaturated dangling bonds are present at the rest atoms in the area of the HUC which is not covered by the cluster [red atoms in Fig. 5.7 (a) and (b)]. It may be assumed that a charge transfer does not only occur between the dangling bonds at the dimer atoms but, as on the bare Si(111)7×7 surface, also between these dangling bonds and the dangling bonds at the rest atoms, leading to their saturation.

Another aspect of the structure model is the Si content within an HUC with a ringlike cluster, which is usually higher than in HUCs without a cluster. For the formation of the basic structure shown in Fig. 5.7 (a), e.g. four additional Si atoms are needed. In other cluster systems such as the magic group-III metal clusters and the magic Co and Fe silicide clusters (see section 3.5.1), often only the three former Si center adatoms contribute to the cluster formation, making a Si diffusion from other HUCs unnecessary. However, the Si diffusion from other HUCs should not represent a large problem in the present case due to the frequent adatom substitutions that are observed here, providing free Si atoms and leading even to the formation of pure Si clusters or Si(111) islands.

In conclusion, the Sb ringlike clusters can be seen as magic clusters regarding their identical basic structure with the same overall number of atoms. However, the different stoichiometries that are proposed should have a huge influence on their electronic properties since the substitution of Si atoms by Sb atoms represents a process similar to a very strong *n*-type doping. Hence, in the following section, the electronic properties of the Sb ringlike clusters are studied in more detail on the basis of voltage dependent STM images as well as tunneling spectroscopy.

### 5.3.2 Electronic properties of Sb ringlike clusters

It was already mentioned in the previous section that the differences in the apparent height of different ringlike clusters are predominantly observed in empty states STM images. This is especially obvious from the voltage dependent STM images presented in Fig. 5.8. While in the filled states STM images all clusters show an identical appearance which, in addition does not change much with decreasing absolute value of the tunneling voltage, different clusters clearly appear with different heights in the empty states images. This is visible best at tunneling voltages between 1.0 V and 1.5 V [Fig. 5.8 (c) and (b)], where at least four different apparent heights are distinguishable. However, the height differences that occur are rather small and thus do not allow to explicitly determine how many different apparent heights are observed. Here, the limit of the resolution of the STM experiment is reached, also because the frequent

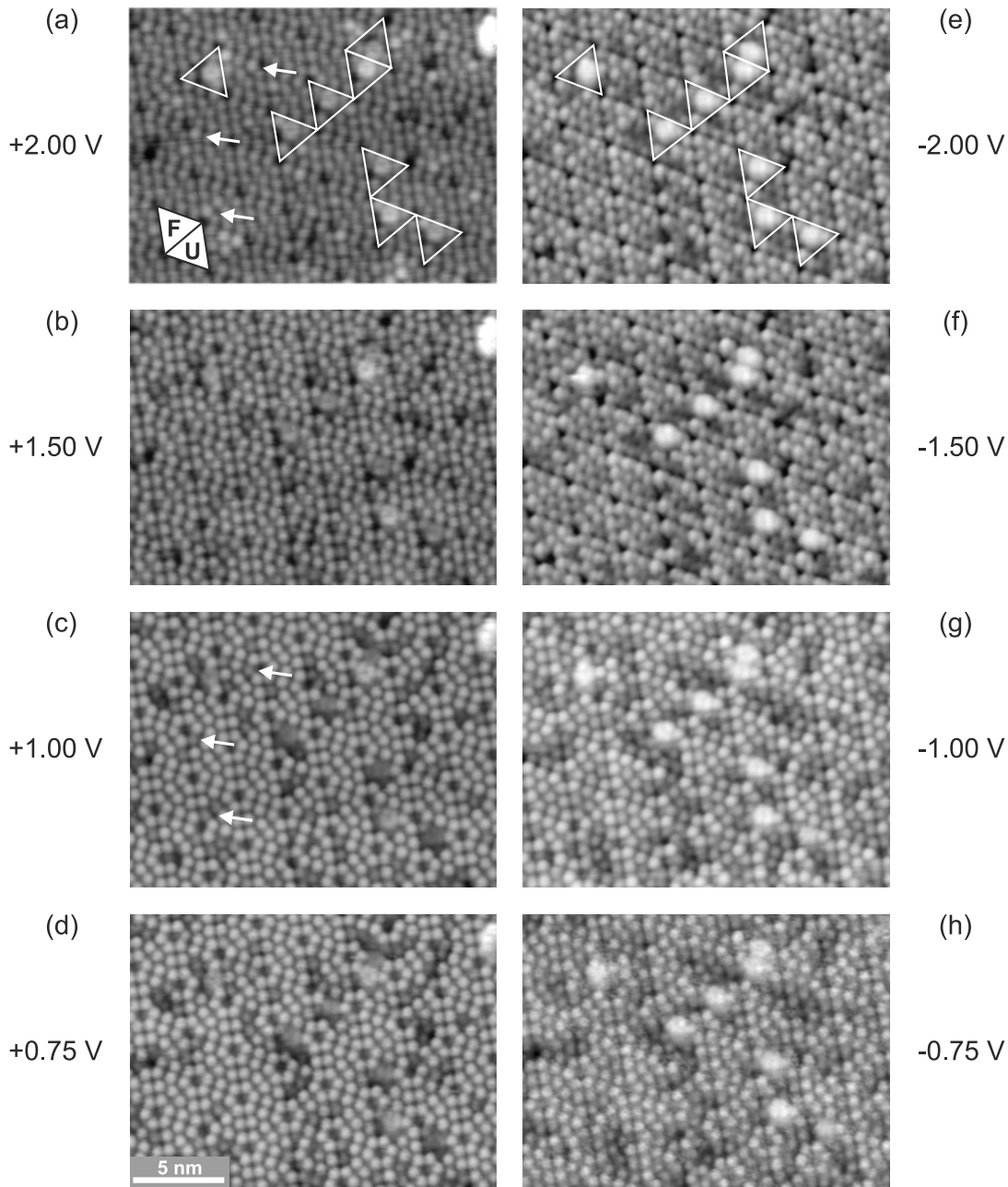


**Figure 5.8:** Voltage dependent STM images of the same area with various Sb ringlike clusters. (a-d) Empty states STM images with sample voltages of +2.0 V, +1.5 V, +1.0 V, and +0.75 V, respectively. (e-h) Corresponding filled states STM images with sample voltages of -2.0 V, -1.5 V, -1.0 V, and -0.75 V, respectively. The white triangles in (a) and (b) mark HUCs in which ringlike clusters formed. In addition, the orientation of the FHUC and UFHUC is indicated in (a) by F and U, respectively, and the white arrows in (a) and (c) exemplarily indicate substituted adatoms that appear higher than common Si adatoms at a sample voltage of +2.0 V, but lower at +1.0 V.

adatom substitutions disturb the  $7\times 7$  surface in between the clusters making it difficult to define a clear height reference.

At a tunneling voltage of +2.0 V [Fig. 5.8 (a)], most ringlike Sb clusters appear higher than the surrounding  $7\times 7$  surface. With decreasing voltage, more and more clusters appear lower than the surrounding surface, although at the lowest applied voltage of +0.75 V [Fig. 5.8 (d)]

some clusters appearing higher are still found. Hence, despite of the decrease in the apparent height which indicates a semiconducting behavior of the ringlike clusters, metallic states around the Fermi level cannot be excluded, since the clusters with a low apparent height still can be imaged. In addition, the apparent height does not show a strong decrease in the filled states STM images, rather indicating a metallic behavior. In the end, the different electronic properties of different ringlike clusters might also lead to a transition from a metallic to a semiconducting behavior. Thus, to investigate the electronic structure of ringlike clusters in more detail, STS measurements were performed. Thereby, special attention was given to the different apparent heights, which different clusters show.

But before discussing the STS measurements, it is interesting to mention a further detail which is observed in the voltage dependent STM images in Fig. 5.8. In the empty states STM image obtained with a rather high tunneling voltage of +2.0 V [Fig. 5.8 (a)], the adatoms which are substituted by Sb atoms interestingly appear higher than the common Si adatoms of the  $7\times 7$  reconstruction, although it was concluded in section 5.1 that, due to fully saturated dangling bonds, these adatoms should appear lower in the empty states STM images. A lower appearance of the same adatoms is indeed observed at lower absolute tunneling voltages. Adatoms showing the mentioned behavior are exemplarily indicated by arrows in Fig. 5.8 (a) and (c). The explanation is again straight forward: Sb has a larger covalent radius as compared to Si [368]. Thus, substituting Sb atoms protrude further into the vacuum than Si adatoms and are thus imaged higher. Due to the larger sensitivity for topographic effects in comparison to electronic ones at higher tunneling voltages, this is predominantly observed for high positive tunneling voltages, while at voltages of +1.5 V and below, the electronic effects dominate.

Figure 5.9 shows tunneling spectra measured on ringlike Sb clusters appearing with different heights. The spectra were obtained after stabilization of the tip height with a sample voltage  $V_S = +1.5$  V and a tunneling current  $I_T = 500$  pA. In addition, the tip was approached by 25 pm towards the sample during the STS measurement shown in (a), while the normalized differential conductivity curves shown in (b) represent the average of STS measurements with the tip approached by 20 pm and by 25 pm, respectively. As already mentioned, it is not possible to clearly assign specific heights of the clusters. Hence, the clusters are classified into three categories, high, middle, and low appearing clusters, and at least 15 tunneling spectra of different clusters belonging to one of these categories are averaged. Examples for such low, middle, and high appearing clusters are indicated in the STM image shown as an inset in Fig. 5.9 (a).

Already in the current-voltage ( $I-V$ ) curves presented in (a), a clear difference between the clusters appearing with a different height is obvious. For negative sample voltages, the steepest increase in the tunneling current is observed for the low appearing clusters and the most shallow one for the high appearing clusters. In contrast, the situation is opposite for positive sample voltages. Here, the low clusters show the lowest tunneling current curve, while the high clusters show the highest tunneling currents, although the difference is not that pronounced since the tunneling contact was stabilized at a sample voltage of +1.5 V. For comparison, also tunneling spectra measured on the uncovered Si(111) $7\times 7$  surface are shown.

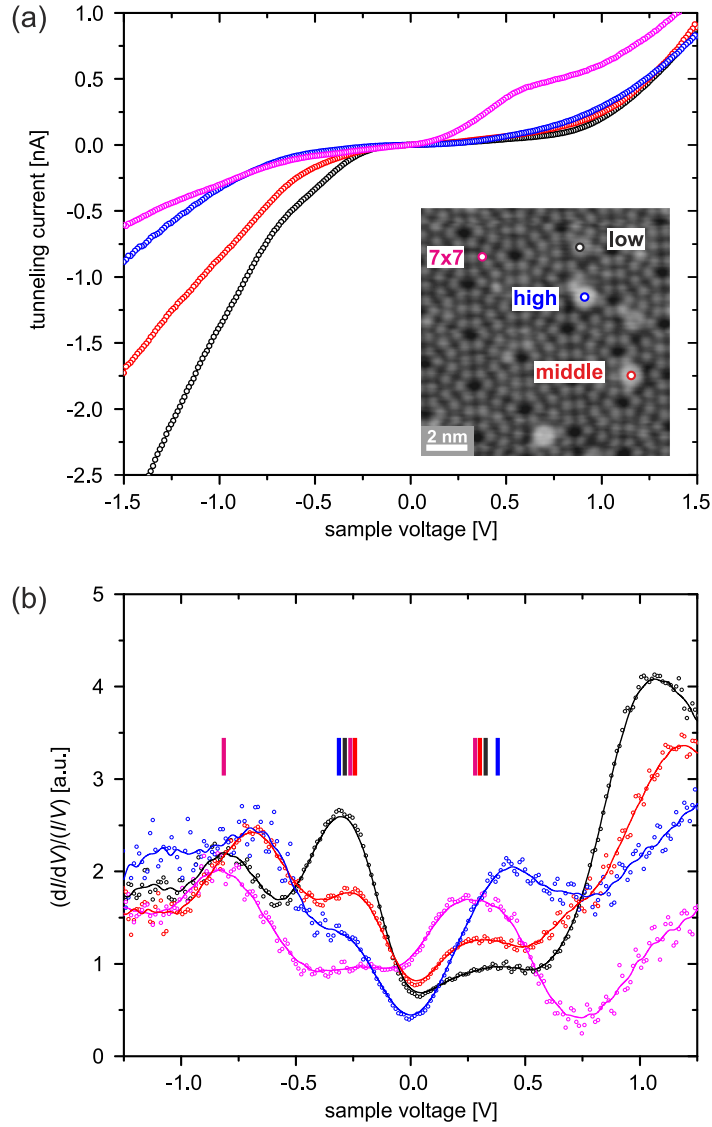


**Figure 5.9:** (a)  $I$ - $V$  curves of ringlike Sb clusters appearing with different heights and the clean Si(111)  $7 \times 7$  surface for comparison. The STM image in the inset ( $V_S = +1.5$  V;  $I_T = 500$  pA) shows examples for the locations on which the STS spectra were measured. Clusters appearing low, middle, and high as well as the clean  $7 \times 7$  surface and the respective spectra are indicated in black, red, blue, and magenta, respectively. (b) Corresponding normalized differential conductivity  $(dI/dV)/(I/V)$ . The magenta colored bars indicate the positions of the rest atom and adatom states of the  $7 \times 7$  reconstruction, the black, red, and blue colored bars that of the dangling bond states of the clusters.

As expected, the  $7 \times 7$  spectrum clearly shows a metallic character with a nonzero slope at the Fermi level (cf. section 3.2.1). For the spectra measured on ringlike Sb clusters, the slope is considerably smaller around the Fermi level. However, it is not zero, indicating also a metallic behavior of the ringlike clusters as it was already supposed above.

For a more detailed discussion, the normalized differential conductivity  $(dI/dV)/(I/V)$  was calculated by differentiating the current-voltage curves numerically. The result is shown in Fig. 5.9 (b). All cluster spectra clearly show two states around the Fermi level at about  $-0.3$  V and  $+0.4$  V and a nonzero density of states at the Fermi level. Hence, the clusters are

found to be metallic as it is expected from the structure models presented in Fig. 5.7, where partially filled dangling bonds are found at the dimer atoms. Thus, it may be assumed that the states arising from these dangling bonds at the cluster dimers lead to the metallic behavior of the clusters, as it is also observed in a similar way for the adatoms of the Si(111)7×7 reconstruction. The spectrum of the 7×7 surface, which shows the occupied and unoccupied adatom states at about -0.3 V and +0.3 V, respectively, and the rest atom state at about -0.8 V as indicated by the magenta bars in Fig. 5.9 (b), is in good agreement with former results [190] (cf. section 3.2.1).

For the ringlike clusters, also two states are found at rather similar energetic positions as mentioned before. These states at -0.3 V and +0.4 V [indicated by colored bars in Fig. 5.9 (b)], which may lead to the metallic behavior, are thus assigned to result from the dangling bonds at the cluster dimers. This view is further confirmed when comparing the behavior of these states for the different apparent heights. From the proposed structure model (see Fig. 5.7) it is expected that the most Sb rich clusters should exhibit the highest occupation of the dangling bonds at the dimers and are thus imaged lowest in empty states STM images. In contrast, the most Si rich clusters with the lowest occupation of the dangling bonds should be imaged highest. Exactly this behavior is observed in the normalized differential conductivity curves displayed in Fig. 5.9 (b): For the lowest appearing clusters the highest density of states is observed in the occupied dangling bond state at -0.3 V, while they exhibit the lowest density of states for the unoccupied dangling bond state at +0.4 V. The highest appearing clusters show exactly the opposite behavior, and the clusters showing an apparent height in the middle also show an intermediate behavior.

Thus, the STS results nicely support the structure model proposed in the previous section assuming different stoichiometries for the clusters appearing with different heights. The substitution of Si dimer atoms of the basic model [Fig. 5.7 (a)] by Sb atoms adds additional valence electrons to the system resulting in a uniform filling of all dangling bond states. Hence, the additional Sb atoms can be seen as dopant atoms that, similar as in *n*-type doping in bulk Si crystals, strongly influence the electronic properties of the ringlike clusters.

## 5.4 Conclusions

In this first detailed investigation of clusters formed from a group-V element on the Si(111)7×7 surface, different cluster types, the so-called double-row clusters, ringlike clusters, and bright clusters are found to form in the explored growth parameter regime.

The double-row clusters form at the lowest investigated Sb coverages. It was found that they are pure Si clusters, which form due to the frequent adatom substitutions that take place in this material system. The assumption that the clusters consist only of Si was further proven by the observation of identical double-row clusters in Si homoepitaxy experiments performed for comparison.

Regarding the bright clusters, always not one specific type is found but different types of bright clusters form, which might correspond to incompletely decomposed Sb<sub>4</sub> molecules.

The most homogeneous cluster growth is achieved for the magic Sb ringlike clusters. For these clusters, an atomic structure model could be developed, also explaining the observed variation in their apparent height by a varying Sb content of the clusters. STS measurements on ringlike clusters appearing with different heights additionally support this model: By adding additional Sb atoms and therewith additional valence electrons to the system, the filling of the dangling bonds increases and the clusters appear lower in the empty states images. Thus, the Sb ringlike clusters can be seen as magic clusters due to their identical basic structure, but with different stoichiometries. Such a behavior, which was, to the best of my knowledge, not observed before for a system of self-assembled magic clusters on the Si(111) $7\times 7$  surface, makes these clusters an ideal model system to study, e.g. the influence of the different stoichiometries on the electronic structure.

---

## Chapter 6

# Magic In and Ga clusters

The growth of magic clusters of the group-III metals In, Ga, and Al was already intensively studied in the past [7–10, 24, 238, 279–296]. As described earlier, their atomic structure is well known and the ability to produce perfectly ordered array of magic clusters was demonstrated (see section 3.5.1). Hence, regarding magic clusters on Si(111)7×7, they represent an ideal model system to investigate general effects, e.g. doping effects or how the transition from single isolated clusters over groups of clusters to two-dimensional arrays of clusters might influence their electronic properties.

Such questions are investigated in this work for magic clusters of the group-III metals In and Ga. In addition, the possibility to grow one-dimensional chains of clusters on the Si(557) surface, which is vicinal to Si(111), was investigated for the magic In clusters.

### 6.1 Magic In clusters on the planar Si(111) surface

#### 6.1.1 General growth behavior

An overview image of the Si(111)7×7 surface with magic In clusters is shown in Fig. 6.1 (a). This sample was prepared by depositing 0.06 ML In at 200 °C. Nearly all clusters show an exactly identical appearance in the STM image with only very few anomalous clusters or different structures appearing, as exemplarily indicated by the white arrows. Hence, the cluster growth is characterized by a strong homogeneity with an almost exclusive formation of the magic In<sub>6</sub>Si<sub>3</sub> clusters described in section 3.5.1. However, to achieve such a homogeneity, the preparation conditions need to be adjusted very precisely as demonstrated by Fig. 6.1 (b) showing a sample, which was prepared using nominally identical conditions as in (a). Again, many magic clusters are found on the surface, but the growth is by far not as homogeneous as for the sample shown in (a). Besides the magic clusters, many defective clusters are found as exemplarily indicated by the white arrows marked with B. In addition, many adatoms of the 7×7 reconstruction appear brighter than the surrounding surface (marked with A). At the positions of the adatoms that appear brighter in empty states STM images as the one shown in Fig. 6.1 (b), a depression appears in filled states STM images. Such a behavior is known for In adatoms that substitute Si adatoms of the 7×7 reconstruction [377,378], as it was also observed

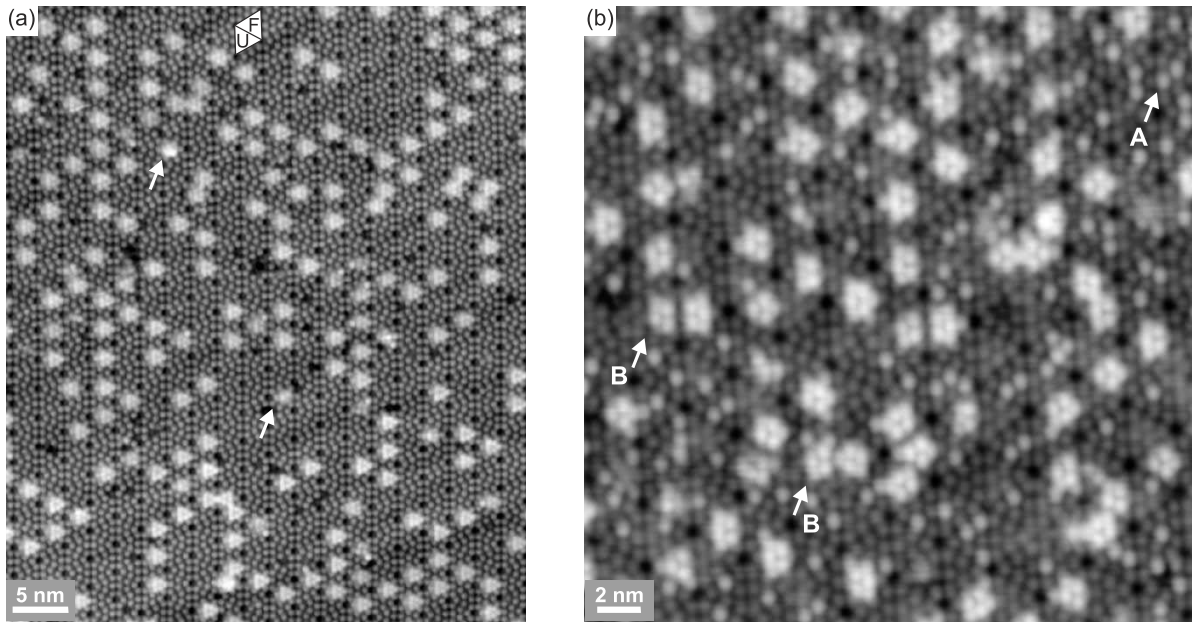


**Figure 6.1:** (a) Overview STM image of magic In clusters on the Si(111)7 $\times$ 7 surface formed with 0.06 ML In coverage deposited at 200 °C ( $V_S = +2.0$  V;  $I_T = 100$  pA). In the image, the orientation of the FHUC (F) and the UFHUC (U) is indicated and two anomalous clusters are exemplarily marked by the white arrows. (b) Overview STM image of a sample prepared using incorrect preparation conditions ( $V_S = +1.4$  V;  $I_T = 100$  pA). As exemplarily indicated by the white arrows, a large number of Si adatoms of the Si(111)7 $\times$ 7 surface has been substituted by In adatoms (A) and many defective clusters form (B).

for Sb in the previous chapter. However, for the group-III metal In the dangling bonds at these atoms are completely unoccupied in contrast to the Si adatoms where they are partly occupied. Hence, the brighter appearing adatoms in Fig. 6.1 (b) can be assigned to In adatoms that did not form magic clusters due to the incorrect preparation conditions, but substituted Si adatoms of the 7 $\times$ 7 reconstruction. The difference between the preparations shown in Fig. 6.1 (a) and (b) might be the result of a malfunction in the pick-a-back construction, maybe caused by an inefficient heat transfer from the underlying highly doped wafer or by a direct heating of the actual Si(111) sample.

Another feature of the growth of the magic In clusters is their strong preference for occupying the faulted half unit cell of the 7 $\times$ 7 surface [10, 238, 279]. This is also the case in Fig. 6.1 (a), where the orientation of the FHUC and the UFHUC is indicated by F and U, respectively. By counting the clusters in several STM images for the shown preparation it was found that 88% of the clusters formed in FHUCs. As it was done for the ringlike Sb clusters in the previous chapter, the difference in the formation energies for magic In clusters in the FHUC and the UFHUC is calculated by employing the Boltzmann distribution (Eq. 5.1). For the above mentioned preparation conditions, an energy difference of  $\Delta E = (0.08 \pm 0.01)$  eV is obtained. This agrees well with former studies, where also an energy difference of 0.08 eV was found as well as with theoretical calculations, where  $\Delta E = 0.1$  eV was derived.

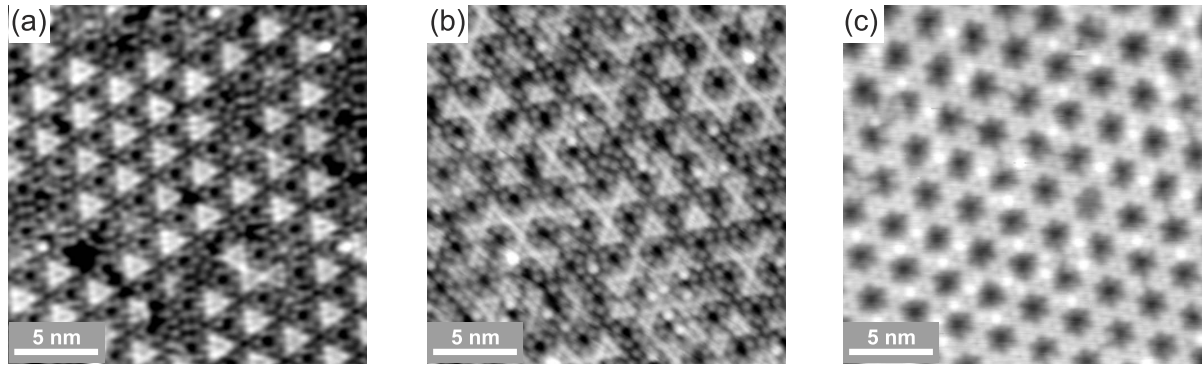


**Figure 6.2:** STM images of the magic In clusters on Si(111)7 $\times$ 7 prepared using a growth temperature of 200 °C and In coverages of (a) 0.11 ML ( $V_S = +1.0$  V;  $I_T = 100$  pA), (b) 0.15 ML ( $V_S = +1.0$  V;  $I_T = 100$  pA), and (c) 0.24 ML ( $V_S = +2.0$  V;  $I_T = 100$  pA).

The preferential formation in FHUCs persists also for higher coverages. In Fig. 6.2, a series of STM images showing Si(111) samples with increasing In coverage is shown. The coverage of 0.11 ML shown in Fig. 6.2 (a) corresponds to 5.4 atoms per 7 $\times$ 7 unit cell and, indeed, a magic In<sub>6</sub>Si<sub>3</sub> cluster is found in almost every unit cell. Even for this high coverage, still 87% of them formed in an FHUC. Only when the coverage exceeds one cluster per 7 $\times$ 7 unit cell, the UFHUCs become occupied with clusters more frequently, as shown in Fig. 6.2 (b) for a coverage of 0.15 ML. Finally, for a coverage of 0.24 ML corresponding to 12 atoms and therewith to two clusters per unit cell, all HUCs are covered with magic clusters as shown in Fig. 6.2 (c). This selectivity for the different HUCs of the 7 $\times$ 7 reconstruction offers the possibility to grow two different types of two-dimensional arrays of clusters, one for 0.12 ML In where all FHUCs are covered with magic clusters, and one for 0.24 ML In with every HUC covered with a magic cluster as shown in Fig. 6.2 (c).

### 6.1.2 Electronic properties

From former STS and PES studies it is known that the magic In clusters show a semiconducting behavior [10, 293, 296]. Thereby, an asymmetric band gap of about 0.8 eV with its center located about 0.2-0.3 eV below the Fermi level was found in Ref. [293]. However, detailed STS measurements were only reported for a single magic In cluster, presumably formed within an FHUC [293].

Here, voltage dependent STM images as well as STS measurements for clusters forming in both UFHUCs and FHUCs are analyzed in detail to obtain information, if there is a difference in their electronic properties. In addition, it is investigated how the electronic properties change, when groups of clusters form in neighboring HUCs.

A series of voltage dependent STM images of two magic In clusters, one formed within an FHUC (marked by the red triangle), the other formed within an UFHUC (marked by the black triangle), is shown in Fig. 6.3. As described already in section 3.5.1, the clusters appear as centered triangles within the corresponding HUC in both the filled and the empty states STM images. In the filled states, a smaller triangle with no further structuring is observed.

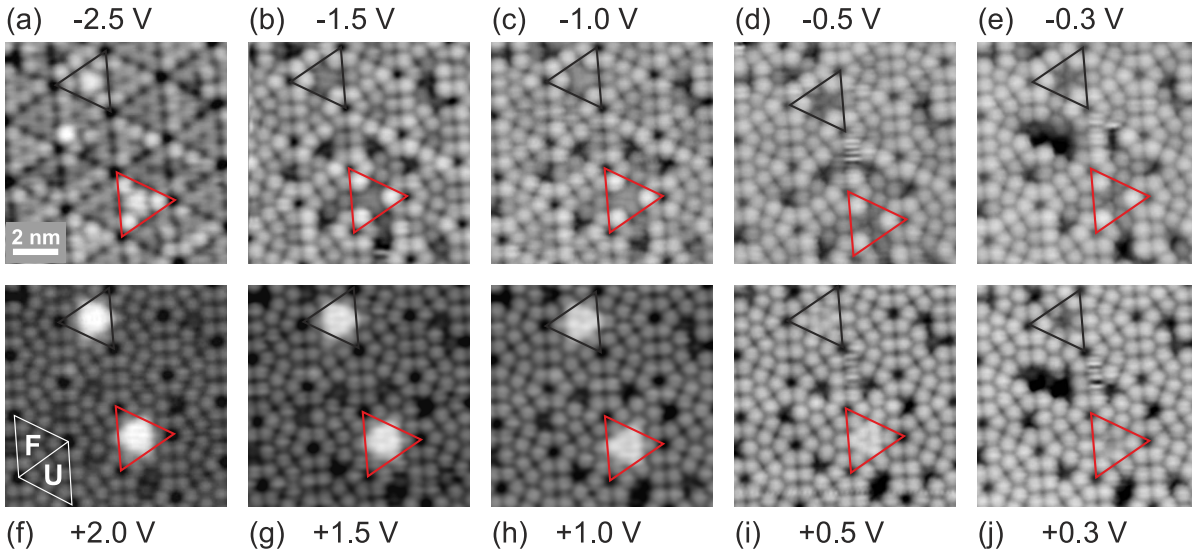


**Figure 6.3:** Voltage dependent (a-e) filled states and (f-j) empty states STM images of two magic In clusters. The cluster marked by a red triangle formed within a faulted half unit cell (F), while the cluster marked by the black triangle formed within an unfaulted half unit cell (U).

When comparing the position of this triangle with the structure model shown in Fig. 3.15 (a), it appears at the locations of the Si atoms. In contrast, in the empty states STM images the clusters appear as larger hollow triangles formed by six spots, which appear at the locations of the In atoms. Hence, due to the charge transfer from In to Si, the filled states are mainly located at the Si atoms, while the empty states are located at the In atoms.

However, the appearance also strongly changes with the absolute value of the tunneling voltage. When the tunneling voltage is decreased, the apparent height of the cluster decreases in both the filled and the empty states images. This behavior is especially obvious in the empty states images shown in (f-j), where the clusters appear much higher than the surrounding  $7 \times 7$  surface for tunneling voltages between +2.0 V and +1.0 V, while for a tunneling voltage of +0.3 V [Fig. 6.3 (j)] both clusters appear lower than the surrounding surface. The same is in principle observed in the filled states images (a-e), although the effect sets in already at higher absolute voltages. This behavior already shows a lower density of states of the cluster in this range of the tunneling voltages with respect to the Si(111) $7 \times 7$  surface, strongly indicating a semiconducting behavior. Using STS, this assumption will be verified and further quantified later in this section.

However, the images shown in Fig. 6.3 contain some more features that need to be discussed. First, the clusters formed on the different HUCs clearly show differences in their apparent height. Especially for a low positive sample voltage such as in (i) and (j), the cluster in the FHUC appears brighter than the cluster formed in the UFHUC. Hence, the HUC in which the clusters form influences their electronic properties, and a smaller band gap is indicated for the clusters formed within FHUCs.

Second, the voltage dependent STM images offer a deeper insight into the redistribution of charge that takes place on this surface. Thereby, several deviations from the clean Si(111) $7 \times 7$  surface are observed. First, the corner adatoms in HUCs containing magic In clusters appear

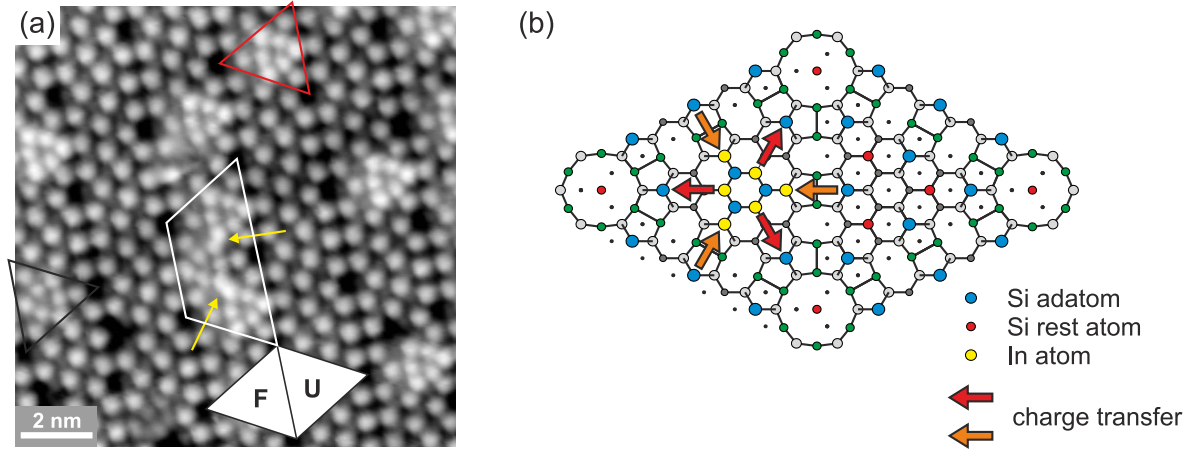


**Figure 6.4:** (a) Empty states STM image of a sample with a coverage of 0.06 ML In deposited at 200 °C ( $V_S = +1.0$  V;  $I_T = 100$  pA). In the image, magic In clusters formed in different surroundings. Thereby, single clusters formed within an UFHUC and an FHUC are exemplarily marked by a black and a red triangle, respectively, while  $7 \times 7$  HUCs with neighboring clusters are marked by the white trapezoid. The yellow arrows exemplarily indicate corner In cluster atoms neighboring other clusters. (b) Atomic structure model for a magic In cluster formed within an FHUC of the Si(111) $7 \times 7$  reconstruction illustrating the charge transfer processes. The red arrows illustrate a charge transfer from the cluster into the Si corner adatoms, the orange arrows a charge transfer from Si center adatoms in neighboring HUCs into the cluster.

brighter than those in bare  $7 \times 7$  HUCs in the filled states STM images such as Fig. 6.3 (b). On the clean Si(111) $7 \times 7$  surface, a charge transfer from the Si corner adatoms to the rest atoms is observed [183, 190, 376]. As a consequence, the rest atom dangling bonds become completely filled and are energetically positioned far below  $E_F$ . However, during the growth of the magic In cluster, covalent In-Si bonds are formed between the rest atoms and the In atoms of the cluster. Hence, a back transfer of charge from the rest atoms or rather the magic cluster into the dangling bonds of the Si corner adatoms may be expected, explaining the enhanced brightness. In Fig. 6.4 (b), the processes of charge redistribution are schematically illustrated. Herein, the discussed back transfer of charge from the cluster into the corner adatoms is indicated by the red arrows.

As a second effect, the center Si adatoms in HUCs of the bare Si(111) $7 \times 7$  reconstruction, which are neighboring HUCs containing a magic cluster, are also influenced. In the filled states images such as Fig. 6.3 (b-e), these adatoms appear slightly darker than unaffected Si center adatoms. In contrast, in empty states images as those shown in (f,g), their height appears slightly increased. This behavior suggests a charge transfer from neighboring unit cells into the magic In clusters as indicated by the orange arrows in Fig. 6.4 (b).

These observations, pointed out here on the basis of voltage dependent STM images, are in nice agreement with the atomically resolved STS measurements performed by Byun *et al.* [293], where similar charge redistribution processes are observed.

However, the transfer of charge from neighboring bare  $7 \times 7$  HUCs raises the question what is occurring during the formation of a complete two-dimensional array of magic clusters, in which

all HUCs become occupied by magic clusters [cf. Fig. 6.2 (c)]. Then, the situation should change since the Si center adatoms, which usually donate charge to the neighboring magic clusters, are no more present, but themselves take part in the cluster formation. To explore these effects in more detail, Fig. 6.4 (a) shows an empty states STM image of an area, in which single clusters in both HUCs as well as several adjacent clusters are found. As in Fig. 6.3, the single clusters formed within FHUCs (exemplarily indicated by a red triangle) appear brighter than the cluster formed within an UFHUC (black triangle). However, the more interesting region here is the one in the center of the image marked in white, where two clusters in FHUCs and one cluster in an UFHUC formed directly besides each other. In the shown empty states image, the In cluster atoms in the corners neighboring clusters in the adjacent HUCs (marked by the yellow arrows), appear slightly brighter than those with neighboring uncovered  $7 \times 7$  HUCs. This might in fact be explained by a decreased charge transfer from the neighboring HUCs, where the former Si center adatoms that might have partly transferred their charge into the cluster are no more present since they are themselves incorporated into magic clusters.

The situation discussed here represents in principle the early stages of the formation of an ordered two-dimensional array of magic clusters and may thus be a model system to study the changes in the electronic structure that may occur during the transition from isolated clusters to two-dimensional arrays of identical clusters. To investigate these processes, STS is the ideal method. Hence, STS spectra were taken on magic In clusters with different surroundings, as shown in Fig. 6.5. In their atomically accurate STS measurements, Byun *et al.* [293] could not find a large difference in the electronic properties for the different sites within the magic In clusters. Thus, in this work, all spectra were taken in the center of the clusters as indicated in the inset in (a). Besides current-voltage ( $I$ - $V$ ) curves,  $dI/dV$ - $V$  spectra were simultaneously measured. Therefore, the tunneling voltage was modulated with a frequency of 1 kHz and a modulation amplitude of 50 mV. To stabilize the tunneling contact,  $V_S = -2.0$  V and  $I_T = 200$  pA were employed and, additionally, the tip was approached towards the sample by 150 pm during the acquisition of the spectra. The results measured on single In clusters in FHUCs and UFHUCs as well as on clusters in FHUCs neighboring other clusters (indicated by FHUC+) are shown in (a) and (b). Therein, each curve represents the average over at least 40 spectra taken on similar clusters.

All spectra show a region with zero intensity around the Fermi level. However, as already observed in the voltage dependent STM images discussed above, a clear difference between the spectra is observed. The current onset for single clusters in FHUCs occurs at lower absolute sample voltages than for the single clusters in UFHUC, while the spectra for clusters in FHUCs neighboring other clusters show an intermediate behavior. This behavior is in nice agreement with the voltage dependent STM images in Fig. 6.3, where the cluster in the FHUC appears brighter at low absolute tunneling voltage. However, in the  $dI/dV$ - $V$  spectra shown in (b), the band gap appears smaller and not as asymmetric as compared to the  $dI/dV$ - $V$  spectra published in [293]. For a more detailed discussion, Fig 6.5 (c) shows again the tunneling current curves already displayed in (a), but with logarithmic scaling, and (d) the normalized differen-

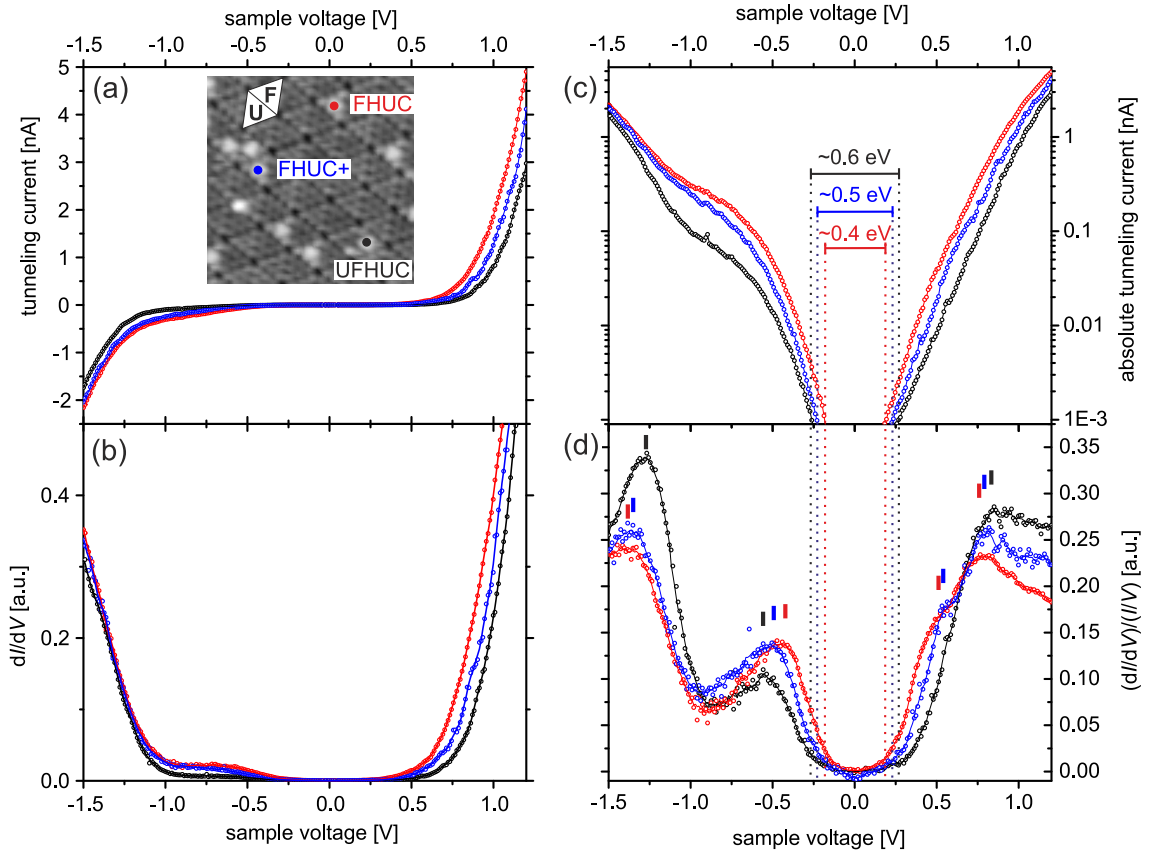


**Figure 6.5:** Scanning tunneling spectroscopy results for magic In clusters formed in different surroundings. As indicated exemplarily in the inset in (a), the red, black, and blue curves show spectra taken on an In cluster formed within FHUCs, UFHUCs, and FHUCs neighboring other clusters, respectively. (a) and (b) show the measured tunneling current curves and the differential conductivity, respectively. (c) Same as (a), but with logarithmic scaling. (d) Normalized differential conductivity. In (c) and (d), the estimated band gaps for the different spectra are indicated.

tial conductivity  $(dI/dV)/(I/V)$  calculated by using the procedure introduced by Prietsch *et al.* [77], as described in section 2.3.2.

In (d), four distinct spectral features at around  $-1.25$  V and  $-0.6$  V in the filled states, and at around  $+0.5$  V and  $+0.8$  V in the empty states are observed, as marked by bars in colors corresponding to the respective spectra. Thereby, the feature around  $+0.5$  V is not visible in the spectrum taken on single clusters in UFHUCs, while the other features are observed in all three spectra, although being slightly shifted in energy. As supposed above, the band gap differs for the clusters in the different surroundings. In (c) and (d), the sizes of the band gaps for the different spectra are estimated as illustrated by the dotted vertical lines. All three spectra show a band gap that appears symmetric around the Fermi level with estimated sizes of 0.4 eV, 0.5 eV, and 0.6 eV for the clusters formed within an FHUC, an FHUC neighboring other clusters, and an UFHUC, respectively. Hence, the band gap of the magic In clusters formed within FHUCs seems to increase when going from single clusters to an agglomeration of clusters.

This is exactly the opposite behavior one would expect from a simple model when molecules are brought together. Here, due to the coupling between the molecules, the molecular states should split into bonding and antibonding states for a combination of two molecules, while when adding more and more molecules, the formation of an electronic band structure should be observed, in analogy to the system shown in Fig. 3.3 (a). The explanation for the observed different behavior might be as follows: The single clusters in FHUCs are surrounded by three uncovered metallic UFHUCs which are assumed to reduce the band gap of the clusters. In contrast, the clusters with one neighboring covered UFHUC are only surrounded by two metallic HUCs, resulting in the larger observed band gap of the FHUC+ clusters.

However, for a more detailed understanding of these processes, the evolution of the electronic properties of the clusters formed within UFHUCs during the formation of such agglomerations needs to be investigated as well. Here, a similar behavior with an increase in the size of the band gap is expected, since the number of uncovered metallic FHUCs decreases in analogy to the case discussed above. Additionally, the evolution for agglomerations with increasing numbers of clusters should also be investigated. Unfortunately, within this work too little spectra could be measured on clusters in UFHUCs neighboring other clusters to obtain unambiguous results. In addition, STS measurements for different coverages including a complete array of clusters are also missing for a complete picture. This remains a challenge for future measurements.

It still needs to be discussed that the tunneling spectra obtained within this work differ from the ones obtained by Byun *et al.* [293], where a very asymmetric band gap with a larger size of 0.8 eV was observed, as shown in Fig. 3.17. The main differences are found in the filled states where the spectra taken on the clusters in Ref. [293] show an extended band gap region. However, at least for the curves F and G in Fig. 3.17, a slight intensity above zero seems to be present. Such an intensity might be caused by the feature at around  $-0.5$  V observed in Fig. 6.5 (d), and might be even better visible in the normalized differential conductivity which is not shown in Ref. [293]. Indeed, when directly comparing the  $dI/dV-V$  spectra shown in Fig. 6.5 (b) with those shown in Fig. 3.17, the spectra appear rather similar. The discussed difference, which might be also caused by different stabilization conditions, may explain both differences between that work and the present work, the symmetry of the band gap with respect to the Fermi level as well as its different size.

In the band gap region another behavior is noticeable. Although a clear band gap is observed in the spectra shown in Fig. 6.5, the local density of states in (d) does not show an abrupt drop to zero. This might be related to the metallic states from the adatoms of the Si(111) $7\times 7$  surface, that might tail into the band gap of the semiconducting clusters. Such metal-induced gap states (MIGS) or virtual gap states (VIGS) are well known to occur at semiconductor-metal interfaces [160, 162]. Since also the observed energetic positions correspond quite well with the positions where the adatom states of the Si(111) $7\times 7$  surface are found, it is concluded, that the observed intensity in the band gap region in Fig. 6.5 (d) results from MIGS or VIGS states that laterally penetrate into the band gap of the semiconducting In clusters.

## 6.2 Magic Ga clusters on the planar Si(111) surface

In addition to magic In clusters on Si(111)7×7, magic Ga clusters were investigated as a second system of group-III metal clusters within this work. As already pointed out in section 3.5.1, the magic clusters of In and Ga on the Si(111)7×7 surface are very similar, e.g. they exhibit an analogous atomic structure. Hence, the observations on the magic Ga clusters mostly resemble those on the magic In clusters described in the previous section. However, the general growth behavior shows some variations described in the following.

In contrast to the magic In clusters, magic Ga clusters form already after deposition of Ga at room temperature as shown in Fig. 6.6 (a). However, the growth is not yet that homogeneous, since besides the magic Ga clusters marked by A, also many irregular clusters form (marked by B). The formation of such irregular clusters can be almost completely suppressed by using a growth temperature around 300 °C, as it is shown in (b). Here, the almost exclusive formation of magic Ga clusters is found, similar to the case of the magic In clusters discussed in the previous section.

Again, the clusters show a preference of occupying the FHUCs of the 7×7 reconstruction. However, as it is already known from earlier studies [7, 238, 279], the preference is by far not as strong as for the magic In clusters. At low coverages as shown in Fig. 6.6 (b), about 60% of the clusters are found in FHUCs. From this value, the difference in the formation energies between FHUC and UFHUC can be estimated for the Ga clusters as it was also done in the previous section for the In clusters by using Eq. 5.1. For the preparation mentioned above, a value of  $\Delta E = (0.02 \pm 0.01)$  eV is obtained. Due to this rather small difference it is not possible to produce an ordered two-dimensional array of magic Ga clusters with almost exclusively the

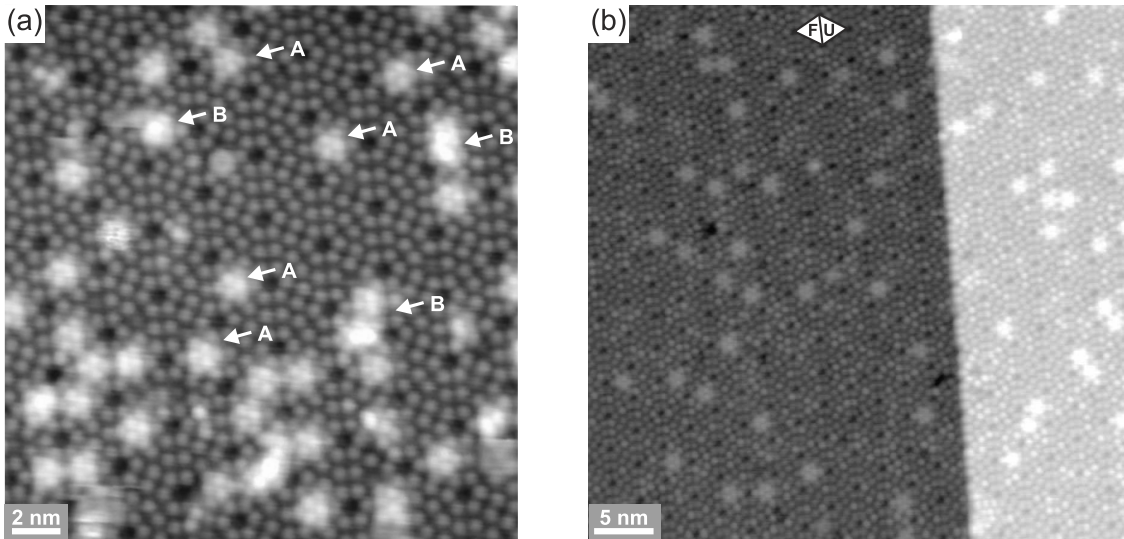


**Figure 6.6:** Overview STM images of Ga clusters formed by depositing (a) 0.03 ML Ga at room temperature ( $V_S = +2.0$  V;  $I_T = 100$  pA) and (b) 0.05 ML Ga at 300 °C ( $V_S = +2.0$  V;  $I_T = 50$  pA). In (a), magic Ga clusters are exemplarily marked by A, while irregular clusters are marked by B. In (b), the FHUC and UFHUC of the 7×7 reconstruction are indicated by F and U, respectively.

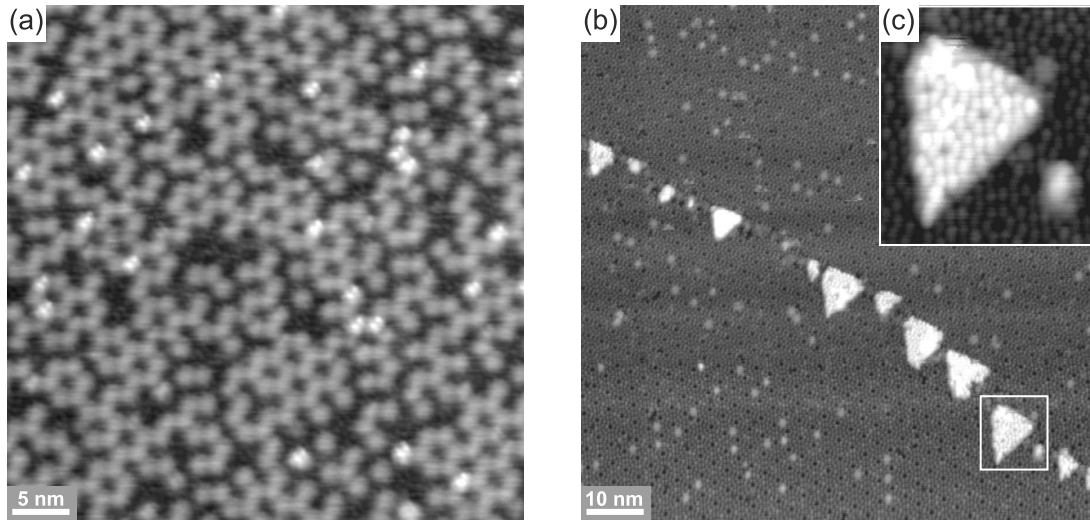


**Figure 6.7:** (a) Overview STM image of magic Ga clusters formed by depositing 0.18 ML Ga at 300 °C ( $V_S = +2.0$  V;  $I_T = 50$  pA). (b) Overview STM image of magic Ga clusters formed by depositing 0.03 ML Ga at 300 °C ( $V_S = +2.0$  V;  $I_T = 100$  pA). (c) Enlarged view of the area marked by the white rectangle in (b).

FHUCs being occupied, as it was demonstrated for the magic In clusters [cf. Figs. 3.16 (b) and 6.2 (a)].

However, the preparation of the complete array with clusters forming in both the FHUCs and the UFHUCs is possible. As an example for an almost complete array, Fig. 6.7 (a) shows an STM image of a Si(111)7×7 sample with a Ga coverage of 0.18 ML.

Besides the magic Ga clusters, also islands are occasionally found on the surface as in Fig. 6.7 (b). A more detailed inspection of these islands reveals that 5×5, 7×7, and 9×9 DAS reconstructions (cf. section 3.2.1) form on their surface [see Fig. 6.7 (c)]. Hence, these islands represent additional Si islands that formed during the growth of the magic Ga clusters. As it was already observed earlier [287], the tendency to substitute adatoms of the Si(111)7×7 reconstruction is much stronger than for In. This is most probably related to the higher growth temperature of 300 °C in comparison to 200 °C for the magic In clusters. Hence, it may be assumed that the Si islands observed in Fig. 6.7 (b) form from Si atoms that are released due to the substitution of Si adatoms by Ga atoms.

In Fig. 6.8, the adatom substitution is shown in more detail. As it was already argued for the In clusters in section 6.1.1, adatoms substituted by Ga atoms appear brighter than common Si adatoms in empty states STM images such as Fig. 6.8 (a), while they appear darker in filled states STM images such as (b). In the STM images shown in (a) and (b), several magic Ga clusters with different numbers of substituted neighboring adatoms are found, as indicated by the colored triangles. Thereby, white triangles mark HUCs, in which a common magic cluster without any additional substituted adatoms has formed. In contrast, in the clusters marked by the red triangle and the red diamond, one corner Si adatom is substituted with a Ga atom, as it is shown in the atomic structure model displayed in (c). In the cluster marked by the

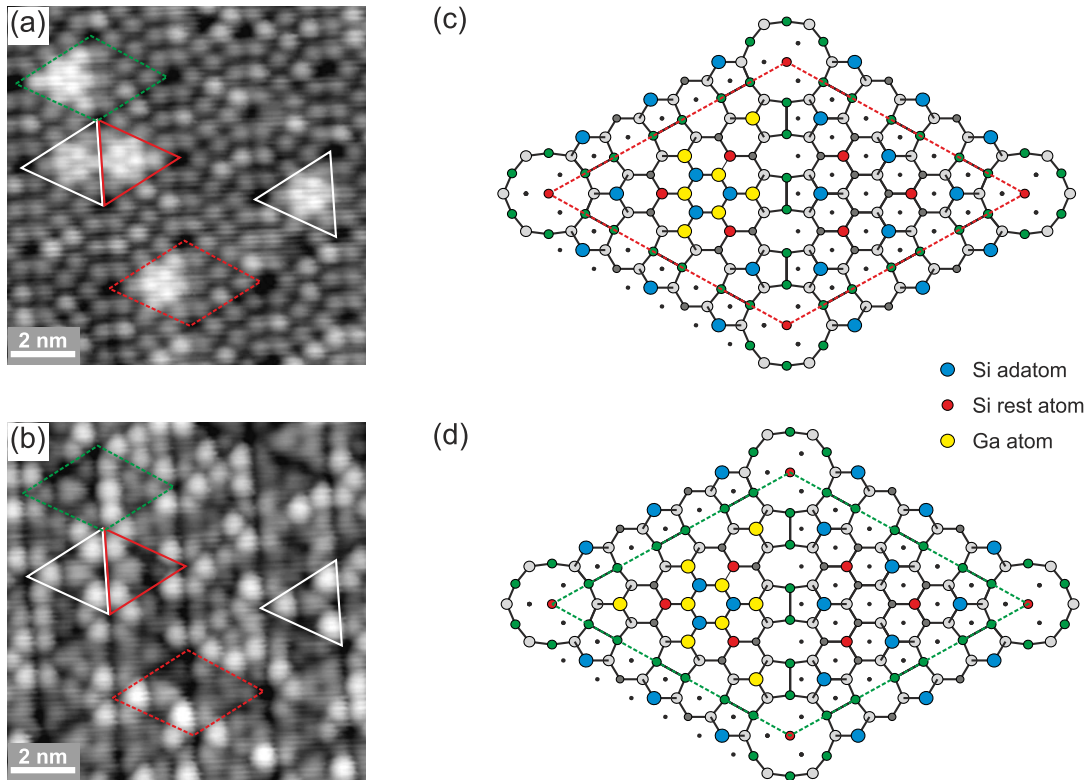


**Figure 6.8:** (a) Empty states STM image ( $V_S = +2.0$  V;  $I_T = 50$  pA) and (b) filled states STM image ( $V_S = -1.5$  V;  $I_T = 50$  pA) of the same area with magic Ga clusters formed by depositing 0.05 ML Ga at 300 °C. (c,d) Atomic structure models showing the situation in the unit cells indicated in (a,b) by (c) the red diamond and (d) the green diamond, respectively.

green diamond even all three corner adatoms are substituted, as shown in the structure model in Fig. 6.8 (d).

### 6.3 Magic In clusters on the Si(557) surface

As shown in the previous sections, two-dimensional arrays of magic Ga and In clusters can easily be produced using the Si(111)7×7 surface as a template. In this section, the possibility to prepare ordered one-dimensional arrays of these clusters is analyzed. Using domain boundaries on a Si(111)-Ge(5×5) surface, a one-dimensional ordering of magic In and Ga clusters was already achieved [17]. However, since the domain boundaries are more or less randomly distributed on the surface, the ordering is achieved only locally. A much better ordering is expected when using a vicinal surface with a regular step array. Here, the clusters may form at the step edges, resulting in one-dimensional chains of clusters. This approach was successfully demonstrated for Si and Ge clusters, where chains consisting of clusters with different sizes were found to grow at the upper step edges of slightly tilted Si(111) substrates [18–20].

The Si(557) surface is expected to be an especially promising substrate, since it forms an ordered array of alternating Si(111) terraces with a width of one unit cell of the 7×7 reconstruction and triple steps (cf. section 3.2.2). Hence, it might be possible to grow equally spaced cluster chains with a width of a single cluster. Since In offers the possibility to grow

two different types of two-dimensional arrays (cf. sections. 3.5.1 and 6.1.1), it is the material of choice within this work.

Recently, it has been demonstrated that it is possible to grow nanowire systems with very interesting properties by using the Si(557) surface as a template. One example are one-dimensional plasmons in arrays of Au atomic wires [379], but also nanowires formed after deposition of Pb [380, 381], Dy [158, 334, 382], and In [383–385] were studied. Regarding In on Si(557), submonolayer coverages deposited at room temperature lead to the formation of atomic wires at the steps of the reconstructed Si(557) surface [384], while deposition at higher temperatures resulted in a restructuring of the surface into the bulk terminated Si(557) structure and the formation of a  $1 \times 3$  nanowire phase [383]. However, the preparation conditions for which an ideal growth of magic clusters is expected, remained unexplored.

Since the structure of the underlying substrate plays a crucial role as it represents the template, on which the growth of magic In clusters takes place, at first STM measurements of the bare Si(557) surface are presented in the following section. Afterwards, the results regarding the formation of magic In clusters on Si(557) are discussed.

### 6.3.1 The clean Si(557) surface

An overview STM image of a clean Si(557) sample is shown in Fig. 6.9 (a). The surface shows a well ordered array with steps running along the  $[\bar{1}10]$  direction. Mainly equally spaced terraces appear. However, also some broader terraces are present in the image and a larger substrate step appears at the bottom of the image. The bowing of the terraces observed in the lower part of the image is related to thermal drift present during data acquisition.

For a more detailed look on the precise structure of the surface reconstruction, atomically resolved STM images of an area with a particularly large amount of irregular Si(111) terraces are shown in Fig. 6.9 (b) and (c). These irregular Si(111) terraces do not contain a single  $7 \times 7$  unit cell, as it is expected for the perfectly ordered Si(557) surface (cf. section 3.2.2). The presence of such irregularities was already observed in earlier studies [203, 205, 208]. Among others, Si(111) terraces containing two  $7 \times 7$  unit cells instead of one and Si(111) terraces with a  $5 \times 5$  reconstruction instead of a  $7 \times 7$  reconstruction were observed. These two types of irregularities are also observed in Fig. 6.9 (b) where the respective structures forming on the Si(111) terraces are indicated. Here, Si(111) terraces containing either two  $7 \times 7$  or two  $5 \times 5$  unit cells are found frequently.

The terraces indicated with  $7 \times 7$  represent regular Si(557) unit cells with one  $7 \times 7$  unit cell forming on the Si(111) terrace. For a more detailed analysis, an enlarged view of the area indicated by the white rectangle in (b) is shown in (c) and a height profile along the blue line in (d). In this profile, a Si(111) terrace and a triple step are exemplarily marked by the green and red dotted lines, respectively. In addition, the width of the Si(557) reconstruction formed in different regions is analyzed. As indicated in (d), the Si(557) unit cells in the middle of the image show a width of  $(16 \pm 0.3)$  atomic rows. This width is in accordance with the structure model proposed by Teys *et al.* [205], in which the step structure consists of a combination of a



double and a single step, while other structure models [203, 206] predict a width of 17 atomic row (see also section 3.2.2). In these models, the triple step forms a Si(112) terrace consisting of three narrow  $2\frac{2}{3}$  atomic rows wide Si(111) terraces. In the images presented in (b) and (c), there is no indication for such a faceting. Only one additional bright row is sometimes found right to the Si(111) facet as indicated by the yellow arrows. The observation of such a row is also in good agreement with the atomically resolved images published in Ref. [205], where it is assigned to an additional row of Si adatoms forming on the upper step terrace [cf. Fig. 3.10 (b,c)]. Thus, indications are found in the STM images that the Si(557) surface observed here may be described by the structure model proposed in Ref. [205]. However, maybe due to slightly different preparation conditions as compared to Ref. [205], also unit cells showing a different faceting are observed. Besides the irregularities described above, also Si(557) unit cells with widths different from 16 atomic rows are found, as it is indicated exemplarily in Fig. 6.9 (d). Hence, due to the different forming structures, it is not possible to describe the surface observed here by one specific atomic structure. A large sensitivity of the forming reconstruction on the preparation conditions was also found by Chaika *et al.* [209]. However, for investigating the possibility to grow one-dimensional arrays of magic In clusters, the detailed surface structure should not be that important as long as Si(111) terraces with a width of a single  $7\times 7$  unit cell form, as it is predominantly the case.

### 6.3.2 Growth of magic In clusters on Si(557)

An example for In growth on the Si(557) surface is shown in Fig. 6.10. For the growth, similar preparation conditions as for the magic In clusters on the planar Si(111) surface, i.e. a growth temperature of 200 °C, were employed. At first sight, the surface looks very similar to the clean Si(557) surface shown in Fig. 6.9, solely a larger number of bright structures, presumably In deposits, is visible. Particularly, still a  $7\times 7$  reconstruction is found on the Si(111) terraces and the faceting appears very similar to the clean surface, with most Si(111) terraces showing a width of a single  $7\times 7$  unit cell and only few Si(111) terraces with other structures such as two unit cells wide  $7\times 7$  or  $5\times 5$  reconstructions, as indicated in (a). However, a restructuring of the reconstructed Si(557) surface is neither expected due to the rather low growth temperature nor desired, since the narrow Si(111) terraces shall represent a template for a one-dimensional ordering of the magic In clusters. Hence, the Si(557) surface seems to fulfill the basic requirements that are necessary for a one-dimensional ordering of the magic In clusters.

However, it is difficult to see from overview images such as Fig. 6.10 (a) if there are really magic In clusters forming on the surface. Therefore, (b) and (c) show more detailed high resolution filled states STM images of the regions marked by the white and yellow rectangles in (a), respectively. And indeed, clearly magic In clusters showing an identical appearance as on the planar Si(111) surface are found on Si(111) terraces with a  $7\times 7$  reconstruction, as demonstrated in (b) and (c). Similar to the planar surface, a strong preference of the FHUC is observed, although also clusters in UFHUCs are found, as indicated in (c). The triangular contrast in the filled states image is mainly caused by the three Si atoms in the center of

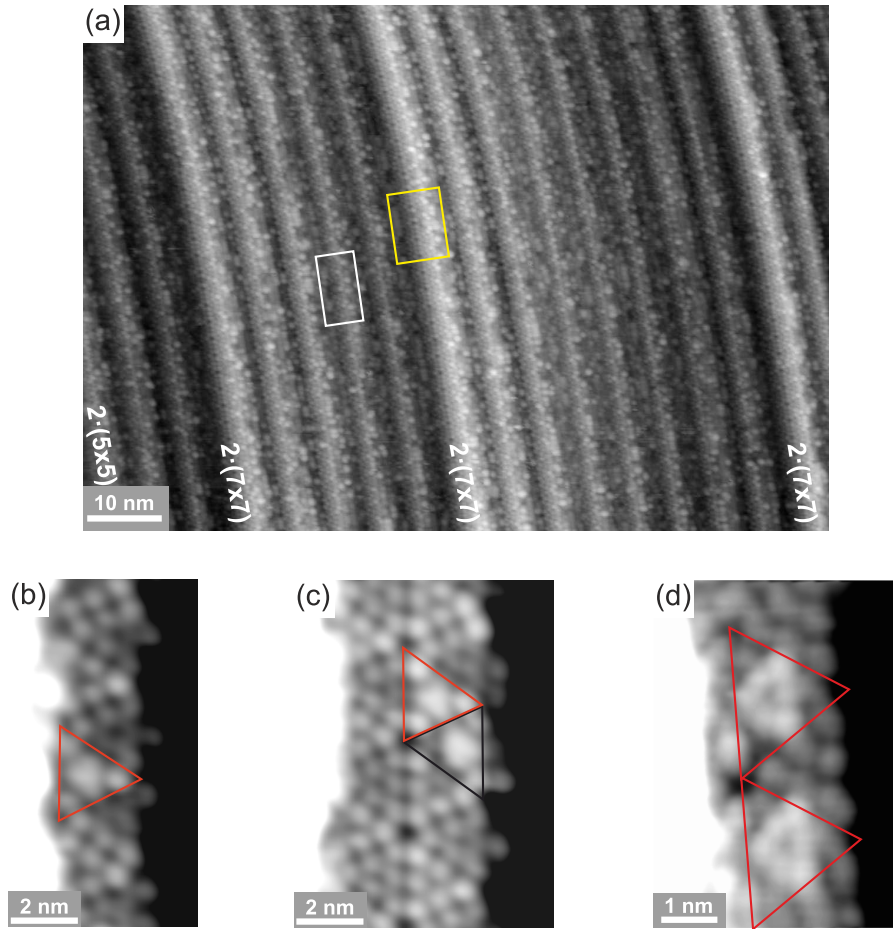


**Figure 6.10:** (a) Overview and (b,c) detailed filled states STM images ( $V_S = -2.5$  V;  $I_T = 100$  pA) of a Si(557) sample with nominally 0.26 ML In deposited at 200 °C. (b) and (c) show the regions marked by the white and yellow rectangles in (a), respectively. (d) Empty states STM image of a Si(557) sample with nominally 0.30 ML In deposited at 200 °C ( $V_S = +1.2$  V;  $I_T = 100$  pA). In (b-d), magic In clusters formed in FHUCs and an UFHUC are indicated by red and black triangles, respectively.

the cluster, since a charge transfer from In to Si occurs as pointed out already earlier in the theoretic background part (see section 3.5.1). To identify, if really identical clusters as on the planar Si(111) surface form, empty states images need to be analyzed as well. Therefore, Fig. 6.10 (d) shows such an empty states image taken on another sample. In this image, two clusters formed within FHUCs. For both clusters, clearly the six bright spots corresponding to the six In atoms of the magic clusters are resolved. Thus, it is concluded that indeed identical  $\text{In}_6\text{Si}_3$  clusters as on the planar Si(111) surface, as described by the structure model shown in Fig. 3.15, grow on the Si(557) surface.

### One-dimensional ordering of magic In clusters on Si(557)

As the growth of magic In clusters on Si(557) was successfully demonstrated in the previous section, now the formation of one-dimensional cluster arrays is investigated. Therefore, Fig. 6.11 shows STM images of an In coverage series on Si(557). For a better visibility of the clusters, the images are leveled with the Si(111) facets being parallel to the image plane. In addition,

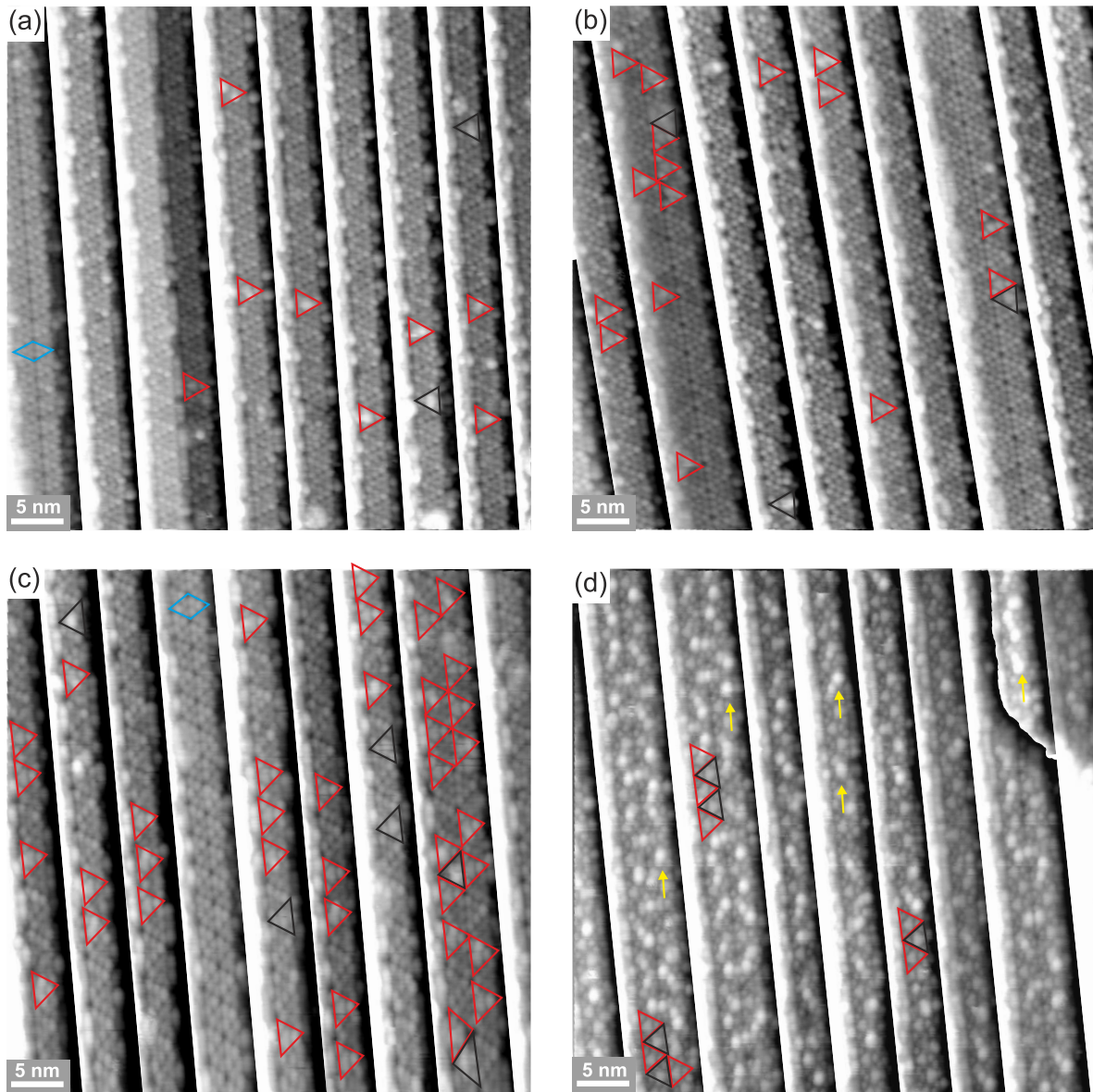


**Figure 6.11:** Overview filled states STM images of Si(557) samples with nominal In coverages of (a) 0.20 ML ( $V_S = -2.5$  V;  $I_T = 100$  pA), (b) 0.26 ML ( $V_S = -2.5$  V;  $I_T = 100$  pA), (c) 0.30 ML ( $V_S = -2.5$  V;  $I_T = 100$  pA), and (d) 0.40 ML ( $V_S = -1.5$  V;  $I_T = 100$  pA) and growth temperatures of 200 °C. For a better representation, the Si(111) facets are leveled and different greyscales are applied for the different (111) terraces. In the images, magic In clusters formed in FHUCs and UFHUCs are indicated by red and black triangles, respectively, and  $5 \times 5$  unit cells are exemplarily marked by the blue rhombus. In (d), a complete array of magic In clusters is obtained. Here, the yellow arrows mark additional bright spots appearing on top of magic In clusters.

different greyscales are applied for the different facets. For a direct comparison, all images are of the same size, and magic In clusters forming in FHUCs and UFHUCs are again marked by red and black triangles, respectively.

From (a) to (c), the cluster density increases with increasing coverage until, as shown in (d), a complete array with both the FHUCs and the UFHUCs being covered with magic In clusters is obtained. In (d), even more In than necessary for a complete array may be present

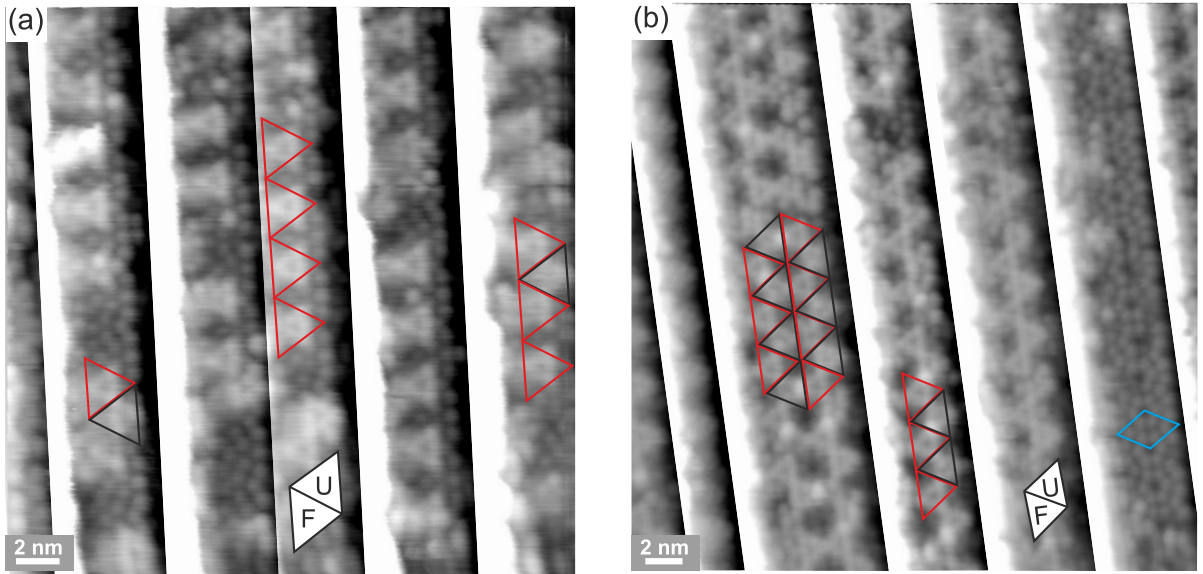


**Figure 6.12:** Empty states STM images of (a) an almost complete one-dimensional array with only the FHUCs being covered by magic clusters, prepared using a nominal In coverage of 0.34 ML and a growth temperature of 200 °C ( $V_S = +1.8$  V;  $I_T = 100$  pA), and (b) a complete one-dimensional array with both the FHUCs and the UFHUCs covered with magic clusters (0.40 ML In deposited at 200 °C;  $V_S = +1.3$  V;  $I_T = 100$  pA). In the images, the Si(111) facets are again leveled and different greyscales are applied for the different (111) terraces. In both images, the orientation of the FHUC and the UFHUC is indicated by F and U, respectively. In addition, in (b), a  $5 \times 5$  unit cell is marked by the blue rhombus.

on the surface, since on many clusters additional bright spots are found, as marked exemplarily by the yellow arrows.

In Fig. 6.11 (a) and (c), also  $5 \times 5$  reconstructed Si(111) facets are present. In contrast to the  $7 \times 7$  reconstruction, no formation of magic clusters is found here. This can be easily understood, when comparing the two DAS reconstructions. In the  $5 \times 5$  reconstruction, only three adatoms and one rest atom is found in each HUC instead of six and three for a  $7 \times 7$  HUC, respectively. Thus, all adatoms of the  $5 \times 5$  reconstruction are corner adatoms. Hence, a formation of clusters with a similar structure as on the  $7 \times 7$  surface is not possible on this surface. This is in nice analogy to the findings of Mark and Lean [17], where the growth of magic In and Ga clusters on Ge- $5 \times 5$  domains on Si(111) was studied, resulting in an exclusive formation of clusters on  $7 \times 7$  domains as well as at domain boundaries between different  $5 \times 5$  domains, which show a local environment similar to the  $7 \times 7$  reconstruction.

As demonstrated in Fig. 6.12, the high preference of the magic In clusters to form in FHUCs offers the possibility to grow two different types of one-dimensional arrays, in analogy to the two types of two-dimensional arrays on the planar Si(111) surface (cf. sections 3.5.1 and 6.1.1). In (a), almost all FHUCs are occupied with magic In clusters, in analogy to the so called half-covered array on the planar surface. Here, linear chains of identical clusters are found to form along the  $[\bar{1}10]$  direction on the Si(111) terraces of the Si(557) surface with a distance between the centers of neighboring clusters being equal to the edge length of a  $7 \times 7$  unit cell of

2.69 nm. In contrast, in (b) almost all HUCs are covered with magic In clusters resulting in the formation of a one-dimensional array in analogy to the complete two-dimensional array on the planar Si(111) surface. Again linear cluster chains form along the  $[\bar{1}10]$  direction, but different from the half-covered array, the chains consist of two nonequivalent cluster types, magic clusters in FHUCs and in UFHUCs. The distance between the centers of two neighboring clusters is reduced to 1.55 nm. As found in section 6.1, the clusters forming in FHUCs and UFHUCs also exhibit different electronic properties. In addition with the different coupling strength, that is expected due to the different distances between neighboring clusters, the two different types of one-dimensional arrays may enable a possibility to adjust the electronic properties of such cluster chains.

### Initial states of In growth on the Si(557) surface

When comparing the In coverages needed for the growth of magic In clusters on the Si(557) surface (see e.g. Fig. 6.11) with those used on the planar Si(111) surface, it is found that much more In has to be deposited until a formation of magic clusters is observed. In Fig. 6.11 (a), 0.20 ML of In were deposited, a coverage for which, on the planar Si(111) surface, almost all HUCs are already covered with magic clusters (cf. e.g. Fig. 6.2). In contrast, on the Si(557) surface magic clusters form only rarely at this coverage. The further growth seems to roughly resemble the growth on the planar surface, since the difference between 0.20 ML and the coverage of 0.40 ML, where a complete array is observed [see Fig. 6.11 (d)], is in good agreement to the respective value on the planar Si(111) surface, where an In coverage of 0.24 ML is needed for a complete array. Thus, a different growth behavior for the initial states of In on the Si(557) is found in comparison to In on the Si(111) surface. Since the two surfaces differ mainly in the density and structure of surface steps, the difference may be assigned to the presence of the steps.

Indeed, Shin *et al.* reported the formation of atomic wires on the triple steps of the Si(557) surface for 0.01 ML In deposited at room temperature [384]. However, in experiments with In deposition on the Si(557) surface at room temperature in the present work, only disordered larger clusters are observed as shown in Fig. 6.13 (a) for 0.10 ML In. After the sample shown in (a) was additionally annealed at 200 °C, the reconstructed Si(557) surface again appears nicely ordered. A closer look indeed reveals that at some areas the formation of additional structures at the steps appears, as indicated by the arrows. These additional structures may represent the starting growth of atomic wires similar to those proposed in Ref. [384]. For a more detailed analysis, (c) and (d) show STM images prepared using the preparation method commonly used within this work, i.e. deposition of In on the sample held at growth temperature. For the coverage of 0.06 ML In shown in (c), no magic In clusters are found on the surface, but again the steps appear different from the bare Si(557) surface (cf. Fig. 6.9). Here, again the beginning formation of chains may be present as indicated by the white arrows. For comparison, (d) shows an STM image of a coverage of 0.26 ML In where magic In clusters are already found occasionally on the surface as exemplarily indicated by the triangles. At this coverage, clearly lines with a similar appearance to the atomic wires reported by Shin *et al.* [384] appear. Also

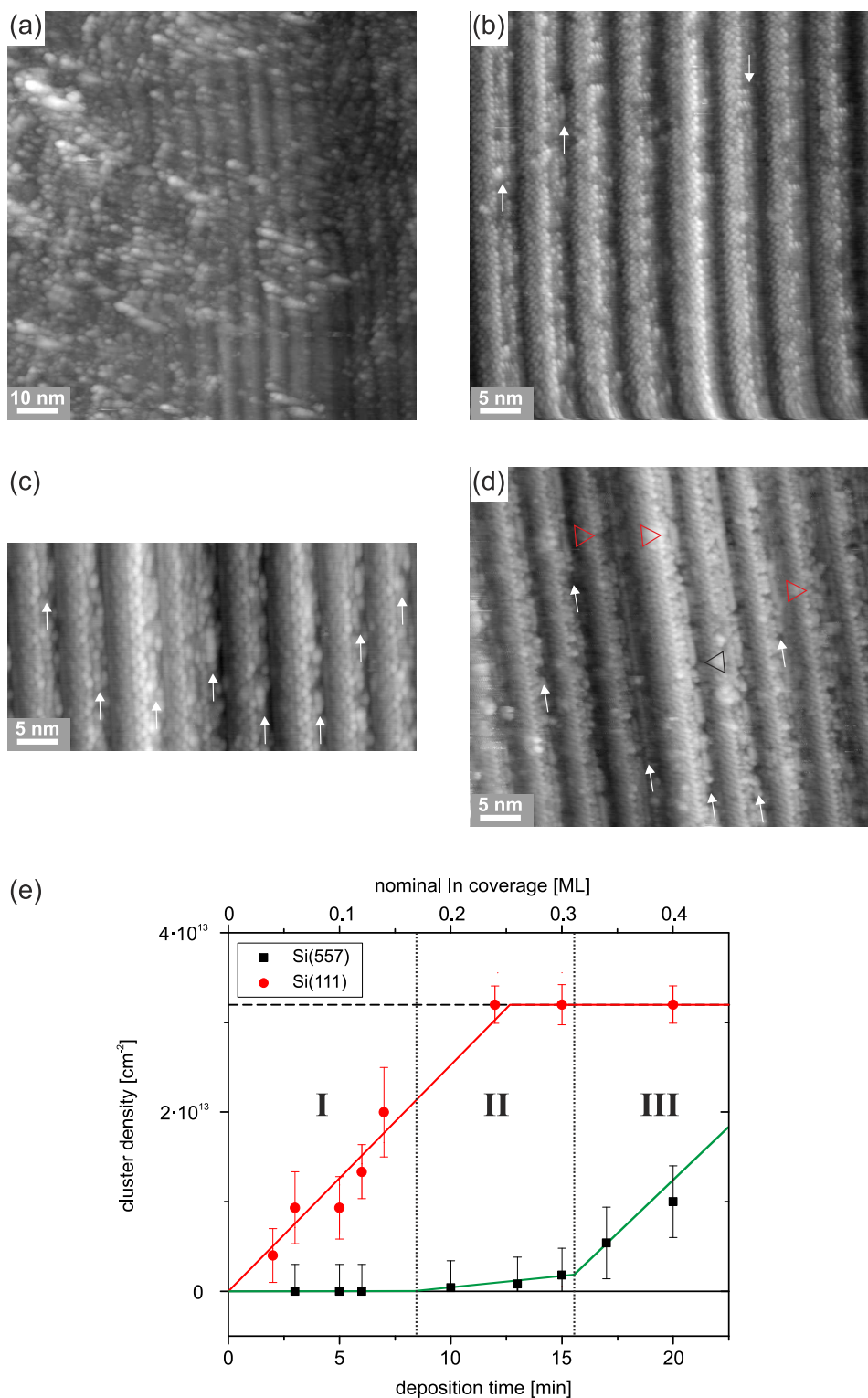


**Figure 6.13:** (a-d) STM images of Si(557) samples with (a) 0.10 ML In deposited at room temperature ( $V_S = -2.5$  V;  $I_T = 100$  pA), (b) 0.10 ML In deposited at room temperature and subsequent annealing at 200 °C for 5 min ( $V_S = +1.5$  V;  $I_T = 200$  pA), (c) 0.06 ML In deposited at 200 °C ( $V_S = -2.5$  V;  $I_T = 100$  pA), and (d) 0.26 ML In deposited at 200 °C ( $V_S = +2.0$  V;  $I_T = 100$  pA). (e) Graph showing the dependence of the cluster density on the In deposition time for the measurements performed on the planar Si(111) surface (red) and the Si(557) surface (black). The dashed black line indicates the maximum cluster coverage that can be obtained on the planar Si(111) surface when a complete two-dimensional array is formed.

the locations of these lines seem to be in nice correspondence to Ref. [384]. Although the preparation conditions are slightly different in the present work, it may be concluded that at low In coverages a formation of atomic chains on the triple steps takes place, as proposed by Shin *et al.* [384]. The magic cluster formation then starts delayed at higher coverages.

In addition to the observation of the mentioned atomic chains, also the stability of different structures including the magic In clusters were calculated in Ref. [384]. In their calculations, Shin *et al.* found that for low coverages the formation of atomic chains is favored, while at higher In coverages the cluster formation becomes energetically favorable as well. This is in excellent correspondence with the findings of the present work. For a more quantitative analysis, a chart showing the dependence of the cluster density on the duration of In deposition is shown in Fig. 6.13 (e). The black points represent measurements on the Si(557) surface, while the red ones show those on the planar Si(111) surface for comparison. While on the Si(111) surface the cluster formation starts already after short In exposure, on the Si(557) surface no clusters are found until a deposition time of 10 min. On the Si(111) surface, an immediate linear increase in the cluster density is found, until at a density of  $3.2 \cdot 10^{13} \text{cm}^{-2}$  the cluster density becomes saturated. This density which is indicated by the dashed horizontal line is equal to two clusters per  $7 \times 7$  unit cell, i.e. the complete two-dimensional array.

In contrast, for the Si(557) surface a different growth behavior is observed. Here, three regimes can be identified, as indicated by the roman numbers. Regime I represents the initial growth regime discussed above with an exclusive formation of atomic chains at the step edges. In regime II, the growth of magic clusters sets in, but the growth rate is still much smaller as compared to the planar Si(111) surface. Hence, a parallel growth of both atomic wires and magic In clusters may occur. Finally, in regime III, the cluster growth rate is about the same as for the Si(111) surface, as it is evident from the equivalent slopes of the red and green lines shown in Fig. 6.13 (e). Thus, all step edges seem to be saturated, and an exclusive formation of magic clusters is observed in this regime. At a deposition time of 20 min, the cluster growth on the Si(557) surface might already start to saturate. An STM image of this preparation is shown in Fig. 6.11 (d). As mentioned before, in this image additional bright spots appear that may be assigned to extra In on top of a complete array of In clusters. The difference in the maximum cluster densities that can be obtained on the Si(111) and on the Si(557) surface is explained by the lower surface area covered with the Si(111) $7 \times 7$  reconstruction on the Si(557) surface with respect to the Si(111) surface.

## 6.4 Conclusions

In order to study fundamental effects in magic cluster systems, such as the influence of the different HUCs, in which the clusters form, or of cluster assemblies, on the electronic properties, magic In and Ga clusters on Si(111) were investigated. These clusters are considered as a model system for magic clusters on the Si(111) $7 \times 7$  surface due to their relatively easy fabrication and their well known fundamental structural and electronic properties.

For In clusters, a detailed investigation of the charge redistribution that takes place when the magic clusters form was conducted on the basis of voltage dependent STM images. Here, also different electronic properties of clusters formed in UFHUCs and FHUCs as well as for clusters neighboring other clusters were found and were studied in more detail using STS.

A second striking result is the demonstration of the formation of two different types of one-dimensional arrays of magic In clusters when using the vicinal Si(557) surface as a template. Here, the growth of the same magic In clusters as on the planar Si(111) surface is observed, but the clusters form one-dimensional chains due to the narrow Si(111) terraces present on the highly stepped substrate. However, the growth of magic clusters on the Si(557) surface is found to start not instantaneously, but the deposited In atoms are assumed to saturate the steps before cluster formation starts.



---

## Chapter 7

# Rare earth silicide clusters on Si(111)

In addition to Sb and the group-III metals In and Ga, clusters of the rare earth metals Tb and Dy were investigated within this work. Since the trivalent rare earth metals are chemically very similar, analogies in the cluster growth of Tb and Dy are expected. Therefore, this chapter covers the results found for the growth of clusters from both rare earth metals.

The self-assembled growth of rare earth silicides on Si surfaces is very interesting because a variety of different nanostructures can be grown, depending on the preparation conditions and the used surface orientation. Examples are thin rare earth silicide films on Si(111) (cf. section 3.6 and chapter 9) and the metallic nanowires that grow on vicinal Si(111) surfaces and in particular on the Si(001) surface [158, 386–391]. However, an interesting growth behavior is expected especially for clusters of the trivalent rare earth metals, which are, to the best of my knowledge, unknown up to now. These trivalent rare earth metals combine properties of two main cluster systems investigated earlier, the group-III metal clusters (see section 3.5.1 and chapter 6) and transition metal silicide clusters, like those formed from Co and Fe [13, 14, 273]: On the one hand, Dy and Tb are trivalent as the group-III metals, on the other hand, rare earth metals tend to form silicides, in that way behaving similar as the transition metals Fe and Co. Since for these two material systems magic clusters with a different atomic structure form, it is interesting to investigate how the trivalent rare earth metals will behave: Will magic clusters grow in the center of the  $7\times 7$  HUCs as it is observed for the group-III metals or near an edge of the HUCs analogous to the clusters of Fe and Co, or will a completely new system with novel properties arise, as it was found e.g. for Sb (cf. chapter 5).

In the following, first the general growth behavior of rare earth silicide clusters on the Si(111) $7\times 7$  surface is described, before the details found for the observed two main cluster types are presented.

## 7.1 General growth behavior

In order to investigate the growth of Tb and Dy clusters on the Si(111) $7\times 7$  surface 0.04 ML to 0.2 ML were deposited for both rare earth metals. The growth temperature was varied between room temperature and 500 °C for Dy and between 300 °C and 500 °C for Tb, whereas the sample was either heated during deposition (RDE) or afterwards (SPE).

At temperatures below 300 °C (not shown here), some clusters forming within single  $7\times 7$  HUCs are already observed, but the resulting structures do not show a uniform shape or size distribution. Thus, no growth of magic clusters can be identified in this temperature range. In contrast, for temperatures between 300 °C and 500 °C the growth becomes more homogeneous and it is possible to identify cluster structures that appear frequently on the surface. In Fig. 7.1 (a) and (d), overview STM images for this regime are shown for Tb and Dy, respectively. For both rare earth metals, a very similar growth behavior is observed. The  $7\times 7$  periodicity of the Si(111) substrate is maintained and mainly clusters form within single  $7\times 7$  HUCs. Besides these clusters, also larger structures spreading over several HUCs are found occasionally as labeled as islands in (a) and (d). The number and size of these islands increases with increasing coverage and temperature. For a measurement with 0.2 ML Dy deposited at 500 °C, where already islands with diameters of about 10 nm are found, the Dy induced  $2\sqrt{3}\times 2\sqrt{3}$  R30° superstructure, which is known to form in the submonolayer coverage regime (see section 3.6.1), could be resolved. Hence, it is concluded that the islands observed in Fig. 7.1 (a) and (d) represent the early stages of the growth of the rare earth induced  $2\sqrt{3}\times 2\sqrt{3}$  R30° superstructure. Since the growth of thin Tb films on Si(111) is the subject of chapter 9, the detailed analysis of this structure will be presented there.

Although the cluster growth is not as homogeneous as for the clusters of the group-III metals In and Ga or for the ringlike Sb clusters that were investigated in the previous chapters, two main cluster types that form frequently on the surface can be identified for both rare earth metals. These are the so-called centered rare earth silicide clusters and the so-called off-center rare earth silicide clusters. In more detailed filled states STM images [Fig. 7.1 (b,c,e,f)], the centered rare earth silicide clusters appear as bright centered triangles within the  $7\times 7$  HUCs (indicated by blue triangles), while the off-center rare earth silicide clusters appear as bright features located near the centers of an edge of the  $7\times 7$  HUCs (indicated by green triangles).

However, always also clusters that cannot be classified into one of the two types are forming, e.g. the very bright appearing structures indicated exemplarily by the arrows in Fig. 7.1. These so called bright clusters often appear centered within the HUCs without any further structure being resolved in the STM images. In addition, their appearance does not change much with varying tunneling voltages. It is thus assumed that these bright clusters correspond to agglomerations of a larger number of rare earth atoms and that they exhibit metallic properties.

When comparing the more detailed images for Tb and Dy, a very similar behavior is found with a simultaneous formation of centered and off-center clusters. However, the ratio of centered and off-center clusters depends on the preparation conditions. While for the centered clusters,

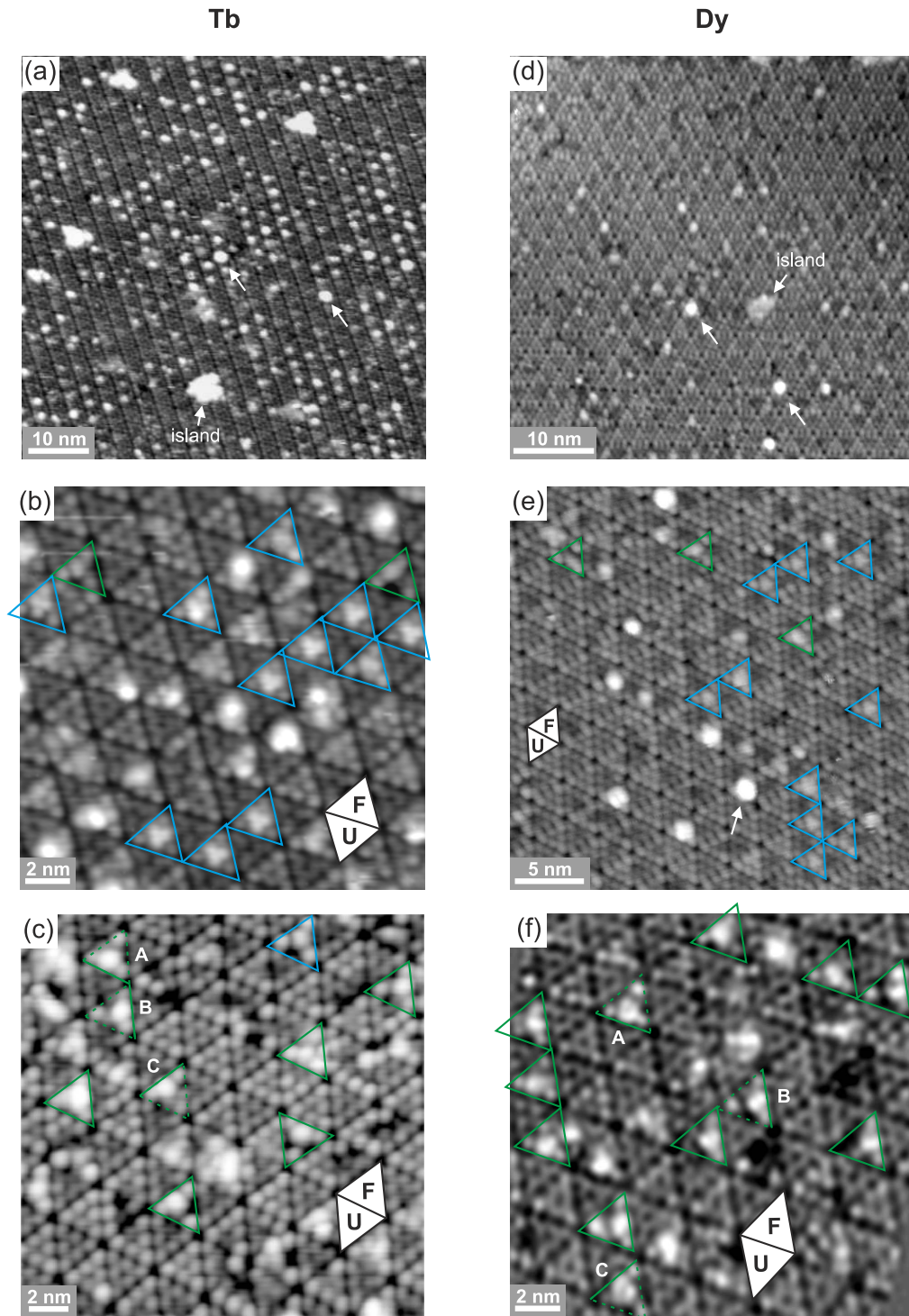


**Figure 7.1:** Filled states STM images showing the growth behavior of (a-c) Tb induced clusters and (d-f) Dy induced clusters on the Si(111)7 $\times$ 7 surface. (a) 0.06 ML Tb deposited at 375  $^{\circ}$ C ( $V_S = -2.5$  V;  $I_T = 100$  pA). (b) 0.06 ML Tb deposited at 375  $^{\circ}$ C ( $V_S = -2.0$  V;  $I_T = 100$  pA). (c) 0.06 ML Tb deposited at 400  $^{\circ}$ C ( $V_S = -2.5$  V;  $I_T = 100$  pA). (d) 0.06 ML Dy deposited at 350  $^{\circ}$ C ( $V_S = -2.5$  V;  $I_T = 70$  pA). (e) 0.06 ML Dy deposited at 350  $^{\circ}$ C ( $V_S = -2.25$  V;  $I_T = 70$  pA). (f) 0.04 ML Dy subsequently annealed at 400  $^{\circ}$ C for 1 min ( $V_S = -2.0$  V;  $I_T = 100$  pA). In the images, islands exceeding over several unit cells are exemplarily marked, the white arrows indicate bright clusters, and the blue and green triangles indicate HUCs with centered and off-center clusters, respectively. For the off-center clusters, the three equivalent orientations are exemplarily marked by A, B, and C in (c,f).

optimum growth temperatures of 350 °C for Dy and 375 °C for Tb are found, the off-center clusters form preferentially at slightly higher temperatures of 400 °C, as can be seen from a comparison of the STM images shown in (b) and (e) with those shown in (c) and (f). As mentioned above, two different growth methods, RDE and SPE were employed. In general, the samples prepared using RDE showed a better homogeneity, hence this method was employed preferentially. However, the growth method also has an influence on the ratio between the different cluster types. This is observed in particular for Dy, where the largest fraction of off-center clusters was found on the sample shown in (f), which was prepared by depositing Dy at room temperature and subsequently annealing the sample at 400 °C for 1 min.

As can be seen from the STM images shown in Fig. 7.1 (b,c,e,f), where the orientation of the FHUC and the UFHUC is indicated, the rare earth silicide clusters show a strong preference for occupying the FHUCs of the  $7\times 7$  reconstruction. This behavior is analyzed in more detail in the following sections, where the properties of the off-center and the centered rare earth silicide clusters are described separately in more detail.

It should be mentioned that, in particular for the Si(111) samples used to investigate Tb induced clusters, it is found that highest densities of identical clusters can only be achieved on fresh Si(111) $7\times 7$  substrates, which have not been exposed to rare earth depositions before. For many other materials, the Si(111) substrates can be used typically several times without a significant degradation since the material desorbs completely during the flashing procedure. However, for Tb it is found that this is at least not completely the case. Here, a behavior similar to the one found e.g. for Ni seems to be present: During the flashing, some metal atoms diffuse into the bulk Si crystal and then diffuse back to the surface during the cool-down [250, 392]. Since this behavior is particularly observed at higher Tb coverages, a detailed investigation will be presented in chapter 9.

## 7.2 Off-center rare earth silicide clusters

Figure 7.2 shows detailed filled and empty states STM images of off-center clusters formed upon Dy and Tb deposition. Thereby, the same off-center Dy silicide cluster is imaged in (a) and (b), while in (c) and (d) filled and empty states images of two different but equally oriented off-center Tb silicide clusters are shown, since it was not possible to obtain images of the same cluster with different polarities of the tunneling voltage due to high thermal drift and instabilities of the tips used in these measurements. However, the similarity between the STM images of the clusters formed from Dy and Tb indicates that analogous clusters form for both rare earth metals. This behavior can be related to the chemical similarity of the trivalent rare earth metals. Thus, the properties of the off-center silicide clusters of Dy and Tb are discussed together in the following, mostly based on results for Dy silicide clusters since more data are present for this rare earth metal.

As mentioned in the previous section, the off-center clusters appear as a bright feature located near the center of an edge of the  $7\times 7$  HUC. As in the cluster systems discussed in the previous chapters, the Si corner adatoms appear unaffected by the cluster formation, while at

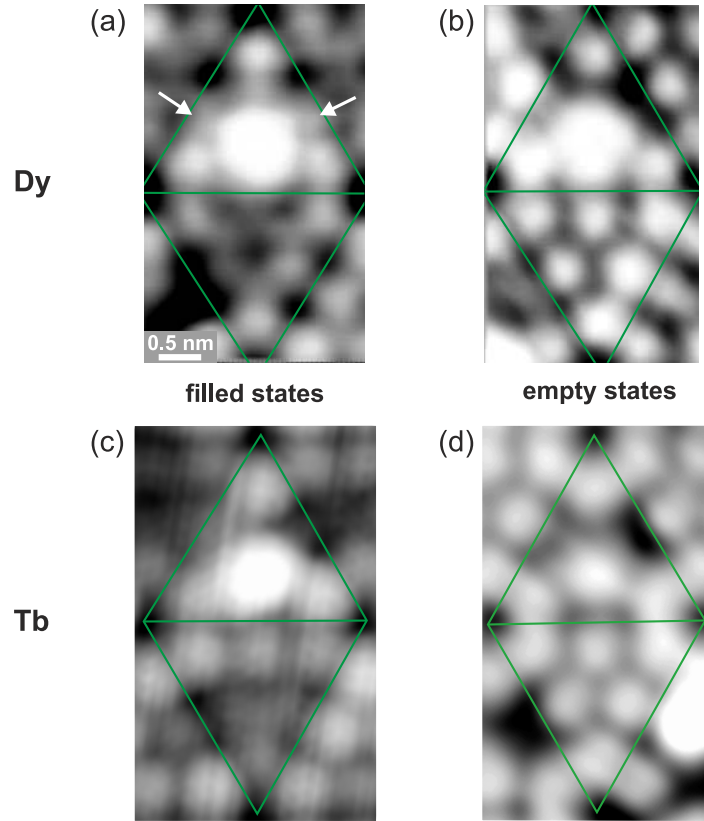


**Figure 7.2:** Detailed filled states and empty states STM images of (a,b) the same off-center Dy silicide cluster and (c,d) two different off-center Tb silicide clusters on the Si(111)7 $\times$ 7 surface. (a)  $V_S = -1.0$  V and  $I_T = 100$  pA, (b)  $V_S = +2.5$  V and  $I_T = 100$  pA (0.04 ML Dy subsequently annealed at 400 °C for 1 min). (c)  $V_S = -2.0$  V and  $I_T = 50$  pA, (d)  $V_S = +1.5$  V and  $I_T = 50$  pA (0.06 ML Tb deposited at 350 °C).

the locations of the former Si center adatoms the contrast in the STM images has vanished, as it is indicated by the white arrows in Fig. 7.2 (a). As it was found for the Sb ringlike clusters in chapter 5, which also form near an edge of the HUC, the off-center cluster formation leads to three equivalent orientations within the 7 $\times$ 7 HUCs. These three orientations are exemplarily indicated in Fig. 7.1 (c,f) by A, B, and C.

Similar to other cluster systems investigated within this work, the off-center clusters show again a strong preference for occupying the FHUC of the Si(111)7 $\times$ 7 reconstruction. For a Dy coverage of 0.04 ML and subsequent annealing at 400 °C, where the highest fraction of off-center Dy silicide clusters was observed, about 92% formed within the FHUC. For Tb, a similar value of about 90% is found for the temperature range between 350 °C and 400 °C. Hence, the formation energy for an off-center cluster is again lower for the FHUC as compared to the UFHUC. As it is expected from the thermal distribution, the occupation of the UFHUC increases with increasing growth temperature. As in the previous chapters, the formation energy difference  $\Delta E$  between an off-center cluster within the FHUC and within an UFHUC is estimated using the Boltzmann distribution (Eq. 5.1). Taking all measurements for the off-center Dy silicide clusters for substrate temperatures between 350 °C and 500 °C into account, an energy difference of  $\Delta E = (0.13 \pm 0.02)$  eV is derived. From the measurements with off-

center Tb silicide clusters in the temperature range between 350 °C and 400 °C, a similar energy difference of  $\Delta E = (0.12 \pm 0.03)$  eV is found.

### 7.2.1 Atomic structure of off-center rare earth silicide clusters

In this section, it is demonstrated that the STM results of the off-center rare earth silicide clusters described in the previous section are well explained by the structure model developed by Zilani *et al.* for the Co and Fe silicide clusters [13,14,273] described in section 3.5.1. The corresponding structure model for the off-center rare earth silicide clusters is shown in Fig. 7.3 (a) and (b). Each off-center cluster consists of six rare earth metal atoms forming a triangle surrounding three Si atoms in the cluster center. This triangular structure is very similar to the one of the group-III metal clusters. However, the off-center clusters do not form centered in the HUC, but the triangle is located near the center of one edge of the HUC. Again, the Si cluster atoms are the former Si center adatoms that moved into the cluster during its forma-

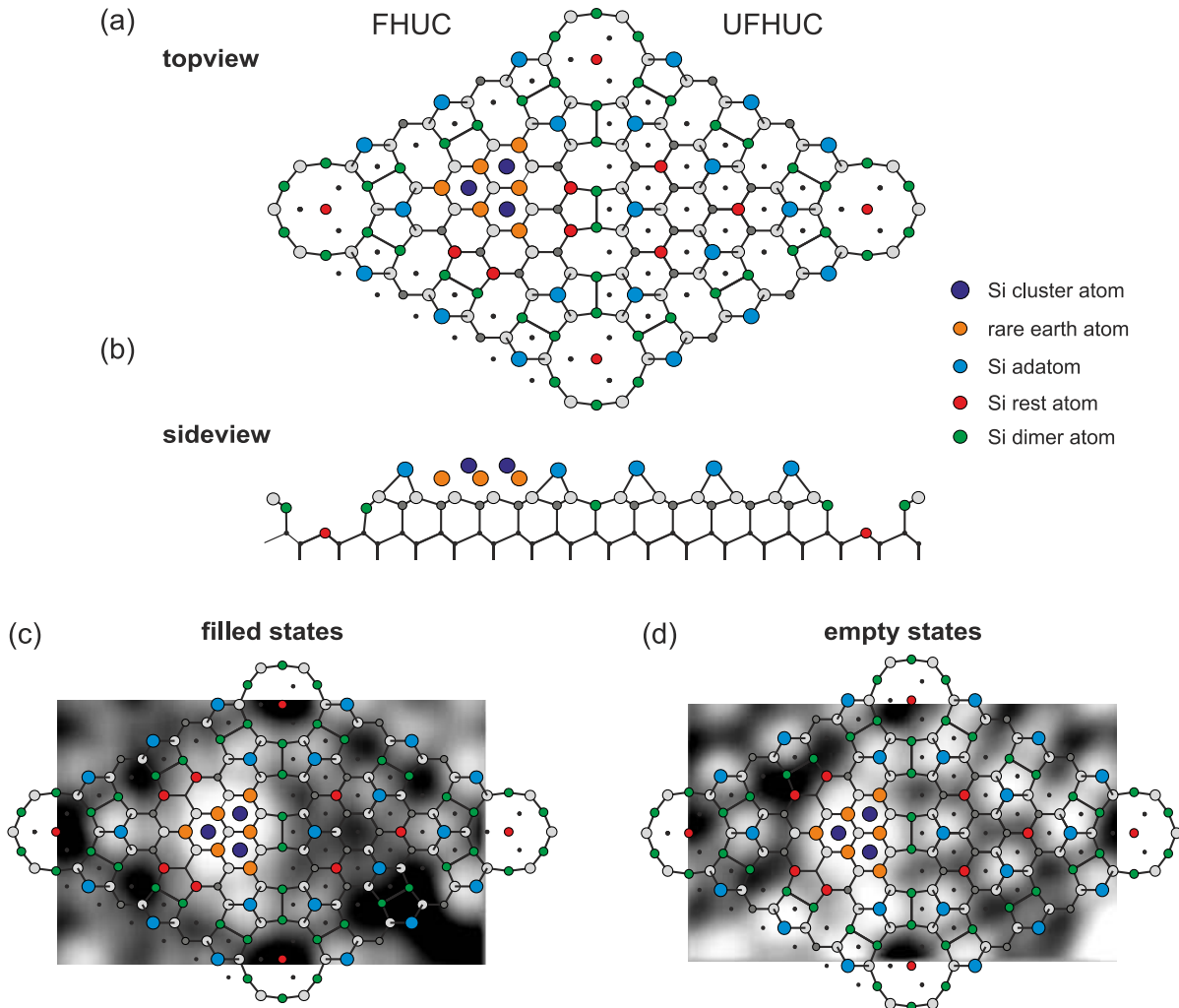


**Figure 7.3:** (a) Atomic structure model for the off-center rare earth silicide clusters in (a) topview and (b) sideview, in analogy to the one proposed for the Co silicide clusters by Zilani *et al.* [13]. (c,d) Atomic structure model overlaid on the filled states ( $V_S = -1.0$  V) and empty states ( $V_S = +2.5$  V) STM images of the Dy silicide clusters already shown in Fig. 7.2 (a) and (b), respectively.

tion, making a Si diffusion from other HUCs unnecessary. Because of the silicide formation it is assumed that the Si atoms are finally located slightly above the rare earth atoms as shown in Fig. 7.3 (b).

Now, the structure model is compared with the experimental data presented in the previous section in more detail, demonstrating that it can nicely explain all experimental observations: First, the observed location of the cluster center within the HUC fits very well to the structure model as can be seen in Fig. 7.3 (c) and (d), where the structure model is overlaid on the filled and empty states STM images already shown in Fig. 7.2 (a) and (b). It is obvious that the cluster center is located at exactly the same position as in the model. In addition, also the extent of the bright contrast in the STM image fits quite well to the dimensions of the cluster in the structure model. Second, the appearance of the off-center rare earth silicide clusters in filled states and empty states STM images taken at various voltages resembles nicely the appearance of the Co and Fe silicide clusters. Also the small depression in the cluster center, which is reported in Ref. [273], is occasionally observed in empty states images such as Fig. 7.4 (b) and (d). Third, a moderate bright contrast appears in filled states STM images in the region of the former Si center adatoms [marked by the white arrows in Fig. 7.2 (a)]. This contrast, which is found similarly in experimental and simulated STM images of the Co and Fe silicide clusters [13,14], is assigned to dangling bonds that remain at the rest atoms in this area after the adatom was removed for the cluster formation [see Fig. 7.3 (a)]. Fourth, as presented in detail in the following section, a semiconducting behavior, indicated by STM images taken with low absolute tunneling bias (Fig. 7.4) as well as by STS spectra showing a band gap of  $\sim 0.7$  eV, is observed, very similar to the behavior of the Co silicide clusters, for which a band gap of  $\sim 0.8$  eV was found [273].

### 7.2.2 Electronic properties of off-center rare earth silicide clusters

In filled and empty states STM images acquired with low absolute tunneling bias as shown in Fig. 7.4 (a) and (b), respectively, the off-center rare earth silicide clusters appear with a significantly reduced height as compared to higher tunneling voltages. In (c) and (d), height profiles taken exemplarily for two clusters in (a) and (b) are shown. Here, the clusters (indicated by red arrows) appear 0.09 nm and 0.12 nm, respectively, lower than the corresponding Si corner adatoms (indicated by blue arrows). This is in strong contrast to the images shown in Fig. 7.2 (a) and (b), where the off-center Dy silicide clusters appear about 0.08 nm and 0.05 nm, respectively, higher than the Si corner adatoms. Such a behavior with a decreasing apparent height with decreasing absolute value of the tunneling bias, as it is also observed e.g. for the group-III metal clusters (cf. chapter 6), suggests a semiconducting nature of the off-center rare earth silicide clusters.

For a more detailed investigation of the electronic properties of the off-center rare earth silicide clusters, tunneling spectra were measured on off-center Tb silicide clusters. Fig. 7.5 (a) and (b) shows  $I-V$  and  $dI/dV-V$  spectra measured simultaneously using a software lock-in amplifier. For comparison, also spectra measured with the same tip on the clean Si(111) $7\times 7$  surface in the vicinity of the clusters are shown. All spectra were measured using a tunneling

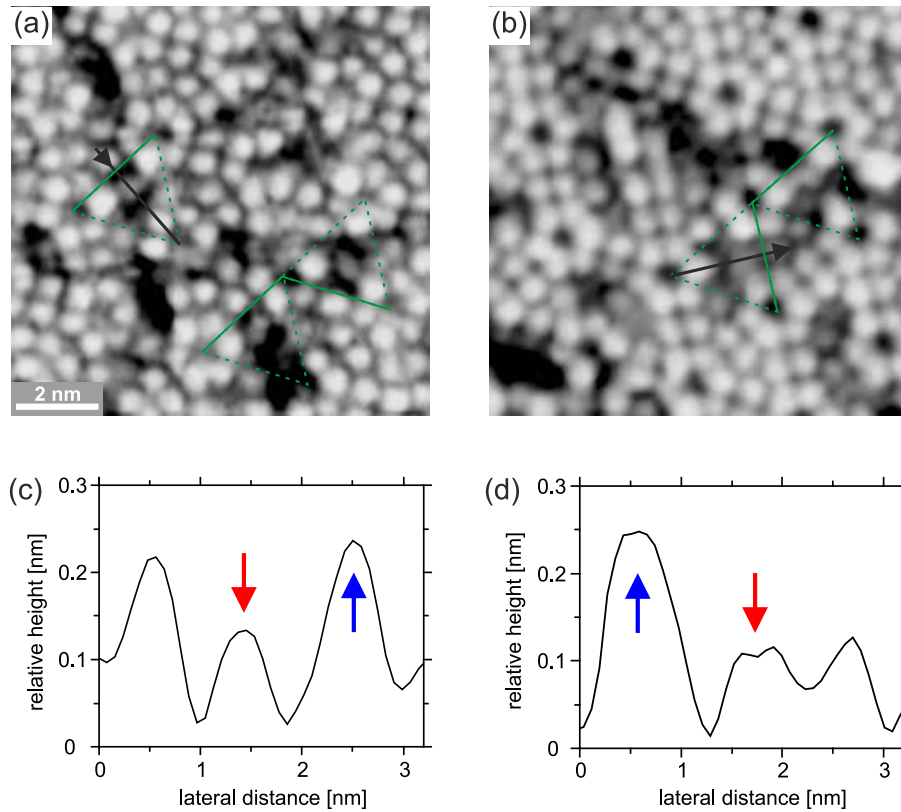


**Figure 7.4:** (a,b) Filled and empty states STM images and (c,d) corresponding height profiles of off-center Dy silicide clusters taken at (a,c) low negative ( $V_S = -0.5$  V;  $I_T = 100$  pA) and (b,d) low positive ( $V_S = +0.5$  V;  $I_T = 100$  pA) tunneling voltage (0.04 ML Dy subsequently annealed at 400 °C for 1 min). In the STM images, HUCs with off-center clusters are indicated by green triangles. Thereby, the solid line indicates the edge of the HUC near which the cluster formed. The height profiles shown in (c) and (d) are taken along the black arrows in (a) and (b), respectively. Within the height profiles, clusters and Si corner adatoms are indicated by the red and blue arrows, respectively.

voltage of  $V_S = -1.5$  V and a tunneling current of  $I_T = 200$  pA to stabilize the tip height and a modulation frequency of 1 kHz with a modulation amplitude of 50 mV for the lock-in measurement. In comparison to the spectra measured on the  $7 \times 7$  surface, the off-center Tb silicide clusters clearly show a semiconducting behavior with a broad region with zero intensity around the Fermi level. However, already at around 0.25 eV a slight increase is observed again (indicted by a red bar), while in the filled states an increase is not observed before about  $-0.5$  eV and a distinct spectral feature is found at around  $-1$  eV as indicated by a red bar. Thus, the size of the band gap forming asymmetrically around the Fermi level is estimated to be  $\sim 0.7$  eV, as it is indicated in Fig. 7.5 (b). Similar values are also found for other magic cluster systems on Si(111) $7 \times 7$  such as the group-III metal clusters investigated in chapter 6 or the Co silicide clusters, for which a band gap of  $\sim 0.8$  eV is found [273].

It should be mentioned that due to the low number of spectra that could be measured on the off-center cluster with the same STM tip and thus a relatively high noise level, a determination of the normalized conductivity is not presented. However, a similar behavior as observed in Fig. 7.5 was also found reproducibly in other STS measurements on off-center Tb silicide

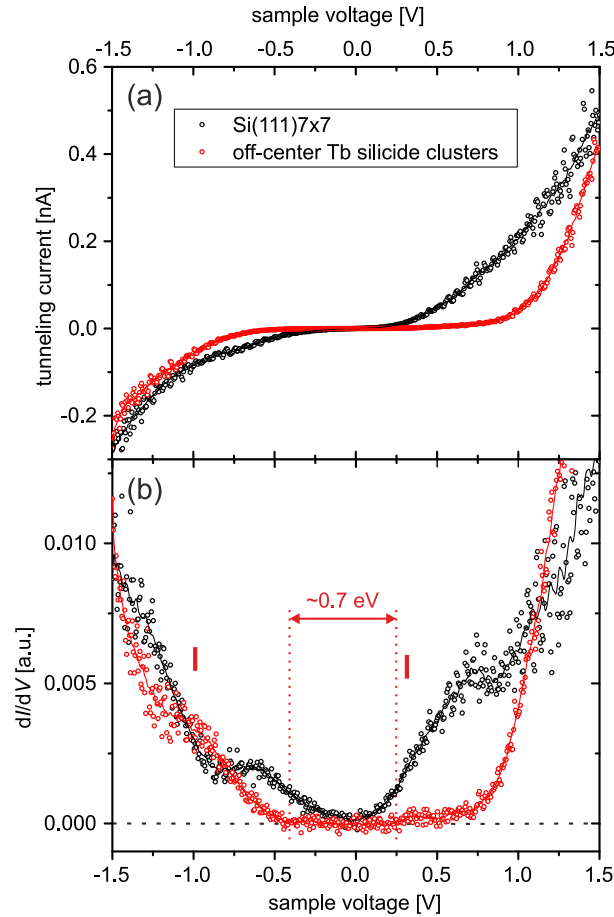


**Figure 7.5:** (a)  $I$ - $V$  and (b)  $dI/dV$ - $V$  spectra measured on off-center Tb silicide clusters (red) and on the clean Si(111)7 $\times$ 7 surface surrounding the clusters (black).

clusters using other tips. Regarding the off-center Dy silicide clusters, STS measurements could not be performed since the measurements on these clusters were done before the new Nanonis STM control system was implemented, and the electronics used before did not allow to obtain tunneling spectra. However, the appearance in STM images acquired with low absolute tunneling voltages as those shown in Fig. 7.4, which was discussed above, suggests a similar behavior also for the off-center Dy silicide clusters.

### 7.3 Centered rare earth silicide clusters

In contrast to the off-center rare earth silicide clusters, the centered clusters appear centered within the Si(111)7 $\times$ 7 HUCs. As mentioned before, the formation of centered clusters is observed for both rare earth metals investigated in this work, Dy and Tb. Again, the clusters of both materials appear very similar in filled and empty states STM images like those shown in Fig. 7.6. Thus, it is again assumed that analogous clusters form in both cases.

In filled states STM images as shown in Fig. 7.6 (a) and (c), the centered rare earth silicide clusters appear as a triangle located in the center of the 7 $\times$ 7 HUC. In STM images with highest resolution, the triangle appears to be formed from three protrusions. As it is found for all magic

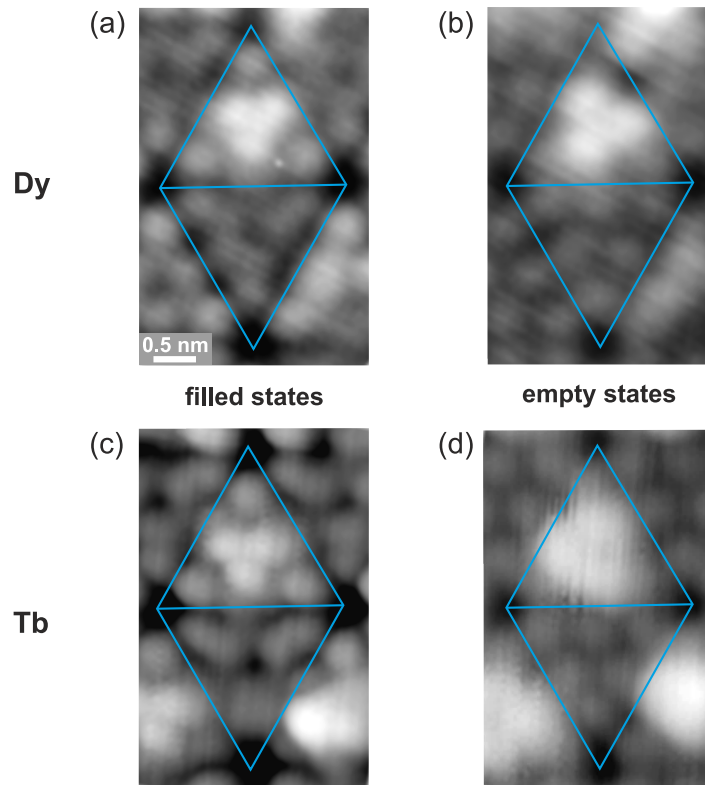


**Figure 7.6:** Detailed filled states and empty states STM images of (a,b) the same centered Dy silicide cluster and (c,d) the same centered Tb silicide cluster on the Si(111)7×7 surface. (a)  $V_S = -2.0$  V and  $I_T = 100$  pA, (b)  $V_S = +2.0$  V and  $I_T = 70$  pA (0.12 ML Dy deposited at 300 °C). (c)  $V_S = -1.5$  V and  $I_T = 100$  pA, (d)  $V_S = +2.5$  V and  $I_T = 100$  pA (0.06 ML Tb deposited at 375 °C).

cluster systems investigated in this work, the Si corner adatoms are unaffected by the cluster formation, while the former Si center adatoms are no more present since the cluster extends up to their locations. The described appearance in the filled states images is very similar to the one of the magic group-III metal clusters investigated in chapter 6. However, this similarity completely vanishes when analyzing the empty states STM images of the centered rare earth silicide clusters such as those shown in Fig. 7.6 (b) and (d). Here, the clusters still show a centered triangular appearance as also the group-III metal clusters do (see e.g. Figs. 3.15 and 6.3), but the clusters appear no more symmetric within the 7×7 HUC but rotated by about 30°. In addition, the triangle does not appear to be formed from six bright spots, as it is observed in empty states images of the group-III metal clusters, where every spot originates from one group-III metal atom, but from three bright spots.

As a consequence of this  $\sim 30^\circ$  rotation, which breaks the symmetry of the 7×7 reconstruction, two equivalent structures, which are rotated by  $\sim 60^\circ$  with respect to each other, should be possible due to the symmetry of the underlying 7×7 HUC. Indeed, such two configurations are observed as can be already seen in Fig. 7.6, where the Dy silicide and the Tb silicide cluster shown in (b) and (d), respectively, are rotated in opposite directions. A more detailed look on this phenomenon is provided in Fig. 7.7. In (a), an empty states STM image with three centered Tb silicide clusters (indicated by the blue triangles) is shown. Among the three cen-

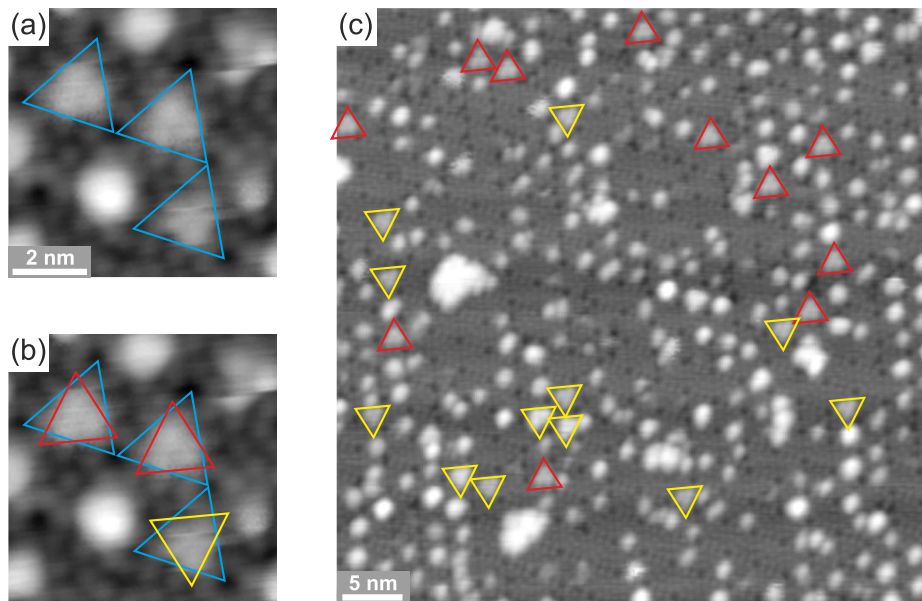


**Figure 7.7:** (a,b) Detailed empty states STM image of centered Tb silicide cluster on Si(111) $7\times 7$  (indicated by blue triangles) showing the two equivalent configurations of the clusters that are observed due to the rotated appearance (0.06 ML Tb deposited at 375 °C;  $V_S = +2.5$  V;  $I_T = 100$  pA). (b) Same image as shown in (a), but with the two configurations being indicated by red and yellow triangles for a clockwise and counterclockwise rotation by  $\sim 30^\circ$ , respectively, with respect to the appearance in filled states images. (c) Overview image of a sample with a Tb coverage of 0.06 ML deposited at 375 °C ( $V_S = +1.5$  V and  $I_T = 200$  pA). Again, the two configurations of the centered clusters are indicated by red and yellow triangles.

tered clusters, two show an orientation with a clockwise rotation of  $\sim 30^\circ$  with respect to the appearance in the filled states image, while one cluster shows a counterclockwise rotation. In (b), these two configurations are indicated by red and yellow triangles for the clockwise and counterclockwise rotation, respectively.

If the two configurations result from equivalent atomic structures that just form rotated within the  $7\times 7$  HUC as assumed above, both configurations should be found with the same probability. By analyzing several overview STM images and counting the clusters with respect to their configuration it was found that this is indeed the case. Figure 7.7 (c) shows an example of such an overview STM image with the two configurations again being marked by yellow and red triangles. Hence, it is assumed that the two configurations are described by identical but mirror inverted atomic structures. A structure model, which is able to explain the experimental findings described here, is developed in the following section.

But before, the occupation of the different HUCs will be addressed. As mentioned earlier and can be seen e.g. from Figs. 7.1 (b,e) and 7.7 (c), also the centered rare earth silicide clusters show a strong preference for the FHUC of the  $7\times 7$  reconstruction. This preference is especially pronounced for the centered Tb silicide clusters, where 98% of all clusters formed within an FHUC in average for all preparations with 0.06 ML Tb deposited at 375 °C. For the centered Dy silicide clusters, about 94% are observed within an FHUC for the ideal preparation conditions of 0.06 ML Dy deposited at 350 °C. Averaged over all measurements, this leads to a

rather large energy difference of  $\Delta E = (0.22 \pm 0.03)$  eV between the formation energies within the FHUC and the UFHUC for the centered Tb silicide clusters and to  $\Delta E = (0.13 \pm 0.03)$  eV for the centered Dy silicide clusters. Hence, despite both forming the same types of magic clusters, the preference of the FHUC for the two investigated rare earth metals Dy and Tb differs noticeably. For the group-III metal cluster a similar variation of the energy difference is observed, with In showing a strong preference of the FHUC while for Ga and Al both HUCs are occupied almost equally (cf. section 3.5.1 and chapter 6), although all group-III metal clusters exhibit an analogous atomic structure.

### 7.3.1 Atomic structure of centered rare earth silicide clusters

To the best of my knowledge, no other magic cluster system on the Si(111) $7 \times 7$  surface has been reported up to now to show such an asymmetric appearance in the empty states STM images as the centered rare earth silicide clusters. Although the appearance in the filled states images [see e.g. Fig. 7.6 (a) and (c)] matches the one of the group-III metal clusters and other centered cluster systems (cf. section 3.5.1), the appearance in the empty states as a rotated triangle [see e.g. Fig. 7.6 (b) and (d)] cannot be described with known structure models. Thus, a new model, which can explain all experimental findings described in the previous section, is developed in the following.

Due to the lower electronegativity of rare earth metals with respect to Si [156], the filled states are assumed to be mainly located at the Si atoms. Hence, in filled states STM images mainly the Si atoms should be imaged, while empty states STM images presumably show the locations of the rare earth metal atoms. Further assuming that each bright spot observed in the STM images corresponds to one atom, the appearance as a triangle formed by three bright spots in both the filled and the empty states STM images may be assigned to a  $\text{RE}_3\text{Si}_3$  stoichiometry of the centered rare earth silicide clusters. The atomic structure is then derived by comparing the locations, where the spots are observed in the STM images, with the structure model of the clean Si(111) $7 \times 7$  surface. Placing the three Si atoms close to the locations, where the spots are observed in the filled states images, and the RE atoms at the locations, where the spots are observed in the empty states images, leads to the structure model presented in Fig. 7.8 (a).

The appearance in filled states images as a centered, symmetric triangle which is formed by three bright spots is thus attributed to the triangular cluster core consisting of Si atoms. A quite similar cluster core consisting of three Si atoms is also formed for the magic group-III metal clusters, explaining the similar appearance in the filled states STM images. Due to the symmetric orientation of this core within the  $7 \times 7$  HUC, the cluster appears symmetrically in filled states STM images, since only the Si atoms are assumed to contribute significantly to the image. In contrast, the three rare earth atoms form an asymmetric triangle surrounding this Si cluster core which may explain the asymmetric appearance in the empty states images. Regarding the sites of the rare earth atoms, two configurations with equivalent sites exists, as shown in Fig. 7.8 (a) and (b). These two configurations can nicely explain the two experimentally observed orientations which appear rotated by  $\sim 60^\circ$  with respect to each other.

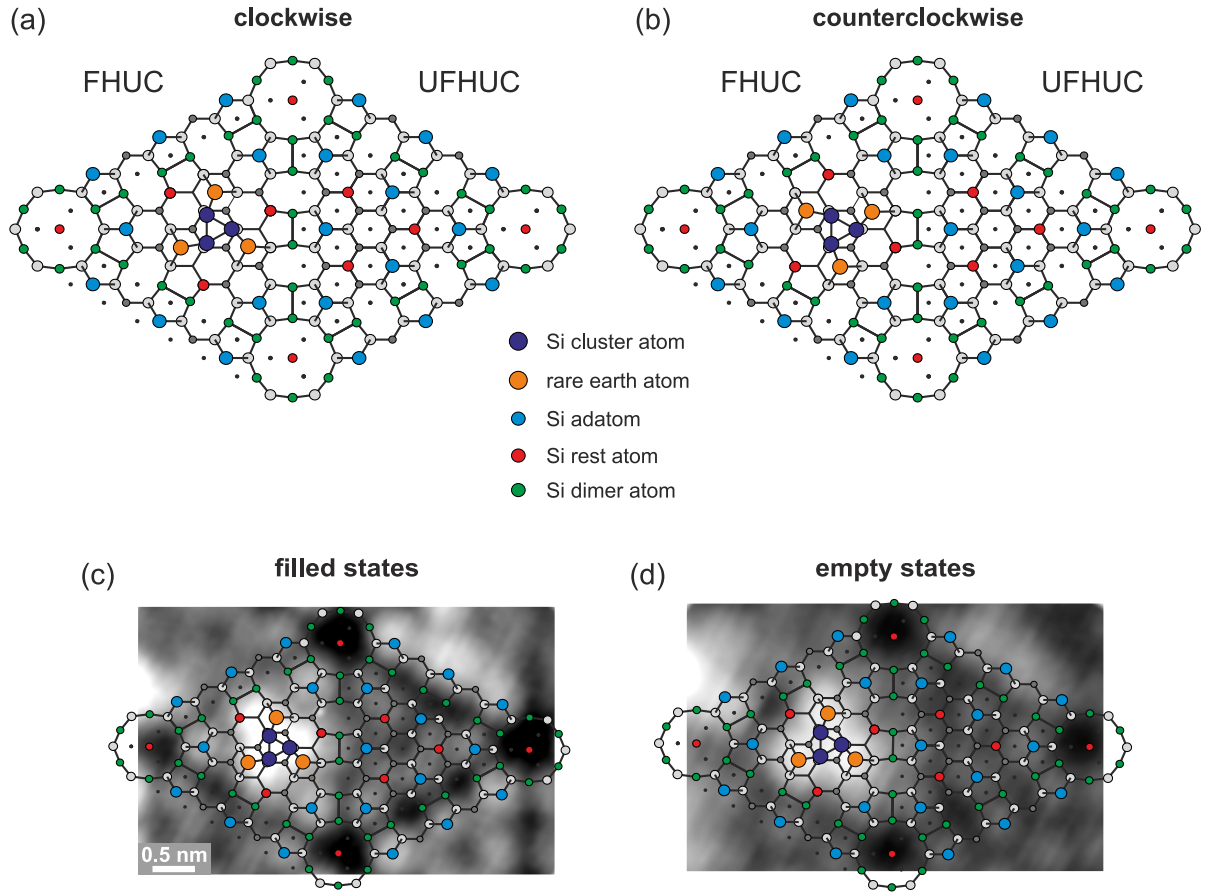


**Figure 7.8:** (a,b) Atomic structure models for the two configurations of the centered rare earth silicide clusters. (c,d) Atomic structure model overlaid on the filled states ( $V_S = -2.0$  V) and empty states ( $V_S = +2.0$  V) STM images of the Dy silicide cluster with a clockwise rotation already shown in Fig. 7.6 (a) and (b), respectively.

To demonstrate the good agreement between the proposed structure model and the experimental data, the structure model is overlaid on filled and empty states STM images of a centered Dy silicide cluster in Fig. 7.8 (c) and (d). A further argument for the proposed cluster structure is the saturation of dangling bonds. Assuming that the bonds within the cluster are completely saturated, the number of dangling bonds in a  $7 \times 7$  HUC reduces from nine to six when a centered rare earth silicide cluster forms.

Another experimental observation supporting the proposed structure model is presented in Fig. 7.9. While in (a,d) and (c,f), the two centered clusters observed in the images appear with the symmetric and asymmetric appearance described above, in filled states images acquired using appropriate tunneling conditions such as Fig. 7.9 (b,e), an additional contrast is found. This contrast is observed besides the cluster as it is indicated by the white arrows and leads to an asymmetric appearance also in this filled states image. When comparing the location of the observed contrast with the atomic structure model as it is done in (e), it turns out that it is located exactly at the position where unsaturated dangling bonds remain at the Si rest atoms after the cluster formation. On the bare Si(111) $7 \times 7$  surface, the rest atom state [ $S_2$  state in Fig. 3.9 (a)] is found at  $\sim 0.9$  eV below  $E_F$ , agreeing well with the observation in

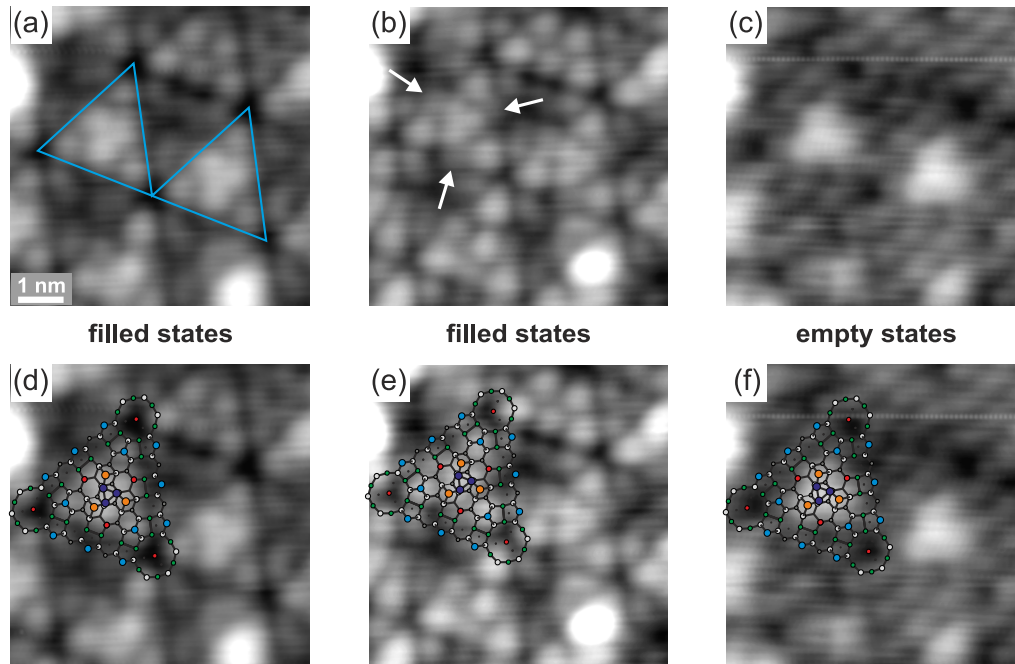


**Figure 7.9:** (a-c) STM images of the same two centered Tb silicide clusters prepared by depositing 0.06 ML Tb at 375 °C. (a)  $V_S = -1.5$  V and  $I_T = 200$  pA, (b)  $V_S = -1.0$  V and  $I_T = 300$  pA, and (c)  $V_S = +1.5$  V and  $I_T = 300$  pA. In (a), the HUCs, in which the two clusters formed, are indicated by blue triangles, and in (b) the white arrows indicate the locations where a slight contrast is observed due to the unsaturated dangling bonds at the remaining rest atoms. (d-f) STM images already shown in (a-c), but with the structure model of the centered rare earth silicide clusters overlaid on one cluster.

the STM image acquired using a tunneling voltage of  $-1$  V, thus further supporting the above assignment. The derived positions of the rest atoms also agree nicely with the positions of the rare earth metal atoms within the cluster, which are identified from the corresponding empty states STM image in (c,f) which was taken subsequently to (a,d) and (b,e).

### 7.3.2 Bistable switching of centered rare earth silicide clusters

Another very interesting behavior of the centered rare earth silicide clusters is illustrated in Fig. 7.10. In (a) to (h), STM images of the same surface area with centered Tb silicide clusters (indicated by the blue triangles) are shown. The STM images were acquired subsequently in the order which is indicated by the black arrows using different tunneling voltages. Since the imaged area has slightly changed with time due to the presence of thermal drift, a characteristic defect is indicated by the white circle for an easier comparison of the locations in the different images. Again, the clusters show a symmetric triangular appearance in the filled states images shown in (a) and (b), while in the empty states image in (d), a rotated asymmetric appearance is found. However, in the empty states images acquired with low positive voltages shown in (e) and (f), the orientation of the clusters cannot be identified any more. Instead of an appearance as one of the two configurations described earlier, only a noisy region appears at the locations of the clusters (indicated by the blue triangles). A less pronounced noisy appearance is also observed at slightly higher positive voltages in the images shown in (c) and (g). In the image shown in

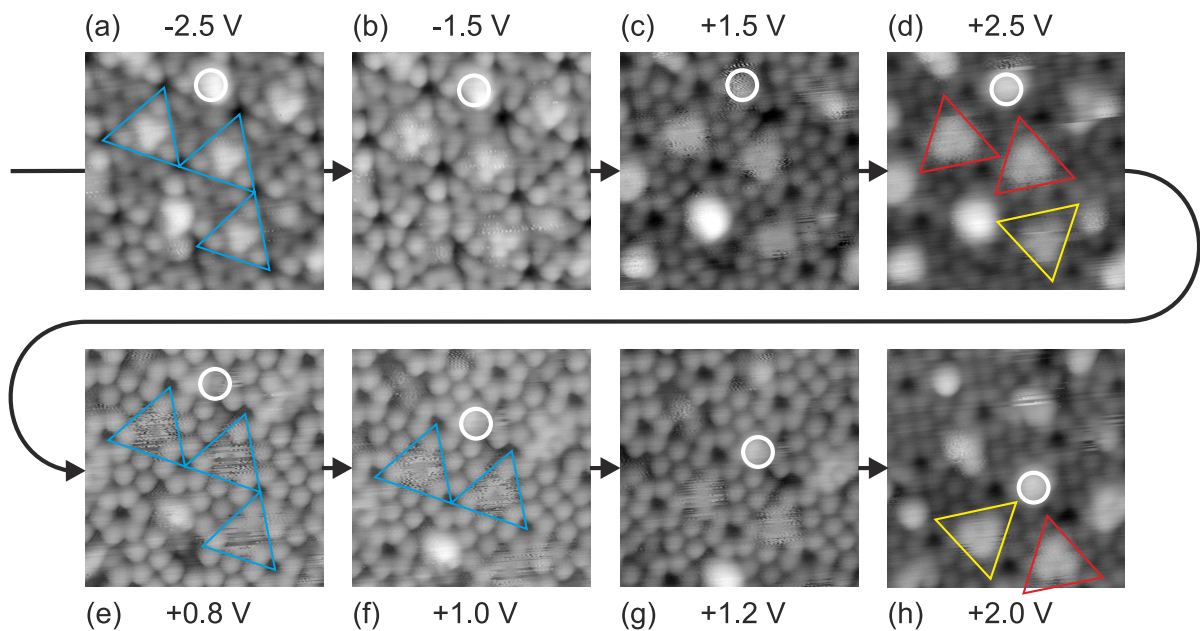


**Figure 7.10:** Subsequently measured voltage dependent STM images of the same centered Tb silicide clusters prepared by depositing 0.06 ML Tb at 375 °C, shown in the sequence of their acquisition (indicated by the black arrows). All images were acquired using the tunneling voltages given in the figure and a tunneling current of  $I_T = 100$  pA. In (a,e,f), the HUCs, in which centered clusters formed, are indicated by blue triangles. While in (a-e), three centered clusters are present completely in the images, (f-h) show only two clusters, since the imaged area has changed due to thermal drift. For an easier comparison of the images, the same defect is indicated by a white circle in every image. In addition, the two configurations of the centered clusters are indicated in (d) and (h) by yellow and red triangles.

(h), which was measured at last using a higher positive voltage of +2 V, the clusters appear again with the rotated triangular appearance. However, when comparing the configurations of the two centered clusters, which are imaged in image (d) as well as in image (h) (indicated by yellow and red triangles), the left cluster has performed a rotation by  $\sim 60^\circ$ , thus switched from a clockwise rotation (red triangle) to a counterclockwise rotation (yellow triangle). In contrast, the right cluster shows the same configuration as previously in image (d).

A possible explanation for this switching can be found in images (e) and (f), where the aforementioned noisy appearance is observed. This noisy appearance of the clusters might be caused by a fast switching between the two equivalent configurations of the clusters. Since the flipping is too fast for the rather slow STM measurement, only a noisy appearance is imaged. However, the most intensive noise is observed at the locations of the Tb atoms in the atomic structure model while the center of the cluster does not appear that noisy. This indicates that the noise may in fact result from the temporal average of the flipping of the Tb atoms between the two configurations while the Si cluster core may not be involved in the switching process due to its assumed identical orientation in both configurations.

But which process is triggering this switching? In Fig. 7.10, all STM images were acquired in constant current mode using an identical tunneling current setpoint of 100 pA, thus the tip approaches the surface when decreasing the absolute value of the tunneling voltage to

obtain a constant tunneling current. It may be assumed that this approach of the tip triggers the switching of the clusters. Thereby, the presence of the tip may lower the energy barrier for the flipping between the two cluster configurations, thus enabling the switching process. Hence, during the acquisition of images (e) and (f), where the tip-sample distance was small, the clusters were repeatedly switching between the two configurations. At larger distances as in (c) and (g), the switching becomes slower and when further increasing the voltage and therewith also the tip-sample distance, the clusters stabilize again with a probability of 50% for both configurations, being in nice agreement with the observed configurations in (h), where one cluster out of two appears in a switched configuration.

If this switching could be performed in a controlled way, a variety of interesting potential applications such as logic gates or memory cells would arise. In literature, several examples of such atomic scale switches exist. The first one was reported by Eigler *et al.*, realized by a Xe atom which switches between an STM tip and a Ni(110) surface when applying a voltage pulse [30]. Until then, a variety of reversible atomic scale switches using STM to manipulate atoms or molecules laterally, to perform rotations, or to induce conformational changes of molecules were demonstrated [31–35]. However, most of these switches only operate at cryogenic temperatures [30,33–35] since the barriers between the configurations can be overcome by thermal excitations. Also on Si surfaces, a reversible switching of atoms and molecules has been demonstrated [31, 32, 34, 35]. In the mentioned examples, the switching is achieved either due to a direct chemical atom-tip interaction [36, 393], a lowering of the energy barrier between the different configurations due to the electric field induced by the STM tip [32, 393, 394], or by overcoming the barrier by exciting a localized surface resonance [31] or by inelastic electron tunneling [33–35], where a climbing of the vibrational ladder is assumed to take place. Another nice example of an atomic scale switch composed of a binary Pb-Si cluster on the Si(111)7×7 surface consisting of three Si and three Pb atoms, thus representing a very similar system to the centered rare earth silicide clusters investigated here, has been reported recently by Inami *et al.* [29]. However, the Pb-Si clusters were constructed using atomic manipulation with an STM, making the fabrication extremely slow, thus eliminating an industrial use of these clusters. In contrast, the centered rare earth silicide clusters investigated here are prepared using self-assembled growth enabling the possibility to produce extremely high densities of clusters in a very short time.

However, it has to be mentioned that, although the behavior shown in Fig. 7.10 with a flipping of the clusters at low positive voltages was reproducibly observed, other measurements also showed a different behavior with respect to the switching of the centered clusters. Figure 7.11 shows empty states STM images with two centered Dy silicide clusters. The images were subsequently acquired using tunneling voltages of +2.0 V and +1.5 V without setting the voltage to lower values between the images. In both images the configurations of the clusters are clearly identifiable and no noisy appearance is found. Thus, assuming the mechanism described above, no flipping should be observed. Nevertheless, when comparing the configurations of the clusters in the two images, one of the two is found in another configuration in (b) as compared to (a). Since only two clusters are present, it cannot be studied, if the flipping occurs

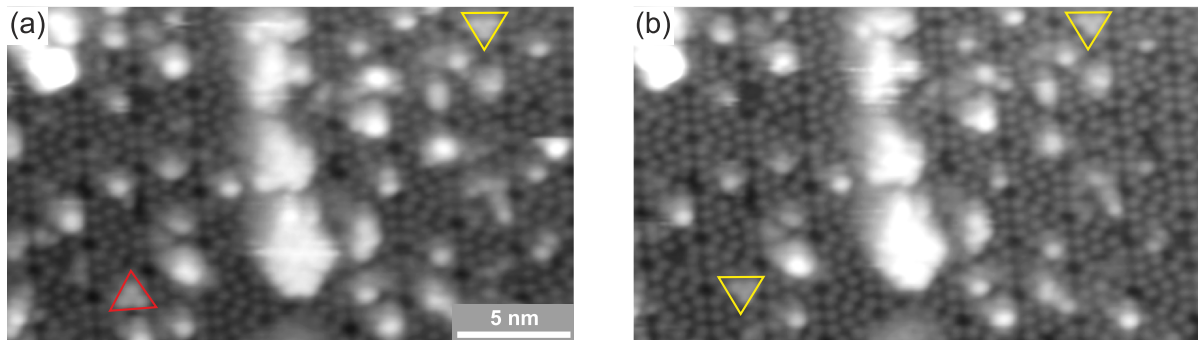


**Figure 7.11:** Subsequently acquired empty states STM images of a Si(111) $7\times 7$  sample with centered Dy silicide clusters (0.12 ML Dy deposited at 300 °C). (a)  $V_S = +2.0$  V and  $I_T = 70$  pA, (b)  $V_S = +1.5$  V and  $I_T = 70$  pA. The configurations of the two centered clusters that appear in the images are indicated by yellow and red triangles. While in (a) both clusters appear with different configurations, the lower cluster has switched in (b).

again for all clusters. However, a similar behavior was also found in one measurement for the centered Tb silicide clusters. In this measurement (not shown here) about 50% of all observed centered clusters flipped between subsequently measured empty states STM images acquired using tunneling voltages between +1.8 V and +2.5 V. Hence it is assumed that conditions exist, where the flipping occurs not only at low voltages like it is found in Fig. 7.10, but also while scanning with higher positive voltages. It has to be mentioned that it is not possible to distinguish, if the flipping also occurs when scanning with a negative tunneling voltage due to the symmetric appearance of the clusters in the filled states images. Unfortunately, a high resolution as in the filled state STM image shown in Fig. 7.9 (b), where the unsaturated rest atoms are visible, is achieved only rarely.

Furthermore, in one measurement of the centered Tb silicide clusters also an opposite behavior was observed. In Fig. 7.12, again subsequently measured empty states STM images are presented, but this time none of the centered clusters observed in the imaged area is found to perform a flipping from one configuration into the other. In addition, the clusters are imaged in Fig. 7.12 (a) without the noisy appearance present in Fig. 7.10, although the same tunneling conditions with a voltage of +1.0 V and a tunneling current setpoint of 100 pA were used. Although the clusters appear relatively low, it is even possible to identify the configuration as indicated again by red and yellow triangles. Hence, the centered clusters in the present measurement do neither show flipping at low voltages as it is observed in the measurement shown in Fig. 7.10, nor a flipping at higher voltages as in Fig. 7.11.

A model that might explain these observations is presented in the following. As mentioned above, the presence of the STM tip might lower the energy barrier between the two configurations. This is schematically shown in Fig. 7.13, where the black line represents a cross section along a hypothetical potential energy surface for the two configurations of the centered rare earth silicide clusters. Herein, the stable configurations of the clusters form minima with an identical depth due to the equivalence of the two configurations. Between these two configurations the aforementioned barrier is present. Now, an STM tip comes into play and lowers

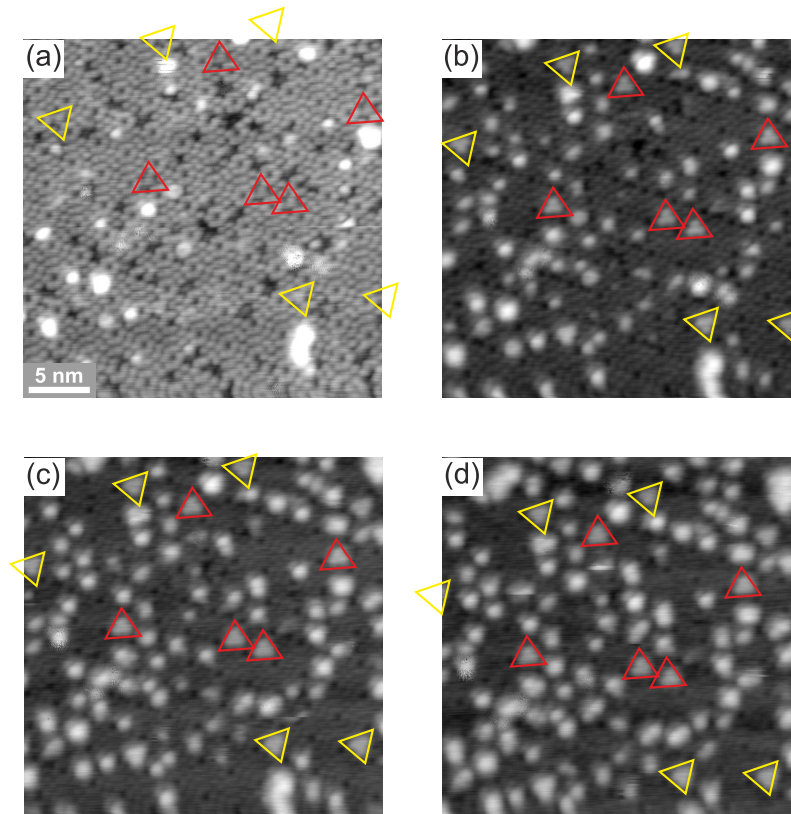


**Figure 7.12:** Subsequently acquired empty states STM images of a Si(111)7×7 sample with centered Tb silicide clusters (0.06 ML Tb deposited at 375 °C). (a)  $V_S = +1.0$  V and  $I_T = 100$  pA, (b)  $V_S = +1.5$  V and  $I_T = 100$  pA,  $V_S = +2.0$  V and  $I_T = 100$  pA, and (d)  $V_S = +2.5$  V and  $I_T = 70$  pA. In the images, the configurations of the clusters are indicated again by yellow and red triangles. For the duration of the measurement, no clusters are found showing a flipping into another configuration.

the barrier between the two configurations as it is illustrated by the green line. When the tip approaches the surface, the barrier becomes smaller and smaller until the Tb atoms can overcome the barrier by thermal excitation or tunneling and the clusters can switch between the two configurations. This is the situation present in the measurement shown in Fig. 7.10, where a flipping of the clusters is only observed at low positive tunneling voltages.

However, when the interaction between the tip and the clusters is stronger, the clusters might already thermally overcome the barrier at tunneling conditions where the tip is further away from the sample. On the other hand, if the interaction is too small, the barrier is not lowered sufficiently and no flipping occurs at all. These two situations are illustrated by the red lines in Fig. 7.13 and might explain the observations in Figs. 7.11 and 7.12 where either a flipping is always or never observed, respectively. The different interaction strengths between the tip and the clusters might be caused by different structures and in particular different terminations of the used STM tips. In the present case, interactions with the sample surface may lead to Si or Tb/Dy terminations instead of a pure W tip. Under these assumptions, a controlled switching of the centered rare earth silicide clusters from one configuration into the other is only possible with an appropriate tip. Unfortunately, also due to the difficulties described here, such a reproducible switching in a controlled way has not been achieved yet.

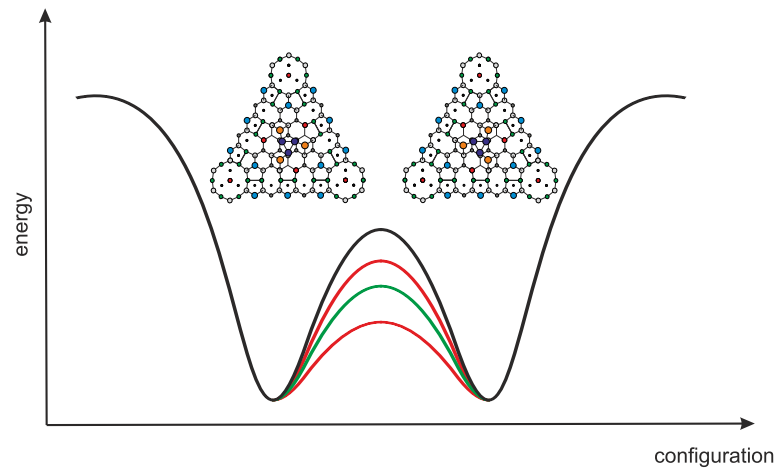


**Figure 7.13:** Schematic model for the flipping process of the centered rare earth silicide clusters. The black line illustrates the assumed potential energy variation without the presence of an STM tip, or with a tip-sample distance too large to disturb the system. When the STM tip approaches the clusters, the energy barrier might be lowered, as it is indicated by the green line, and the clusters may overcome the barrier and flip between the two configurations. On the other hand, the red lines indicate smaller and larger interactions between the tip and the clusters, leading to either a flipping already at larger tip-sample distances or to a complete suppression of the flipping.

However, due to a better understanding of the processes that take place in this system, this might be achieved in the near future, although further experiments are required to distinguish which processes might be responsible for the assumed lowering of the energy barrier.

### 7.3.3 Electronic properties of centered rare earth silicide clusters

Similar to the off-center rare earth silicide clusters, also the apparent height of the centered clusters with respect to the surrounding Si(111)7×7 surface decreases with decreasing absolute value of the tunneling voltage (see e.g. Figs. 7.10 and 7.12). Hence, it is assumed that the centered rare earth silicide clusters exhibit a semiconducting behavior, as already shown for the off-center clusters. Again, STS is used for a more detailed investigation of the electronic properties of the centered Tb silicide clusters. As it was already discussed earlier for the off-center Dy silicide clusters, it was not possible to perform STS measurements for this material system because of the STM control unit installed at that time. However, due to the very similar behavior of both systems, it is assumed that the STS results obtained for the centered Tb silicide clusters are similarly valid also for the centered Dy silicide clusters.

In Fig. 7.14 (a) and (b),  $I-V$  and  $dI/dV-V$  spectra measured on centered Tb silicide clusters are shown. The  $dI/dV-V$  spectra were measured simultaneously with the  $I-V$  curves using a software lock-in amplifier with a modulation frequency of 1 kHz and a modulation amplitude of 50 mV. The tip height was stabilized using conditions of  $V_S = -2.0$  V and  $I_T = 100$  pA, additionally the tip was approached towards the sample by 100 pm during the STS measurements. Fig. 7.14 (c) shows the normalized differential conductivity, which was calculated by using the procedure introduced by Prietsch *et al.* [77] and averaging over measurements with the tip approached by 100 pm and by 120 pm. For comparison and to ensure

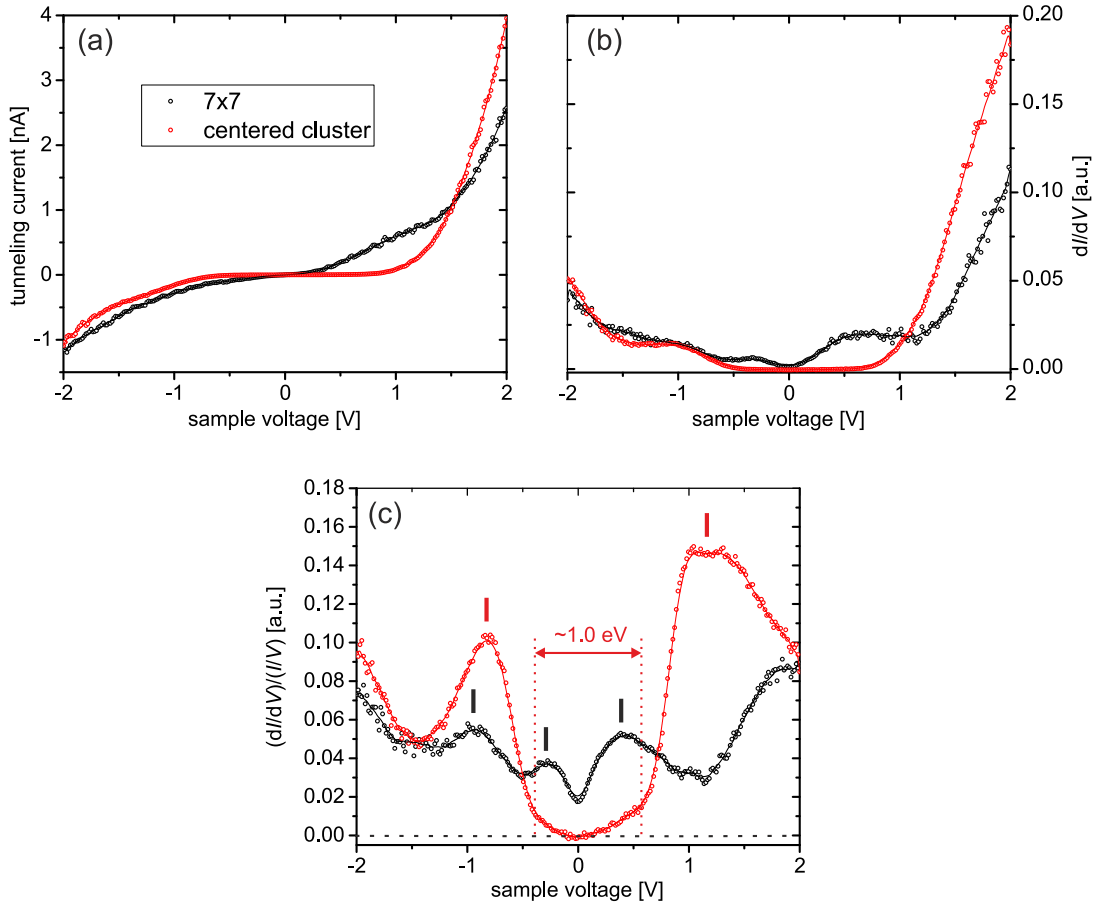


**Figure 7.14:** (a)  $I$ - $V$  and (b)  $dI/dV$ - $V$  spectra measured on centered Tb silicide clusters (red) and the surrounding Si(111) $7\times 7$  surface (black) using the same tip. (c) Normalized differential conductivity  $(dI/dV)/(I/V)$ . Features in the spectra of the centered clusters and the clean  $7\times 7$  surface are marked by red and black bars, respectively. The band gap of the centered Tb silicide clusters is estimated to  $\sim 1.0$  eV as indicated.

the quality of the used tip, STS measurements were also performed on the clean Si(111) $7\times 7$  surface surrounding the clusters. In contrast to the spectra measured on the centered Tb silicide clusters (red curves), the  $7\times 7$  surface clearly shows a metallic behavior with the occupied and unoccupied adatom states at  $-0.3$  V and  $+0.4$  V, respectively, and the rest atom state at  $-0.9$  V, as it is indicated by the black bars in Fig. 7.14 (c), being in good agreement with the data from literature (cf. section 3.2.1), in this way demonstrating the quality of the tip. In the spectra measured on the centered clusters, clearly a band gap separating two distinct features appears. One sharp feature occurs at about  $-0.8$  V and a second broad feature which might consist of two peaks at around  $+1.1$  V. The band gap in between is estimated to about 1.0 eV as it is indicated in (c). However, as it was also observed in tunneling spectra of the magic In clusters (cf. section 6.1.2), the local density of states is not zero in the entire band gap, but an increase in the signal is observed already at the positions where the adatom states are found in the spectrum measured on the clean Si(111) $7\times 7$  surface. This is again assigned to MIGS resulting from the adatom states of the surrounding  $7\times 7$  surface penetrating into the band gap of the centered Tb silicide clusters.

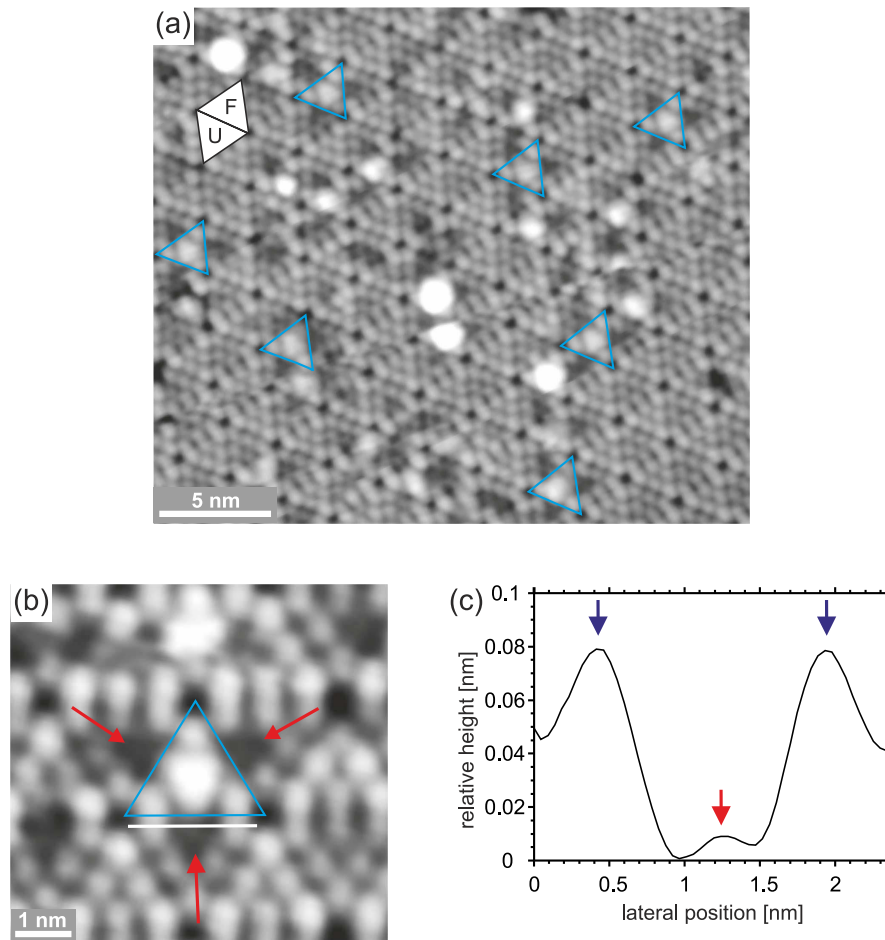


**Figure 7.15:** (a) Overview and (b) detailed filled states STM images ( $V_S = -2.0$  V and  $I_T = 70$  pA) of centered Dy silicide clusters formed after deposition of 0.06 ML Dy at 350 °C. HUCs with centered clusters are indicated by blue triangles. In (b), the darker appearing Si center adatoms in neighboring HUCs are indicated by red arrows. (c) Height profile taken along the white line indicated in (b). Again, the Si center adatom is indicated by the red arrow while the blue arrows indicate Si corner adatoms.

In addition, another effect which is observed for the magic In clusters is also observed here for the centered rare earth silicide clusters. Figure 7.15 (a) and (b) shows filled states STM images of centered Dy silicide clusters. In clean  $7 \times 7$  HUCs, which are neighboring HUCs with centered clusters, the Si center adatoms nearest to the centered clusters [indicated by red arrows in (b)] appear with a significantly reduced height, as can be also seen in the height profile shown in (c). Here, the Si center adatom next to the centered Dy silicide cluster in the neighboring HUC (again indicated by the red arrow) is imaged about 0.7 nm lower than the Si corner adatoms (indicated by blue arrows). As pointed out earlier for the magic In clusters (see section 6.1.2), this behavior may be the result of a charge transfer from these center adatoms into the clusters. Such a behavior was also observed by Zhou *et al.* for Zn clusters on Si(111) $7 \times 7$  [16].

## 7.4 Conclusions

In this chapter, clusters forming after deposition of the trivalent rare earth metals Dy and Tb on Si(111)7×7 were investigated. For both materials, a similar growth with the formation of two main cluster types, the so-called off-center and centered rare earth silicide clusters is found.

Regarding both cluster types, the atomic structure could be determined and the electronic properties were investigated using STS. The off-center clusters thereby exhibit an analogous atomic structure as magic Co and Fe silicide clusters [13,14,273] with an RE<sub>6</sub>Si<sub>3</sub> stoichiometry, while the centered clusters exhibit a RE<sub>3</sub>Si<sub>3</sub> stoichiometry and form asymmetrically within the 7×7 HUC. This asymmetric orientation leads to two equivalent configurations which appear rotated by ~60° with respect to each other in empty states images.

The STS measurements performed on both cluster types for Tb show a semiconducting nature of the clusters with band gaps of ~0.7 eV for the off-center Tb silicide clusters and ~1.0 eV for the centered Tb silicide clusters. Although no STS measurements were performed on Dy silicide clusters, voltage dependent STM images also suggest a semiconducting behavior with similar band gaps.

Although exhibiting a different atomic structure, several similarities exist between the centered rare earth silicide clusters and other material systems where centered clusters form. Besides showing a similar appearance in filled states images, a semiconducting behavior and a charge transfer from Si adatoms in neighboring HUCs is observed. However, the switching behavior, which occurs due to the two equivalent asymmetric orientations, distinguishes the centered rare earth silicide clusters found here from the other centered cluster systems. A model explaining this switching process via an interaction between the Tb cluster atoms and the STM tip was developed. Such a bistable switching is, when it can be performed in a controlled way, extremely interesting for potential future applications of these clusters, e.g. as logic gates or as memory cells. In the past, already several other atomic scale switches using an STM to perform a reversible switching were demonstrated [29–35]. However, most of them are constructed using atomic manipulation or operate only at cryogenic temperatures. Since the centered rare earth silicide clusters investigated here are prepared by self-assembled growth, many times higher cluster densities can be obtained in a very short time. In addition, the growth on a Si substrate would allow an easy and cost efficient implementation in existing semiconductor fabrication processes. Moreover, operation might be possible at room temperature.

---

## Chapter 8

# Dy silicide clusters on the Si(001) $2\times 1$ surface

Regarding the rare earth metal Dy, besides the growth of clusters on the Si(111) $7\times 7$  surface, also the cluster growth on the Si(001) surface is investigated within this thesis. In contrast to the  $7\times 7$  reconstruction on the Si(111) surface, where a multitude of materials are found to form magic clusters due to the distinct template effect that this reconstruction offers, on the Si(001) $2\times 1$  surface only clusters of the group-III metals In and Al where, to the best of my knowledge, investigated up to now (cf. section 3.5.2).

In order to discover the growth of magic clusters, the measurements performed within this work concentrated on the low Dy coverage and low growth temperature regime, since for higher coverages and temperatures the formation of different types of surface reconstructions and nanowires was found [158, 386, 389–391, 395–398].

In the following section, first the general growth behavior for Dy on the Si(001) $2\times 1$  surface is described, before the Dy induced magic clusters, which are found to form chains consisting of identical clusters, are analyzed in detail in sections 8.2 to 8.4.

### 8.1 General growth behavior

Within this work, the growth parameters in the low Dy coverage and low growth temperature regime were systematically varied to investigate the growth behavior of magic Dy clusters on Si(001). Therefore, Dy coverages between 0.05 ML and 0.47 ML were employed, and growth temperatures between room temperature and 500 °C were used. It was found that RDE, where Dy is deposited on the sample held at growth temperature, results in a more homogeneous growth than SPE, where Dy is deposited at room temperature and the sample is subsequently annealed. Hence, RDE was employed in the majority of the preparations.

While for deposition at room temperature and very low Dy coverages (not shown) only inhomogeneous structures are found to appear sporadically, at growth temperatures between 300 °C and 400 °C the formation of ordered structures is observed, as shown in Fig. 8.1. At low coverages, as shown in (a), many of the structures form separately from each other, while with

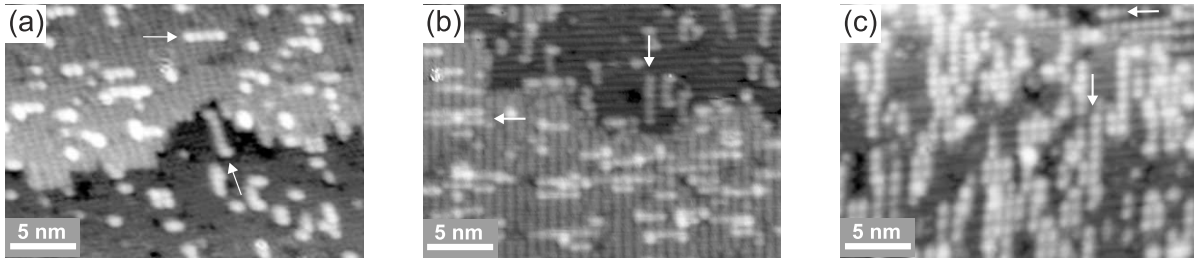


**Figure 8.1:** Overview empty states STM images showing the growth behavior of Dy induced clusters on the Si(001)2×1 surface. (a) 0.12 ML Dy deposited at 300 °C ( $V_S = +2.0$  V;  $I_T = 200$  pA). (b) 0.23 ML Dy deposited at 300 °C ( $V_S = +2.0$  V;  $I_T = 200$  pA). (c) 0.47 ML Dy deposited at 300 °C ( $V_S = +2.3$  V;  $I_T = 500$  pA).

increasing coverage [Fig. 8.1 (b) and (c)], the formation of chains running perpendicular to the dimer rows of the Si(001)2×1 reconstruction is observed. Since the orientation of the Si dimers rotates by 90° when crossing a monoatomic step (cf. section 3.2.3), also the chain orientation changes from one terrace to the neighboring one as indicated by the arrows in Fig. 8.1. It was found that these chains consist of different numbers of identical clusters. These magic clusters and cluster chains will be analyzed in detail in the following sections.

When going to higher annealing temperatures of around 500 °C, the growth behavior changes and the growth regime is reached, in which the Dy induced submonolayer reconstructions and nanowires mentioned earlier start to form. This situation is shown in Fig. 8.2, where 0.47 ML Dy were deposited followed by an annealing to 500 °C. In (a), an overview STM image of the obtained sample surface is shown. As indicated by the white arrows, distinct nanowires are found on the surface. From literature, it is known that these nanowires consist of anisotropically strained, hexagonal DySi<sub>2</sub> [158, 389–391, 398, 399]. Due to a large mismatch in the hexagonal *c*-direction and an almost perfect matching of the lattice constants in the hexagonal *a*-direction, a one-dimensional growth occurs in this system. It has to be mentioned

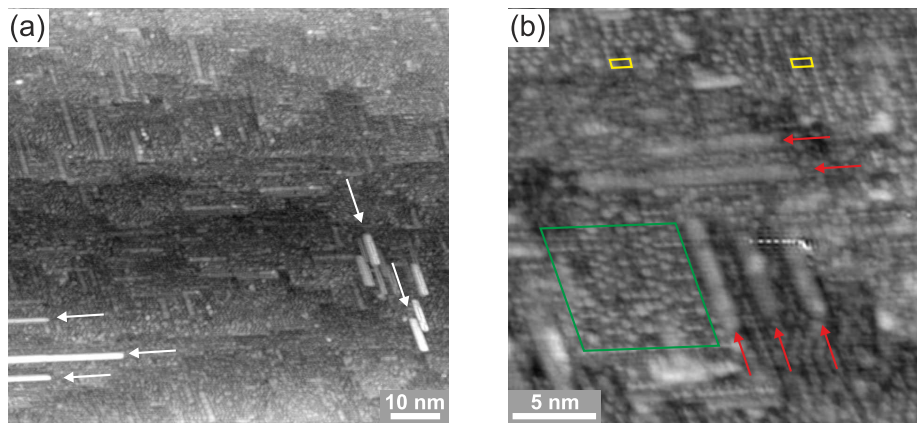


**Figure 8.2:** (a) Overview ( $V_S = -1.0$  V;  $I_T = 1$  nA) and (b) detailed ( $V_S = +0.5$  V;  $I_T = 200$  pA) STM images of a Si(001) surface with a Dy coverage of 0.47 ML and subsequent annealing at 500 °C. In (a), DySi<sub>2</sub> nanowires are marked by the white arrows, in (b) the red arrows mark the local formation of the 2×7 reconstruction, 2×4 unit cells are exemplarily indicated in yellow, and a more disordered region in green.

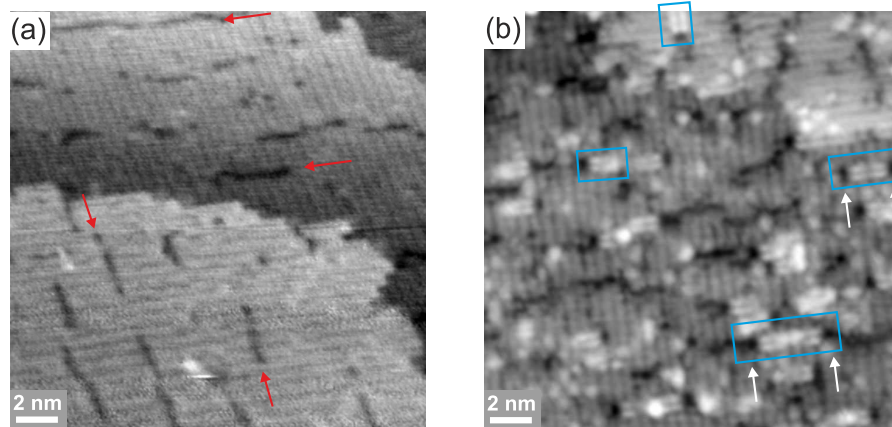


**Figure 8.3:** (a) Empty states STM image ( $V_S = +2.5$  V;  $I_T = 300$  pA) of a Si(001) surface without deposition of Dy, and (b) empty states STM image of the same surface after deposition of 0.09 ML Dy at 400 °C ( $V_S = +1.5$  V;  $I_T = 100$  pA). In (a), an ordering of missing dimer defects into rows indicating a Ni contamination is found, as exemplarily marked by red arrows. In (b), the blue rectangles mark Dy induced structures that are assumed to form due to the Ni contamination observed in (a).

that a tip artifact, a so-called multiple tip, is present in the image, thus identical nanowires are imaged several times.

In the areas between the nanowires, no clean Si(001) $2\times 1$  reconstruction is found, but other Dy induced reconstructions form. In Fig. 8.2 (b), a detailed STM image of such a region is shown, with different structures appearing. However, also these structures are well known from other studies and can thus be assigned by a comparison with the data published in literature [386, 391, 395–398]. By measuring their periodicities, the structures indicated by the red arrows can be assigned to the  $2\times 7$  reconstruction. However, it seems that the patches of this reconstruction present on the surface represent rather the initial stages of the growth of this reconstruction since no larger arrays of the reconstruction are present as it is usually observed. The second structure, which can be identified in the image in Fig. 8.2 (b), is the  $2\times 4$  reconstruction [390, 396]. Exemplarily, two  $2\times 4$  unit cells are indicated. However, a long range order is missing also because this reconstruction shows two different appearances: A  $2\times 4$  unit always appears as three maxima with different heights in the STM image, either showing a high-low-high appearance or a low-high-low arrangement. Besides the two mentioned superstructures, which are assumed to represent a wetting layer for the growth of the DySi<sub>2</sub> nanowires, also regions with a less ordered appearance such as the area indicated by the green rectangle in Fig. 8.2 (b) are present.

It should be mentioned that, in some preparations, also other cluster-like structures were found, as shown in Fig. 8.3. These structures which are exemplarily indicated by blue boxes in Fig. 8.3 (b) appear as two parallel rows, often being located between two missing dimer defects of the Si(001) $2\times 1$  substrate as exemplarily indicated by the white arrows. The measurements, where these structures are found, were all done using the same Si(001) substrate, of which an STM image is shown in Fig. 8.3 (a). In the image, dark lines are present, as exemplarily indicated by the red arrows, which are assigned to a linear ordering of missing dimer defects,

probably induced by a small Ni contamination (cf. section 3.2.3). Since the structures found in (b) are only observed on this surface, it is concluded that they form at the line defects that are present due to the Ni contamination, a view that is further supported by the observation of such defects at the ends of the structures. However, since no such structures are found when depositing Dy on clean Si(001) samples, they were not further investigated, and the detailed analysis in the following section concentrates on the Dy induced magic clusters forming the chains shown in Fig. 8.1.

## 8.2 One-dimensional ordering of Dy induced magic clusters on Si(001)

Overview empty states STM images of magic Dy induced clusters are shown in Fig. 8.4 (a) and (b). At the applied relatively high positive tunneling voltages, the clusters, which are indicated by the yellow rectangles, appear as two bright protrusions. At the lower coverage shown in (a), single clusters are frequently found, while for the higher coverage shown in (b), mostly chains appear on the surface. A detailed investigation of these chains reveals that they are composed of identical structural units, which are the magic Dy clusters. In the STM images, all the chains show an appearance that can be derived by stringing together magic clusters, each with an appearance as two bright protrusions. This is exemplarily indicated in the STM images, where green rectangles represent chains formed from two clusters and blue rectangles those from three clusters.

In the following, it is argued that these nanostructures can indeed be considered as magic clusters instead of a common two-dimensional surface reconstruction. As can be seen from Fig. 8.4 (a), the clusters form randomly distributed on the surface at low coverages. This is in contrast to common superstructures, where a preferential nucleation at step edges or other defect sites and an instantaneous growth of larger domains with the respective superstructure occurs already at low coverages. Although the clusters often form at defects as it is indicated by the white arrows in Fig. 8.4 (a), such a behavior is definitely not observed in the present case. Especially a preferential nucleation at step edges can easily be ruled out by the STM images shown in Fig. 8.1, where no domain formation at the step edges is found. The chains are then built up as one-dimensional assemblies of clusters similar to the case of the In and Al clusters on Si(001), where at low coverages first a random distribution is observed, while at higher coverages the clusters form an array, which is two-dimensional in that case (cf. section 3.5.2). Hence, the nanostructures discovered here do indeed represent a new system of magic clusters that additionally forms chains due to a one-dimensional ordering of the clusters at higher coverages, a behavior that was, to the best of my knowledge, never observed before on the Si(001) surface.

Already from the STM images in Fig. 8.4 (a) and (b), with the dimer rows of the Si(001)2×1 surface being visible besides the clusters, the length of a magic cluster can be estimated to correspond to about four times the surface lattice constant, since one cluster extends over roughly two dimer rows. However, for a more detailed analysis also in the direction perpendicular to

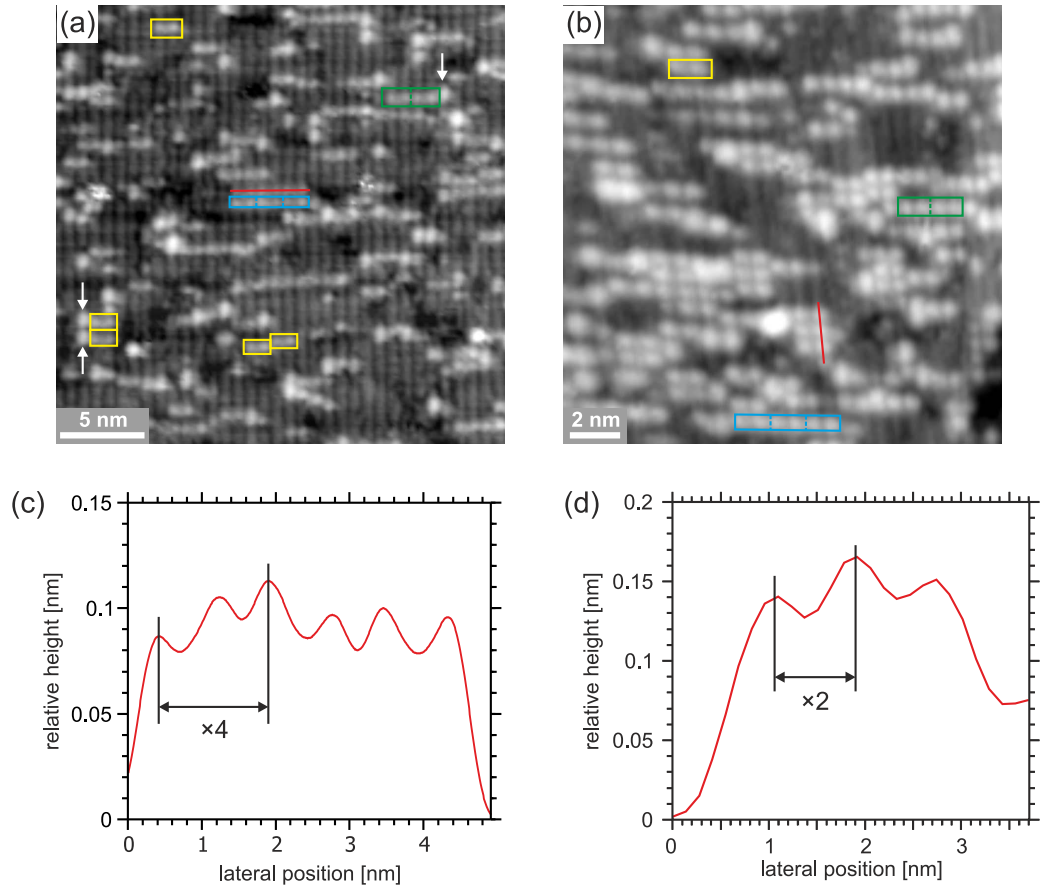


**Figure 8.4:** (a,b) Empty states STM images of Dy induced clusters on the Si(001) surface prepared by depositing (a) 0.23 ML Dy ( $V_S = +2.0$  V;  $I_T = 1$  nA) and (b) 0.47 ML Dy at 300 °C ( $V_S = +2.3$  V;  $I_T = 500$  pA). Single clusters are exemplarily indicated in yellow, chains consisting of two and three clusters in green and blue, respectively. Often, the clusters form at defects as indicated by the white arrows in (a). (c,d) Height profiles taken along the red lines in (a) and (b), respectively.

the cluster, Fig. 8.4 (c) and (d) show height profiles taken along the lines indicated in (a) and (b). Thereby, the height profile in (c) shows a chain composed of three magic clusters, enabling the determination of the periodicity within the chains. As indicated in the image, a periodicity of four times the lattice constant of the Si(001) surface of 0.384 nm (cf. Table 3.1), as it was supposed above, is indeed found. The determination of the dimensions of the clusters perpendicular to the chain direction, i.e. in the direction of the dimer rows, is more difficult, since no resolution was achieved within the Si dimer rows simultaneously with the clusters. Hence, to calibrate the height profiles in this direction, images with monoatomic steps and thus the presence of the second domain, in which the dimers are rotated by 90°, were used such as the STM image shown in Fig. 8.4 (b). The height profile shown in Fig. 8.4 (d) shows three clusters formed with the closest observed distance. The distance between two maxima in the height profile corresponds to about two times the lattice constant as indicated. Hence, one cluster extends over an area of  $2 \times 4$  times the surface lattice constant. However, no formation of a two-dimensional array showing a  $2 \times 4$  periodicity is observed for a larger area, also not for the rather high coverage in in Fig. 8.4 (b). Such a formation might be hindered by the random nucleation of the clusters, which often results in odd numbered spacings of e.g. three

times the lattice constant perpendicular to the cluster chains, which are possible due to the  $\times 1$  periodicity of the Si(001) substrate along the dimer rows. This allows also an alignment with a displacement of the clusters by one lattice constant within a cluster chain. Such a displacement, as it is observed e.g. in Fig. 8.4 (a) for two clusters marked by yellow boxes, results in the occasional observation of chains that exhibit a slight bending.

### 8.3 Voltage dependent appearance of Dy induced magic clusters on Si(001)

The STM images of the magic Dy induced clusters presented up to now were all acquired using relatively high positive tunneling voltages of +2 V and more. In this voltage range, usually the best image quality for the magic clusters is achieved. Certainly, also STM images using other tunneling voltages of both polarities were recorded. The STM images show a strong voltage dependency, but depend also strongly on the quality of the used STM tip. This is especially the case for filled states STM images such as Fig. 8.5 (a). However, in principle, a similar behavior with the cluster chains being imaged best at relatively high absolute values of the tunneling voltage is found also for the filled states images.

A comparison between the appearance in the filled states and empty states images is presented in Fig. 8.5 where the same area of the surface was measured using a tunneling voltage of (a)  $-2.0$  V and (b)  $+2.0$  V. In this area, a single cluster as well as a chain consisting of two clusters are formed, as indicated by the yellow and green rectangles, respectively. In the empty states image in (b), the appearance already known from the previously presented STM images is found, with the clusters appearing as two bright protrusions. In contrast, the clusters appear less bright in the filled states image. In addition, they do not appear as two bright protrusions, but only as one bright protrusion in the cluster center. This bright protrusion is surrounded by two darker protrusions close to the locations of the Si dimer rows. It has to be mentioned that the alignment of the rectangles indicating the clusters in (a) with respect

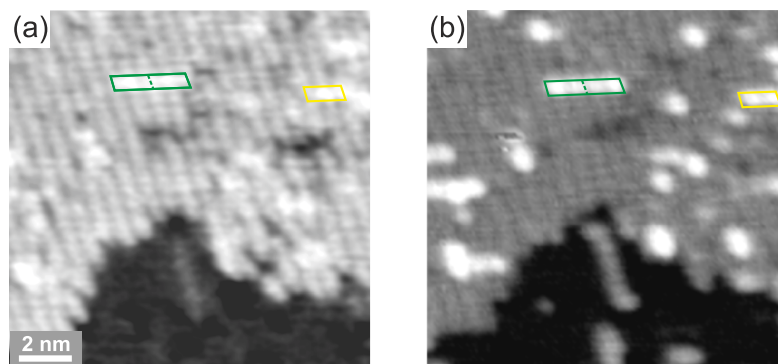


**Figure 8.5:** (a) Filled states STM image ( $V_S = -2.0$  V;  $I_T = 200$  pA) and (b) empty states STM image ( $V_S = +2.0$  V;  $I_T = 200$  pA) of the same area of a Si(001) sample with Dy induced clusters prepared by a deposition of 0.12 ML Dy at 300 °C. In both images, the yellow and green rectangles indicate a single cluster and a chain of two clusters, respectively.

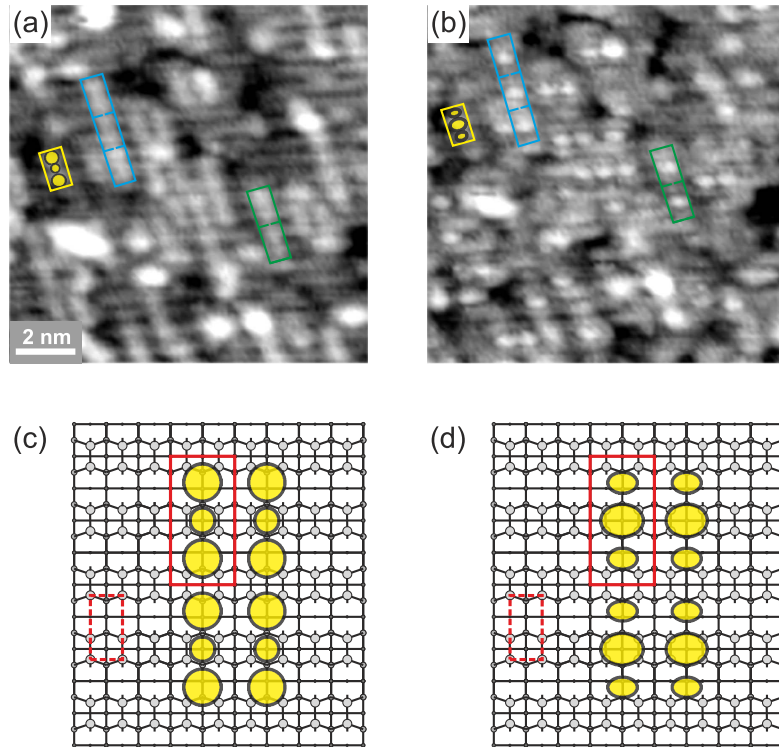


**Figure 8.6:** (a,b) Empty states STM images of the same area of a Si(001) sample with Dy induced clusters, prepared by depositing 0.47 ML Dy at 300 °C, acquired using (a) a higher tunneling voltage ( $V_S = +2.0$  V;  $I_T = 200$  pA) and (b) a lower tunneling voltage ( $V_S = +1.5$  V;  $I_T = 200$  pA). In the images, the yellow, green, and blue rectangles exemplarily indicate a single cluster, a chain of two clusters and one of three clusters, respectively. For one single cluster, the appearance in the respective images is indicated. (c,d) Atomic structure models of the Si(001) $2\times 1$  reconstruction with the appearance of the cluster at (c) higher and (d) lower positive tunneling voltages. A  $2\times 1$  unit cell is indicated by the dashed red line, a  $4\times 2$  unit cell by the solid red line.

to (b) is correct, although the bright protrusions in the clusters are in both images observed near the positions of the bright lines of the Si(001) $2\times 1$  substrate. This effect is related to the inversion of the contrast observed for the Si(001) $2\times 1$  surface, where a bright contrast in the filled states is observed at the location of the dimer rows, but in empty states STM images the bright contrast appears at the location of the trenches in between the dimer rows [225, 226], as it has been also described earlier in section 3.2.3. Hence, an inversion of the contrast is observed also for the Dy induced clusters, although it cannot be excluded that the contrast might change again when varying the negative tunneling voltage since no adequate resolution could be achieved here.

Indeed, such a contrast inversion when varying the absolute value of the tunneling voltage is observed in the empty states images, as shown in Fig. 8.6. In the STM image acquired using a higher voltage shown in (a), the clusters appear again as two bright protrusions. However, due to a better resolution, even a third, darker maximum is observed in the cluster center in between the two bright protrusions, as exemplarily indicated by yellow circles. This appearance is reproducibly observed also using other STM tips. Thus, a tip artifact can be excluded, also since a multiple tip would result in additional artifacts at the ends of cluster chains. As

mentioned above, the appearance changes at lower positive tunneling voltages as shown in Fig. 8.6 (b). Here, like in the filled states image shown in Fig. 8.5 (a), the clusters show an appearance with the brighter protrusion being located at the cluster center surrounded by two darker protrusions, as indicated exemplarily for one cluster. In addition, the protrusions exhibit a pronounced elliptical shape as compared to a rather round appearance observed in (a). In the following, the two appearances are referred to as high-low-high (HLH) for an appearance as found e.g. at high positive tunneling voltages such as Fig. 8.6 (a), and low-high-low (LHL) for the appearance found e.g. for lower positive voltages such as Fig. 8.6 (b).

These two appearances are again shown together with the structure model of the Si(001)2×1 surface in Fig. 8.6 (c) for an HLH appearance and in (d) for an LHL appearance. The registry in the direction perpendicular to the dimer rows can therein be assigned from the STM images. Since the STM image in (a) with the HLH appearance shows a dark contrast at the dimer rows of the Si(001)2×1 reconstruction, the position of the darker appearing protrusions can be assigned to be located in registry with the dimer rows, while the bright protrusions are found to be located in the area of the trenches between the dimer rows. Thereby, they do not appear centered within the trenches, but are shifted slightly outwards. In the LHL appearance, apart from the contrast inversion, the protrusions seem to appear at the same locations as shown in Fig. 8.5 (d). However, it has to be mentioned that, due to a lack of resolution within the dimer rows of the 2×1 reconstruction, the registry of the clusters with respect to the dimers along the dimer rows cannot be determined. Hence, in this direction, the registry shown in Fig. 8.5 (c) and (d) is only tentative.

## 8.4 Structural considerations

In order to develop an atomic structure model for the Dy induced magic clusters on the Si(001) surface, first the Dy content of the clusters is estimated. Therefore, the fraction of the surface covered with Dy induced structures is determined taking into account STM images from measurements with 0.23 ML Dy and 0.47 ML Dy deposited at 300 °C, with an overall area corresponding to about 7000 2×1 unit cells. All Dy induced structures are thereby estimated to exhibit the same Dy content per area. From this, a Dy content in the clusters of  $(2.6 \pm 0.3)$  Dy atoms per 2×1 unit cell is obtained, thus a magic cluster is estimated to contain about 10 Dy atoms. However, the given uncertainty applies only for this estimation. Due to the formation of a large number of structures with an unknown Dy content besides the magic clusters, the error in the Dy content might be much larger. Nevertheless, the estimation gives a hint for the range, in which the Dy content should be.

In a second step, the Dy induced magic clusters are compared with other structures known from literature which show similarities to the system investigated here, in order to draw conclusion on the atomic structure. One such system is the Dy induced 2×4 reconstruction [390,396], which is also found in the present work at higher annealing temperatures (see Fig. 8.2). In the STM images published in Ref. [396], this structure shows a very similar appearance to the Dy induced magic clusters with an HLH or an LHL arrangement of three protrusions, thus

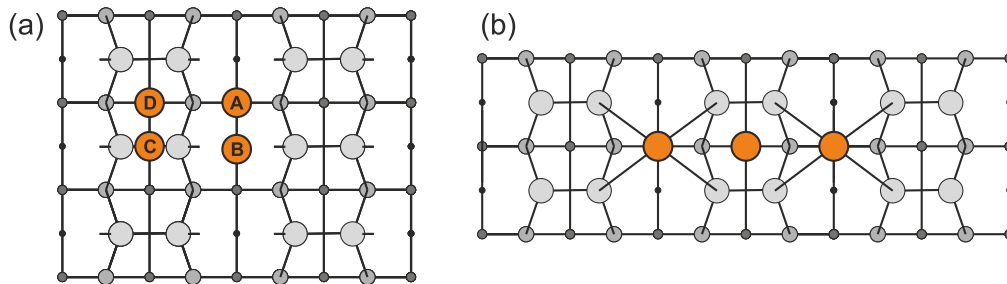


**Figure 8.7:** (a) Structure models of the  $\text{Si}(001)2\times 1$  surface with a La atom at the high symmetry adsorption sites indicated with A to D. Adapted from [400]. (b) Tentative structure model for the Dy induced clusters on  $\text{Si}(001)$  by simply placing Dy atoms at the energetically most favorable adsorption sites.

one could assume that the magic clusters represent an early stage of the formation of this reconstruction and consist of identical building blocks. However, for the  $2\times 4$  reconstruction the HLH and LHL features are observed simultaneously in the same image, in contrast to the case of the magic clusters, where they correspond to different appearances of the same cluster at different tunneling voltages. In addition, the LHL and HLH features of the Dy induced  $2\times 4$  reconstruction form parallel to the Si dimer rows while in the present work, the three protrusions are aligned perpendicular to the dimer rows. Hence, a similar structure of the  $2\times 4$  reconstruction and the Dy induced magic clusters can be excluded. In addition, as mentioned before, the  $2\times 4$  reconstruction forms at much higher temperatures of at least  $500\text{ }^\circ\text{C}$ , as compared with the Dy induced magic clusters forming between  $300\text{ }^\circ\text{C}$  and  $400\text{ }^\circ\text{C}$ . At such high temperatures, a silicide formation very likely takes place, which might be suppressed for the present cluster growth due to the low growth temperatures. Thus, also a formation of cagelike structures, which is often observed for rare earth silicides such as the Dy induced  $2\times 7$  reconstruction [395], does not seem likely here.

Other systems showing similarities to the present one are obviously the magic In and Al clusters on the  $\text{Si}(001)$  surface, since they represent the only other known cluster systems on  $\text{Si}(001)$  (cf. section 3.5.2). The structure model of these clusters is shown in Fig. 3.19 (b). However, in contrast to the Dy induced clusters, the In and Al clusters cover an area of  $4\times 3$  unit cells of the unreconstructed  $\text{Si}(001)$  surface. In addition, as can be seen from Fig. 3.19 (a), the center of the cluster is located above the trench between the dimer rows and not, as in the present case of the Dy induced clusters, above a dimer row of the  $2\times 1$  reconstruction. Hence, the atomic structure model of these clusters has also to be excluded as a candidate for the Dy induced clusters.

Since none of the published structure models is able to explain the features observed for the new system of Dy induced magic clusters, independent structural considerations need to be conducted. For La, which is chemically very similar to Dy, Ashman *et al.* calculated the preferential adsorption sites of atoms, dimers, and chains on the  $\text{Si}(001)$  surface using DFT [400]. For single La atoms, the situation is shown in Fig. 8.7 (a). The most stable adsorption site is found at the position between four dimers indicated by A. The positions

indicated by D, B, and C have energies, which are by 0.23 eV, 0.51 eV, and 1.7 eV higher, respectively.

However, by only utilizing single atoms as building blocks of the clusters, a maximum Dy content of three atoms is achieved, as it is exemplarily shown in Fig. 8.7 (b), where three Dy atoms are placed at positions indicated by A and D in (a), corresponding to the two lowest energy sites. Although a structure model as shown in (b) might be able to explain the contrast observed in the experimental STM images, the Dy content of three atoms is much lower than the one estimated for a Dy induced cluster. Hence, more Dy atoms need to be included to approach the estimated content of  $\sim 10$  atoms. In Ref. [400], also La dimers were investigated, and dimers forming perpendicular to the Si dimers, and thus parallel to the dimer rows, were found to be the most stable ones. However, the distance between the La dimer atoms was found to be 0.41 nm, being larger than the surface lattice constant of 0.384 nm, and thus preventing the formation of structures with a  $\times 2$  periodicity in this direction. Nevertheless, due to the lanthanide contraction Dy has a smaller covalent radius than La, so that a shorter bond length is expected. Hence, structures including Dy dimers parallel to the dimer rows might be possible, but a structure model formed exclusively by parallel Dy dimers above the trenches of the  $2\times 1$  reconstruction would result in a  $\times 2$  periodicity along the cluster chains instead of the  $\times 4$  periodicity, which is experimentally observed. In addition, the Dy content of four atoms would be still too low.

To explain the  $\times 4$  periodicity, further Dy atoms can be incorporated at the location of the central dimer row of the Si(001). Figure 8.8 (a) and (b) shows two possible structure models with such an additional Dy incorporation. In (a), only a single Dy atom is incorporated in the cluster center leading to an overall Dy content of five atoms. This is still much less than the estimated value of  $\sim 10$  atoms. However, the deviation may be explained by the unknown error resulting from assuming a similar Dy content per area for all structures found on the surface. The dimers therein are assumed to have a length corresponding to the surface lattice constant of 0.384 nm (cf. Table 3.1) as it is derived from the covalent radius of 0.192 nm for Dy [368]. It is further assumed that the Si dimer bonds in the central dimer chain are broken, enabling a better incorporation of the central Dy atoms in an environment similar to the most stable adsorption site A in Fig. 8.7 (a).

Another possible structure model is shown in Fig. 8.8 (b). It also contains two Dy dimers above the trenches of the Si dimer rows, but in contrast to the model shown in (a), a third dimer is proposed to form in the cluster center. Therefore, as it was also proposed for the model shown in (a), the Si dimer bonds for the central Si dimer row are removed and replaced by bonds to a Dy dimer. This leads to a Dy content of six atoms being more compatible with the expected one. As will be discussed in the following, this model is also best suited to explain the experimental observations described in the previous sections. For a comparison with the experimental STM images, (c-f) show again the discussed structure models, but with the HLH and LHL appearances, which are observed for different tunneling voltages, overlaid on the atomic structure models. For the model shown in (a), a more or less symmetric formation of the Dy dimers in the center of the trenches between the Si dimer rows is expected. In

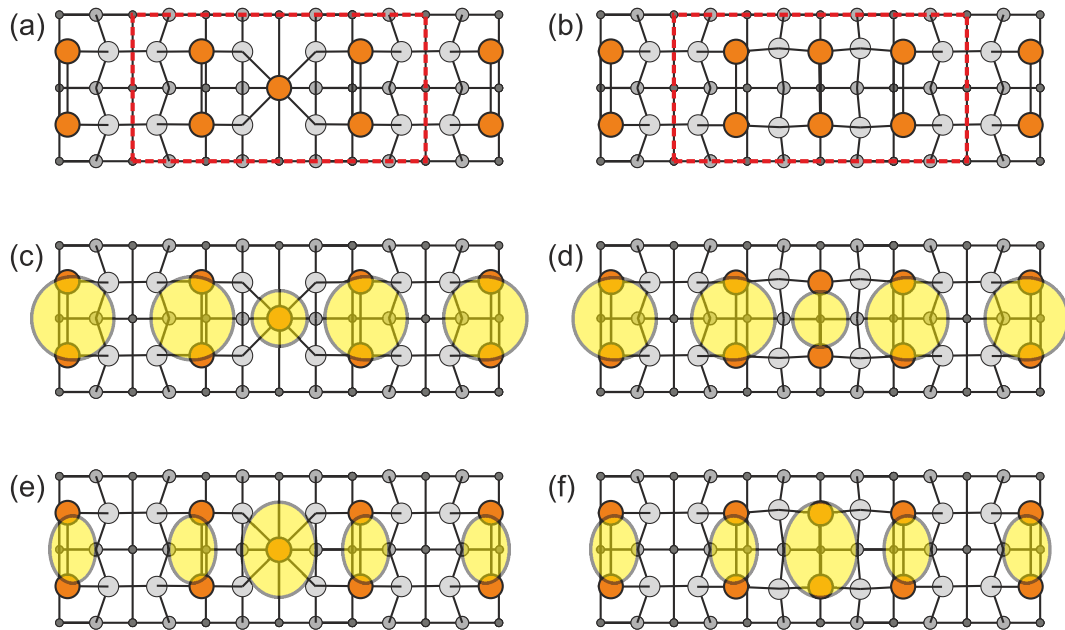


**Figure 8.8:** (a,b) Possible atomic structure models for the Dy induced magic clusters on the Si(001) surface with a Dy content of (a) five atoms and (b) six atoms. A  $4 \times 2$  unit cell is indicated by the dashed red line. (c,d) Atomic structure models shown in (a) and (b), overlaid with the HLH appearance found in STM images acquired using high positive tunneling voltages. (e,f) Same as (c,d), but for the LHL appearance found in STM images acquired using low positive or arbitrary negative tunneling voltages.

contrast, for the formation of a Dy dimer at the central location, its different bond geometry may lead to an outward displacement of the outer dimers. Thus, the locations of the Dy dimers fit much better to the positions of the observed protrusions in the STM images for both appearances, as can be seen from a comparison of (c) and (d) as well as (e) and (f). In addition, an elliptical shape of all three protrusions is observed in the STM images, especially for the LHL arrangement. For the structure in (a), the central atom is not expected to lead to such an elliptical appearance in contrast to dimers, as proposed in the model in (b). Hence, the structure model proposed in Fig. 8.8 (b) fits the available experimental data best.

## 8.5 Conclusions

In this chapter, the growth of magic Dy induced clusters on the Si(001) surface has been demonstrated. Thus, with the results obtained here, the list of materials that form magic clusters on the Si(001) surface, which up to now included only In and Al, has to be extended to Dy and presumably also to other trivalent rare earth metals, since they are chemically very similar and often form analogous structures, as it was found e.g. for the clusters on the Si(111) surface in chapter 7 or for thin rare earth silicide films (cf. section 3.6). Hence, it is assumed that the conclusions drawn in this chapter are not only valid for Dy, but also for other trivalent rare earth metals as it is also indicated by recent results for Tb on Si(001) [401].

It is found that the Dy induced clusters show a one-dimensional ordering into cluster chains, consisting of different numbers of magic clusters, a behavior that was, to the best of my

knowledge, never observed before on Si(001). Thus, besides the magic In clusters on Si(557), a second system showing the formation of one-dimensional cluster arrays has been discovered within this work.

In addition, structural considerations were conducted and an atomic structure model that might explain the experimental observations was developed. However, to ensure that it really represents the structure of the magic Dy induced clusters discovered here, further measurements, maybe with better resolution especially in the filled states images, but also theoretical investigations are required. Moreover, the cluster chains consisting of different numbers of magic clusters may represent a model system to study the effects that a chain formation might have on the electronic structure. This should be studied in future STS experiments.

---

## Chapter 9

# Thin Tb silicide films on Si(111)

The main topic of this thesis is the investigation of the growth and the properties of self-assembled magic clusters formed from various materials on Si surfaces. Regarding Tb on the Si(111) surface, very interesting clusters as described in chapter 7 were found. However, also in order to understand the growth behavior in the cluster regime, where already small islands of structures that preferentially form at higher coverages and temperatures are observed, the growth parameter range was extended in order to study also the properties of thin Tb silicide films on the Si(111) surface.

Such thin rare earth silicide films also are themselves a very interesting field of research and already attracted much attention for quite some time (cf. section 3.6) due to the possibility to grow a variety of nanostructures depending on the detailed preparation conditions. In addition, they might be also interesting for applications, e.g. as ohmic contacts on *n*-type Si due to extremely low Schottky barriers that were found for the monolayer rare earth silicides [39,50,57].

Regarding Tb, only the deposition at room temperature and much thicker Tb films were investigated up to now [38,40,53–55,402]. To the best of my knowledge, the parameter regime investigated in this work remained unexplored.

Here, a similar growth behavior is found as for other trivalent rare earth metals as described in the following section. Section 9.2 then presents a detailed analysis of the structures that are found in the submonolayer Tb coverage regime, and in section 9.3 the structures found in the monolayer-to-multilayer Tb coverage regime are described in detail.

### 9.1 General growth behavior

In contrast to the cluster growth investigated in chapter 7, higher Tb coverages of up to 2.5 ML were used in order to prepare different types of Tb induced nanostructures on the Si(111) surface, and SPE growth, where Tb is first deposited at room temperature and the sample is subsequently annealed, was typically employed.

The ideal annealing temperatures are found to be between 500 °C and 550 °C, although small islands of the structures found for submonolayer Tb coverages are already observed at

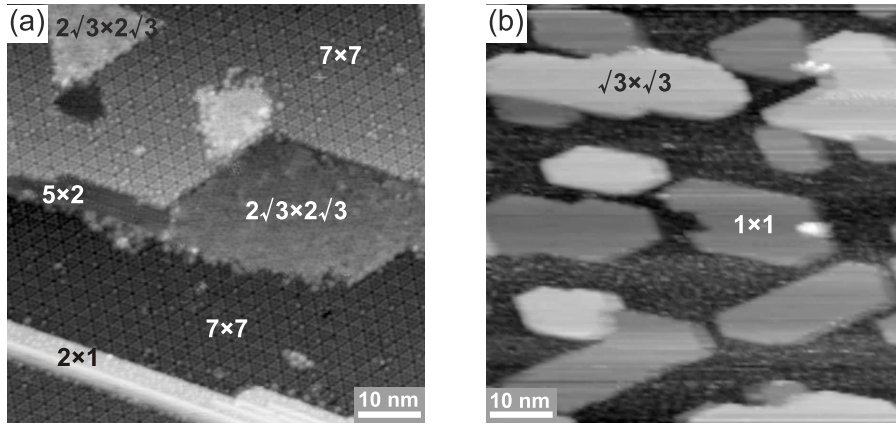


**Figure 9.1:** Overview filled states STM images of the different growth regimes. (a) The submonolayer Tb coverage regime: 0.4 ML Tb subsequently annealed at 550 °C for 2 min ( $V_S = -2.0$  V;  $I_T = 100$  pA). (b) The monolayer-to-multilayer Tb coverage regime: 1.1 ML Tb subsequently annealed at 550 °C for 2 min ( $V_S = -2.5$  V;  $I_T = 100$  pA). In both images, the periodicities of the formed structures are indicated.

lower temperatures starting at about 400 °C. At higher temperatures above 600 °C, it is found that the structures already start to dissolve as described in detail further below.

In Fig. 9.1, overview STM images of two samples prepared using different Tb coverages and annealing temperatures in the ideal temperature range mentioned above are shown. When comparing the images, a different growth behavior is found for the two shown preparations. On the sample with a submonolayer Tb coverage shown in (a), still large areas with the clean Si(111) $7\times 7$  reconstruction are present. Additionally, the growth of different nanostructures with a well structured appearance occurs, either as islands on the  $7\times 7$  surface, as holes within the surface, or as domains attached to steps of the substrate. As indicated in the image, these nanostructures can be assigned either to a  $2\sqrt{3}\times 2\sqrt{3}$  R30° superstructure or a  $5\times 2$  superstructure, or to nanorods with a  $2\times 1$  superstructure. In other preparations also nanorods with a  $4\times 1$  superstructure appear. The relative surface coverages of the different structures can be influenced by adjusting the preparation conditions.

For higher Tb coverages in the monolayer-to-multilayer regime, the growth behavior changes and the formation of islands with a rather flat, unstructured appearance in overview STM images is observed, as shown in Fig. 9.1 (b). At even higher coverages, the islands coalesce and form closed films. As will be demonstrated in section 9.3, these structures correspond either to the monolayer silicide with a  $\text{TbSi}_2$  stoichiometry or to the multilayer silicide with a  $\text{Tb}_3\text{Si}_5$  stoichiometry known from other trivalent rare earth metals (see section 3.6). Thereby, the two-dimensional  $\text{TbSi}_2$  monolayer is found to exhibit a  $1\times 1$  surface periodicity, while the three-dimensional  $\text{Tb}_3\text{Si}_5$  multilayer shows a  $\sqrt{3}\times \sqrt{3}$  periodicity.

Before the detailed analysis of the structures introduced here will be conducted in the following sections, another behavior that emerges for measurements with Tb on Si(111) is discussed. Figure 9.2 (a) to (c) shows STM images measured on samples, which were only flashed using the standard procedure employed within this work as described in section 4.4,

without the nominal deposition of any Tb. However, Tb has been deposited on the used Si(111) substrate in an earlier measurement. Usually, the deposited material desorbs from the surface again during the flashing process, so that the Si substrates can be used several times. However, as it has been also found for the Tb induced clusters on Si(111), a repeated deposition of Tb leads to a degradation of the Si(111) substrates. This is nicely demonstrated in Fig. 9.2 (a) and (b) where, besides the clean  $7\times 7$  reconstruction, also other structures appear. From the more detailed STM image shown in (b), these structures can be assigned to the Tb induced  $2\sqrt{3}\times 2\sqrt{3}$  R30° and  $5\times 2$  superstructures. Hence, a significant fraction of the Tb deposited on the sample before has not desorbed from the sample during flashing and forms the observed Tb induced structures.

It is assumed, that a similar process as observed e.g. for Ni takes place [250, 392]. During the flashing process, a significant fraction of the Tb diffuses into the bulk Si crystal. Then, when cooling down the sample in order to prepare a well reconstructed surface or during the annealing, a fraction of the Tb diffuses back towards the surface and forms the structures observed in the STM images in Fig. 9.2 (a) to (c). Often also the obtained surface coverage, which is estimated on the basis of the material incorporated in the structures formed on the surface, appears to be lower than the nominal coverage determined using the quartz crystal microbalance. Thus, a diffusion into the bulk crystal might already occur during the annealing, which is performed to enable the self-assembled formation of the nanostructures. Thus, in addition to making the measurements with Tb more time-consuming as compared to other materials, since the Si(111) substrates need to be replaced more often, these processes also hinder a reliable estimation of the Tb coverage, since it has to be taken into account that a significant amount of Tb might have diffused into the bulk. For the measurements shown here, the nominal Tb coverages are given, as determined from the evaporation rates measured using the quartz-crystal microbalance, although the actual amount of Tb available on the surface might deviate.

A further observation, is shown in Fig. 9.2 (c). Here, large domains with triangular structures are found within areas of the  $2\sqrt{3}\times 2\sqrt{3}$  R30° superstructure [marked as destroyed in Fig. 9.2 (c)]. In addition to samples, which were already used in earlier measurements, such triangular structures are also observed on samples prepared using high growth temperatures of 600 °C and above, as exemplarily shown in Fig. 9.2 (d). Here, they form mainly at the borders but also within domains of the  $2\sqrt{3}\times 2\sqrt{3}$  R30° superstructure, as indicated by the arrows.

It may be assumed that at high temperatures, as they were present during the growth of the samples shown in (c) and (d), the submonolayer reconstructions like the  $2\sqrt{3}\times 2\sqrt{3}$  R30° superstructure, but maybe also the  $5\times 2$  superstructure, become unstable and start to decompose. The observed triangles might then be remainders of the structures. Since their sizes are similar to the sizes of single  $2\sqrt{3}\times 2\sqrt{3}$  R30° domains, they might represent the former domain boundaries that form the triangular network in the  $2\sqrt{3}\times 2\sqrt{3}$  R30° superstructure. However, up to now no atomic resolution STM images further supporting this view could be obtained. Nevertheless, the formation of the structures within large areas of the  $2\sqrt{3}\times 2\sqrt{3}$  R30°

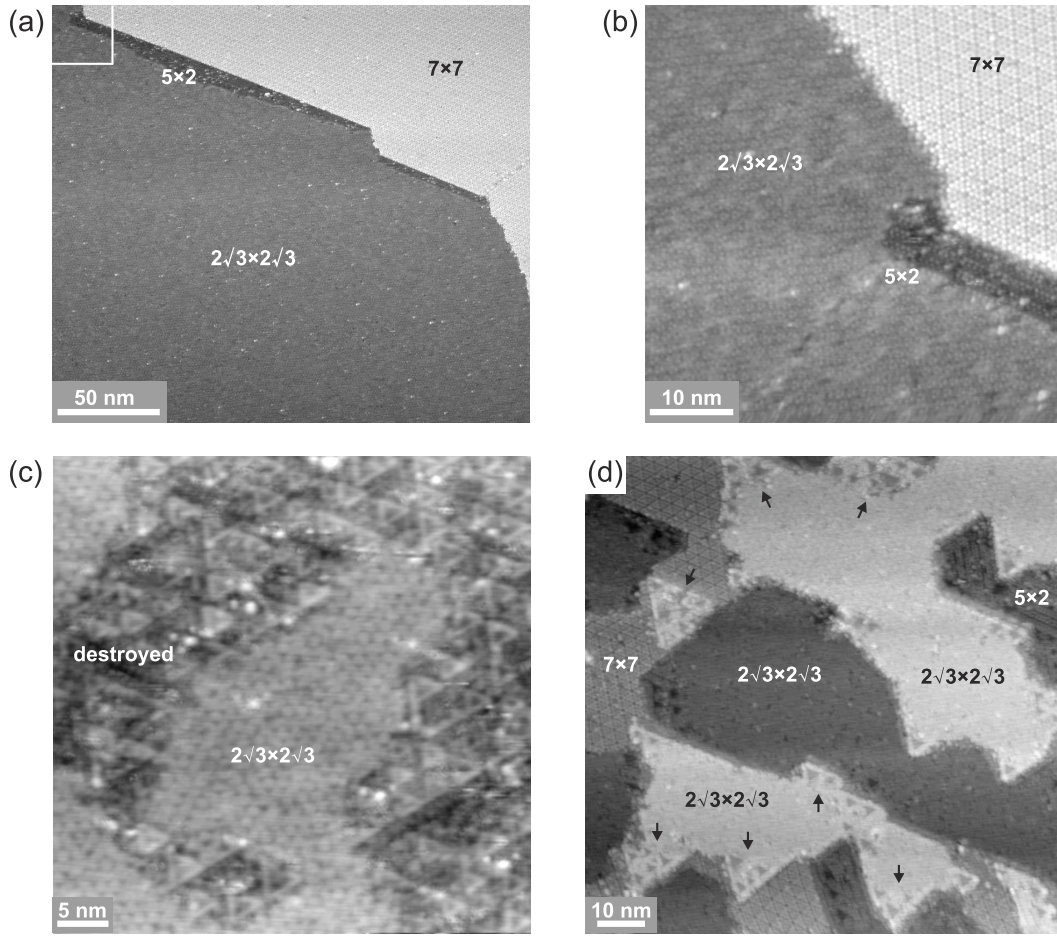


**Figure 9.2:** (a,b) STM images of a sample, which was flashed using the standard procedure, but with a substrate, on which 1.1 ML Tb was deposited in an earlier measurement. (a) Overview filled states STM image ( $V_S = -2.5$  V;  $I_T = 100$  pA) and (b) more detailed filled states STM image ( $V_S = -2.5$  V;  $I_T = 100$  pA) of the area indicated by the white box in (a). (c) STM image of another sample, which was prepared by just flashing a Si(111) substrate already used in an earlier measurement with a Tb coverage of 1.2 ML, followed by annealing at 600 °C for 1 min ( $V_S = +1.5$  V;  $I_T = 100$  pA). (d) STM image of a sample with 2.0 ML Tb coverage and subsequent annealing at 600 °C for 2 min ( $V_S = -2.0$  V;  $I_T = 100$  pA). In the images, the periodicities of the formed structures are indicated. In (c) an area, in which triangular structures assigned to a partial destruction of the  $2\sqrt{3}\times 2\sqrt{3}$  R30° superstructure are present, is marked as destroyed while in (d) such triangular structures are indicated by the arrows.

superstructure like in Fig. 9.2 (c) suggests a formation mechanism with the  $2\sqrt{3}\times 2\sqrt{3}$  R30° superstructure as the starting point.

However, the process of a destruction of the  $2\sqrt{3}\times 2\sqrt{3}$  R30° superstructure discussed here might also correspond to the beginning rearrangement into another structure. Similar triangular structures are also found for Er [45, 403]. Here, they also appeared after subsequently annealing samples with the Er induced  $2\sqrt{3}\times 2\sqrt{3}$  R30° superstructure supporting the above discussion. A systematic further annealing in that case resulted in the formation of  $2\times 1$  nanorods. Hence, the observed triangular structures might also in the present case correspond to an intermediate structure in the restructuring process of the  $2\sqrt{3}\times 2\sqrt{3}$  R30° superstructure into nanorods. However, further investigations with a systematic annealing of samples

with submonolayer Tb coverages, ideally directly during the STM measurement, need to be conducted to further prove this assumption.

## 9.2 The submonolayer Tb coverage regime

### 9.2.1 The $2\sqrt{3}\times 2\sqrt{3}$ R30° superstructure

The first structure, which forms in the submonolayer regime, is the  $2\sqrt{3}\times 2\sqrt{3}$  R30° superstructure. At coverages below 0.5 ML, as shown in Fig. 9.3 (a) and (b), this structure first forms islands as well as holes within the Si(111)7×7 surface. In between, mostly areas with the clean 7×7 reconstruction and occasionally also with other Tb induced superstructures are present. Only around the saturation coverage around 0.5 ML, almost the whole surface may be covered by the  $2\sqrt{3}\times 2\sqrt{3}$  R30° superstructure. Here, only small domains of other structures are found on the surface, as it is shown in Fig. 9.3 (c).

The growth parameters employed in Figure 9.3 (a) with RDE growth at 400 °C and a coverage of 0.08 ML Tb are, as mentioned above, not ideal to prepare larger islands of the  $2\sqrt{3}\times 2\sqrt{3}$  R30° superstructure. It rather represents the transition regime between the cluster growth investigated in chapter 7 and the submonolayer regime. Hence, a formation of clusters in between the islands is still occasionally found, as indicated by the arrows. Similar small islands are also frequently observed in STM images during the cluster measurements, as shown e.g. in Fig. 7.1 (a) and (d) for Dy and Tb, respectively. Regarding Tb, no atomic resolution could be achieved on these small islands. However, on the basis of atomically resolved images for measurements with Dy, these islands were already assigned in chapter 7 to early stages of the  $2\sqrt{3}\times 2\sqrt{3}$  R30° superstructure. Although it is very likely that this assignment can be simply transferred to Tb due to the chemical similarity of both rare earth metals, further indications are given by a comparison of the islands and holes forming in the transition regime [Fig. 9.3 (a)] with those forming at higher coverages, as shown e.g. in Fig. 9.3 (b). The latter

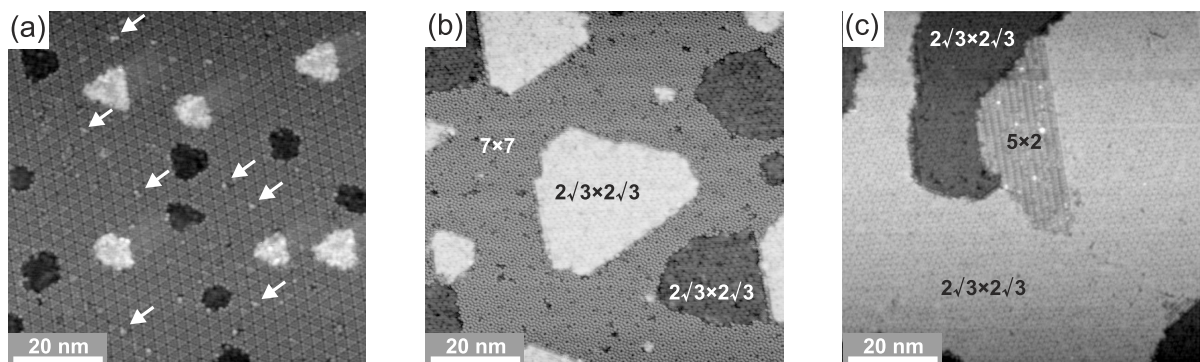


**Figure 9.3:** (a) Overview STM images of samples with the  $2\sqrt{3}\times 2\sqrt{3}$  R30° superstructure. (a) 0.08 ML Tb deposited at 400 °C ( $V_S = -2.5$  V;  $I_T = 100$  pA). (b) 0.4 ML Tb subsequently annealed at 550 °C for 2 min ( $V_S = +1.2$  V;  $I_T = 100$  pA). (c) 0.7 ML Tb subsequently annealed at 500 °C for 2 min ( $V_S = +1.5$  V;  $I_T = 100$  pA). In (a) the arrows exemplarily indicate clusters, and in (b) and (c) the forming superstructures are indicated.

can clearly be assigned to the  $2\sqrt{3}\times 2\sqrt{3}$  R30° superstructure on the basis of atomically resolved STM images. First, the general growth as well as the shapes of the islands and holes found in Fig. 9.3 (a) and (b) appear very similar. Second, the heights of the islands as well as those of the holes with respect to the Si(111) surface were measured. Since the measured height varies with the applied tunneling voltage, only height profiles measured in images acquired with identical tunneling conditions were analyzed. For both the islands and holes forming in the transition regime as well as the islands and holes forming at higher coverages and annealing temperatures, identical height differences were found. As an example, at a tunneling voltage of +2 V, the holes appear  $(0.14 \pm 0.01)$  nm lower as compared with the Si(111)7×7 surface, while the islands appear  $(0.18 \pm 0.01)$  nm higher than the Si(111)7×7. Thus it is concluded that the islands and holes observed in the transition regime and already in the cluster regime indeed correspond to the beginning growth of the Tb induced  $2\sqrt{3}\times 2\sqrt{3}$  R30° superstructure.

The measurements above found a difference of 0.32 nm between the islands and holes of the  $2\sqrt{3}\times 2\sqrt{3}$  R30° superstructure. Taken also measurements with other tunneling conditions into account a mean height difference of  $(0.31 \pm 0.01)$  nm is found, in nice agreement with the height of a single Si(111) step (see Table 3.1). This indicates, that the holes correspond to  $2\sqrt{3}\times 2\sqrt{3}$  R30° domains, which penetrated into the Si(111) surface during growth. The Si atoms that are released by this process may then participate in the formation of the islands. Such a process seems to be especially probable at low growth temperatures, as employed e.g. in Fig. 9.3 (a), where a diffusion of Si atoms from step edges may be limited.

In Fig. 9.4 (a), a more detailed empty states STM image of the  $2\sqrt{3}\times 2\sqrt{3}$  R30° superstructure is shown. Here, a network of triangular domains with  $2\sqrt{3}\times 2\sqrt{3}$  periodicity appears, as exemplarily indicated by the dashed black lines in (a). The domain boundaries thereby appear as meandering bright lines (indicated by the blue line). In addition, two  $2\sqrt{3}\times 2\sqrt{3}$  R30° unit cells in neighboring domains are indicated in red. As can be seen, the orientation of the  $2\sqrt{3}\times 2\sqrt{3}$  R30° structure rotates by 60° when crossing a domain boundary.

As mentioned in section 3.6, a  $2\sqrt{3}\times 2\sqrt{3}$  R30° superstructure is also found for Er [42, 45, 315], Dy [46, 316, 317], and Ho [47]. The corresponding structure model is shown in Fig. 3.22 (c). It is based on the model proposed by Roge *et al.* for the Er induced  $2\sqrt{3}\times 2\sqrt{3}$  R30° superstructure [42], which was extended by Engelhardt *et al.* in order to explain also the structure of the domain boundaries for the Dy induced  $2\sqrt{3}\times 2\sqrt{3}$  R30° superstructure [46]. In this model, the  $2\sqrt{3}\times 2\sqrt{3}$  R30° structure consists of hexagons of rare earth metal atoms that adsorb on an unreconstructed Si(111) surface. The domain boundaries represent a quite similar structure, but with incomplete hexagons forming a meandering line.

As mentioned earlier, typically the Tb atoms are imaged in empty states images such as Fig. 9.4 (a), while in filled states images such as (b), STM is more sensitive for the Si atoms due to their higher electronegativity. Hence, in the empty states image in (a), the bright features with  $2\sqrt{3}\times 2\sqrt{3}$  periodicity can be assigned directly to Tb hexagons forming an analogous structure as discussed above for Dy and Er. In addition, the meandering line, at which the domain boundaries appear, can be nicely explained by the structure model proposed

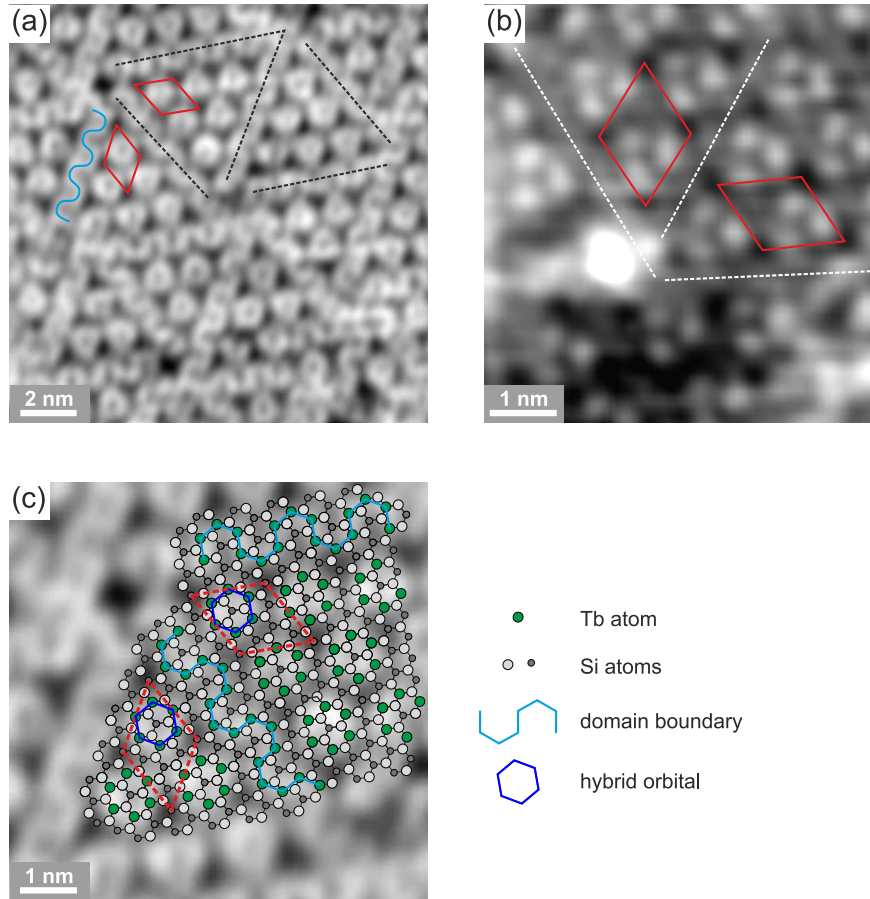


**Figure 9.4:** Detailed (a) empty states STM image ( $V_S = +1.5$  V;  $I_T = 100$  pA) and (b) filled states STM image ( $V_S = -2.5$  V;  $I_T = 100$  pA) of the  $2\sqrt{3} \times 2\sqrt{3}$   $R30^\circ$  superstructure. (c) Detail of the empty states STM image shown in (a) with an overlaid structure model for the  $2\sqrt{3} \times 2\sqrt{3}$   $R30^\circ$  superstructure including the structure of the domain boundaries according to Engelhardt *et al.* [46]. The red rhombuses indicate  $2\sqrt{3} \times 2\sqrt{3}$   $R30^\circ$  unit cells, the dashed black and white lines in (a) and (b) the triangular domain network. In addition, the light blue line in (a) exemplarily traces the meandering appearance of the domain boundaries.

by Engelhardt *et al.* [see Fig. 3.22 (c)]. In Fig. 9.4 (c), the corresponding structure model is overlaid on the empty states STM image demonstrating the good agreement.

In the filled states image, in contrast, triangular features formed by three bright spots are observed. In addition, the bright contrast is observed in the opposite half of the  $2\sqrt{3} \times 2\sqrt{3}$  unit cell as compared to the empty states images. According to Engelhardt *et al.*, these so-called windmill-like features arise from an asymmetric bonding configuration of the Si atoms to the rare earth hexagons [46].

In the model, every Tb atom saturates two Si dangling bonds. Thus, for trivalent rare earth metals, one electron per Tb atom remains. It is assumed that these electrons form a hybrid orbital leading to a further stabilization of the Tb hexagons as it is exemplarily indicated in Fig. 9.4 (c) [45, 46]. Due to a similar situation at the domain boundaries, a formation of meandering hybrid orbitals may also be assumed there.

Since the unit cell contains six Tb atoms, a saturation coverage of 0.5 ML results, as already mentioned above. The observation of a surface covered almost exclusively with the  $2\sqrt{3}\times 2\sqrt{3}$  R30° superstructure on the sample with a nominally higher coverage of 0.7 ML shown in Fig. 9.3 (c) might be related to the difficulties to estimate the actual surface coverage, as discussed in the previous section.

In comparison to the  $2\sqrt{3}\times 2\sqrt{3}$  R30° superstructures observed for Er [42, 45, 315], Dy [46], and Ho [47], the Tb induced  $2\sqrt{3}\times 2\sqrt{3}$  R30° superstructures, however, seems to form smaller domains. This might be related to strain effects due to the lanthanide contraction since Tb has the largest ionic radius of the rare earth metals for which a  $2\sqrt{3}\times 2\sqrt{3}$  R30° superstructures has been observed.

### Electronic properties

In order to investigate the electronic properties of the Tb induced  $2\sqrt{3}\times 2\sqrt{3}$  R30° superstructure, STS measurements were performed. The electronic structure of the  $2\sqrt{3}\times 2\sqrt{3}$  R30° superstructure has been ambiguous up to now. To the best of my knowledge, the only investigations published so far are STS results obtained on the Er induced  $2\sqrt{3}\times 2\sqrt{3}$  R30° superstructure. Here, Roge *et al.* found a metallic or semi-metallic character in their  $I$ - $V$  curves [42] while Saranin *et al.* claim semiconducting properties [315].

The results of the STS measurements performed in this work are summarized in Fig. 9.5. In (a) and (b),  $I$ - $V$  and  $dI/dV$ - $V$  spectra measured simultaneously using a software lock-in amplifier are shown. Thereby, the shown spectra represent the average of several hundred single spectra measured with stabilization conditions of  $V_S = +1.5$  V;  $I_T = 100$  pA and an additional tip approach towards the sample by 100 pm at different positions on the  $2\sqrt{3}\times 2\sqrt{3}$  R30° superstructure. In (c), the normalized differential conductivity which was again calculated by using the procedure introduced by Prietsch *et al.* [77] is displayed. The black line shows the measurement already shown in (a) and (b), but represents the average of spectra obtained by approaching the tip by 70 pm and 100 pm. The red curve shows a measurement, which was performed using stabilization conditions of  $V_S = +1.5$  V and  $I_T = 200$  pA and a tip approach by 100 pm, but with a different STM tip.

The  $I$ - $V$  curve presented in (a) shows a flat region in the central part of the spectrum, thus indicating a semiconducting behavior at first sight. However, especially when regarding the inset in (a), where only the part of the spectrum around  $V_S = 0$  V is shown with a different scaling of the current axis, it clearly shows a nonzero slope around the Fermi level, very similar to the observations of Roge *et al.* [42]. However, the small slope in this region indicates a rather low density of states and thus, similar to the conclusions drawn in Ref. [42], rather a semi-metallic than a metallic behavior. A semi-metallic behavior is further affirmed when regarding the normalized differential conductivity shown in (c). Here, a clear drop in the LDOS down to zero is observed in both measurements. However, a DOS close to zero is only observed directly at the Fermi level, without the appearance of a distinct band gap.

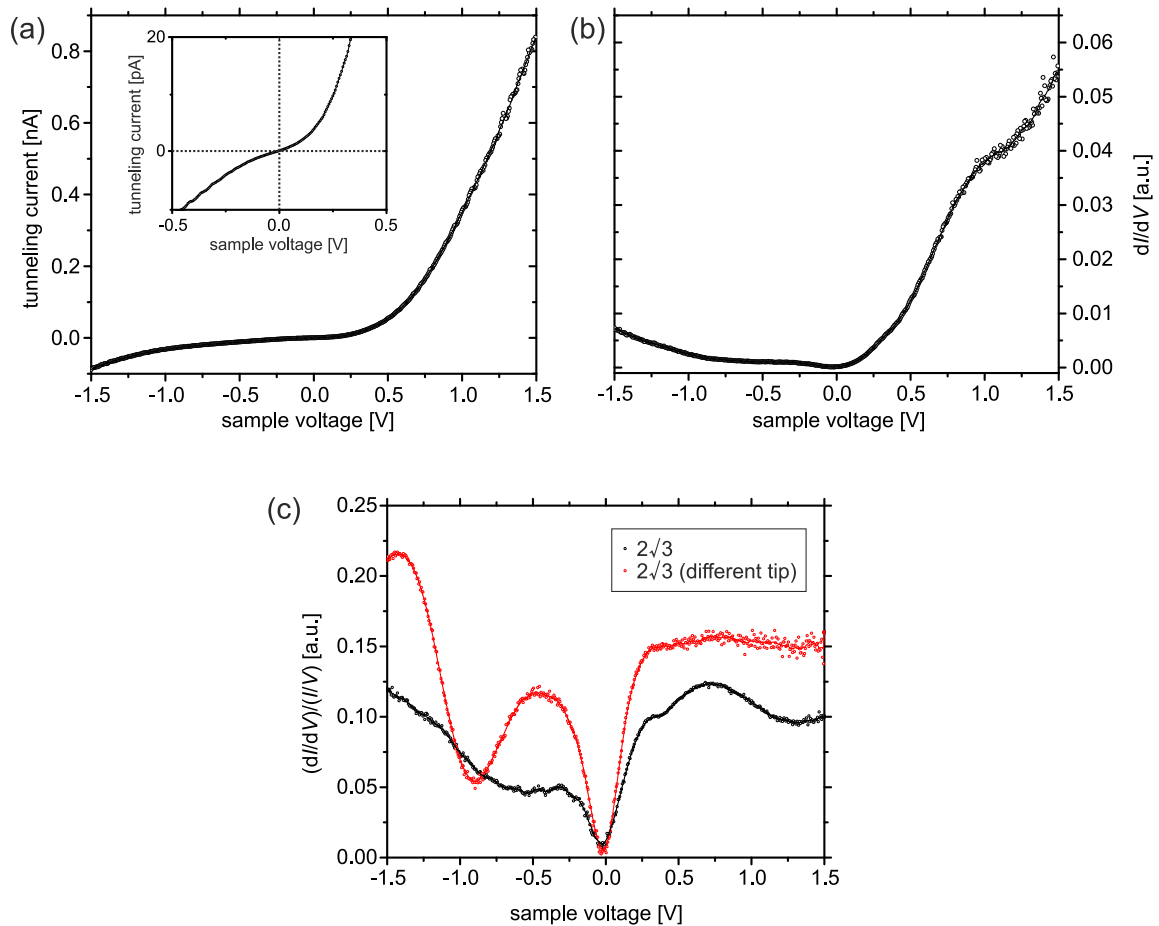


**Figure 9.5:** (a)  $I$ - $V$  and (b)  $dI/dV$ - $V$  spectra measured on the  $2\sqrt{3}\times 2\sqrt{3}$   $R30^\circ$  superstructure. The inset in (a) shows an enlarged view of the region around the Fermi level. (c) Normalized differential conductivity of the  $2\sqrt{3}\times 2\sqrt{3}$   $R30^\circ$  superstructure. The red curve shows a spectrum obtained using a different STM tip.

It has to be mentioned that the measurements obtained with different tips show differences, although the normalized differential conductivity should in principle look similar. However, regarding the main features such as the drop in the LDOS mentioned above, the spectra behave similar. Besides this drop, both spectra show an increase in the density of states above a tunneling voltage of 0 V and below a tunneling voltage of about  $-1$  V. Thus it may be concluded that, although an influence of the DOS of the tip might be present, the spectra mainly show the features of the  $2\sqrt{3}\times 2\sqrt{3}$   $R30^\circ$  superstructure.

### 9.2.2 The $5\times 2$ superstructure

The second structure, which is observed at submonolayer Tb coverages, is the  $5\times 2$  superstructure. At lower coverages, as shown e.g. in Fig. 9.1 (a), often a formation at step edges is observed, while, especially at higher coverages, it forms domains in between other Tb induced structures like the  $2\sqrt{3}\times 2\sqrt{3}$   $R30^\circ$  superstructure [see Fig. 9.3 (c)] or the  $1\times 1$  superstructure. In comparison to the  $2\sqrt{3}\times 2\sqrt{3}$   $R30^\circ$  superstructure larger domains of the  $5\times 2$  superstructure preferentially form at slightly higher temperatures of  $550$  °C to  $600$  °C, although the  $5\times 2$  su-

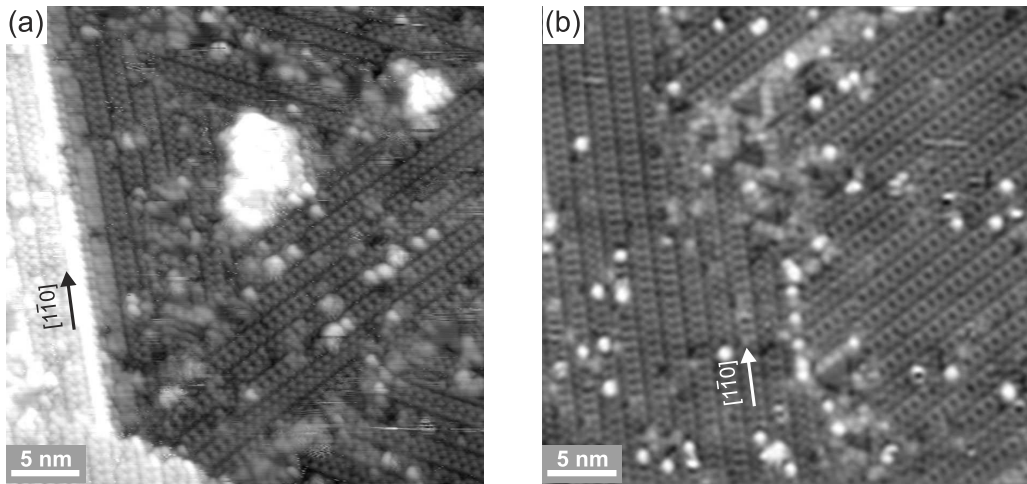


**Figure 9.6:** (a,b) Overview filled states STM images ( $V_S = -2.0$  V;  $I_T = 100$  pA) of the Tb induced  $5 \times 2$  superstructure formed with 1.2 ML Tb coverage and subsequent annealing at  $600$  °C for 2 min.

perstructure was never found to be the dominating structure on any of the samples investigated within this work.

As can be seen in the overview STM images shown in Fig. 9.6, where large areas with the  $5 \times 2$  superstructure are present on the surface, the  $5 \times 2$  superstructure forms chains running along the  $\langle 1\bar{1}0 \rangle$  directions. Thus, three different chain orientations are possible, which are all found in (a), while only two different chain orientations are present in (b).

More detailed filled and empty states images of the same region of the  $5 \times 2$  superstructure are shown in Fig. 9.7. Similar to the  $2\sqrt{3} \times 2\sqrt{3}$  R30° structure, a strong voltage dependence is found. In the filled states image shown in Fig. 9.7 (a), each chain is formed by three rows of bright spots. Thereby, the spots appear slightly brighter and larger in two of the rows. Additionally, two different configurations regarding the alignment of the spots are observed. In the first, the two brighter appearing spot rows are aligned in phase, while in the second one, a zigzag arrangement of the two bright spot rows is observed, as it is indicated by the yellow circles in Fig. 9.7 (a). The numbers 1 and 2 thereby indicate the in phase and the zigzag arrangement of the spots, respectively.

In contrast, only two rows of bright spots are observed in high resolution empty states images as shown in Fig. 9.7 (b). Again two different configurations are observed, but in this case both exhibit a small phase shift between neighboring spot rows of the same row pair. Here, the configurations differ in the direction of this phase shift, resulting in a tilting of the spot pairs, which can be either upwards or downwards. This is again indicated by the yellow circles in the STM image. In this case, 1 indicates a downward tilting, while the spots marked with 2 show an upward tilting when going from left to right.

As already mentioned in section 3.6.1, a  $5 \times 2$  superstructure is also found for the rare earth metals Dy [46], Er [45, 315], Ho [47], and Gd [43, 44, 319]. These structures show a very similar appearance in the STM images, although STM images with a resolution comparable with the one achieved here have not been published up to now. A structure model for the Gd induced  $5 \times 2$  reconstruction was developed by Battaglia *et al.* in 2007 [43] based on LEED and STM

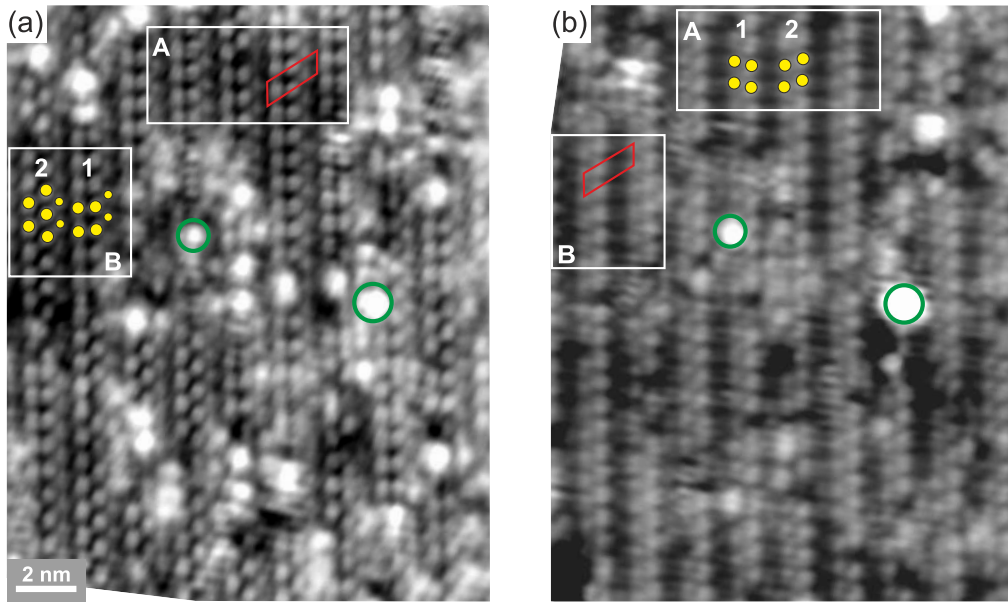


**Figure 9.7:** (a) Filled states STM image ( $V_S = -1.5$  V;  $I_T = 100$  pA) and (b) empty states STM image ( $V_S = +1.5$  V;  $I_T = 100$  pA) of the same region with the  $5 \times 2$  superstructure formed for a coverage of 0.7 ML Tb and subsequent annealing at 500 °C for 2 min. In the images, a typical  $5 \times 2$  unit cell is indicated in red, and the numbers 1 and 2 mark the different configurations, which are indicated by the large yellow dots marking the bright protrusions. The two green circles indicate prominent adsorbates, which were used to align the regions A and B in the images relative to each other.

investigations together with electron counting considerations. This model is based on Si Seiwatz and Si honeycomb chains with the Gd atoms forming atomic chains with a  $\times 2$  periodicity in the channels between the Si chains [see Fig. 3.23 (c)]. Assuming locally different spacings between neighboring Gd atoms within the same channel, the model also provides an explanation for the different configurations observed in the STM images. The main features in the STM images were assigned to the structural elements of the model as follows: In the empty states a bright contrast is observed around the Seiwatz chains, while in the filled states, the Seiwatz chains appear darker and the bright contrast appears at the honeycomb chains. However, it should be noted that the exact adsorption sites of the Gd atoms remained ambiguous.

In the following, it is demonstrated that, based on the high resolution STM images obtained in this work, not only the correct adsorption sites are identified, but also a more detailed understanding of the effects that lead to the observation of the different configurations is derived. Therefore, the areas indicated with A and B in Fig. 9.7 are picked as examples and are compared with the structure model. Figure 9.8 shows enlarged views of these areas for both filled and empty states. In addition, structure models, which show the situation in the corresponding regions, are presented separately as well as overlaid on the STM images. In comparison to the former study [43], a better resolution is achieved here, with clearly two independent rows of bright spots being resolved in the empty states STM images [see Figs. 9.7 (b) and 9.8 (b,e) in comparison with Fig. 3.23 (a)]. Since here mainly the Tb atoms contribute to the contrast, the positions of the bright spots can be related directly to the positions of the Tb atoms. Thus, from Fig. 9.8 (b) and (e) with the structure model overlaid

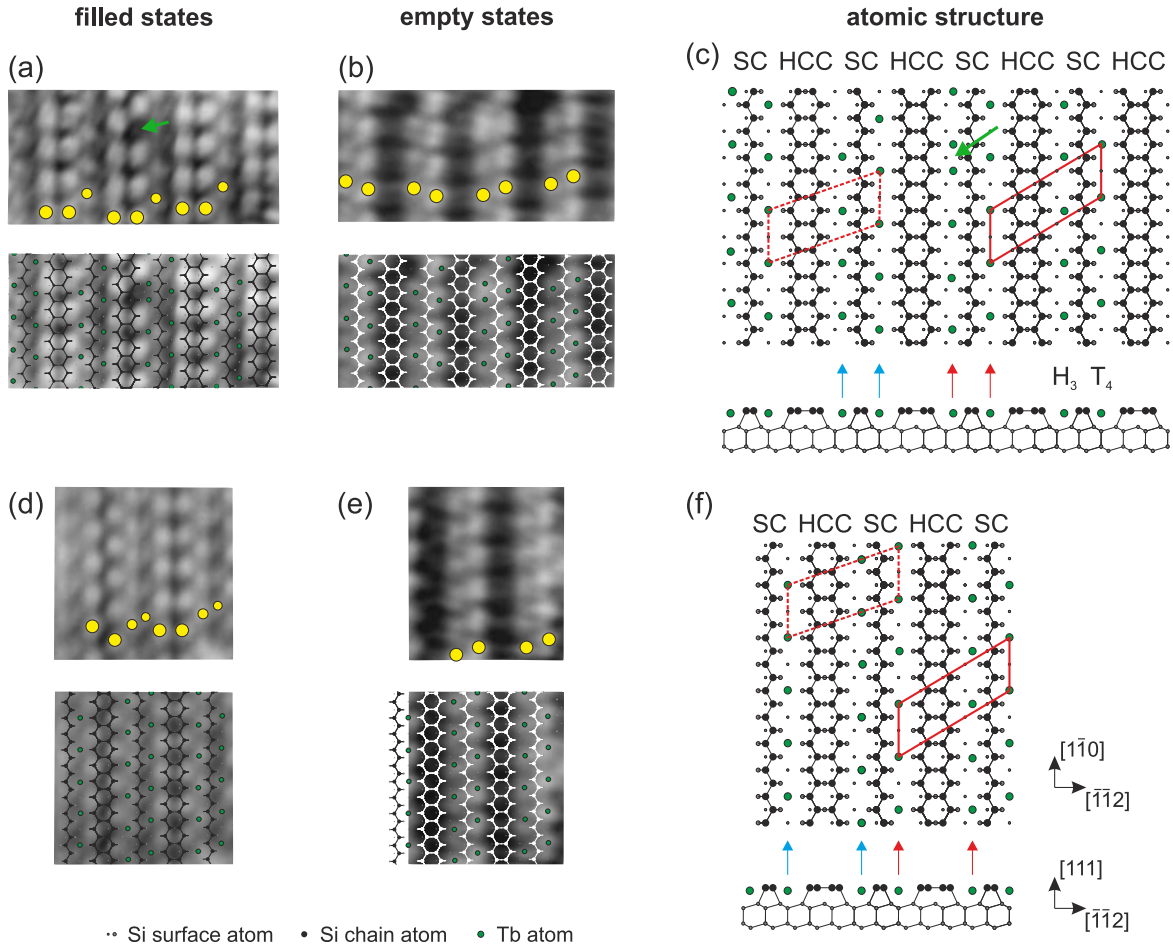


**Figure 9.8:** (a) Detailed filled states STM image ( $V_S = -1.5$  V;  $I_T = 100$  pA) and (b) detailed empty states STM image ( $V_S = +1.5$  V;  $I_T = 100$  pA) of region A in Fig. 9.7. (c) Corresponding structure model, also overlaid on the STM images in (a,b). (d) Detailed filled states STM image ( $V_S = -2.0$  V;  $I_T = 100$  pA) and (e) detailed empty states STM image ( $V_S = +1.5$  V;  $I_T = 100$  pA) of region B in Fig. 9.7. (f) Corresponding structure model, also overlaid on the STM images in (d,e). The dashed and solid red parallelograms in (c) and (f) indicate nonequivalent  $5 \times 2$  unit cells resulting from different registries, while the arrows in (a) and (c) indicate a position, where an anomalous spacing between two Tb atoms within a row is observed. In (c), the  $H_3$  and  $T_4$  adsorption sites of the Tb atoms in the two channels are additionally indicated.

on the STM images, the position of the Tb atoms within the channels can be identified. As indicated in (c), their positions correspond to  $H_3$  sites left of the Seiwatz chain and to  $T_4$  sites right of the Seiwatz chain. It should be mentioned that these sites also show a different appearance in the empty states STM images, where they appear with different brightnesses. In accordance to the assignment done in Ref. [43], the region where the honeycomb chain forms appears dark in the empty states images.

However, it is not possible to determine the orientation of the Si(111) substrate based on the STM images. Hence, the substrate might also be rotated by  $180^\circ$  with respect to the orientation drawn in the structure model. Anyway, this would only result in an exchange of

the locations of the  $H_3$  and  $T_4$  with respect to each other without any further influence on the discussion conducted here.

It should be noted furthermore that the assigned adsorption sites differ from those proposed in Ref. [43], where the rare earth atoms were assumed to be located much closer to the honeycomb chains and furthermore shifted in  $[1\bar{1}0]$  direction. Nevertheless, such adsorption sites are inconsistent with the high resolution empty states STM images obtained here.

Now, the assignment of the features observed in filled states STM images such as Figs. 9.7 (a) and 9.8 (a,d) is discussed. Since the shown filled states and empty states STM images were not acquired simultaneously, the relative assignment between the images was done based on defect structures (exemplarily indicated in Fig. 9.7 by the green circles) as well as on the following considerations: It may be assumed that the charge transfer that leads to the observation of the empty states near the Tb atoms leads at the same time to a saturation of the dangling bonds of every second Si atom of the honeycomb chains and a brighter contrast at the remaining dangling bonds. Thus, the bright spots appearing in the filled states images are assigned to the outer Si atoms of the honeycomb chain between the Tb atoms. In addition, also the Tb atoms are detected in the filled states images. Here, the dark third row is assigned to the Tb atoms right of the honeycomb chain as indicated by the medium sized yellow circles in Fig. 9.8 (a) and (d). In STM images acquired using certain tunneling conditions such as Fig. 9.8 (d), also the second Tb row appears as a faint row left of the honeycomb chain, as indicated by the small yellow circles. The different appearance of both Tb rows may again be explained by the different subsurface structure due to the different adsorption sites in the two rows.

In summary, the structure model is able to nicely explain the features observed in filled and empty states STM images of the  $5 \times 2$  superstructure. Nevertheless, a valid structure model should also be able to explain the different configurations observed for this superstructure. In fact, this is possible with the structure model developed here on the basis of the model proposed by Battaglia *et al.* [43], as will be demonstrated in the following.

In principle, equivalent Tb sites exist with a  $\times 1$  lattice spacing in  $[1\bar{1}0]$  direction within each channel. Since the initial Tb incorporation is assumed to occur randomly within each channel, different alignments of the Tb atoms in neighboring rows will arise, in the following called registries. In addition, odd numbered lattice spacings of two neighboring Tb atoms within the same row also result in registry shifts, as it has been proposed already in Ref. [43]. As will be demonstrated in the following on the basis of the detailed STM images shown in Fig. 9.8, these different registries as well as registry shifts lead to the different configurations.

In area A, which is displayed in Fig. 9.8 (a-c), all  $5 \times 2$  chains appear with a similar appearance in the filled states, with the bright spots being aligned in phase, as indicated by yellow circles (with the exception of the small region above the green arrow). In contrast, in the empty states image shown in (b), a change from a downward tilting of the spots, which is observed in the left two row pairs, to an upward tilting of the spots on the right is observed, again indicated by yellow circles. As can be seen in the structure model shown in (c), this behavior can be explained by different registries of the Tb atoms at the Seiwatz chain. When comparing the situations at the two Seiwatz chains marked by the blue and red arrows, the Tb atoms show a

downward phase shift at the Seiwatz chain marked in blue, while for the Tb rows marked by the red arrows an upward phase shift is found. On the other hand, the registry with respect to the honeycomb chain remains in phase explaining the unchanged appearance in the filled states image.

As mentioned above, odd numbered lattice spacings within one Tb row also lead to registry shifts. An example of such a shift is found at the position marked by the green arrow in Fig. 9.8 (a) and (c). Here, a dark region appears in the filled states image and the configuration changes from an in phase alignment of the bright spots to a zigzag one. In the empty states image, the configuration changes from an upward tilting to a downward tilting at the same position and the corresponding protrusion appears elongated in  $[1\bar{1}0]$  direction. Thus, probably a  $\times 1$  instead of a  $\times 2$  lattice spacing is present here, as drawn in the structure model. This defect is visible at both polarities: In the filled states, the two neighboring saturated dangling bonds result in an extended dark region [Fig. 9.8 (a)], while in the empty states the two neighboring Tb atoms are responsible for the elongated bright protrusion [Fig. 9.8 (b)].

Another example, how registry shifts can lead to configuration changes, is found in area B in Fig. 9.7, shown in detail in Fig. 9.8 (d-f). Here, as opposed to (a-c), the configuration in the filled states image changes from zigzag to in phase, while no change is observed in the empty states image, where both row pairs exhibit an upward tilting. Hence, the registry of the Tb atoms now has to change with respect to the honeycomb chain, since this registry determines the alignment of the bright spots in the filled states image. As shown in the corresponding structure model shown in (f), this is indeed the case. While the Tb atoms in the channels marked by the blue arrows show a zigzag alignment with respect to the honeycomb chain, the alignment is in phase for the Tb rows marked by the red arrows. Regarding the registry of the Tb atoms with respect to the Seiwatz chains no change is found, thus the tilting remains upwards in the empty states image.

Another consequence of the different configurations is the impossibility to define a universal unit cell for the  $5\times 2$  superstructure. As illustrated in the structure models shown in Fig. 9.8 (c) and (f), different unit cells arise due to the different configurations. Since both Tb channels can show a registry shift with respect to each other, altogether four different unit cells are possible.

As shown on the basis of these examples, besides being able to nicely explain the features observed in the STM images, the structure model also leads to a detailed understanding of the processes that result in the observation of the different configurations for the Tb induced  $5\times 2$  superstructure. Since the  $5\times 2$  superstructures formed from other rare earth metals show very similar properties and due to the chemical similarity of all the trivalent rare earth metals, it is assumed that the conclusions conducted here are not exclusive for the Tb induced  $5\times 2$  superstructure, but might be also valid for the  $5\times 2$  superstructures found for Dy [46], Er [45, 315], Ho [47], and Gd [43, 44, 319].

According to the structure model, 0.2 ML Tb are incorporated into the  $5\times 2$  superstructure, thus it should represent the ideal coverage for preparing large areas covered with this structure. However, as mentioned in the beginning of this section, the  $5\times 2$  superstructure is always found to cover only small areas, while most of the surface is covered with other superstructures such

as the  $2\sqrt{3}\times 2\sqrt{3}$  R30° superstructure or the  $1\times 1$  superstructure, explaining the rather high Tb coverages used in the measurements of the  $5\times 2$  superstructure shown here.

### 9.2.3 The $2\times 1$ and $4\times 1$ nanorods

Occasionally, also elongated islands are observed to form on the Si(111) surface after Tb deposition, as shown e.g. in Figs. 9.1 (a) and 9.9. Such nanorods are found for the complete range of growth parameters. However, predominantly a formation in the submonolayer Tb coverage regime is observed, hence these nanostructures are described within this section. Figure 9.9 (a) and (b) shows typical overview STM images of samples with nanorods. As indicated in the images, their long sides always are aligned along the  $\langle 1\bar{1}0 \rangle$  directions. The lengths of these nanorods may exceed  $0.4\ \mu\text{m}$ , in contrast to typical observed widths in the range of 5 nm to 30 nm, leading to a high aspect ratio of these nanostructures.

As can be seen in Fig. 9.9 (b), the growth of the nanorods can even influence the terrace structure of the Si(111) substrate. In the proximity of the nanorod formed in this image, Si(111) $7\times 7$  terraces with four different heights are present as indicated by the numbers 1 to 4. The nanorod is found to extend over the step edge in the upper part of the image, while it seems that it has carved itself into the upper terrace in the lower part. Thus, it may be assumed that the formation of the nanorod has induced a diffusion of Si atoms from the substrate to reorder the terrace structure in order to reach a maximum length of the nanorod. Such a so-called snow-plow effect was also found to take place during the formation of silicide nanowires of different rare earth metals on the Si(001) surface [387,404–406], as well as for Gd nanowires on Si(111) [322]. Nevertheless, the low Tb coverage of 0.06 ML and the low growth temperature of 375 °C for the sample shown in Fig. 9.9 (b) need to be discussed, since at such low growth temperatures a massive Si diffusion that would be necessary for the observed restructuring of the surface is not assumed. However, the measurement shown here is not conducted on a fresh Si(111) substrate, but Tb had been evaporated on the same sample before. As mentioned earlier, it is found that Tb does not desorb from the sample completely during the flashing procedure, which is used for the cleaning of the sample before each preparation. Hence, the nanorod might have formed from Tb that diffused back from the bulk during the flashing of the sample or the subsequent cooling down, where higher temperatures were present on the sample. However, nanorods are also found on samples that were not exposed to Tb before, but in these cases only for higher growth temperatures between 500 °C and 700 °C and higher Tb coverages. Thus, an exclusive formation due to Si diffusion from the bulk can be excluded and ideal formation temperatures for the nanorods between 500 °C and 700 °C are assumed.

In Fig. 9.9 (c) and (d), detailed high resolution STM images of the structure present on top of the nanorods shown in (a) and (b), respectively, are shown. Here, a different periodicity is found on the two nanorods. While the nanorod shown in (a) and (c) exhibits a  $2\times 1$  superstructure, the nanorod in (b) and (d) exhibits a  $4\times 1$  superstructure, as indicated by the unit cells drawn in red. A similar  $2\times 1$  superstructure was also found for Er [42,45,315] and Dy [321] on Si(111), while for Gd the growth of nanowires was observed on vicinal Si(111) samples [322]. Also, these

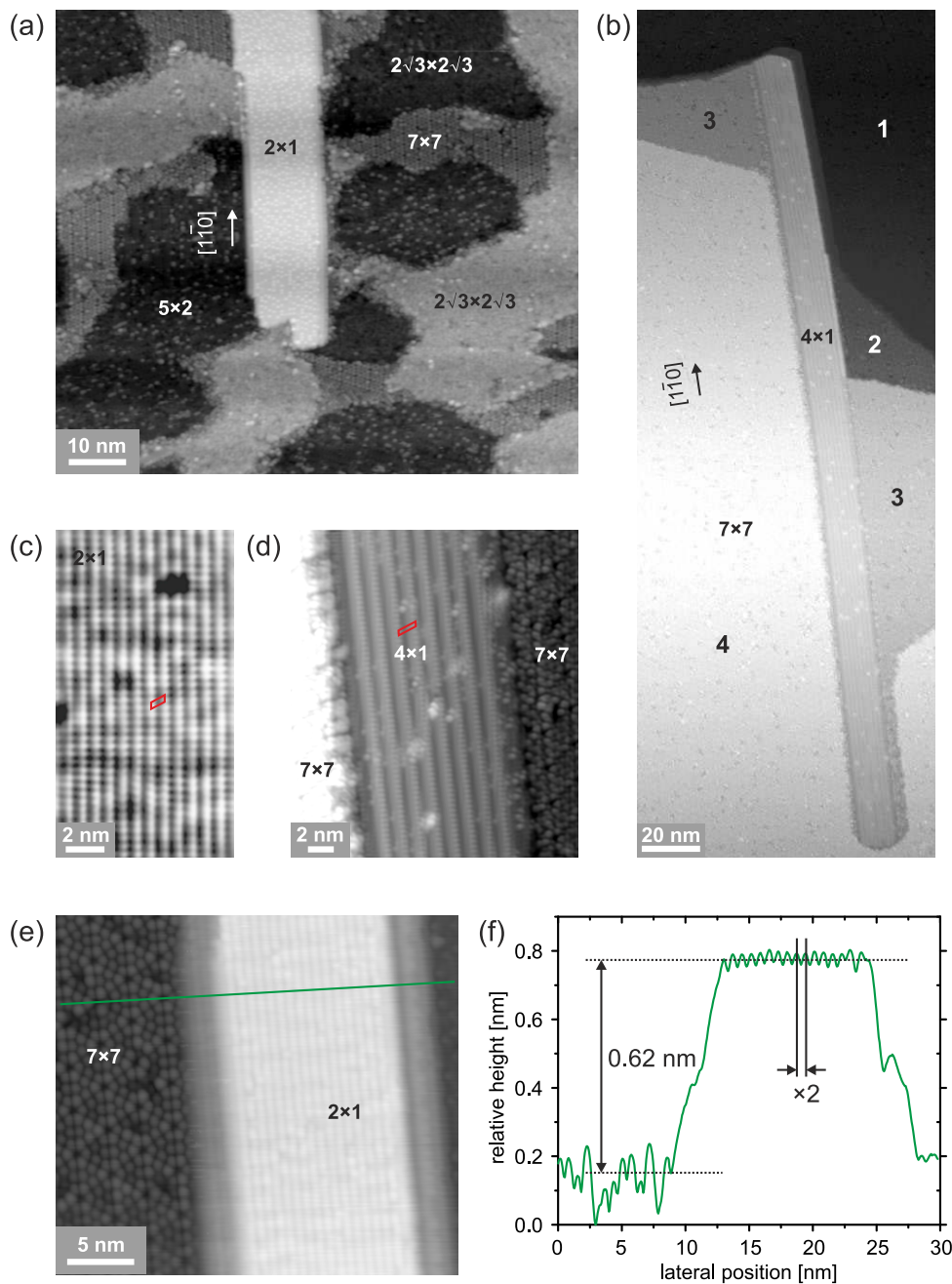


**Figure 9.9:** (a) Overview STM image of a sample with 0.6 ML Tb subsequently annealed at 500 °C for 1 min ( $V_S = -2.0$  V;  $I_T = 100$  pA). (b) Overview STM image of a nanorod formed on a sample with nominally 0.06 ML Tb subsequently annealed at 375 °C for 1 min ( $V_S = -2.0$  V;  $I_T = 100$  pA). However, the sample used in this experiment was exposed to Tb already in an earlier measurement. (c,d) Detailed filled states STM images of (c) the nanorods in the center of the image in (a) showing a  $2 \times 1$  superstructure ( $V_S = -2.0$  V;  $I_T = 100$  pA) and (d) of the nanorod in (b) showing a  $4 \times 1$  superstructure ( $V_S = -2.0$  V;  $I_T = 100$  pA). (e) STM image of a nanorod with a  $2 \times 1$  superstructure on a sample with a coverage of 0.4 ML Tb subsequently annealed at 650 °C ( $V_S = -1.0$  V;  $I_T = 100$  pA). (f) Height profile taken along the green line in (e). In the profile, the height of the nanorod with respect to the Si(111) $7 \times 7$  reconstruction and the  $\times 2$  periodicity of the chains on the nanorod surface are indicated.

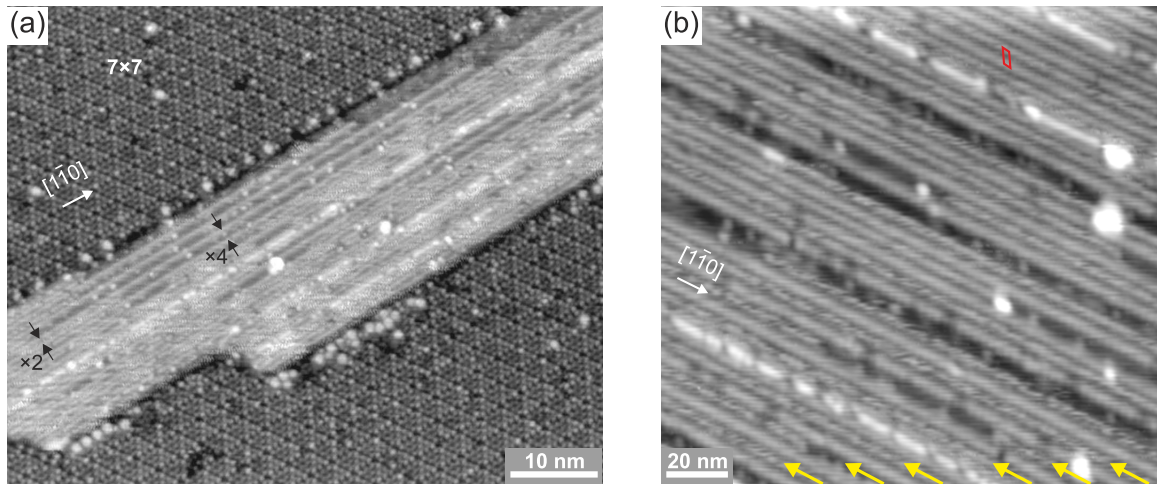


**Figure 9.10:** STM images of nanorods on a sample with a coverage of 0.3 ML Tb subsequently annealed at 700 °C for 2 min [(a)  $V_S = -1.7$  V and  $I_T = 100$  pA, (b)  $V_S = -2.0$  V and  $I_T = 100$  pA]. In (a), chains with  $\times 2$  and  $\times 4$  periodicity are exemplarily marked, in (b) the arrows indicate chains with a fuzzy appearance. In addition, a  $2 \times 1$  unit cell is drawn in red.

nanowires appear quite similar to the nanorods observed in the present work with a chain like reconstruction with either a  $\times 2$  or a  $\times 4$  periodicity on top.

Regarding the atomic structure of these nanostructures, different assumptions were made. Since the height observed for the Er nanorods corresponds to that of two monolayer high  $\text{Er}_3\text{Si}_5$  islands, the authors of Ref. [45] assume that the nanorods correspond to a special type of  $\text{Er}_3\text{Si}_5$  with a  $2 \times 1$  vacancy ordering instead of the common  $\sqrt{3} \times \sqrt{3}$  arrangement. In contrast, a hexagonal  $\text{RESi}_2$  structure is assumed for the Gd silicide nanowires in Ref. [322]. However, a formation of hexagonal  $\text{RESi}_2$  already leads to the formation of the two-dimensional monolayer silicide forming a  $1 \times 1$  superstructure (cf. section 3.6.1). In addition, a formation with the hexagonal  $c$ -axis perpendicular to the surface as in this case should not lead to a formation of nanorods, because of an equal lattice mismatch in all  $\langle 1\bar{1}0 \rangle$  directions. A formation with the hexagonal  $c$ -direction in the surface plane also does not seem to be probable, since such an orientation would lead to extremely large lattice mismatches, e.g. about 25% for  $\text{TbSi}_2$  [407]. Hence, a hexagonal  $\text{TbSi}_2$  structure is not assumed to be able to explain the formation of the nanorods observed here.

As can be seen from Fig. 9.9 (e) and (f), the height of the nanorods can even exceed 0.6 nm, thus they may be considered several monolayers high. In this case, a nanorod with a  $\times 2$  chain periodicity on top is shown, as indicated in (f), but similar heights are also measured for the  $4 \times 1$  nanorods. Hence, the nanorods might in fact consist of  $\text{Tb}_3\text{Si}_5$  with a  $2 \times 1$  arrangement of the Si vacancies in the bulk layers as suggested in Ref. [45]. However, the amount of data on the nanorods is rather limited. Hence, suggestions on their atomic structure would be too speculative at present. Therefore, further measurements are required.

The images shown in Fig. 9.10 demonstrate that the nanorods with either a  $2 \times 1$  or a  $4 \times 1$  superstructure indeed correspond to the same structure, and there are indications that the  $4 \times 1$  structure is a preliminary stage of the  $2 \times 1$  structure. In (a), long chains with a chain-

to-chain periodicity of four lattice constants form on the present nanorod in the upper part of the image. However, in the lower part of the image, e.g. at the end of the nanorod, additional chains in between the  $\times 4$  chains are found leading to a  $\times 2$  periodicity perpendicular to the chain direction. Hence, it may be assumed that the  $2\times 1$  superstructure results from the  $4\times 1$  superstructure due to a filling of the space in between the chains upon further growth. An even further growth may then lead to the additional bright chains that are occasionally observed in (a) and (b). In (b), basically the same behavior is observed. Here, also the  $4\times 1$  superstructure and the  $2\times 1$  superstructure are found to coexist on the surface of a nanorod. In addition, sometimes every second chain that is responsible for the  $2\times 1$  superstructure appears fuzzy, as it is indicated in the lower part by the yellow arrows. These fuzzily appearing chains are observed in areas with an incomplete formation of the  $2\times 1$  superstructure, while in the area in the upper part of the image, where the unit cell is indicated, a well ordered  $2\times 1$  superstructure seems to be present. Hence, it is assumed that both the  $2\times 1$  and the  $4\times 1$  periodicity do in principle correspond to the same structure but represent different stages in the formation of the nanorods. While the  $2\times 1$  periodicity is assumed to correspond to the final structure, the  $4\times 1$  periodicity seems to represent a metastable intermediate structure. However, under some conditions also large areas with  $4\times 1$  periodicity may be found, e.g. on the nanorod shown in Fig. 9.9 (b). Here, a low Tb availability on the surface might be responsible for the formation of this superstructure. A similar behavior with chains with a  $\times 2$  and a  $\times 4$  periodicity forming on the same nanorod or nanowire is also observed for the Gd silicide nanowires reported in Ref. [322]. In addition, the nanowires described there show heights of 0.6 nm, very similar to heights found in this study [see Fig. 9.9 (e) and (f)]. Hence, it is assumed that not only the Dy and Er induced  $2\times 1$  superstructures [42, 45, 315, 321], but also the Gd silicide nanowires correspond to an analogous structure. A formation of nanowires with lengths exceeding  $1\ \mu\text{m}$  might thus also be possible with Tb when using a vicinal Si(111) surface. This should be investigated in the future together with additional measurements and theoretical investigations in order to find out, if the structural considerations discussed here are reasonable.

### 9.3 The monolayer-to-multilayer regime

As mentioned earlier, the formation of islands with a surface appearing flat in overview STM images such as Figs. 9.1 (b) or 9.11 is observed in the monolayer-to-multilayer regime. Thereby, first smaller islands form at Tb coverages of around one monolayer [Figs. 9.1 (b) and 9.11 (a)], while at higher coverages [Fig. 9.11 (b)], these islands coalesce and form larger connected areas.

A formation of similar islands is also observed for other rare earth metals where they correspond either to a two-dimensional hexagonal  $\text{RESi}_2$  monolayer forming a  $1\times 1$  superstructure or to a three-dimensional hexagonal  $\text{RE}_3\text{Si}_5$  multilayer forming a  $\sqrt{3}\times\sqrt{3}$   $R30^\circ$  superstructure (cf. sections 3.6.2 and 3.6.3). Due to the chemical similarity of the trivalent rare earth metals, it is assumed that analogous structures also form for Tb. Indeed, the islands can already be assigned to these two structures by analyzing the edges of the islands, although no atomic resolution is achieved in the images shown in Fig. 9.11. A closer inspection of the island edges

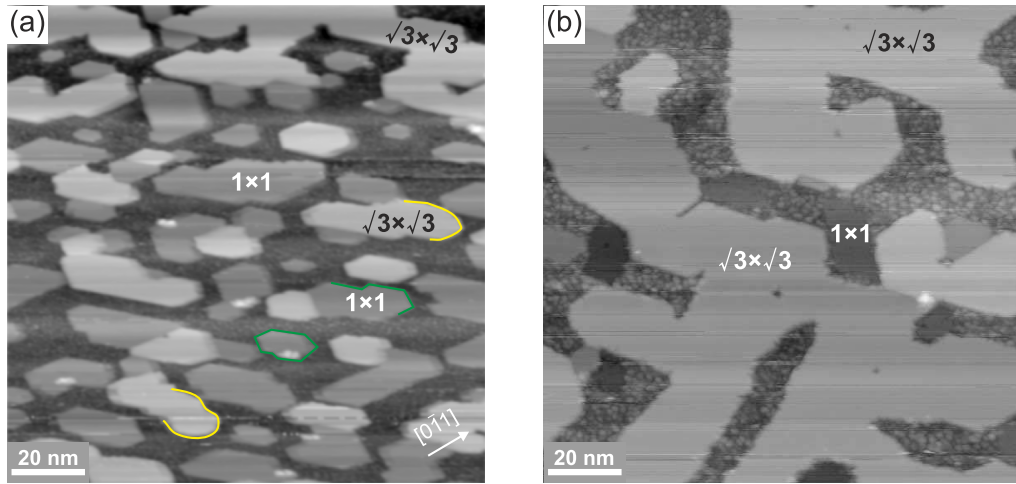


**Figure 9.11:** Overview STM images of the monolayer-to-multilayer regime. (a) 1.1 ML Tb coverage subsequently annealed at 550 °C for 2 min ( $V_S = -2.5$  V;  $I_T = 100$  pA). (b) 2.4 ML Tb coverage subsequently annealed at 550 °C for 2 min ( $V_S = -1.5$  V;  $I_T = 200$  pA). In the images, the forming structures are indicated. The green and yellow lines indicate the sharp edges of the  $\text{TbSi}_2$  monolayer and the rounder edges of the  $\text{Tb}_3\text{Si}_5$  multilayer, respectively.

reveals that the islands are either characterized by straight edges along the  $\langle 1\bar{1}0 \rangle$  directions (indicated by green lines) or by rounder edges with no distinct preferential orientation (indicated by yellow lines). For the monolayer silicide, the dangling bond density is noticeably smaller for edges along these directions in comparison to edges along  $\langle 11\bar{2} \rangle$  [46, 158, 334]. Thus, the islands with the straight edges are assigned to a  $\text{TbSi}_2$  monolayer. The islands with the rounder edges can be assigned to a  $\text{Tb}_3\text{Si}_5$  multilayer, since the vacancies, which are present in the bulk Si layers, reduce the influence of the edge orientation on the dangling bond density, leading to the rounder edges.

However, the assignments done here are further proven by atomically resolved STM images in the following sections, where the different silicide structures are described in more detail.

### 9.3.1 The $1 \times 1$ superstructure

Characteristic flat islands of the  $\text{TbSi}_2$  monolayer are already occasionally found at submonolayer Tb coverages above 0.5 ML. At Tb coverages around 1 ML, as shown in Fig. 9.12 (a) and (b), the number and the size of the islands increases. In the regions in between the  $\text{TbSi}_2$  islands, different submonolayer superstructures are found. Which structure thereby forms mainly depends on the growth temperature. At lower growth temperatures of around 500 °C as shown in (a) mainly the  $2\sqrt{3} \times 2\sqrt{3}$  R30° superstructure is found, while at higher growth temperatures as shown in (b) the  $5 \times 2$  superstructure is found more often.

In Fig. 9.12 (c) and (d), detailed high resolution filled states and empty states STM images measured on top of a monolayer island are shown. In the images, clearly a  $1 \times 1$  periodicity is observed, as indicated by the unit cell drawn in red. A  $1 \times 1$  superstructure is also known to form for the two-dimensional monolayer silicides of other trivalent rare earth metals, thus further supporting the assignment made above by analyzing the island edges. In addition, the

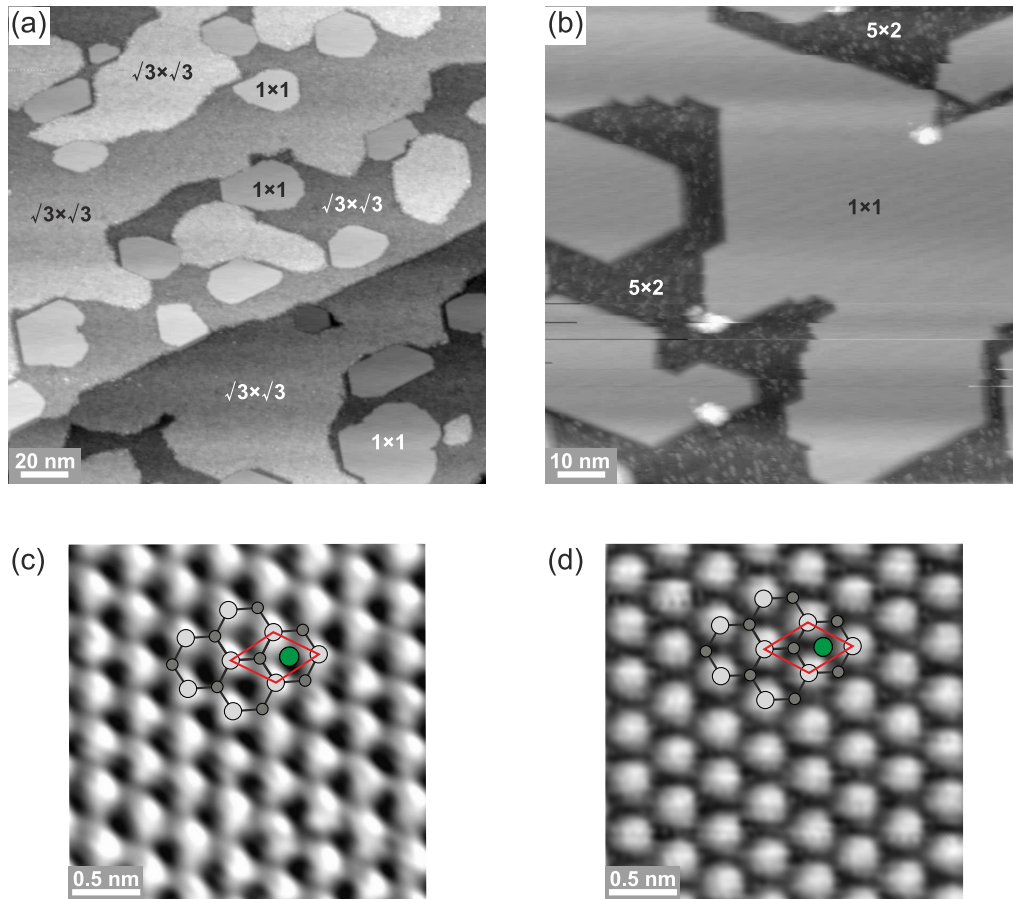


**Figure 9.12:** (a,b) Overview STM images of the  $\text{TbSi}_2$  monolayer. (a) 0.9 ML Tb coverage subsequently annealed at  $500^\circ\text{C}$  for 2 min ( $V_S = -2.5\text{ V}$ ;  $I_T = 100\text{ pA}$ ). (b) 1.2 ML Tb coverage subsequently annealed at  $600^\circ\text{C}$  for 2 min ( $V_S = -2.0\text{ V}$ ;  $I_T = 100\text{ pA}$ ). In the images, the forming structures are indicated. (c,d) High resolution (c) filled states STM image ( $V_S = -0.4\text{ V}$ ;  $I_T = 4\text{ nA}$ ) and (d) empty states STM image ( $V_S = +0.3\text{ V}$ ;  $I_T = 4\text{ nA}$ ) of the  $1\times 1$  superstructure. In both images, the atomic structure model is overlaid on the STM images. The red line therein indicates the  $1\times 1$  unit cell.

structure model of the two-dimensional hexagonal  $\text{RESi}_2$  monolayer is overlaid on the STM images in Fig. 9.12 (c) and (d). It again demonstrates the good agreement with the assumed structure. In both images, the buckled Si top layer is imaged. Especially in (c), alternating brighter and darker appearing spots are observed, which can be assigned to the upper and lower Si atoms, respectively, of the buckled  $1\times 1$  surface layer, which is similar to an unreconstructed Si(111) surface. In the empty states image mainly the upper Si atoms are observed with a  $1\times 1$  periodicity. Even in this empty states image, the Tb atoms are not visible since they are located far underneath the Si surface layer [cf. Fig. 3.24 (b)]. It should be noted that rather extreme tunneling conditions with low tunneling voltages and high tunneling currents need to be employed to obtain such atomically resolved STM images of the  $1\times 1$  superstructure due to the low corrugation of the buckled Si surface layer.

## Electronic properties

In addition to the growth and the atomic structure, also the electronic properties of the  $1 \times 1$  superstructure are investigated using STS. The results are shown in Fig. 9.13 (a) and (b). For the STS measurements, the tip position was stabilized at  $V_S = -2.0$  V and  $I_T = 100$  pA, then the tip was additionally approached towards the sample by 700 pm. The  $dI/dV$ - $V$  curves shown in (b) were measured simultaneously using a lock-in amplifier, employing a modulation frequency of 1 kHz and a modulation amplitude of 50 mV.

The electronic properties of two-dimensional monolayer silicides of other rare earth metals were already intensively studied using ARPES (cf. section 3.6.2). In these measurements a similar band structure for the different two-dimensional rare earth disilicides was found, with one band crossing the Fermi level near the  $\bar{M}$  point forming an electron pocket and one band crossing the Fermi level near the  $\bar{\Gamma}$  point forming a hole pocket (see Fig. 3.25). Thus the  $1 \times 1$  superstructure exhibits a metallic behavior which is also clearly observed in the present STS measurements, characterized by a nonzero slope at the Fermi level in Fig. 9.13 (a) resulting in the nonzero  $dI/dV$  signal in (b).

However, the spectra show some more features. For a detailed discussion, the normalized differential conductivity is shown in Fig. 9.13 (c). It has to be mentioned that, although spectra similar to those shown in Fig. 9.13 (a) and (b) could be reproducibly obtained on the  $1 \times 1$  superstructure also with different STM tips, one measurement showed a different behavior. The calculated normalized differential conductivity for this measurement, in which a different tip was used and the tip position was stabilized at  $V_S = +1.5$  V and  $I_T = 100$  pA, is included in (c) as the red curve. Although it shows very different spectral features, again a metallic behavior is found. Thus, the STS measurements can clearly confirm the metallic properties of the  $1 \times 1$  superstructure that were also found in ARPES measurements as mentioned above.

The differences between the two measurements might result from different influences of the DOS of the STM tip, which might modify one or even both spectra. To evaluate, which spectrum shows a better agreement with the LDOS of the  $1 \times 1$  structure, they are compared with the band structure calculated for  $\text{YSi}_2$  using DFT by Rogero *et al.* [327]. Since the DOS projected on the first layers is additionally plotted in Ref. [327], the normalized differential conductivity curves shown in Fig. 9.13 (c) are directly compared with these plots. Therefore, Fig. 9.13 (d) shows an enlarged view of the first three layers of the projected DOS shown in Fig. 5 in Ref. [327]. Since predominantly the Si surface layer contributes to the STM images as discussed previously, a comparison with these curves seems sufficient.

When comparing the spectra shown in Fig. 9.13 (c) with the DOS shown in (d), the black curve shows a much better agreement. The main spectral features of this measurement (indicated by A-F) are all present in the calculated DOS, although some appear slightly shifted in energy: Both the  $(dI/dV)/(I/V)$ - $V$  spectrum and the DOS show a minimum slightly below the Fermi level, while a maximum (indicated by D) is found slightly above. Also the feature indicated by B is well reproduced in the DOS, and a slight shoulder appears at the position of the feature indicated by C. At around 0.5 V, where feature E is found, several peaks are

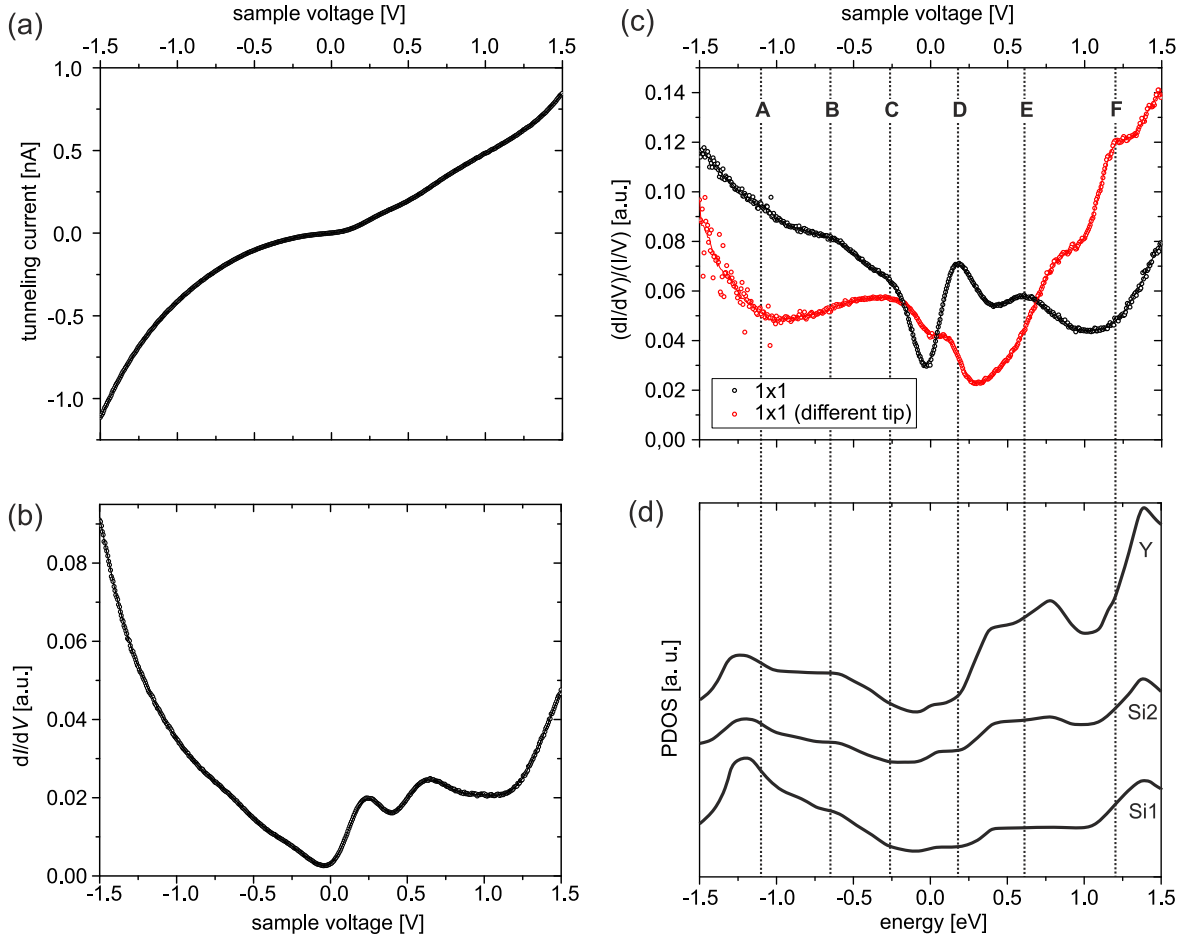


**Figure 9.13:** STS results for the TbSi<sub>2</sub> monolayer forming a 1×1 superstructure. (a,b) Measured  $I$ - $V$  and  $dI/dV$ - $V$  spectra. (c) Calculated normalized differential conductivity. The black curve represents the measurement already shown in (a,b), while the red curve shows an STS measurement with another STM tip. The spectral features observed in the black spectrum are indicated by A-F. (d) DOS projected on the first three layers of the YSi<sub>2</sub> monolayer calculated by Rogero *et al.* [327]. Adapted from [327].

found in the DOS of the three different layers, which might be responsible for the rather broad maximum in (c). Finally, also the increasing LDOS at about  $-1.0$  V and  $+1.2$  V (A and F) is reproduced in (d). Thus, a good overall agreement between the experimental normalized differential conductivity and the calculated DOS is found. Since the electronic band structure calculated in Ref. [327] for Y is very similar to the band structure measured using ARPES for Gd, Dy, and Er [327–329], also a good agreement with the ARPES measurements is expected.

The slight energy shifts that are observed might be caused by a minimum remaining semi-conducting behavior of the tip. The different appearance of the red curve shown Fig. 9.13 (c) may be assigned to problems with the STS measurement, probably caused by the different tip, which seems to strongly influence the spectrum. The measured spectrum might then not show the pure LDOS of the sample surface, but a mixture between the LDOS of the surface and the DOS of the STM tip. However, due to the different spectra that are obtained here, the STS measurements have to be seen as preliminary results. To definitely decide, which

spectrum represents the LDOS of the  $1\times 1$  superstructure better, further measurements and a direct comparison with calculations for  $\text{TbSi}_2$  are necessary.

### 9.3.2 The $\sqrt{3}\times\sqrt{3}$ superstructure

In comparison to the monolayer, in detailed STM images of the multilayer a larger unit cell appears, as indicated in Fig. 9.14. As also observed in multilayer silicides formed from other trivalent rare earth metals, here a  $\sqrt{3}\times\sqrt{3}$  R30° superstructure forms due to vacancies in the planar Si bulk layers. Since the surface layer is a buckled Si layer similar to the unreconstructed Si(111) surface, being identical to that formed in the monolayer case, an arrangement of the protrusions in hexagons, with every second protrusion appearing lower is still observed. In Fig. 9.14 (a), however, the distances between neighboring bright protrusions show a small variation, leading to a triangular grouping of the brighter protrusions and a  $\sqrt{3}\times\sqrt{3}$  R30° periodicity. In contrast, in (b) the  $\sqrt{3}\times\sqrt{3}$  R30° periodicity is caused by an appearance of the holes inside the Si hexagons with different depths. This effect can be explained on the basis of the structure model shown in Fig. 3.26. As mentioned above, the Si bulk layers are not buckled any more, and the corresponding reduction of the Si-Si bond length leads to the formation of an ordered array of Si vacancies, with every sixth Si atom missing, resulting in a  $\sqrt{3}\times\sqrt{3}$  R30° periodicity. These layers even modify the tunneling probability at the Si surface layer, leading to the observation of the  $\sqrt{3}\times\sqrt{3}$  bulk periodicity in the STM images instead of the  $1\times 1$  surface geometry. This effect might be enhanced by a slight replacement of the surface atoms caused by a structural relaxation of these atoms towards the vacancy leading to the triangular grouping mentioned above.

The filled states STM image shown in (a) is in good agreement to former STM experiments of  $\text{Dy}_3\text{Si}_5$  multilayers [46] and  $\text{Er}_3\text{Si}_5$  multilayers on Si(111) [408]. However, in the empty states image shown in (b), the holes inside the Si hexagons show a variation in their apparent depth, which is responsible for the  $\sqrt{3}\times\sqrt{3}$  periodicity. On a first glance, such a variation is incompatible with the mentioned structure model, from which identical apparent depths of the three holes within one  $\sqrt{3}\times\sqrt{3}$  unit cell are expected (see Fig. 3.26). However, this is only true

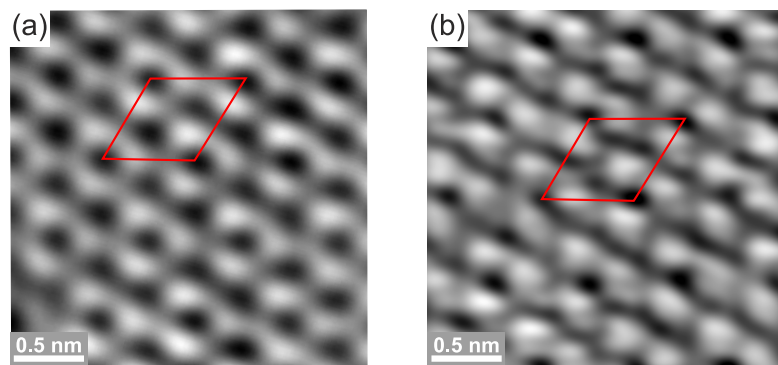


**Figure 9.14:** High resolution (a) filled states STM image ( $V_S = -0.3$  V;  $I_T = 4$  nA) and (b) empty states STM image ( $V_S = +0.3$  V;  $I_T = 4$  nA) of the  $\sqrt{3}\times\sqrt{3}$  superstructure. In both images, a  $\sqrt{3}\times\sqrt{3}$  unit cell is indicated.

for a tip with a perfect cylindrical symmetry. In the case of a tip geometry without cylinder symmetry, the tunneling probability may vary for the three holes, resulting in a contrast like the one observed in (b). As for the  $1\times 1$  superstructure, again rather extreme tunneling conditions need to be employed to obtain atomic resolution on the  $\sqrt{3}\times\sqrt{3}$  R30° superstructure.

## 9.4 Conclusions

In this chapter, thin Tb silicide films forming for submonolayer to multilayer Tb coverages on the Si(111) surface were studied.

In the submonolayer regime, different Tb induced structures form. Here, besides the Tb induced  $2\sqrt{3}\times 2\sqrt{3}$  R30° and the  $5\times 2$  superstructure, also nanorods with either a  $2\times 1$  or a  $4\times 1$  superstructure are found. The Tb induced  $2\sqrt{3}\times 2\sqrt{3}$  R30° superstructure is found to exhibit an analogous structure as the  $2\sqrt{3}\times 2\sqrt{3}$  R30° superstructures induced by other trivalent rare earth metals like Dy or Er. Using STS, a semi-metallic behavior is found for this superstructure similar as observed for Er. Hence, regarding both the atomic structure and the electronic properties, a nice agreement in the properties of the Tb induced  $2\sqrt{3}\times 2\sqrt{3}$  R30° superstructure and those induced by other trivalent rare earth metals is found. However, small deviations are observed, e.g. smaller domains, which are assigned to the different ionic radii for different rare earth metals. Regarding the  $5\times 2$  superstructure, a structure model could be developed, explaining nicely the observed features in the STM images as well as the different configurations that are observed for this structure. Here, a detailed understanding how different registry shifts lead to configuration changes for this superstructure could be developed. Furthermore, up to  $0.4\ \mu\text{m}$  long nanorods with either a  $2\times 1$  or a  $4\times 1$  superstructure, the latter presumably representing a preliminary stage of the  $2\times 1$  superstructure, are observed predominantly for submonolayer Tb coverages.

In the monolayer-to-multilayer regime, the formation of  $\text{TbSi}_2$  islands forming a  $1\times 1$  superstructure and  $\text{Tb}_3\text{Si}_5$  islands forming a  $\sqrt{3}\times\sqrt{3}$  R30° superstructure is observed. In addition to their atomic structure, which could be identified to be identical to the hexagonal two-dimensional and three-dimensional silicides of other rare earth metals, the electronic structure of the  $1\times 1$  superstructure was investigated using STS. Also here, a good agreement with the band structure of other monolayer rare earth silicides is found.

---

## Chapter 10

# Summary and outlook

In the present work, the atomic and electronic properties of self-assembled clusters formed from various materials on silicon surfaces were studied in detail using scanning tunneling microscopy and spectroscopy. Thereby, Sb, In, Ga, Dy, Tb, and Si were used as cluster materials and Si(111), Si(001), and Si(557) surfaces as substrates.

For Sb on the Si(111) surface, the growth parameters were systematically varied over a wide range, in which a formation of different cluster types was found. Besides the formation of so-called bright clusters, also the formation of so-called double-row clusters and magic ringlike clusters has been observed. It was found that the Sb induced double-row clusters are pure Si clusters that formed from Si atoms that are released by the numerous adatom substitutions found for this system. For comparison, Si(111) homoepitaxy experiments were conducted, in which identical Si clusters could be observed.

The Sb clusters exhibiting the most promising properties are the magic ringlike clusters. For these clusters, an extremely homogeneous growth was observed and an atomic structure model was developed, which is also able to explain the observed variations in their apparent height. These height variations were assigned to different stoichiometries of the clusters, leading to a modification of their electronic structure, which was also observed in STS measurements. Hence, a system of clusters that exhibits an identical structure but different stoichiometries was found. It is thus an ideal model system to investigate how the incorporation of an increasing number of impurity atoms changes the properties of the system. This is particularly interesting since Sb, as a group-V element, represents a dopant when being incorporated into Si. For further proving the developed structure model, DFT calculations are conducted within the group of Prof. Dr. Karsten Reuter at the Technische Universität München.

The basic structural and electronic properties of the magic clusters formed from the group-III metals Ga, In, and Al on Si(111) are well established. In addition, they are very easy to fabricate. Thus, magic Ga and In clusters on Si(111) were chosen as a model system to study how different environments influence the electronic properties of the clusters and to investigate the possibility of preparing one-dimensional arrays of clusters using a vicinal substrate. For magic In clusters on the planar Si(111) surface, a detailed investigation of the charge redistribution that takes place during the formation of the clusters was performed on

the basis of voltage dependent STM images and STS. In addition, it was found that clusters in UFHUCs, FHUCs as well as clusters with neighboring clusters show different electronic properties, in particular different band gap sizes. In the future, STS measurements should be performed also on clusters on UFHUCs neighboring other clusters as well as on larger agglomerations of clusters to study the transition from single clusters to two-dimensional arrays of magic clusters in more detail.

Using the Si(557) surface as a substrate for the growth of magic In clusters, a formation of two different one-dimensional arrays was demonstrated. Similar to the two-dimensional arrays on the planar Si(111) surface, the magic In clusters first occupy only the FHUCs, followed by the occupation of the UFHUCs. However, it was found that the cluster formation does not start instantaneously, but a saturation of the steps with In is assumed to take place before. For this system, STS measurements should also be performed to investigate the influence of the one-dimensional ordering on the electronic structure.

The most comprehensively studied material systems were nanostructures induced by the deposition of the rare earth metals Dy and Tb on silicon surfaces. Here, Dy and Tb induced clusters on Si(111), Dy induced clusters on Si(001), and thin Tb silicide films on Si(111) were investigated.

Regarding rare earth silicide clusters on Si(111), the formation of different cluster types was observed with two main types of magic clusters. For both the so-called off-center rare earth silicide clusters and the so-called centered rare earth silicide clusters, the atomic structure could be identified and a semiconducting nature was found by STS. Furthermore, the centered clusters were found to perform a bistable switching between two configurations. This switching was assigned to be triggered by the STM tip when it approaches the clusters. Based on this switching, very interesting applications are imaginable, e.g. logic gates or high density memory devices. However, at present the switching only occurs randomly. In the future, it should be investigated, if this switching can be performed in a controlled way. Additionally, DFT calculations are currently performed within the group of Prof. Dr. Karsten Reuter at the Technische Universität München to verify the proposed atomic structure model and to investigate the energy barriers for the switching.

Depositing Dy on Si(001) resulted in the formation of clusters showing a completely different growth behavior. Again, the formation of magic clusters was observed, but the clusters showed a strong tendency to assemble into one-dimensional arrays. Thereby, chains consisting of different numbers of identical clusters were found, growing perpendicular to the dimer rows of the Si(001)2×1 substrate. Based on STM images acquired at different voltages for both polarities, an atomic structure model that might explain the experimental observations was proposed. However, for a definite assignment of the atomic structure, DFT calculations including STM image simulations are required. In addition, STS measurements would be extremely interesting, because these clusters may represent a model system to investigate the effects of chain formation on the electronic structure.

In addition to clusters, also thin films that grow at higher coverages in the submonolayer to multilayer range were investigated for Tb on Si(111). Here, the growth in principal resembled

the one of other rare earth metals, e.g. Dy, Tb, or Gd, due to the chemical similarity of all the trivalent rare earth metals. In the submonolayer regime, various Tb induced superstructures were found. For the Tb induced  $2\sqrt{3}\times 2\sqrt{3}$  R30° superstructure, domains separated by a triangular network of domain boundaries were observed. Based on high resolution STM images, it could be demonstrated that its atomic structure is analogous to the one identified for Er and Dy. STS measurements performed on this structure showed a semi-metallic behavior. The second submonolayer structure is the  $5\times 2$  superstructure, which was found to form chains along the  $\langle 1\bar{1}0 \rangle$  directions. Its detailed atomic structure was identified based on a model proposed for the Gd induced  $5\times 2$  superstructure on the basis of Si Seiwatz and Si honeycomb chains with the rare earth atoms forming rows with  $\times 2$  periodicity in between the Si chains. The existing model could be refined regarding the correct adsorption sites of the rare earth atoms. In addition, a detailed analysis was conducted on how different registries lead to the different configurations that are observed for this superstructure. A third type of nanostructures observed in the submonolayer regime are nanorods with either a  $2\times 1$  or a  $4\times 1$  superstructure. However, the amount of data on these nanorods remained rather limited not allowing the development of a structure model yet. Here, further experiments are necessary.

A different growth behavior was observed in the monolayer-to-multilayer Tb coverage regime. Here, extended islands of either the monolayer silicide with a  $\text{TbSi}_2$  stoichiometry or the multilayer silicide with a  $\text{Tb}_3\text{Si}_5$  stoichiometry formed. On the basis of atomically resolved STM images it was found that, similar to other rare earth silicides, the monolayer forms a  $1\times 1$  superstructure, while the multilayer forms a  $\sqrt{3}\times\sqrt{3}$  R30° superstructure due to the presence of an ordered array of vacancies in the planar Si bulk layers. STS measurements performed on the monolayer silicide confirmed the metallic properties known from ARPES measurements. Currently, DFT calculations on the rare earth silicide films studied here are performed within the group of Prof. Dr. Wolf Gero Schmidt at the University of Paderborn to verify the structure models and the measured electronic properties.

In conclusion, the results obtained within this work expand the knowledge on magic clusters on silicon surfaces and on thin rare earth silicide films on Si(111). For the investigated systems, clusters exhibiting completely different and extremely interesting properties were found. This demonstrates that, by choosing an appropriate combination of cluster materials and substrates as well as preparation conditions, it is possible to strongly influence the physical properties. Thus, in the future a creation of tailored materials with the desired properties might be possible on the basis of these fascinating nanostructures leading e.g. to applications in novel nanodevices.



---

# Bibliography

- [1] O. Echt, K. Sattler, and E. Recknagel, *Phys. Rev. Lett.* **47**, 1121 (1981).
- [2] W.D. Knight, K. Clemenger, W.A. de Heer, W.A. Saunders, M.Y. Chou, and M.L. Cohen, *Phys. Rev. Lett.* **52**, 2141 (1984).
- [3] H. Haberland (Ed.), *Clusters of Atoms and Molecules. Theory, experiment, and clusters of atoms*, Springer-Verlag, Berlin, 1994.
- [4] J. Dąbrowski and H.-J. Müssig, *Silicon Surfaces and Formation of Interfaces: Basic Science in the Industrial World*, World Scientific Publishing, Singapore, 2000.
- [5] M.Y. Lai and Y.L. Wang, *Phys. Rev. Lett.* **81**, 164 (1998).
- [6] K. Takayanagi, Y. Tanishiro, M. Takahashi, and S. Takahashi, *J. Vac. Sci. Technol. A* **3**, 1502 (1985).
- [7] M.Y. Lai and Y.L. Wang, *Phys. Rev. B* **64**, 241404 (2001).
- [8] J.-F. Jia, J.-Z. Wang, X. Liu, Q.-K. Xue, Z.-Q. Li, Y. Kawazoe, and S.B. Zhang, *Appl. Phys. Lett.* **80**, 3186 (2002).
- [9] V.G. Kotlyar, A.V. Zotov, A.A. Saranin, T.V. Kasyanova, M.A. Cherevik, I.V. Pisarenko, and V.G. Lifshits, *Phys. Rev. B* **66**, 165401 (2002).
- [10] J.-L. Li, J.-F. Jia, X.-J. Liang, X. Liu, J.-Z. Wang, Q.-K. Xue, Z.-Q. Li, J.S. Tse, Z. Zhang, and S.B. Zhang, *Phys. Rev. Lett.* **88**, 066101 (2002).
- [11] K. Wu, Y. Fujikawa, T. Nagao, Y. Hasegawa, K.S. Nakayama, Q.K. Xue, E.G. Wang, T. Briere, V. Kumar, Y. Kawazoe, S.B. Zhang, and T. Sakurai, *Phys. Rev. Lett.* **91**, 126101 (2003).
- [12] S.-C. Li, J.-F. Jia, R.-F. Dou, Q.-K. Xue, I.G. Batyrev, and S.B. Zhang, *Phys. Rev. Lett.* **93**, 116103 (2004).
- [13] M.A.K. Zilani, Y.Y. Sun, H. Xu, L. Liu, Y.P. Feng, X.-S. Wang, and A.T.S. Wee, *Phys. Rev. B* **72**, 193402 (2005).
- [14] M.A.K. Zilani, Y.Y. Sun, H. Xu, G.W. Peng, Y.P. Feng, X.-S. Wang, and A.T.S. Wee, *Surf. Sci.* **601**, 2486 (2007).

- [15] Y. Wu, Y. Zhou, C. Zhou, H. Zhan, and J. Kang, *J. Chem. Phys.* **133**, 124706 (2010).
- [16] C. Zhou, Q. Xue, J. Jia, H. Zhan, and J. Kang, *J. Chem. Phys.* **130**, 024701 (2009).
- [17] A.G. Mark and A.B. McLean, *Phys. Rev. B* **85**, 195448 (2012).
- [18] T. Sekiguchi, S. Yoshida, and K.M. Itoh, *Phys. Rev. Lett.* **95**, 106101 (2005).
- [19] T. Sekiguchi, S. Yoshida, K.M. Itoh, J. Mysliveček, and B. Voigtländer, *Appl. Phys. Lett.* **90**, 013108 (2007).
- [20] T. Sekiguchi, S. Yoshida, Y. Shiren, K.M. Itoh, J. Mysliveček, and B. Voigtländer, *J. Appl. Phys.* **101**, 081702 (2007).
- [21] M. Valden, X. Lai, and D.W. Goodman, *Science* **281**, 1647 (1998).
- [22] B. Yoon, H. Häkkinen, U. Landman, A.S. Wörz, J.-M. Antonietti, S. Abbet, K. Judai, and U. Heiz, *Science* **307**, 403 (2005).
- [23] U. Heiz and U. Landman (Eds.), *Nanocatalysis*, Springer-Verlag, Berlin, 2007.
- [24] Z. Zhang, Q. Fu, H. Zhang, Y. Li, Y. Yao, D. Tan, and X. Bao, *J. Phys. Chem. C* **111**, 13524 (2007).
- [25] S. Sun, C.B. Murray, D. Weller, L. Folks, and A. Moser, *Science* **287**, 1989 (2000).
- [26] Y. Gao, Y. Bao, M. Beerman, A. Yasuhara, D. Shindo, and K.M. Krishnan, *Appl. Phys. Lett.* **84**, 3361 (2004).
- [27] M.-H. Pan, H. Liu, J.-Z. Wang, J.-F. Jia, Q.-K. Xue, J.-L. Li, S. Qin, U. M. Mirsaidov, X.-R. Wang, J. T. Markert, Z. Zhang, and C.-K. Shih, *Nano Lett.* **5**, 87 (2005).
- [28] K. He, M.-H. Pan, J.-Z. Wang, H. Liu, J.-F. Jia, and Q.-K. Xue, *Surf. Interface Anal.* **38**, 1028 (2006).
- [29] E. Inami, I. Hamada, K. Ueda, M. Abe, S. Morita, and Y. Sugimoto, *Nat. Commun.* **6**, 6231 (2015).
- [30] D.M. Eigler, C.P. Lutz, and W.E. Rudge, *Nature* **352**, 600 (1991).
- [31] U.J. Quaade, K. Stokbro, C. Thirstrup, and F. Grey, *Surf. Sci.* **415**, L1037 (1998).
- [32] Y.W. Mo, *Science* **261**, 886 (1993).
- [33] P. Liljeroth, J. Repp, and G. Meyer, *Science* **317**, 1203 (2007).
- [34] Ch. Nacci, J. Lagoute, X. Liu, and S. Fölsch, *Phys. Rev. B* **77**, 121405 (2008).
- [35] Ch. Nacci, S. Fölsch, K. Zenichowski, J. Dokić, T. Klamroth, and P. Saalfrank, *Nano Lett.* **9**, 2996 (2009).
- [36] D.M. Eigler and E.K. Schweizer, *Nature* **344**, 524 (1990).

- [37] G. Binnig, H. Rohrer, Ch. Gerber, and E. Weibel, *Phys. Rev. Lett.* **49**, 57 (1982).
- [38] J.E. Baglin, F.M. d'Heurle, and C.S Petersson, *Appl. Phys. Lett.* **36**, 594 (1980).
- [39] K.N. Tu, R.D. Thompson, and B.Y. Tsaur, *Appl. Phys. Lett.* **38**, 626 (1981).
- [40] J.A. Knapp and S.T. Picraux, *Appl. Phys. Lett.* **48**, 466 (1986).
- [41] F.P. Netzer, *J. Phys.: Condens. Matter* **7**, 991 (1995).
- [42] T.P. Roge, F. Palmino, C. Savall, J.C. Labrune, and C. Pirri, *Surf. Sci.* **383**, 350 (1997).
- [43] C. Battaglia, H. Cercellier, C. Monney, M.G. Garnier, and P. Aebi, *Europhys. Lett.* **77**, 36003 (2007).
- [44] A. Kirakosian, J.L. McChesney, R. Bennewitz, J.N. Crain, J.-L. Lin, and F.J. Himpsel, *Surf. Sci.* **498**, L109 (2002).
- [45] P. Wetzel, C. Pirri, G. Gewinner, S. Pelletier, P. Roge, F. Palmino, and J.C. Labrune, *Phys. Rev. B* **56**, 9819 (1997).
- [46] I. Engelhardt, C. Preinesberger, S.K. Becker, H. Eisele, and M. Dähne, *Surf. Sci.* **600**, 755 (2006).
- [47] E.W. Perkins, I.M. Scott, and S.P. Tear, *Surf. Sci.* **578**, 80 (2005).
- [48] M.H. Tuilier, P. Wetzel, C. Pirri, D. Bolmont, and G. Gewinner, *Phys. Rev. B* **50**, 2333 (1994).
- [49] P. Wetzel, S. Saintenoy, C. Pirri, D. Bolmont, G. Gewinner, T.P. Roge, F. Palmino, C. Savall, and J.C. Labrune, *Surf. Sci.* **355**, 13 (1996).
- [50] S. Vandr e, T. Kalka, C. Preinesberger, and M. Dähne-Prietsch, *Phys. Rev. Lett.* **82**, 1927 (1999).
- [51] T.P. Roge, F. Palmino, C. Savall, J.C. Labrune, P. Wetzel, C. Pirri, and G. Gewinner, *Phys. Rev. B* **51**, 10998 (1995).
- [52] M. Lohmeier, W.J. Huisman, E. Vlieg, A. Nishiyama, C.L. Nicklin, and T.S. Turner, *Surf. Sci.* **345**, 247 (1996).
- [53] F.H. Kaatz, J. Van der Spiegel, and W.R. Graham, *J. Appl. Phys.* **69**, 514 (1991).
- [54] C.H. Luo, G.H. Shen, and L.J. Chen, *Appl. Surf. Sci.* **113**, 457 (1997).
- [55] J-Y. Veuillen, S. Kennou, and T.A. Nguyen Tan, *Solid State Commun.* **79**, 795 (1991).
- [56] S. Vandr e, T. Kalka, C. Preinesberger, and M. Dähne-Prietsch, *J. Vac. Sci. Technol. B* **17**, 1682 (1999).
- [57] S. Vandr e, C. Preinesberger, W. Busse, and M. Dähne, *Appl. Phys. Lett.* **78**, 2012 (2001).

- [58] G. Binnig, H. Rohrer, Ch. Gerber, and E. Weibel, *Phys. Rev. Lett.* **50**, 120 (1983).
- [59] G. Binnig and H. Rohrer, *Rev. Mod. Phys.* **59**, 615 (1987).
- [60] G. Binnig and D.P.E. Smith, *Rev. Sci. Instrum.* **57**, 1688 (1986).
- [61] J. Bardeen, *Phys. Rev. Lett.* **6**, 57 (1961).
- [62] C.J. Chen, *Introduction to Scanning Tunneling Microscopy*, Oxford University Press, New York, 1993.
- [63] R. Wiesendanger, *Scanning probe microscopy and spectroscopy: methods and applications*, Cambridge University Press, Cambridge, 1994.
- [64] D.A. Bonnell (Ed.), *Scanning Tunneling Microscopy and Spectroscopy: Theory, Techniques, and Applications*, VCH Publishers, New York, 1993.
- [65] J.A. Stroscio and W.J. Kaiser (Eds.), *Scanning Tunneling Microscopy*, Academic Press, San Diego, 1993.
- [66] C.J. Chen, *Mod. Phys. Lett. B* **5**, 107 (1991).
- [67] J. Tersoff and D.R. Hamann, *Phys. Rev. Lett.* **50**, 1998 (1983).
- [68] J. Tersoff and D.R. Hamann, *Phys. Rev. B* **31**, 805 (1985).
- [69] C.J. Chen, *J. Vac. Sci. Technol. A* **6**, 319 (1988).
- [70] R.J. Hamers, *Ann. Rev. Phys. Chem.* **40**, 531 (1989).
- [71] N.D. Lang, *Phys. Rev. B* **34**, 5947 (1986).
- [72] J.A. Stroscio, R.M. Feenstra, and A.P. Fein, *Phys. Rev. Lett.* **57**, 2579 (1986).
- [73] R.M. Feenstra, J.A. Stroscio, and A.P. Fein, *Surf. Sci.* **181**, 295 (1987).
- [74] R.M. Feenstra, *Surf. Sci.* **299/300**, 965 (1994).
- [75] R.M. Feenstra, *Phys. Rev. B* **50**, 4561 (1994).
- [76] R.M. Feenstra, *J. Vac. Sci. Technol. B* **7**, 925 (1989).
- [77] M. Prietsch, A. Samsavar, and R. Ludeke, *Phys. Rev. B* **43**, 11850 (1991).
- [78] H. Haberland, K. Kleinerhans, and F. Träger, *Cluster, in: Bergmann/Schaefer, Lehrbuch der Experimentalphysik, Band 5: Gase, Nanosysteme, Flüssigkeiten*, Walter de Gruyter, Berlin, 2006.
- [79] R.L. Johnston, *Atomic and Molecular Clusters*, Taylor & Francis, London, 2002.
- [80] M. Neeb, *Cluster: Einführung, Synthese und Schalenmodelle, in: Physik der Nanostrukturen, Vorlesungsmanuskripte des 29. IFF-Ferienkurses*, Schriften des Forschungszentrums Jülich, Jülich, 1998.

- [81] K.-H. Meiwes-Broer and H.O. Lutz, *Phys. Bl.* **47**, 283 (1991).
- [82] V.N. Popok, I. Barke, E.E.B. Campbell, and K.-H. Meiwes-Broer, *Surf. Sci. Rep.* **66**, 347 (2011).
- [83] C. Binns, *Surf. Sci. Rep.* **44**, 1 (2001).
- [84] W.A. de Heer, *Rev. Mod. Phys.* **65**, 611 (1993).
- [85] A.L. Mackay, *Acta Cryst.* **15**, 916 (1962).
- [86] W. Miehle, O. Kandler, T. Leisner, and O. Echt, *J. Chem. Phys.* **91**, 5940 (1989).
- [87] W. Miehle, O. Echt, O. Kandler, T. Leisner, and E. Recknagel, *Z. Phys. D* **12**, 273 (1989).
- [88] I.A. Harris, R.S. Kidwell, and J.A. Northby, *Phys. Rev. Lett.* **53**, 2390 (1984).
- [89] I.A. Harris, K.A. Norman, R.V. Mulkern, and J.A. Northby, *Chem. Phys. Lett.* **130**, 316 (1986).
- [90] T.P. Martin, *Phys. Rep.* **273**, 199 (1996).
- [91] S.S. Kim and G.D. Stein, *J. Colloid Interface Sci.* **87**, 180 (1982).
- [92] J. Farges, M.F. de Feraudy, B. Raoult, and G. Torchet, *Surf. Sci.* **106**, 95 (1981).
- [93] J. Farges, M.F. de Feraudy, B. Raoult, and G. Torchet, *J. Chem. Phys.* **84**, 3491 (1986).
- [94] J.W. Lee and G.D. Stein, *J. Phys. Chem.* **91**, 2450 (1987).
- [95] R. Pflaum, K. Sattler, and E. Recknagel, *Chem. Phys. Lett.* **138**, 8 (1987).
- [96] T.P. Martin, *Phys. Rep.* **95**, 167 (1983).
- [97] M.Y. Chou, A. Cleland, and M.L. Cohen, *Solid State Commun.* **52**, 645 (1984).
- [98] W.D. Knight, W.A. de Heer, W.A. Saunders, K. Clemenger, M.Y. Chou, and M.L. Cohen, *Chem. Phys. Lett.* **134**, 1 (1987).
- [99] W. Ekardt, *Phys. Rev. B* **29**, 1558 (1984).
- [100] S. Bjørnholm, J. Borggreen, O. Echt, K. Hansen, J. Pedersen, and H.D. Rasmussen, *Phys. Rev. Lett.* **65**, 1627 (1990).
- [101] T.P. Martin, T. Bergmann, H. Göhlich, and T. Lange, *Z. Phys. D* **19**, 25 (1991).
- [102] S. Bjørnholm, J. Borggreen, O. Echt, K. Hansen, J. Pedersen, and H.D. Rasmussen, *Z. Phys. D* **19**, 47 (1991).
- [103] M. Brack, *Rev. Mod. Phys.* **65**, 677 (1993).
- [104] K. Clemenger, *Phys. Rev. B* **32**, 1359 (1985).

- [105] W. Ekardt and Z. Penzar, Phys. Rev. B **38**, 4273 (1988).
- [106] Z. Penzar and W. Ekardt, Z. Phys. D **17**, 69 (1990).
- [107] H.A. Jahn and E. Teller, Proc. Roy. Soc. A **161**, 220 (1937).
- [108] W.A. Saunders, K. Clemenger, W.A. de Heer, and W.D. Knight, Phys. Rev. B **32**, 1366 (1985).
- [109] W.D. Knight, W.A. de Heer, K. Clemenger, and W.A. Saunders, Solid State Commun. **53**, 445 (1985).
- [110] I. Katakuse, T. Ichihara, Y. Fujita, T. Matsuo, T. Sakurai, and H. Matsuda, Int. J. Mass Spectrom. Ion Proc. **67**, 229 (1985).
- [111] I. Katakuse, T. Ichihara, Y. Fujita, T. Matsuo, T. Sakurai, and H. Matsuda, Int. J. Mass Spectrom. Ion Proc. **74**, 33 (1986).
- [112] H.W. Kroto, J.R. Heath, S.C. O'Brien, R.F. Curl, and R.E. Smalley, Nature **318**, 162 (1985).
- [113] K.S. Novoselov, A.K. Geim, S.V. Morozov, D. Jiang, Y. Zhang, S.V. Dubonos, I.V. Grigorieva, and A.A. Firsov, Science **306**, 666 (2004).
- [114] H. Kroto, Science **242**, 1139 (1988).
- [115] R.F. Curl and R.E. Smalley, Science **242**, 1017 (1988).
- [116] S.N. Khanna and A.W. Castleman Jr. (Eds.), *Quantum Phenomena in Clusters and Nanostructures*, Springer-Verlag, Berlin, 2003.
- [117] R. Busani, M. Folkers, and O. Cheshnovsky, Phys. Rev. Lett. **81**, 3836 (1998).
- [118] C.M. Rohlfing and K. Raghavachari, Chem. Phys. Lett. **167**, 559 (1990).
- [119] K.-M. Ho, A.A. Shvartsburg, B. Pan, Z.-Y. Lu, C.-Z. Wang, J.G. Wacker, J.L. Fye, and M.F. Jarrold, Nature **392**, 582 (1998).
- [120] L. Guo, G. Zhao, Y. Gu, X. Liu, and Z. Zeng, Phys. Rev. B **77**, 195417 (2008).
- [121] S.M. Beck, J. Chem. Phys. **87**, 4233 (1987).
- [122] S.M. Beck, J. Chem. Phys. **90**, 6306 (1989).
- [123] V. Kumar and Y. Kawazoe, Phys. Rev. Lett. **87**, 045503 (2001).
- [124] H. Kawamura, V. Kumar, and Y. Kawazoe, Phys. Rev. B **70**, 245433 (2004).
- [125] K. Koyasu, M. Akutsu, M. Mitsui, and A. Nakajima, J. Am. Chem. Soc. **127**, 4998 (2005).

- [126] P. Claes, E. Janssens, V.T. Ngan, P. Gruene, J.T. Lyon, D.J. Harding, A. Fielicke, M.T. Nguyen, and P. Lievens, *Phys. Rev. Lett.* **107**, 173401 (2011).
- [127] D. Palagin, M. Gramzow, and K. Reuter, *J. Chem. Phys.* **134**, 244705 (2011).
- [128] J. Ulises Reveles and S.N. Khanna, *Phys. Rev. B* **72**, 165413 (2005).
- [129] J. Ulises Reveles and S.N. Khanna, *Phys. Rev. B* **74**, 035435 (2006).
- [130] M.B. Torres, E.M. Fernández, and L.C. Balbás, *Phys. Rev. B* **75**, 205425 (2007).
- [131] K. Koyasu, J. Atobe, M. Akutsu, M. Mitsui, and A. Nakajima, *J. Phys. Chem. A* **111**, 42 (2007).
- [132] E. Janssens, P. Gruene, G. Meijer, L. Wöste, P. Lievens, and A. Fielicke, *Phys. Rev. Lett.* **99**, 063401 (2007).
- [133] P. Gruene, A. Fielicke, G. Meijer, E. Janssens, V.T. Ngan, M.T. Nguyen, and P. Lievens, *Chem. Phys. Chem.* **9**, 703 (2008).
- [134] J.T. Lau, K. Hirsch, Ph. Klar, A. Langenberg, F. Lofink, R. Richter, J. Rittmann, M. Vogel, V. Zamudio-Bayer, T. Möller, and B. von Issendorff, *Phys. Rev. A* **79**, 053201 (2009).
- [135] J.T. Lau, M. Vogel, A. Langenberg, K. Hirsch, J. Rittmann, V. Zamudio-Bayer, T. Möller, and B. von Issendorff, *J. Chem. Phys.* **134**, 041102 (2011).
- [136] J. Rittmann, *Electronic Properties of Transition Metal Doped Silicon Clusters*, PhD thesis, Technische Universität Berlin, 2011.
- [137] K. Koyasu, J. Atobe, S. Furuse, and A. Nakajima, *J. Chem. Phys.* **129**, 214301 (2008).
- [138] M. Ohara, K. Miyajima, A. Pramann, A. Nakajima, and K. Kaya, *J. Phys. Chem. A* **106**, 3702 (2002).
- [139] A. Grubisic, H. Wang, Y.J. Ko, and K.H. Bowen, *J. Chem. Phys.* **129**, 054302 (2008).
- [140] F.C. Frank and J.S. Kasper, *Acta Cryst.* **11**, 184 (1958).
- [141] P. Jena and A.W. Castleman, Jr. (Eds.), *Nanoclusters: a bridge across disciplines*, Elsevier, Amsterdam, 2010.
- [142] A.W. Castleman and K.H. Bowen, *J. Phys. Chem.* **100**, 12911 (1996).
- [143] F. Baletto and R. Ferrando, *Rev. Mod. Phys.* **77**, 371 (2005).
- [144] W. Ekardt (Ed.), *Metal Clusters*, John Wiley & Sons, Chichester, 1999.
- [145] K.-H. Meiwes-Broer (Ed.), *Metal Clusters at Surfaces: Structure, Quantum Properties, Physical Chemistry*, Springer-Verlag, Berlin, 2000.
- [146] K.-H. Meiwes-Broer, *Phys. Bl.* **55**, 21 (1999).

- [147] S. Messerli, S. Schintke, K. Morgenstern, A. Sanchez, U. Heiz, and W.-D. Schneider, *Surf. Sci.* **465**, 331 (2000).
- [148] K. Bromann, C. Félix, H. Brune, W. Harbich, R. Monot, J. Buttet, and K. Kern, *Science* **274**, 956 (1996).
- [149] A. Perez, P. Melinon, V. Dupuis, P. Jensen, B. Prevel, J. Tuaille, L. Bardotti, C. Martet, M. Treilleux, M. Broyer, M. Pellarin, J.L. Vaille, B. Palpant, and J. Lerme, *J. Phys. D: Appl. Phys.* **30**, 709 (1997).
- [150] B. Yoon, V.M. Akulin, Ph. Cahuzac, F. Carlier, M. de Frutos, A. Masson, C. Mory, C. Colliex, and C. Bréchnac, *Surf. Sci.* **443**, 76 (1999).
- [151] A.K. Santra and D.W. Goodman, *J. Phys.: Condens. Matter* **15**, R31 (2002).
- [152] M. Haruta, *Catal. Today* **36**, 153 (1997).
- [153] G.R. Bamwenda, S. Tsubota, T. Nakamura, and M. Haruta, *Catal. Lett.* **44**, 83 (1997).
- [154] A. Sanchez, S. Abbet, U. Heiz, W.-D. Schneider, H. Häkkinen, R.N. Barnett, and U. Landman, *J. Phys. Chem. A* **103**, 9573 (1999).
- [155] A. Bettac, L. Köller, V. Rank, and K.-H. Meiwes-Broer, *Surf. Sci.* **402**, 475 (1998).
- [156] W.M. Haynes (Ed.), *CRC Handbook of Chemistry and Physics*, Ed. 94, CRC Press, Taylor&Francis Group, Boca Raton, 2013.
- [157] O. Madelung (Ed.), *Semiconductors - Basic Data*, Ed. 2, Springer-Verlag, Berlin, 1996.
- [158] M. Wanke, *Rare earth silicide nanowires on silicion surfaces*, PhD thesis, Technische Universität Berlin, 2008.
- [159] J.R. Chelikowsky and M.L. Cohen, *Phys. Rev. B* **14**, 556 (1976).
- [160] H. Lüth, *Surfaces and interfaces of solid materials*, Ed. 3, Springer-Verlag, Berlin, 1995.
- [161] F. Bechstedt, *Principles of Surface Physics*, Springer-Verlag, Berlin, 2003.
- [162] W. Mönch, *Semiconductor Surfaces and Interfaces*, Ed. 3, Springer-Verlag, Berlin, 1995.
- [163] E.A. Wood, *J. Appl. Phys.* **35**, 1306 (1964).
- [164] K.C. Pandey, *Phys. Rev. Lett.* **49**, 223 (1982).
- [165] R.M. Feenstra, W.A. Thompson, and A.P. Fein, *Phys. Rev. Lett.* **56**, 608 (1986).
- [166] F.J. Himpsel, P. Heimann, and D.E. Eastman, *Phys. Rev. B* **24**, 2003 (1981).
- [167] R.I.G. Uhrberg, G.V. Hansson, J.M. Nicholls, and S.A. Flodström, *Phys. Rev. Lett.* **48**, 1032 (1982).
- [168] R. Feder, *Solid State Commun.* **45**, 51 (1983).

- [169] R. Feder and W. Mönch, *Solid State Commun.* **50**, 311 (1984).
- [170] R.M. Tromp, L. Smit, and J.F. van der Veen, *Phys. Rev. B* **30**, 6235 (1984).
- [171] H. Sakama, A. Kawazu, and K. Ueda, *Phys. Rev. B* **34**, 1367 (1986).
- [172] J.E. Northrup and M.L. Cohen, *Phys. Rev. Lett.* **49**, 1349 (1982).
- [173] K.C. Pandey, *Physica B* **117/118**, 761 (1983).
- [174] P. Badziag and W.S. Verwoerd, *Surf. Sci.* **201**, 87 (1988).
- [175] F. Ancilotto, W. Andreoni, A. Selloni, R. Car, and M. Parrinello, *Phys. Rev. Lett.* **65**, 3148 (1990).
- [176] J.E. Northrup, M.S. Hybertsen, and S.G. Louie, *Phys. Rev. Lett.* **66**, 500 (1991).
- [177] R.E. Schlier and H.E. Farnsworth, *J. Chem. Phys.* **30**, 917 (1959).
- [178] K. Takayanagi, Y. Tanishiro, S. Takahashi, and M. Takahashi, *Surf. Sci.* **164**, 367 (1985).
- [179] W.A. Harrison, *Surf. Sci.* **55**, 1 (1976).
- [180] F.J. Himpsel, *Phys. Rev. B* **27**, 7782 (1983).
- [181] E.G. McRae, *Phys. Rev. B* **28**, 2305 (1983).
- [182] I. Štich, M.C. Payne, R.D. King-Smith, J-S. Lin, and L.J. Clarke, *Phys. Rev. Lett.* **68**, 1351 (1992).
- [183] K.D. Brommer, M. Needels, B. Larson, and J.D. Joannopoulos, *Phys. Rev. Lett.* **68**, 1355 (1992).
- [184] G.-X. Qian and D.J. Chadi, *Phys. Rev. B* **35**, 1288 (1987).
- [185] R.S. Becker, J.A. Golovchenko, G.S. Higashi, and B.S. Swartzentruber, *Phys. Rev. Lett.* **57**, 1020 (1986).
- [186] R.M. Feenstra and M.A. Lutz, *J. Vac. Sci. Technol. B* **9**, 716 (1991).
- [187] P. Martensson, W.-X. Ni, G.V. Hansson, J.M. Nicholls, and B. Reihl, *Phys. Rev. B* **36**, 5974 (1987).
- [188] R. I. G. Uhrberg, T. Kaurila, and Y.-C. Chao, *Phys. Rev. B* **58**, R1730 (1998).
- [189] J.M. Nicholls and B. Reihl, *Phys. Rev. B* **36**, 8071 (1987).
- [190] R. Wolkow and Ph. Avouris, *Phys. Rev. Lett.* **60**, 1049 (1988).
- [191] R.J. Hamers, R.M. Tromp, and J.E. Demuth, *Phys. Rev. Lett.* **56**, 1972 (1986).
- [192] S.H. Ke, T. Uda, and K. Terakura, *Phys. Rev. B* **62**, 15319 (2000).

- [193] S.Y. Tong, H. Huang, C.M. Wei, W.E. Packard, F.K. Men, G. Glander, and M.B. Webb, *J. Vac. Sci. Technol. A* **6**, 615 (1988).
- [194] R.I.G. Uhrberg, G.V. Hansson, U.O. Karlsson, J.M. Nicholls, P.E.S. Persson, S.A. Flodström, R. Engelhardt, and E.-E. Koch, *Phys. Rev. B* **31**, 3795 (1985).
- [195] R. Losio, K.N. Altmann, and F.J. Himpsel, *Phys. Rev. B* **61**, 10845 (2000).
- [196] R.J. Hamers, R.M. Tromp, and J.E. Demuth, *Surf. Sci.* **181**, 346 (1987).
- [197] Ph. Avouris and R. Wolkow, *Phys. Rev. B* **39**, 5091 (1989).
- [198] L. Stauffer, S. Van, D. Bolmont, J.J. Koulmann, and C. Minot, *Solid State Commun.* **85**, 935 (1993).
- [199] K.D. Brommer, M. Galván, A. Dal Pino Jr., and J.D. Joannopoulos, *Surf. Sci.* **314**, 57 (1994).
- [200] J.J. Lander, *Surf. Sci.* **1**, 125 (1964).
- [201] P.A. Bennett and M.W. Webb, *Surf. Sci.* **104**, 74 (1981).
- [202] W. Telieps and E. Bauer, *Surf. Sci.* **162**, 163 (1985).
- [203] A. Kirakosian, R. Bennewitz, J.N. Crain, Th. Fauster, J.-L. Lin, D.Y. Petrovykh, and F.J. Himpsel, *Appl. Phys. Lett.* **79**, 1608 (2001).
- [204] M. Henzler and R. Zhachuk, *Thin Solid Films* **428**, 129 (2003).
- [205] S.A. Teys, K.N. Romanyuk, R.A. Zhachuk, and B.Z. Olshanetsky, *Surf. Sci.* **600**, 4878 (2006).
- [206] D.-H. Oh, M.K. Kim, J.H. Nam, I. Song, C.-Y. Park, S.H. Woo, H.-N. Hwang, C.C. Hwang, and J.R. Ahn, *Phys. Rev. B* **77**, 155430 (2008).
- [207] R. Zhachuk and S. Pereira, *Phys. Rev. B* **79**, 077401 (2009).
- [208] M.K. Kim, D.-H. Oh, J. Baik, C. Jeon, I. Song, J.H. Nam, S.H. Woo, C.-Y. Park, and J.R. Ahn, *Phys. Rev. B* **81**, 085312 (2010).
- [209] A.N. Chaika, D.A. Fokin, S.I. Bozhko, A.M. Ionov, F. Debontridder, V. Dubost, T. Cren, and D. Roditchev, *J. Appl. Phys.* **105**, 034304 (2009).
- [210] D.J. Chadi, *Phys. Rev. Lett.* **59**, 1691 (1987).
- [211] J. Dąbrowski and M. Scheffler, *Appl. Surf. Sci.* **56-58**, 15 (1992).
- [212] M. Aono, Y. Hou, C. Oshima, and Y. Ishizawa, *Phys. Rev. Lett.* **49**, 567 (1982).
- [213] R.M. Tromp, R.G. Smeenk, F.W. Saris, and D.J. Chadi, *Surf. Sci.* **133**, 137 (1983).
- [214] B.W. Holland, C.B. Duke, and A. Paton, *Surf. Sci.* **140**, L269 (1984).

- [215] R. Felici, I.K. Robinson, C. Ottaviani, P. Imperatori, P. Eng, and P. Perfetti, *Surf. Sci.* **375**, 55 (1997).
- [216] H. Over, J. Wasserfall, W. Ranke, C. Ambiatello, R. Sawitzki, D. Wolf, and W. Moritz, *Phys. Rev. B* **55**, 4731 (1997).
- [217] D.J. Chadi, *J. Vac. Sci. Technol.* **16**, 1290 (1979).
- [218] D.J. Chadi, *Phys. Rev. Lett.* **43**, 43 (1979).
- [219] J.E. Northrup, *Phys. Rev. B* **47**, 10032 (1993).
- [220] P. Krüger and J. Pollmann, *Phys. Rev. Lett.* **74**, 1155 (1995).
- [221] R.M. Tromp, R.J. Hamers, and J.E. Demuth, *Phys. Rev. Lett.* **55**, 1303 (1985).
- [222] R.J. Hamers, R.M. Tromp, and J.E. Demuth, *Phys. Rev. B* **34**, 5343 (1986).
- [223] R.J. Hamers and U.K. Köhler, *J. Vac. Sci. Technol. A* **7**, 2854 (1989).
- [224] P.C. Weakliem, G.W. Smith, and E.A. Carter, *Surf. Sci.* **232**, L219 (1990).
- [225] X.R. Qin and M.G. Lagally, *Phys. Rev. B* **59**, 7293 (1999).
- [226] K. Hata, S. Yasuda, and H. Shigekawa, *Phys. Rev. B* **60**, 8164 (1999).
- [227] R.A. Wolkow, *Phys. Rev. Lett.* **68**, 2636 (1992).
- [228] H.J.W. Zandvliet, H.K. Louwsma, P.E. Hegeman, and B. Poelsema, *Phys. Rev. Lett.* **75**, 3890 (1995).
- [229] V.A. Ukraintsev and J.T. Yate, Jr., *Surf. Sci.* **346**, 31 (1996).
- [230] H.J.W. Zandvliet, *Surf. Sci.* **377**, 1 (1997).
- [231] M.A. Herman and H. Sitter, *Molecular Beam Epitaxy: Fundamentals and Current Status*, Ed. 2, Springer-Verlag, Berlin, 1996.
- [232] B. Voigtländer, *Surf. Sci. Rep.* **43**, 127 (2001).
- [233] K. Oura, V.G. Lifshits, A. Saranin, A.V. Zotov, and M. Katayama, *Surface Science: An Introduction*, Springer-Verlag, Berlin, 2003.
- [234] M.A. Herman, W. Richter, and H. Sitter, *Epitaxy: Physical Foundation and Technical Implementation*, Springer-Verlag, Berlin, 2004.
- [235] G. Rosenfeld, A.F. Becker, B. Poelsema, L.K. Verheij, and G. Comsa, *Phys. Rev. Lett.* **69**, 917 (1992).
- [236] T. Michely, M. Hohage, S. Esch, and G. Comsa, *Surf. Sci.* **349**, L89 (1996).
- [237] M.Y. Lai and Y.L. Wang, *Phys. Rev. B* **60**, 1764 (1999).

- [238] Y.L. Wang, A.A. Saranin, A.V. Zotov, M.Y. Lai, and H.H. Chang, *Int. Rev. Phys. Chem.* **27**, 317 (2008).
- [239] B. Voigtländer, M. Kästner, and P. Šmilauer, *Phys. Rev. Lett.* **81**, 858 (1998).
- [240] S.-F. Tsay, M.-H. Tsai, M.Y. Lai, and Y.L. Wang, *Phys. Rev. B* **61**, 2699 (2000).
- [241] A.M. Mebel, M.Y. Lai, and Y.L. Wang, *Chem. Phys. Lett.* **318**, 27 (2000).
- [242] Y.-P. Chiu, L.-W. Huang, C.-M. Wei, C.-S. Chang, and T.-T. Tsong, *Phys. Rev. Lett.* **97**, 165504 (2006).
- [243] I.-S. Hwang, M.-S. Ho, and T.T. Tsong, *Phys. Rev. Lett.* **83**, 120 (1999).
- [244] P.A. Bennett, M. Copel, D. Cahill, J. Falta, and R.M. Tromp, *Phys. Rev. Lett.* **69**, 1224 (1992).
- [245] M.-H. Tsai, J.D. Dow, P.A. Bennett, and D.G. Cahill, *Phys. Rev. B* **48**, 2486 (1993).
- [246] S.A. Parikh, M.Y. Lee, and P.A. Bennett, *J. Vac. Sci. Technol. A* **13**, 1589 (1995).
- [247] W.J. Ong and E.S. Tok, *Phys. Chem. Chem. Phys.* **9**, 991 (2007).
- [248] M. Odagiri, I. Mochizuki, Y. Shigeta, and A. Tosaka, *Appl. Phys. Lett.* **97**, 151911 (2010).
- [249] R.J. Wilson and S. Chiang, *Phys. Rev. Lett.* **58**, 2575 (1987).
- [250] T. Ichinokawa, T. Tani, and A. Sayama, *Surf. Sci.* **219**, 395 (1989).
- [251] T. Yao, S. Shinabe, and M. Yoshimura, *Appl. Surf. Sci.* **104/105**, 213 (1996).
- [252] G. Kinoda and K. Ogawa, *Surf. Sci.* **461**, 67 (2000).
- [253] M.V. Ivanchenko, E.A. Borisenko, V.G. Kotlyar, O.A. Utas, A.V. Zotov, A.A. Saranin, V.V. Ustinov, N.I. Solin, L.N. Romashev, and V.G. Lifshits, *Surf. Sci.* **600**, 2623 (2006).
- [254] K. Cho and E. Kaxiras, *Europhys. Lett.* **39**, 287 (1997).
- [255] K. Cho and E. Kaxiras, *Surf. Sci.* **396**, L261 (1998).
- [256] P. Sonnet, L. Stauffer, and C. Minot, *Surf. Sci.* **407**, 121 (1998).
- [257] C. Polop, E. Vasco, J. A. Martín-Gago, and J. L. Sacedón, *Phys. Rev. B* **66**, 085324 (2002).
- [258] E. Vasco, C. Polop, and E. Rodríguez-Cañás, *Phys. Rev. B* **67**, 235412 (2003).
- [259] E. Vasco, *Surf. Sci.* **575**, 247 (2005).
- [260] L. Vitali, M.G. Ramsey, and F.P. Netzer, *Phys. Rev. Lett.* **83**, 316 (1999).

- [261] L. Vitali, F.P. Leisenberger, M.G. Ramsey, and F.P. Netzer, *J. Vac. Sci. Technol. A* **17**, 1676 (1999).
- [262] A.V. Zotov, A.A. Saranin, V.G. Kotlyar, O.A. Utas, and Y.L. Wang, *Surf. Sci.* **600**, 1936 (2006).
- [263] Z.A. Ansari, T. Arai, and M. Tomitori, *Surf. Sci.* **574**, L17 (2005).
- [264] H.F. Ma, Z.H. Qin, M.C. Xu, D.X. Shi, H.-J. Gao, S. Wang, and S.T. Pantelides, *Phys. Rev. B* **75**, 165403 (2007).
- [265] M. Yoon, X. F. Lin, I. Chizhov, H. Mai, and R. F. Willis, *Phys. Rev. B* **64**, 085321 (2001).
- [266] D.-Y. Wang, L.-J. Chen, W. He, Q.-F. Zhan, and Z.-H. Cheng, *J. Phys. D: Appl. Phys.* **39**, 347 (2006).
- [267] H. Wang and Z.-Q. Zou, *Appl. Phys. Lett.* **88**, 103115 (2006).
- [268] J.-Z. Wang, J.-F. Jia, Z.-H. Xiong, and Q.-K. Xue, *Phys. Rev. B* **78**, 045424 (2008).
- [269] A.V. Zotov, D.V. Gruznev, O.A. Utas, V.G. Kotlyar, and A.A. Saranin, *Surf. Sci.* **602**, 391 (2008).
- [270] I.-S. Hwang, M.-S. Ho, and T.-T. Tsong, *Surf. Sci.* **514**, 309 (2002).
- [271] M.-S. Ho, I.-S. Hwang, and T.T. Tsong, *Surf. Sci.* **564**, 93 (2004).
- [272] F.-C. Chuang, B. Liu, C.-Z. Wang, T.-L. Chan, and K.-M. Ho, *Surf. Sci.* **598**, L339 (2005).
- [273] M.A.K. Zilani, H. Xu, T. Liu, Y.Y. Sun, Y.P. Feng, X.-S. Wang, and A.T.S. Wee, *Phys. Rev. B* **73**, 195415 (2006).
- [274] P. Sobotík, I. Ošťádal, and P. Kocán, *Surf. Sci.* **604**, 1778 (2010).
- [275] N. Mariotti, C. Didiot, E.F. Schwier, C. Monney, L.-E. Perret-Aebi, C. Battaglia, M.G. Garnier, and P. Aebi, *Surf. Sci.* **606**, 1755 (2012).
- [276] K. Wu, Y. Fujikawa, T. Briere, V. Kumar, Y. Kawazoe, and T. Sakurai, *Ultramicroscopy* **105**, 32 (2005).
- [277] K. Wu, *Sci. Tech. Adv. Mater.* **6**, 789 (2005).
- [278] J.-P. Chou, C.-R. Hsing, J.-C. Chen, J.-Y. Lee, and C.-M. Wei, *Surf. Sci.* **616**, 137 (2013).
- [279] J.-F. Jia, X. Liu, J.-Z. Wang, J.-L. Li, X.S. Wang, Q.-K. Xue, Z.-Q. Li, Z. Zhang, and S.B. Zhang, *Phys. Rev. B* **66**, 165412 (2002).

- [280] J.-F. Jia, J.-Z. Wang, X. Liu, X.S. Wang, Q.-K. Xue, Z.-Q. Li, and S.B. Zhang, *Nanotechnology* **13**, 736 (2002).
- [281] M. Yoshimura, K. Takaoka, T. Yao, T. Sato, T. Sueyoshi, and M. Iwatsuki, *Phys. Rev. B* **47**, 13930 (1993).
- [282] X.F. Lin, H.A. Mai, I. Chizhov, and R.F. Willis, *J. Vac. Sci. Technol. B* **14**, 995 (1996).
- [283] H.H. Chang, M.Y. Lai, J.H. Wei, C.M. Wei, and Y.L. Wang, *Phys. Rev. Lett.* **92**, 066103 (2004).
- [284] S. Gangopadhyay, T. Schmidt, and J. Falta, *Surf. Sci.* **552**, 63 (2004).
- [285] Z. Liu, H. Xie, D. Fang, F. Dai, Q. Xue, H. Liu, and J. Jia, *Appl. Phys. Lett.* **87**, 201908 (2005).
- [286] L. Zhang, S.B. Zhang, Q.-K. Xue, J.-F. Jia, and E.G. Wang, *Phys. Rev. B* **72**, 033315 (2005).
- [287] A. Ohtake, *Phys. Rev. B* **73**, 033301 (2006).
- [288] R.-W. Li, J.H.G. Owen, S. Kusano, and K. Miki, *Appl. Phys. Lett.* **89**, 073116 (2006).
- [289] H. Narita, A. Kimura, M. Taniguchi, M. Nakatake, T. Xie, S. Qiao, and H. Namatame, *Phys. Rev. B* **76**, 115405 (2007).
- [290] R.-W. Li, H. Liu, J.H.G. Owen, Y. Wakayama, K. Miki, and H.W. Yeom, *Phys. Rev. B* **76**, 075418 (2007).
- [291] H. Liu, J.-P. Chou, R.-W. Li, C.-M. Wei, and K. Miki, *Phys. Rev. B* **83**, 075405 (2011).
- [292] Q.H. Wang and M.C. Hersam, *Small* **4**, 915 (2008).
- [293] J.H. Byun, J.S. Shin, P.G. Kang, H. Jeong, and H.W. Yeom, *Phys. Rev. B* **79**, 235319 (2009).
- [294] M. Saito, H. Sasaki, M. Mori, T. Tambo, and C. Tatsuyama, *e-J. Surf. Sci. Nanotech.* **3**, 244 (2005).
- [295] H. Narita, A. Kimura, M. Taniguchi, M. Nakatake, T. Xie, S. Qiao, H. Namatame, S. Yang, L. Zhang, and E. G. Wang, *Phys. Rev. B* **78**, 115309 (2008).
- [296] J.H. Byun, J.R. Ahn, W.H. Choi, P.G. Kang, and H.W. Yeom, *Phys. Rev. B* **78**, 205314 (2008).
- [297] A.A. Baski, J. Nogami, and C.F. Quate, *Phys. Rev. B* **43**, 9316 (1991).
- [298] A.A. Saranin, A.V. Zotov, V.G. Kotlyar, H. Okado, M. Katayama, and K. Oura, *Surf. Sci.* **598**, 136 (2005).

- [299] A.V. Zotov, A.A. Saranin, V.G. Lifshits, J.-T. Ryu, O. Kubo, H. Tani, M. Katayama, and K. Oura, *Phys. Rev. B* **57**, 12492 (1998).
- [300] O.A. Utas, N.V. Denisov, V.G. Kotlyar, A.V. Zotov, A.A. Saranin, J.P. Chou, M.Y. Lai, C.M. Wei, and Y.L. Wang, *Surf. Sci.* **604**, 1116 (2010).
- [301] V.G. Kotlyar, A.V. Zotov, A.A. Saranin, E.N. Chukurov, T.V. Kasyanova, M.A. Cherevik, I.V. Pisarenko, H. Okado, M. Katayama, K. Oura, and V.G. Lifshits, *Phys. Rev. Lett.* **91**, 026104 (2003).
- [302] A.A. Saranin, A.V. Zotov, I.A. Kuyanov, M. Kishida, Y. Murata, S. Honda, M. Katayama, K. Oura, C.M. Wei, and Y.L. Wang, *Phys. Rev. B* **74**, 125304 (2006).
- [303] A.V. Zotov, O.A. Utas, V.G. Kotlyar, I.A. Kuyanov, and A.A. Saranin, *Phys. Rev. B* **76**, 115310 (2007).
- [304] M.Y. Lai, J.P. Chou, O.A. Utas, N.V. Denisov, V.G. Kotlyar, D. Gruznev, A. Matetsky, A.V. Zotov, A.A. Saranin, C.M. Wei, and Y.L. Wang, *Phys. Rev. Lett.* **106**, 166101 (2011).
- [305] O. Bunk, G. Falkenberg, L. Seehofer, J.H. Zeysing, R.L. Johnson, M. Nielsen, R. Feidenhans'l, and E. Landemark, *Appl. Surf. Sci.* **123-124**, 104 (1998).
- [306] O. Bunk, G. Falkenberg, J.H. Zeysing, R.L. Johnson, M. Nielsen, and R. Feidenhans'l, *Phys. Rev. B* **60**, 13905 (1999).
- [307] V.G. Kotlyar, A.V. Zotov, A.A. Saranin, T.V. Kasyanova, M.A. Cherevik, O.V. Bekhtereva, M. Katayama, K. Oura, and V.G. Lifshits, *e-J. Surf. Sci. Nanotech.* **1**, 33 (2003).
- [308] J.R. Ahn, J.H. Byun, W.H. Choi, H.W. Yeom, H. Jeong, and S. Jeong, *Phys. Rev. B* **70**, 113304 (2004).
- [309] C. Zhu, A. Kawazu, S. Misawa, and S. Tsukahara, *Phys. Rev. B* **59**, 9760 (1999).
- [310] G.H. Coccoletzi and N. Takeuchi, *Surf. Sci.* **504**, 101 (2002).
- [311] V.G. Zavodinsky, *Surf. Sci.* **516**, 203 (2002).
- [312] V.G. Kotlyar, Yu.V. Luniakov, A.V. Zotov, and A.A. Saranin, *Surf. Sci.* **604**, 674 (2010).
- [313] T.M. Schmidt, J.L.P. Castineira, and R.H. Miwa, *Surf. Sci.* **482-485**, 1468 (2001).
- [314] N. Takeuchi, *Phys. Rev. B* **63**, 245325 (2001).
- [315] A.A. Saranin, A.V. Zotov, I.V. Pisarenko, V.G. Lifshits, M.K., and K. Oura, *Jpn. J. Appl. Phys.* **43**, 1110 (2004).
- [316] S. Vandr e, T. Kalka, C. Preinesberger, I. Manke, H. Eisele, M. D ahne-Prietsch, R. Meier, E. Weschke, and G. Kaindl, *Appl. Surf. Sci.* **123-124**, 100 (1998).

- [317] A. Imai, H. Kakuta, K. Mawatari, A. Harasawa, N. Ueno, T. Okuda, and K. Sakamoto, *Appl. Surf. Sci.* **256**, 1156 (2009).
- [318] A.L. Allred, *J. Inorg. Nucl. Chem.* **17**, 215 (1961).
- [319] C. Battaglia, P. Aebi, and S.C. Erwin, *Phys. Rev. B* **78**, 075409 (2008).
- [320] R. Seiwatz, *Surf. Sci.* **2**, 473 (1964).
- [321] S. Vandr e, *Growth and electronic structure of lanthanide silicides on Si(111) and Si(001)*, PhD thesis, Technische Universit at Berlin, 2000.
- [322] J.L. McChesney, A. Kirakosian, R. Bennewitz, J.N. Crain, J.-L. Lin, and F.J. Himpsel, *Nanotechnology* **13**, 545 (2002).
- [323] P. Paki, U. Kafader, P. Wetzel, C. Pirri, J.C. Peruchetti, D. Bolmont, and G. Gewinner, *Phys. Rev. B* **45**, 8490 (1992).
- [324] P. Wetzel, C. Pirri, P. Paki, J.C. Peruchetti, D. Bolmont, and G. Gewinner, *Solid State Commun.* **82**, 235 (1992).
- [325] L. Stauffer, A. Mharchi, C. Pirri, P. Wetzel, D. Bolmont, G. Gewinner, and C. Minot, *Phys. Rev. B* **47**, 10555 (1993).
- [326] P. Wetzel, C. Pirri, P. Paki, D. Bolmont, and G. Gewinner, *Phys. Rev. B* **47**, 3677 (1993).
- [327] C. Rogero, C. Koitzsch, M.E. Gonz alez, P. Aebi, J. Cerd a, and J.A. Mart n-Gago, *Phys. Rev. B* **69**, 045312 (2004).
- [328] M. Wanke, M. Franz, M. Vetterlein, G. Pruskil, B. H opfner, C. Prohl, I. Engelhardt, P. Stojanov, E. Huwald, J.D. Riley, and M. D ahne, *Surf. Sci.* **603**, 2808 (2009).
- [329] P. Wetzel, S. Saintenoy, C. Pirri, D. Bolmont, and G. Gewinner, *Phys. Rev. B* **50**, 10886 (1994).
- [330] L. Stauffer, A. Mharchi, S. Saintenoy, C. Pirri, P. Wetzel, D. Bolmont, and G. Gewinner, *Phys. Rev. B* **52**, 11932 (1995).
- [331] J.A. Mart n-Gago, J.M. G omez-Rodr guez, and J.Y. Veullen, *Surf. Sci.* **366**, 491 (1996).
- [332] C. Rogero, J.A. Mart n-Gago, and J.I. Cerd a, *Phys. Rev. B* **74**, 121404 (2006).
- [333] P. Wetzel, L. Haderbache, C. Pirri, J.C. Peruchetti, D. Bolmont, and G. Gewinner, *Surf. Sci.* **251/252**, 799 (1991).
- [334] M. Wanke, K. L oser, G. Pruskil, and M. D ahne, *Phys. Rev. B* **79**, 155428 (2009).
- [335] I. Horcas, R. Fern andez, J.M. G omez-Rodr guez, J. Colchero, J. G omez-Herrero, and A.M. Baro, *Rev. Sci. Instrum.* **78**, (2007).

- [336] J.P. Ibe, P.P. Bey, S.L. Brandow, R.A. Brizzolara, N.A. Burnham, D.P. DiLella, K.P. Lee, C.R.K. Marrian, and R.J. Colton, *J. Vac. Sci. Technol. A* **8**, 3570 (1990).
- [337] A.J. Melmed, *J. Vac. Sci. Technol. B* **9**, 601 (1991).
- [338] I. Ekvall, E. Wahlström, D. Claesson, H. Olin, and E. Olsson, *Meas. Sci. Technol.* **10**, 11 (1999).
- [339] P. Bedrossian, R.D. Meade, K. Mortensen, D.M. Chen, J.A. Golovchenko, and D. Vanderbilt, *Phys. Rev. Lett.* **63**, 1257 (1989).
- [340] T.C. Shen, C. Wang, J.W. Lyding, and J.R. Tucker, *Phys. Rev. B* **50**, 7453 (1994).
- [341] A.V. Zotov, M.A. Kulakov, S.V. Ryzhkov, A.A. Saranin, V.G. Lifshits, B. Bullemer, and I. Eisele, *Surf. Sci.* **345**, 313 (1996).
- [342] K. Löser, *Strukturelle und elektronische Eigenschaften von Silizid- Nanodrähten auf Si(557)*, Diploma thesis, Technische Universität Belin, 2007.
- [343] J. Reichow, *Technical Reference Manual: DCA Instruments High Temperature Effusion Cell 2000 °C Series (Model DCA EC 2000-6-35-21)*, DCA Instruments Oy, 2011.
- [344] J.C. Bean, *Appl. Phys. Lett.* **33**, 654 (1978).
- [345] U. König, H. Kibbel, and E. Kasper, *J. Vac. Sci. Technol.* **16**, 985 (1979).
- [346] M. Tabe and K. Kajiyama, *Jpn. J. Appl. Phys.* **22**, 423 (1983).
- [347] R.A. Metzger and F.G. Allen, *J. Appl. Phys.* **55**, 931 (1984).
- [348] H. Jorke, H.-J. Herzog, and H. Kibbel, *Appl. Phys. Lett.* **47**, 511 (1985).
- [349] H.J. Osten, J. Klatt, G. Lippert, B. Dietrich, and E. Bugiel, *Phys. Rev. Lett.* **69**, 450 (1992).
- [350] M. Copel, M.C. Reuter, M. Horn-von Hoegen, and R.M. Tromp, *Phys. Rev. B* **42**, 11682 (1990).
- [351] M. Horn-von Hoegen, F.K. LeGoues, M. Copel, M.C. Reuter, and R.M. Tromp, *Phys. Rev. Lett.* **67**, 1130 (1991).
- [352] M. Horn-von Hoegen, M. Copel, J.C. Tsang, M.C. Reuter, and R.M. Tromp, *Phys. Rev. B* **50**, 10811 (1994).
- [353] M. Horn-von Hoegen, *Appl. Phys. A* **59**, 503 (1994).
- [354] B. Voigtländer and A. Zinner, *J. Vac. Sci. Technol. A* **12**, 1932 (1994).
- [355] C.-Y. Park, T. Abukawa, T. Kinoshita, Y. Enta, and S. Kono, *Jpn. J. Appl. Phys.* **27**, 147 (1988).

- [356] T. Abukawa, C.Y. Park, and S. Kono, *Surf. Sci.* **201**, L513 (1988).
- [357] P. Mårtensson, G. Meyer, N.M. Amer, E. Kaxiras, and K.C. Pandey, *Phys. Rev. B* **42**, 7230 (1990).
- [358] H.B. Elswijk, D. Dijkkamp, and E.J. van Loenen, *Phys. Rev. B* **44**, 3802 (1991).
- [359] V.G. Lifshits, A.A. Saranin, and A.V. Zotov, *Surface Phases on Silicon*, Wiley, New York, 1994.
- [360] Y. Kusumi, K. Fujita, and M. Ichikawa, *Surf. Sci.* **372**, 28 (1997).
- [361] K.-H. Park, J.S. Ha, W.S. Yun, E.-H. Lee, J.-Y. Yi, and S.-J. Park, *J. Vac. Sci. Technol. A* **15**, 1572 (1997).
- [362] A.A. Saranin, A.V. Zotov, V.G. Lifshits, O. Kubo, T. Harada, M. Katayama, and K. Oura, *Surf. Sci.* **447**, 15 (2000).
- [363] V.K. Paliwal, A.G. Vedeshwar, and S.M. Shivaprasad, *Surf. Sci.* **513**, L397 (2002).
- [364] L. Lapena, P. Müller, G. Quentel, H. Guesmi, and G. Tréglia, *Appl. Surf. Sci.* **212-213**, 715 (2003).
- [365] M.T. Cuberes, H. Ascolani, M. Moreno, and J.L. Sacedón, *J. Vac. Sci. Technol. B* **14**, 1655 (1996).
- [366] Y. Kusumi, K. Fujita, and M. Ichikawa, *J. Vac. Sci. Technol. A* **15**, 1603 (1997).
- [367] S.A. Barnett, H.F. Winters, and J.E. Greene, *Surf. Sci.* **165**, 303 (1986).
- [368] B. Cordero, V. Gomez, A.E. Platero-Prats, M. Reves, J. Echeverria, E. Cremades, F. Baragan, and S. Alvarez, *Dalton Trans.* **2008**, 2832 (2008).
- [369] A. Ichimiya, T. Hashizume, K. Ishiyama, K. Motai, and T. Sakurai, *Ultramicroscopy* **42-44**, 910 (1992).
- [370] W. Shimada and H. Tochihara, *J. Cryst. Growth* **237-239**, 35 (2002).
- [371] S. Filimonov, V. Cherepanov, Y. Hervieu, and B. Voigtländer, *Phys. Rev. B* **76**, 035428 (2007).
- [372] S.N. Filimonov, V. Cherepanov, Yu. Hervieu, and B. Voigtländer, *Surf. Sci.* **601**, 3876 (2007).
- [373] B. Voigtländer and T. Weber, *Phys. Rev. Lett.* **77**, 3861 (1996).
- [374] J. Mysliveček, T. Jarolímek, P. Šmilauer, B. Voigtländer, and M. Kästner, *Phys. Rev. B* **60**, 13869 (1999).
- [375] E. Martínez-Guerra, G. Falkenberg, R.L. Johnson, and N. Takeuchi, *Phys. Rev. B* **73**, 075302 (2006).

- [376] J.E. Northrup, Phys. Rev. Lett. **57**, 154 (1986).
- [377] J. Nogami, S.-il Park, and C.F. Quate, J. Vac. Sci. Technol. B **6**, 1479 (1988).
- [378] M. Yoon and R.F. Willis, Surf. Sci. **512**, 255 (2002).
- [379] T. Nagao, S. Yaginuma, T. Inaoka, and T. Sakurai, Phys. Rev. Lett. **97**, 116802 (2006).
- [380] C. Tegenkamp, Z. Kallassy, H. Pfnür, H.-L. Günter, V. Zielasek, and M. Henzler, Phys. Rev. Lett. **95**, 176804 (2005).
- [381] K.S. Kim, H. Morikawa, W.H. Choi, and H.W. Yeom, Phys. Rev. Lett. **99**, 196804 (2007).
- [382] M. Wanke, M. Franz, M. Vetterlein, G. Pruskil, C. Prohl, B. Höpfner, P. Stojanov, E. Huwald, J.D. Riley, and M. Dähne, J. Appl. Phys. **108**, 64304 (2010).
- [383] I. Song, D.-H. Oh, J.H. Nam, M.K. Kim, C. Jeon, C.-Y. Park, S.H. Woo, and J.R. Ahn, New J. Phys. **11**, 063034 (2009).
- [384] B.G. Shin, M.K. Kim, D.-H. Oh, I. Song, J.H. Lee, S.H. Woo, C.-Y. Park, and J.R. Ahn, Appl. Phys. Lett. **102**, 201611 (2013).
- [385] A.K.S. Chauhan, N.M. Eldose, M. Mishra, A. Niazi, L. Nair, and G. Gupta, Appl. Surf. Sci. **314**, 586 (2014).
- [386] C. Preinesberger, S. Vandr e, T. Kalka, and M. D ahne-Prietsch, J. Phys. D: Appl. Phys. **31**, L43 (1998).
- [387] Y. Chen, D.A.A. Ohlberg, G. Medeiros-Ribeiro, Y.A. Chang, and R.S. Williams, Appl. Phys. Lett. **76**, 4004 (2000).
- [388] J. Nogami, B.Z. Liu, M.V. Katkov, C. Ohbuchi, and N.O. Birge, Phys. Rev. B **63**, 233305 (2001).
- [389] C. Preinesberger, S.K. Becker, S. Vandr e, T. Kalka, and M. D ahne, J. Appl. Phys. **91**, 1695 (2002).
- [390] B.Z. Liu and J. Nogami, J. Appl. Phys. **93**, 593 (2003).
- [391] M. D ahne and M. Wanke, J. Phys.: Condens. Matter **25**, 014012 (2013).
- [392] P.A. Bennett, M.Y. Lee, S.A. Parikh, K. Wurm, and R.J. Phaneuf, J. Vac. Sci. Technol. A **13**, 1728 (1995).
- [393] J.A. Stroscio and D.M. Eigler, Science **254**, 1319 (1991).
- [394] J.J. Boland, Science **262**, 1703 (1993).
- [395] C Preinesberger, S.K. Becker, and M. D ahne, AIP Conf. Proc. **696**, 837 (2003).

- 
- [396] B.Z. Liu and J. Nogami, *Surf. Sci.* **488**, 399 (2001).
- [397] B.Z. Liu and J. Nogami, *Surf. Sci.* **540**, 136 (2003).
- [398] M. Wanke, K. Löser, G. Pruskil, D.V. Vyalikh, S.L. Molodtsov, S. Danzenbächer, C. Laubschat, and M. Dähne, *Phys. Rev. B* **83**, 205417 (2011).
- [399] C. Preinesberger, G. Pruskil, S.K. Becker, M. Dähne, D.V. Vyalikh, S.L. Molodtsov, C. Laubschat, and F. Schiller, *Appl. Phys. Lett.* **87**, 083107 (2005).
- [400] Ch.R. Ashman, C.J. Först, K. Schwarz, and P.E. Blöchl, *Phys. Rev. B* **70**, 155330 (2004).
- [401] S. Appelfeller, private communication, 2015.
- [402] S. Kennou, J.-Y. Veullen, and T.A. Nguyen Tan, *Appl. Surf. Sci.* **56**, 520 (1992).
- [403] F. Palmino, S. Pelletier, E. Ehret, B. Gautier, and J.C. Labrune, *J. Vac. Sci. Technol. A* **18**, 2239 (2000).
- [404] Y. Chen, D.A.A. Ohlberg, and R.S. Williams, *J. App. Phys.* **91**, 3213 (2002).
- [405] D. Lee and S. Kim, *Appl. Phys. Lett.* **82**, 2619 (2003).
- [406] S. Appelfeller, S. Kuls, and M. Dähne, *Surf. Sci.* **641**, 180 (2015).
- [407] M.V. Bulanova, A.N. Mikolenko, K.A. Meleshevich, G. Effenberg, and P.A. Saltykov, *Z. Metallkd.* **90**, 216 (1999).
- [408] J.A. Martín-Gago, J.M. Gómez-Rodríguez, and J.Y. Veullen, *Phys. Rev. B* **55**, 5136 (1997).

---

# List of abbreviations

<b>AFM</b>	atomic force microscopy
<b>ARPES</b>	angle resolved photoelectron spectroscopy
<b>DAS</b>	dimer-atom-stacking fault
<b>DFT</b>	density functional theory
<b>DOS</b>	density of states
<b>fcc</b>	face centered cubic
<b>FHUC</b>	faulted half unit cell
<b>HCC</b>	honeycomb chain
<b>HLH</b>	high-low-high
<b>HOMO</b>	highest occupied molecular orbital
<b>HUC</b>	half unit cell
<b>LDOS</b>	local density of states
<b>LEED</b>	low energy electron diffraction
<b>LHL</b>	low-high-low
<b>LPE</b>	liquid phase epitaxy
<b>LUMO</b>	lowest unoccupied molecular orbital
<b>MBE</b>	molecular beam epitaxy
<b>MIGS</b>	metal-induced gap states
<b>ML</b>	monolayer
<b>MOVPE</b>	metalorganic vapor phase epitaxy
<b>PES</b>	photoelectron spectroscopy
<b>RDE</b>	reactive deposition epitaxy

<b>RE</b>	rare earth
<b>RHEED</b>	reflection high energy electron diffraction
<b>SC</b>	Seiwatz chain
<b>SMC</b>	surface magic cluster
<b>SPA-LEED</b>	spot-profile analysis LEED
<b>SPE</b>	solid phase epitaxy
<b>SPM</b>	scanning probe microscopy / microscope
<b>STM</b>	scanning tunneling microscopy / microscope
<b>STS</b>	scanning tunneling spectroscopy
<b>UFHUC</b>	unfaulted half unit cell
<b>UHV</b>	ultra-high vacuum
<b>VIGS</b>	virtual gap states
<b>XSTM</b>	cross-sectional scanning tunneling microscopy / microscope

---

# List of publications

## Parts of this work have been published in:

*Antimony induced cluster formation on the Si(111)7×7 surface*

S. Appelfeller, M. Franz, M. Dähne, Surf. Sci. **608**, 109 (2013).

*Formation and atomic structure of self-assembled Dy silicide clusters on the Si(111)7×7 surface*

M. Franz, S. Appelfeller, M. Rychetsky, M. Dähne, Surf. Sci. **609**, 215 (2013).

*Terbium induced nanostructures on Si(111)*

M. Franz, J. Große, R. Kohlhaas, M. Dähne, Surf. Sci. **637-638**, 149 (2015).

## Further publications:

*Energy surfaces of rare-earth silicide films on Si(111)*

M. Wanke, M. Franz, M. Vetterlein, G. Pruskil, B. Höpfner, C. Prohl, I. Engelhardt, P. Stojanov, E. Huwald, J. D. Riley, and M. Dähne, Surf. Sci. **603**, 2808 (2009).

*Electronic properties of dysprosium silicide nanowires on Si(557)*

M. Wanke, M. Franz, M. Vetterlein, G. Pruskil, C. Prohl, B. Höpfner, P. Stojanov, E. Huwald, J. D. Riley, and M. Dähne, J. Appl. Phys. **108**, 64304 (2010).



---

# Instruction of students

**Parts of the results of this thesis were obtained within the following student theses, which were performed under my guidance:**

S. Appelfeller, *Wachstum von Antimon- und Dysprosiumclustern auf Siliziumoberflächen*, Master thesis, Technische Universität Berlin, 2011.

Parts of chapters 5 and 8.

J. Schmermbeck, *Eigenschaften von Indium – Clustern auf Siliziumoberflächen*, Master thesis, Technische Universität Berlin, 2013.

Parts of chapter 6.

J. Große, *Elektronische Eigenschaften von Silizid-Nanostrukturen auf der Si(111)-Oberfläche*, Master thesis, Technische Universität Berlin, 2015.

Parts of chapters 7 and 9.

S. Appelfeller, *STM-Untersuchung von Silizidclustern auf Siliziumoberflächen*, Bachelor thesis, Technische Universität Berlin, 2009.

Parts of chapter 7.

M. Rychetsky, *Struktur von Dysprosiamsilizidclustern auf der Si(111)-Oberfläche*, Bachelor thesis, Technische Universität Berlin, 2010.

Parts of chapter 7.

M. Theurer, *Wachstum von Dysprosiamsilizid-Submonolagen auf Si(001)*, Bachelor thesis, Technische Universität Berlin, 2011.

Parts of chapter 8.

R. Kohlhaas, *Untersuchung von Terbium-Nanostrukturen auf der Si(111)-Oberfläche*, Bachelor thesis, Technische Universität Berlin, 2013.

Parts of chapters 7 and 9.

**Further guidance of students not related to the present thesis:**

M. Sauppe, *Oberflächenuntersuchungen an Gruppe-III-Nitrid-Halbleitern*,  
Bachelor thesis, Technische Universität Berlin, 2009.

T. Brückmann, *Homoepitaxie von Silizium auf verschieden orientierten Substraten*,  
Bachelor thesis, Technische Universität Berlin, 2011.

L.S. Hoppe, *Wachstum von Übergangsmetallsilizid-Nanostrukturen auf Silizium*,  
Bachelor thesis, Technische Universität Berlin, 2011.

M. Kubicki, *Überwachen von Silizid-Nanodrähten*,  
Bachelor thesis, Technische Universität Berlin, 2012.

K. Irmer, *Rastertunnelspektroskopie an  $DySi_2$ -Nanodrähten auf  $Si(001)$* ,  
Bachelor thesis, Technische Universität Berlin, 2012.

Guidance in cooperation with S. Appelfeller.

---

# Acknowledgments

At this point, I want to express my thanks to all the people that contributed to the success of this thesis.

At first, I would like to acknowledge Prof. Dr. Mario Dähne, not only for supervising this thesis, but also for giving me the opportunity to work, to study, and to teach in his group. Thank you for your support and the possibility to research freely in this fascinating field, your enthusiasm for new results and physics in general, and for the careful proofreading of this thesis.

Dr. Philipp Ebert is gratefully acknowledged for refereeing this thesis. Thank you very much for your interest in my work and many inspiring discussions during your stays in Berlin.

Furthermore, I thank Prof. Dr. Thomas Möller for chairing the final defense.

My special thanks go to all students, who completed their master and bachelor theses under my guidance. Thank you for your support at experiments, maintenance, and repairs and with this for contributing to the successful operation of the “old STM-setup”. With their measurements, Stephan Appelfeller, Jan Große, Julia Schmermbeck, Robert Kohlhaas, Monir Rychetsky, and Michael Theurer greatly contributed to this work.

My deepest thanks belong to Dr. Andrea Lenz, Christopher Prohl, Stephan Appelfeller, Dr. Holger Eisele and all the current and former members of the AG Dähne for creating a great atmosphere, their helpfulness, and many nice discussions not only during the daily work, but also on various “Ostsee” seminars and all the private get-togethers. I will never forget the great experiences we had.

I additionally thank Dr. Andrea Lenz, Dr. Rainer Timm, and Dr. Martina Wanke for bringing me in touch with the fascinating technique of scanning tunneling microscopy and Dr. Andrea Lenz for the very nice time in the shared office.

Dr. Holger Eisele is gratefully acknowledged for many fruitful discussions and for teaching me not only many science related things, but also for sharing his huge knowledge on how to construct UHV systems and STMs with me.

Ein großer Dank geht auch an Angela Berner. Deine Arbeit, die für uns oft im Verborgenen stattfindet, ermöglichte es mir, mehr Zeit für die wissenschaftliche Arbeit zu haben.

Jörg Döhring danke ich für die Unterstützung in allen technischen Angelegenheiten, die für den erfolgreichen Betrieb der experimentellen Apparaturen so wichtig war.

Ein besonderer Dank gilt den Mitarbeiter\_innen der feinmechanischen Werkstatt, die, auch wenn es mal schnell gehen musste, immer halfen und bei der Anfertigung der vielen ungeliebten Molybdäen Probenhalter stets gut gelaunt und hilfsbereit blieben.

Prof. Dr. Karsten Reuter, Dr. Dennis Palagin, and Dr. Chiara Panosetti from the Technische Universität München as well as Prof. Dr. Wolf Gero Schmidt und Dr. Simone Sanna from the University of Paderborn are gratefully acknowledged for the fruitful cooperation.

Mein großer Dank gilt meiner Familie für ihr Interesse an meiner Arbeit und die großartige Unterstützung über all die Jahre des Studiums und der Promotion.

Ein ganz besonders großes Dankeschön geht an meine Frau Mareike Blank. Danke für die großartige Unterstützung während aller Phasen der Promotion, ob während der Experimente, als sich oft genug die STM-Spitze genau dann änderte und gute Ergebnisse brachte, wenn man eigentlich verabredet war, während diverser Nachtschichten aber auch insbesondere während der Zeit des Schreibens dieser Arbeit.

This work was supported by the Elsa-Neumann-Stipendium des Landes Berlin and the Deutsche Forschungsgemeinschaft through FOR1282 project D.